

# **Low-Noise Cost-Efficient Nanowire Structures for Biosensing Applications**

Vorgelegt in der Fakultät Physik der Technische Universität  
Dortmund zur Erlangung des akademischen Grades eines Doktors  
der Naturwissenschaften

von

Master of Science

**Volodymyr Handziuk**

aus Kryzhopil

Winniza Region, Ukraine



*To my family*



# TABLE OF CONTENTS

<b>TABLE OF CONTENTS</b> . . . . .	<b>v</b>
<b>ABSTRACT</b> . . . . .	<b>vii</b>
<b>ZUSAMMENFASSUNG</b> . . . . .	<b>ix</b>
<b>ACKNOWLEDGMENTS</b> . . . . .	<b>xi</b>
<b>1 INTRODUCTION</b> . . . . .	<b>1</b>
1.1 Common Biosensing Approaches . . . . .	3
1.1.1 Optical Biosensors . . . . .	4
1.1.2 Techniques Based on Field-Effect Transistors . . . . .	14
1.2 Nanowire-Based Biosensors . . . . .	19
1.2.1 Current Fabrication Technologies . . . . .	20
1.2.2 Advantages and Applications of Nanowire Biosensors . . . . .	25
1.2.3 Main Challenges . . . . .	28
1.3 Noise Spectroscopy Techniques . . . . .	29
1.3.1 What is Electrical Noise? . . . . .	29
1.3.2 Theoretical Background . . . . .	30
1.3.3 Noise Components . . . . .	31
1.3.4 Noise Spectroscopy for Biosensing . . . . .	38
1.4 Summary . . . . .	39
<b>2 OPTIMIZATION OF Si &amp; Au NWs FABRICATION TECHNOLOGY</b> . . . . .	<b>41</b>
2.1 Fabrication of Si NW Biosensors . . . . .	41
2.1.1 Fabrication of Si NW Mold . . . . .	42
2.1.2 Si NW FET Fabrication . . . . .	46
2.1.3 Fabrication of Nanoribbons and Patterned NW Structures . . . . .	53
2.2 Fabrication of Tunable Nanoconstrictions . . . . .	58
2.3 Summary . . . . .	60
<b>3 MODERNIZATION OF TRANSPORT CHARACTERIZATION SETUPS</b> . . . . .	<b>61</b>
3.1 Automation of Experimental Setups . . . . .	61
3.1.1 Transport Characterization . . . . .	61
3.1.2 Low-Frequency Noise Spectroscopy . . . . .	68

---

3.2	Development of Microfluidics for FET Biosensors . . . . .	73
3.3	Summary . . . . .	75
<b>4</b>	<b>DEVELOPMENT OF Si NW-BASED BIOSENSORS . . . . .</b>	<b>77</b>
4.1	Characterization of Si NW FETs . . . . .	77
4.1.1	Electrical Transport Studies . . . . .	77
4.1.2	Noise Spectroscopy Characterization . . . . .	81
4.2	Si NWs: Towards the Detection of Cardiac Biomarkers . . . . .	84
4.2.1	Sensing of the Human C-Reactive Protein . . . . .	85
4.2.2	Human Cardiac Troponin I Sensing . . . . .	88
4.3	Summary . . . . .	93
<b>5</b>	<b>Au NW STRUCTURES FOR SINGLE MOLECULE SENSING . . . . .</b>	<b>95</b>
5.1	Ultrathin Au NW Structures . . . . .	95
5.1.1	Synthesis and Contacting of Ultrathin Au NWs . . . . .	96
5.1.2	Features of the Noise Behavior . . . . .	97
5.2	Investigations of Single (Bio)Molecules . . . . .	100
5.2.1	Features of Transport . . . . .	101
5.2.2	Conductance Traces of Tunable Nanoconstrictions . . . . .	102
5.3	Noise Spectroscopy of Molecular Junctions . . . . .	104
5.3.1	Peculiarities of the Flicker Noise Behavior . . . . .	104
5.4	Summary . . . . .	116
<b>6</b>	<b>CONCLUSIONS AND OUTLOOK . . . . .</b>	<b>119</b>
	<b>LIST OF ABBREVIATIONS . . . . .</b>	<b>123</b>
	<b>REFERENCES . . . . .</b>	<b>127</b>
	<b>PERSONAL PUBLICATION LIST . . . . .</b>	<b>143</b>

# ABSTRACT

The sensitive detection of different biochemical species is of great interest both for the fundamental research and for practical applications concerning the disease diagnostics and drug screening. The high demand in selective, sensitive, fast and low-cost diagnostic techniques has resulted in the rapid development of various-types biochemical sensors (biosensors). Being analytical devices for the qualitative or/and quantitative determination of biological targets, biosensors usually consist of three main components: a bioselective membrane, a physicochemical transducer, and a detector. Nanowires (NWs) have increased surface-to-volume ratios (SVRs) in comparison to bulk materials. This significantly enhances the role of the surface effects on the physicochemical properties of the NW-based devices, and thus makes them appealing for sensing applications. Specifically, nanowires can serve as efficient and highly-sensitive transducers, and therefore improve the sensing capabilities of biosensors.

This work describes the development of nanowire-based biochemical sensors. Efforts have been made to address several critical performance-regarding questions including:

- optimization of the fabrication technology;
- electrical transport and noise characterization of the fabricated structures, and finding their optimal operation regimes;
- optimization of the nanowire structures for *in-vitro* detection of biochemical species.

Liquid-gated (LG) silicon nanowire (Si NW) field-effect transistor (FET) devices are fabricated on the basis of *p*-type silicon-on-insulator (SOI) wafers using the “top-down” approach. The nanowire patterning is performed using thermal nanoimprint lithography (NIL). This technique allows reducing the fabrication cost while maintaining excellent spatial resolution (50 nm or below) and high CMOS-compatibility of the process. The nanoimprint process is developed for mr-I 70xx R thermal NIL resists with the optimized values for the imprint pressure  $P = 575$  PSI and temperature  $T = 140$  °C, respectively. It allows high-quality simultaneous patterning of the tiny nanowire structures and large feed lines and contact pads. The Si NW devices are designed and fabricated with different geometries (variable widths from 50 nm to 500 nm, and lengths from 2  $\mu$ m to 22  $\mu$ m) and configurations (accumulation-mode  $p^+ - p - p^+$  or  $n^+ - p - n^+$  inversion-mode FETs, depending on the impurity type chosen for the source and drain electrodes). The electrical current between the source and drain electrodes can be effectively controlled utilizing the electrolyte liquid gate and the back gate electrodes, thus allowing fine tuning of the conducting channel within the nanowire. The devices are characterized using current-voltage (I-V) measurements and low-frequency noise spectroscopy. The Si NW FETs

demonstrate high-quality transistor-type behavior of the electrical characteristics and stable operation without leakage currents. The obtained values of the threshold voltage  $V_{Th} \simeq 0.8$  V, the subthreshold swing  $SS \simeq 130$  mV dec<sup>-1</sup>, and the carrier mobility  $\mu \simeq 95$  cm<sup>2</sup> V<sup>-1</sup> s<sup>-1</sup> are in good agreement with reported literature for Si NW FET structures and indicate the excellent performance of the fabricated devices. The Si NW FETs are tested for the *in-vitro* detection of the important cardiac diseases biomarkers: C-reactive protein (CRP) and human cardiac troponin (cTn) I. The devices demonstrate linear response (in semi-logarithmic scale) of electrical characteristics to changes in analyte concentration in the range from 10 pg ml<sup>-1</sup> to 5 ng ml<sup>-1</sup> for CRP, and from 0.5 ng ml<sup>-1</sup> to 10 ng ml<sup>-1</sup> for cTnI, respectively. According to our measurements, the fabricated Si NWs exhibit superior sensitivity to the analyte-induced surface charge changes, and therefore they can serve as promising candidates for future applications in diagnostics and medicine.

This work also describes studies of unique metallic nanowire structures including ultrathin ( $\sim 2$  nm in diameter) chemically-synthesized gold nanowire (Au NW)-bundles and lithographic tunable gold nanoconstrictions ( $< 100$  nm in cross-section). It is revealed that the presence of organic molecules at the nanowire/contact interface, or on the NW surface, significantly alter the noise behavior of the system. Molecular interfaces between the contact and ultrathin Au NWs lead to the appearance of excess generation-recombination (GR) noise components with characteristic frequencies determined by the molecules.

Noise studies on tunable gold nanoconstrictions are performed for a wide range of the system resistances  $R$  from 10  $\Omega$  to 10 M $\Omega$ . The results reveal that the flicker noise level demonstrates characteristic power dependence on the system resistance  $S_I/I^2 \sim R^m$ ,  $m = 2 - 0.5$ . Changes of the exponent  $m$  magnitude are attributed to changes of the charge transport in the structure. Indeed, reducing the cross-section of the gold nanoconstriction due to controlled bending allows ballistic transport in the structure to be achieved. Furthermore, after the constriction breaking, the transport is defined by quantum tunneling through a nanosized gap. Modification of the sample surface with benzene-1,4-dithiol (BDT) molecules results in almost one order of magnitude decrease of the flicker noise level in the ballistic regime of the sample conductance. Models describing noise behavior for bare gold and BDT modified samples are developed and compared with the experimental data for three transport regimes: diffusive, ballistic and tunneling. Parameters extracted from models by fitting are used for the characterization of nanoconstriction devices. The results obtained indicate that ultrathin gold nanowires and tunable nanoconstrictions are promising for chemical and biochemical sensing, as well as for applications of molecular electronics.

# ZUSAMMENFASSUNG

Der sensitive Nachweis verschiedener biochemischer Spezies ist sowohl für die Grundlagenforschung als auch für praktische Anwendungen in der Krankheitsdiagnostik und beim Wirkstoffscreening von großem Interesse. Die hohe Nachfrage nach selektiven, sensitiven, schnellen und kostengünstigen Diagnosetechniken hat zur raschen Entwicklung von biochemischen Sensoren (Biosensoren) unterschiedlicher Art geführt. Als Analysegeräte für die qualitative und/oder quantitative Bestimmung biologischer Marker bestehen Biosensoren in der Regel aus drei Hauptkomponenten: einer bioselektiven Rezeptormembran oder -schicht, einem physikalisch-chemischen Wandler und einem Detektor. Nanodrähte (NWs) haben im Vergleich zu makroskopischen Materialien ein erhöhtes Oberflächen-Volumen-Verhältnis (SVRs). Dies erhöht den Einfluss der Oberflächenatome bzw. Oberflächeneffekte auf die physikalisch-chemischen Eigenschaften der NW-basierten Geräte erheblich, was auch für Sensoranwendungen attraktiv sind. Insbesondere können Nanodrähte als effiziente und hochempfindliche Wandler dienen und damit die Leistungsfähigkeit von Biosensoren verbessern.

Diese Arbeit beschreibt die Entwicklung von nanodrahtbasierten biochemischen Sensoren. Es wurden Anstrengungen unternommen, um mehrere kritische Leistungsmerkmale zu adressieren - unter anderem in Bezug auf die Fragen:

- Optimierung der Prozessierung;
- Elektrische Transport- und Rauschcharakterisierung der hergestellten Strukturen und Ermittlung der optimalen Bedingungen für ihren Betrieb;
- Optimierung der NW-Strukturen für den *in-vitro* Nachweis von biochemischen Spezies.

Flüssigkeitsgesteuerte (LG) Silizium-Nanodraht (Si NW) Feldeffekttransistoren (FET) werden auf der Basis von *p*-Typ Silizium-auf-Isolator (SOI)-Wafeln nach dem "Top-Down"-Ansatz hergestellt. Die Nanodrahtstrukturierung erfolgt mittels optimierter thermischer Nanoimprint-Lithographie (NIL). Diese Technik ermöglicht es, die Herstellungskosten zu senken, während gleichzeitig eine ausgezeichnete räumliche Auflösung (50 nm oder weniger) und eine hohe CMOS-Kompatibilität des Prozesses gewährleistet werden. Der Nanoimprint-Prozess wurde für thermische NIL-Lacke (mr-I 70xx R) mit den optimierten Werten für den Prägedruck  $P = 575$  PSI und der Temperatur  $T = 140$  °C entwickelt. Die Si NW-Transistoren wurden mit unterschiedlichen Geometrien (variable Breiten von 50 nm bis 500 nm und Längen von 2 µm bis 22 µm) und Konfigurationen (Akkumulationsmodus  $p^+ - p - p^+$  oder  $n^+ - p - n^+$  Inversionsmodus-FETs, je nach dem für die Source- und Drain-Elektroden gewählten Dotierungstyp) entworfen und hergestellt. Der elektrische Strom zwischen der Source- und der Drain-Elektrode kann unter

Verwendung des Flüssigkeitsgate-Elektrode bzw. der Backgate-Elektrode effektiv gesteuert werden. Die Bauelemente wurden durch Strom-Spannungsmessungen (I-V) und mit Hilfe der Niederfrequenzrauschspektroskopie charakterisiert. Die Si NW FETs zeigen hochwertig transistorartige Eigenschaften und einen stabilen Betrieb ohne Fehlerströme. Die erhaltenen Werte der Schwellenspannung  $V_{Th} \simeq 0.8$  V, des Unterschwellenschwungs  $SS \simeq 130$  mV dec<sup>-1</sup> und der Ladungsträgerbeweglichkeit  $95$  cm<sup>2</sup> V<sup>-1</sup> s<sup>-1</sup> stimmen gut mit der Literatur für Si NW FET-Strukturen überein und belegen die ausgezeichnete Leistungsdaten der hergestellten Bauelemente. Die Si NW FETs wurden für den *in-vitro*-Nachweis der wichtigsten Biomarker für Herzkrankheiten eingesetzt: C-reaktives Protein (CRP) und humanes kardiales Troponin (cTn) I. Die Sensoren zeigen eine lineare Abhängigkeit (im semilogarithmischen Maßstab) der elektrischen Eigenschaften von der Analytkonzentration im Bereich von 10 pg ml<sup>-1</sup> bis 5 ng ml<sup>-1</sup> für CRP und von 0.5 ng ml<sup>-1</sup> bis 10 ng ml<sup>-1</sup> für cTnI. Unseren Messungen zufolge zeigen die hergestellten Si NWs eine überragende Empfindlichkeit gegenüber analytassozierten Oberflächenladungsänderungen und können daher als vielversprechende Kandidaten für zukünftige Anwendungen in Diagnostik und Medizin angesehen werden.

Diese Arbeit beinhaltet auch Studien zu einzigartigen metallischen Nanodrahtstrukturen bestehend aus ultradünnen ( $\sim 2$  nm im Durchmesser), chemisch synthetisierten Gold-Nanodrähten (Au NW) bzw. aus lithografisch hergestellten Gold-Nanoeinschnürungen Nanokontakte ( $< 100$  nm im Querschnitt). Es wird gezeigt, dass das Vorhandensein organischer Moleküle an der Nanodraht/Kontakt-Schnittstelle oder an der NW-Oberfläche das Rauschverhalten des Systems signifikant verändert. Molekulare Schnittstellen zwischen dem Kontakt und ultradünnen AuNWs führen zum Auftreten von Rauschkomponenten mit charakteristischen Frequenzen, die charakteristisch für die untersuchten Moleküle sind.

Für einen großen Bereich an Systemwiderstände  $R$  von  $10 \Omega$  bis  $10 \text{ M}\Omega$  wurden Rauschuntersuchungen an den Goldnanoeinschnürungen durchgeführt. Die Ergebnisse zeigen, dass der Rauschpegel eine charakteristische Leistungsabhängigkeit vom Systemwiderstand  $S_I/I^2 \sim R^m$ ,  $m = 2 - 0.5$  aufweist. Änderungen des Exponenten  $m$  werden auf Veränderungen des Ladungstransports in der Struktur zurückgeführt. Die Reduzierung des Querschnitts der Goldnanoeinschnürung ermöglicht einen ballistischen Transport der Ladungsträger in der Struktur. Wird die Einschnürung gebrochen, so lässt sich der Transport durch den entstandenen Bruchkontakt mittels eines Quanten-Tunnel-Prozesses beschreiben. Die Modifizierung der Probenoberfläche mit Benzol-1,4-dithiolmolekülen (BDT) führt zu einem fast um eine Größenordnung geringeren Rauschpegel im ballistischen Regime der Probenleitfähigkeit. Modelle wurden entwickelt, die das Rauschverhalten für reine Gold und für BDT-modifizierte Proben beschreiben. Die Modelle wurden für drei Grenzfälle mit experimentellen Daten verglichen: Diffusion, ballistischer Transport und Tunneln. Parameter, die aus Modellen durch Anpassung extrahiert werden, wurden für die Charakterisierung von Nanoeinschnürungen verwendet. Ultradünne Gold-Nanodrähten und Nanoeinschnürungen für die chemische Sensorik vielversprechend sind.

# ACKNOWLEDGMENTS

I would like to thank to *Prof. Dr. Svetlana Vitusevich* for the support given to me during my master's and doctoral work. Thank you for the neat supervision and for a plenty of your great (sometimes incredible) ideas that helped me a lot to achieve success in my scientific work. Thank you for being constantly positive and supporting. You are always charging people around with your inexhaustible energy. The experience I gained being a part of your research group is priceless.

I am very appreciative to *Prof. Dr. Andreas Offenhäusser* for giving an opportunity to work in Forschungszentrum Jülich GmbH (FZJ). I enjoyed all my four years at the Bioelectronics (ICS-8) institute. Thank you very much for your great job in coordinating scientific life at the institute and for the excellent team-building. I enjoyed all summer and winter schools that I attended. I will never forget my hiking and climbing experience in mountains, as well as my first skiing adventure.

I thank to *Prof. Dr. Manfred Bayer* for acting as a co-supervisor for my PhD thesis.

I would like to thank *Dr. Dirk Mayer* for being the second supervisor during my master project. Thank you for a plenty of useful scientific discussions we had during all the time I spent at FZJ. They helped me a lot to achieve success in important parts of my work.

I would like to thank *Dr. Mykhailo Petrychuk*, *Dr. Sergii Pud*, and *Dr. Viktor Sydoruk* for help with practical and theoretical aspects of my research. It was a pleasure and honor to learn from you. You have made a significant contribution to my skills and knowledge.

I would like to express my sincere gratitude to *Maristella Coppola*. Thank you for introducing me to the nanofabrication technology, for your help, collaboration, and support. Thank you for being cheerful, friendly, and positive.

I am very grateful to my friend *Ihor Zadorozhnyi*. Thank you for your great support. It was a faith that after graduation from Taras Shevchenko National University of Kyiv I and you, one of my best friends, have chosen to start a scientific career and accidentally came to work at the same research group at the Bioelectronics (ICS-8) institute of the FZJ. Thank you for always being there helping and supporting me even in tough moments. It was a great pleasure to work and to spend a spare time with you.

I thank my friends *Hanna Hlukhova* and *Yurii Kutovyi* for their collaboration and cooperation in conducting experiments as well as for the wonderful spare time we spent together.

I acknowledge other members of our *Electronic Sensing* research group: *Nataliia Piechniakova*, *Nazarii Boichuk*, *Dr. Jie Li*, *Rasel Ferdaus* for a warm, friendly and collaborative

atmosphere.

I am thankful to our collaborators: *Prof. Ir. Lode Vandamme*, *Prof. Dr. F. Gasparyan*, *Dr. Nataliia Naumova*, *Dmytro Zhulai*, *Dr. Hongchu Du*, *Dr. Shigeru Tsukamoto*, and *Dr. Alexandre Kisner*. Thank you for the valuable contribution to our scientific work.

I am grateful to all members of the *ICS-8* institute for the nice and cooperative working environment. I especially thank *Bohdan Lenyk* and *Dr. Volker Schöps* for their collaboration and support.

I thank to all the Helmholtz Nanoelectronic Facility (HNF) staff for their assistance in technological processes. I am particularly grateful to *Dr. Stefan Trelenkamp* for the electron-beam patterning, and to *Dr. Elmar Neumann* for his help with scanning electron microscopy imaging and focused ion beam sectioning.

I am grateful to *Stefan Kirch* and all the staff of the *software* and *technical* branches of the institute *IT-department* for help with computers, software and hardware related issues, 3D printing, etc.

Lastly, I thank my *family* for support. Knowing that you always believe in me is one of the greatest sources of my inspiration and inner peace.

# INTRODUCTION

The question of healthcare has always been important to the mankind. Many efforts have been made to struggle against different diseases including those causing people's deaths. However, unfortunately not all illnesses are yet defeated. Nowadays, among the most widespread human mortality reasons cardiovascular diseases stay in the first place. According to the World Health Organization (WHO) report<sup>1</sup>, 17.9 million people around the World died from cardiovascular diseases in 2016, which is 31 % of all global deaths. Most of the deaths (around 85 %) were caused by heart attacks and strokes. If the current tendency continues, the number of deaths from cardiovascular diseases is expected to rise up to 22.2 million by 2030.

Science and medicine made a big step forward in recent years. Indeed, the achievements done helped to decrease the mortality a lot by providing a fast diagnosis and proper medical treatment. Among those, fast and reliable diagnosis plays a crucial role: the faster the diagnosis, the higher the probability to rescue a patient. Patients with weak hearts must regularly monitor their health. Nowadays, lots of techniques have already been developed to determine the state of the heart health and to predict an upcoming aggravation, e.g., acute myocardial infarction (AMI). Usually, special enzymes in blood or blood serum that can be found only in the case of heart injury or malfunction are used for diagnosis [1]. Increased levels of creatine kinase (CK), CK-myocardial band (MB), aspartate aminotransferase (AST) and lactate dehydrogenase (LDH) in blood are considered as symptoms of myocardial infarction according to WHO reports from 1979 [2]. However, more recently the Joint European Society of Cardiology and the American College of Cardiology Committee emphasized the importance of sensitive and serological biomarkers for the diagnosis of AMI and proposed cardiac troponin (cTn) as the gold standard [3]. Lagrand et al. revealed the link between the concentration of another biomarker C-reactive protein (CRP) and cardiovascular diseases [4]. Authors claimed that high CRP levels indicate body response to the inflammatory reactions in the coronary vessels and neighboring myocardium. Sensing of aforementioned biomolecules and tracking the development of their concentrations over time can provide useful or in some cases even vital information about the current state of the disease.

The highest mortality risk due to AMI occurs within the first few hours of onset of AMI. Thus, proper timing still remains a challenging issue. One of the most commonly used diagnostic techniques, which provides both high sensitivity and selectivity to target biomolecules (analyte) is the enzyme-linked immunosorbent assay (ELISA) [5]. However, the complete analysis using ELISA may require up to 6 h [6, 7]. Such a delay in applying medical treatment

---

<sup>1</sup>[http://www.who.int/cardiovascular\\_diseases/publications/en/](http://www.who.int/cardiovascular_diseases/publications/en/)

can be lethal for a patient. Furthermore, this approach requires expensive laboratory equipment and the presence of a well-trained operator, which makes the ELISA not well-suited for real biomedical applications. Therefore, the development of fast, precise and cost-efficient diagnostic techniques is of extreme importance. In this respect, biochemical sensors (biosensors) are perfect candidates for use in medical applications. A biosensor is an analytical device, used for the detection of an analyte. It combines a biological component (functional layer) with a physicochemical detector (transducer). Functional layer implements exclusive selectivity to the analyte. Interaction of the functional layer with analyte leads to change in its state, e.g., charge, which is then transformed into an electrical signal by a transducer and transferred via readout electronics to a personal computer (PC).

Nanosized devices based on nanowires are shown to be perfect candidates for the role of transducer elements in potentiometric chemical sensors and biosensors [8]. Silicon nanowire (Si NW) field-effect transistors (FETs), in particular, are attractive for real medical applications due to their remarkable properties such as biocompatibility, scalability, and reliability. Si NW FETs possess high surface-to-volume ratio, which makes them extremely sensitive to changes in surface potential. They can be fabricated using well-developed complementary metal-oxide-semiconductor (CMOS) compatible technology with good size/shape control, low device-to-device variation, and the possibility of mass-production. Devices based on Si NW FETs can be successfully utilized in a variety of different applications, including recordings of extracellular potentials of cardiac cells [9] and neuronal action potentials [10, 11]. Integrated electrical circuits, based on Si NW FETs, may be used for the mapping of signals from 2D artificial cellular networks with the future perspectives for real *in vivo* applications. Si NW FETs are also promising for applications in gas sensing [12], chemical and biosensing [13]. They were successfully applied for detection of various types of deoxyribonucleic acids (DNAs) [14–16] and antibodies [17, 18], viruses [19, 20], bacteria [21, 22], etc.

Metallic nanostructures can also be used for conductance-based sensing applications. At first look, metallic wires may seem not as sensitive to changes in surface charge as their semiconducting counterparts. The majority of semiconductor-based nanosized sensors work through analyte-induced modulation of the space-charge region. Typical Thomas-Fermi screening length in metals is approximately  $\sim 0.1$  nm [23], which testifies against this mechanism in metallic nanowires. However, as characteristic sizes of metallic nanostructures shrink down, the situation changes. The surface affects resistivity disproportionately for metal films thinner than the electron mean free path,  $\lambda_e$  [24]. Shrinking the dimensions of metal nanostructures enhances their surface-to-volume ratios (SVRs) and intensifies the contribution of each adsorbed molecule to the entire conductance change, thus achieving ultimately high sensitivity. In favorable cases, this sensitivity can approach the single molecule level [25].

This work describes the development of nanostructured biochemical sensors based on Si NW FETs and tunable gold nanoconstrictions. The first chapter of the work provides a brief

overview of several state of the art biosensing approaches that can be used for detection of target species. It also describes the theoretical and practical basics of measurement and analysis techniques used in the thesis. The second chapter of the work is devoted to technological aspects of devices fabrication. Nanoimprint technology and colloidal lithography are used as alternatives to the electron beam lithography (EBL) for cost-efficient fabrication of advanced Si NW FET based sensors. Tunable gold nanoconstrictions are fabricated on the basis of flexible substrates using electron beam lithography and reactive ion etching (RIE). The high quality of manufactured samples is confirmed by scanning electron microscopy (SEM), atomic force microscopy (AFM), and focused ion beam (FIB) sectioning. The second chapter also covers the modernization and automation of measurement setups for electrical transport and noise characterization of fabricated devices. The third chapter is describing results obtained on fabricated nanowire structures. It covers:

- The performance characterization of manufactured liquid-gated Si NW FET biosensors.
- A brief overview of surface functionalization procedure to create a bioselective membrane and thus implement superior biosensor selectivity.
- Application of the fabricated Si NW FET devices for the detection of biomarkers for cardiac diseases: CRP and cTn antigens. In addition to the standard  $I_D - V_G$  shift approach, the low-frequency noise spectroscopy is used as a novel promising non-destructive sensing technique.
- Studies of the noise behavior of ultrathin gold nanowire ( $< 2$  nm in diameter) bundles fabricated by wet chemical synthesis.
- Analysis of transport and flicker noise behavior of bare and molecule-modified tunable gold nanoconstrictions.

All the steps performed are important for the successful utilization of fabricated nanowire structures for biosensing purposes. The fourth and the last chapter contains a brief summary of the work and outlook.

## 1.1 Common Biosensing Approaches

Biosensing is a new branch of analytical biotechnology, one of the key concepts of which is the development of electrochemical biosensors. Important characteristics of biosensor devices are the high sensitivity and selectivity, ease of use, high detection speed, and broadness of the range of substances that can be detected. This defines the possibility and necessity of their use in different branches of human activities, including medical, pharmacological, food, and

biochemical industries, agriculture, environment protection, etc. Compared to other analytical techniques, biosensors can provide fast and reliable analysis of various biochemical substances at low-costs.

Generally, a biosensor can be considered as a device, which consists of two parts:

- a **bioselective element**, which is responsible for the selective recognition and transferring information from the biological domain to a chemical or physical output signal with defined sensitivity;
- a **transducer**, which is used to transform this signal into the electrical domain with its further transformation into an analytically interpretable information.

Usually, several chemical modification steps are needed to implement a proper bioselective membrane. They include surface treatment, immobilization of linker molecules and a biorecognition layer. The latter commonly consists of special biomolecules (either natural or synthesized) including antibodies, aptamers, DNAs, etc.

A variety of physical phenomena are considered when creating transducer elements. Depending on the transducer type, biosensors can be divided into a few large groups: electrical (amperometric, conductometric and potentiometric), optical, acoustic, etc. Several biosensor techniques that are most frequently used nowadays are described below.

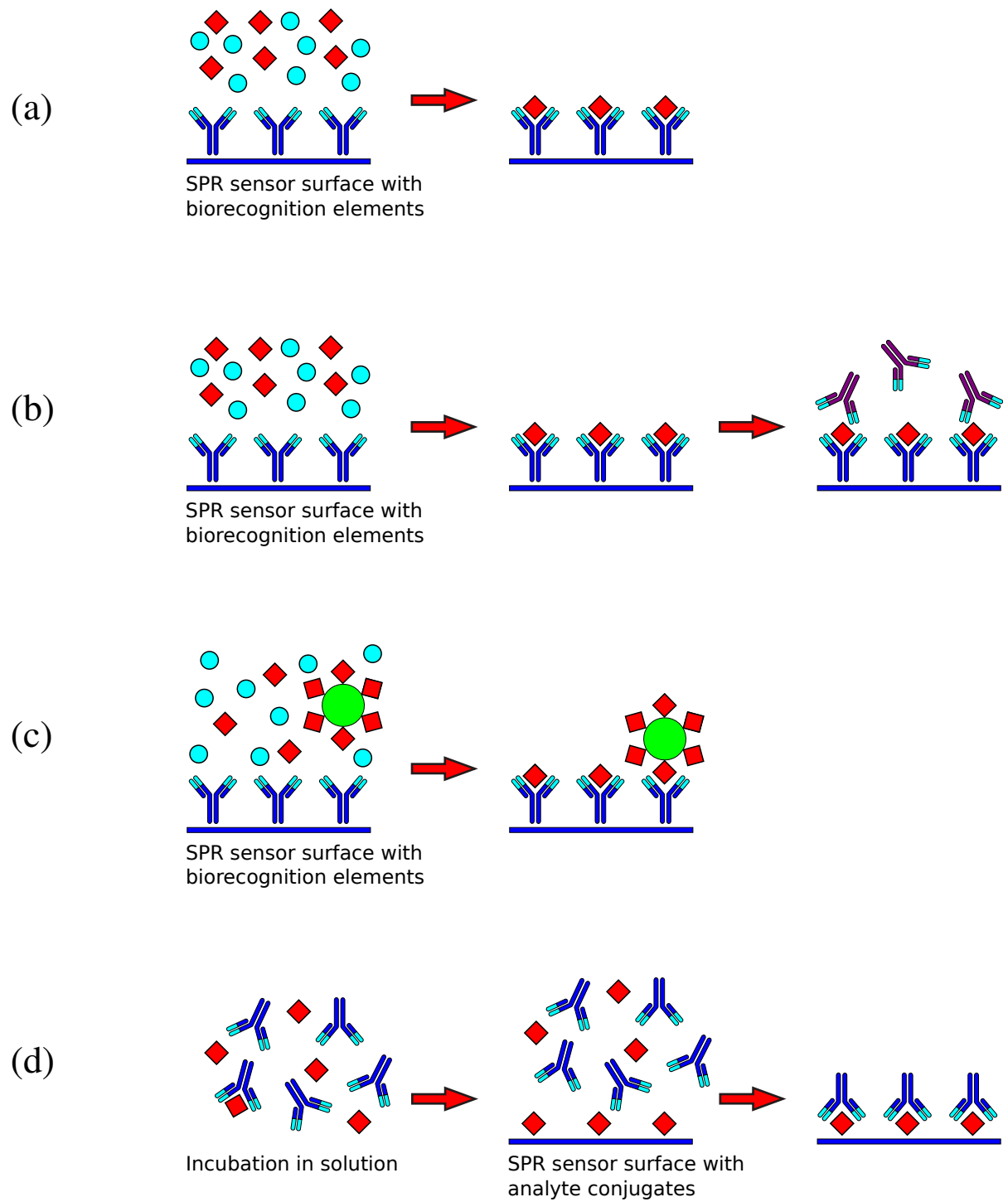
### 1.1.1 Optical Biosensors

Optical biosensors are one of the most common types of biosensor devices. They allow selective and sensitive detection of a wide range of analytes [26]. The detection principle of this type of sensors is based on measuring changes of the optical properties of the sensing medium (optical density, color, turbidity, refraction index, etc.) induced by the presence of a biological agent.

#### Techniques based on surface plasmon resonance

At present, optical biosensors based on the surface plasmon resonance (SPR) effect, are being extensively developed. The surface plasmon resonance phenomenon was discovered in 1902 and firstly used for biosensing applications in the second half of the XX century [27]. SPR occurs at the interface between two optical media with different refractive indices when the conditions of total internal reflection are fulfilled. Interaction of the analyte and bioselective element lead to changes in the refraction index that can be measured. The SPR technique allows label-free detection of intermolecular interactions in studied media.

In SPR biosensors biological receptor is immobilized on the sensor surface in order to minimize non-specific bindings to the surface and to eliminate its own biological influence. The



## Designations:

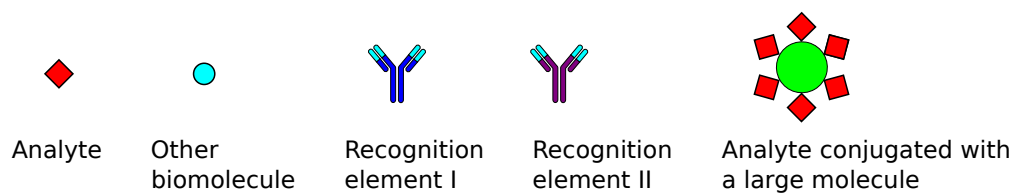


**Figure 1.1:** SPR detection techniques: (a) direct detection; (b) sandwich detection format; (c) competitive detection; (d) inhibitive detection.

most common three-dimensional matrix for immobilization of molecules in a structured environment is carboxymethylated dextran. Self-assembled monolayers (SAMs) of alkanethiols and disulfides are widely used for two-dimensional (surface) immobilization of biological receptors to the active sensing surface (usually gold) [28]. There are several approaches to biomolecule detection using SPR: “direct”, “sandwich”, “competitive”, and “inhibitive”. Sketches of the aforementioned SPR techniques are shown in **Figure 1.1**.

In the direct configuration, biological receptors, e.g., antibodies are immobilized on the SPR sensing surface. Analyte molecules, which are in the solution, bind receptors on the surface inducing changes in its refractive index (see **Figure 1.1** (a)). These changes are then attributed to the concentration of analyte molecules.

Specificity and sensitivity can be improved using the sandwich detection configuration. In this approach (see **Figure 1.1** (b)) the SPR sensing surface is firstly modified with capture antibodies and then the analyte solution is introduced. After target molecules are captured, the sensing surface is incubated with special secondary antibodies and detection is performed.

Small analyte molecules (molecular weight < 5 kDa) often do not induce significant changes in refractive index and therefore are measured using competitive or inhibitive detection configurations (see **Figure 1.1** (c) and (d), respectively). In the competitive measurement mode the sensing surface is covered with antibodies specific to the analyte. Then conjugated analyte is added to the probe. The analyte and its conjugated form are competing for a limited number of binding sites on the sensor surface. Sensor response is inversely proportional to the analyte concentration.

In the inhibitive measurement mode, a constant concentration of antibodies (similar to the concentration of the analyte) is mixed with the probe, containing an unknown concentration of the studied substance. This mixture is introduced into the flow cell of the SPR sensor. It flows in the vicinity of the sensing surface, where analyte or its analog is immobilized. Non-complex antibodies are measured when they bind analyte molecules, immobilized on the surface. The sensor response is inversely proportional to the analyte concentration.

### **Fiber-optics biosensors**

Other types of optical biosensors are also receiving considerable attention nowadays. Analytical devices on the basis of optical fibers are a convenient and affordable platform for creating fiber-optics biosensors.

Optical fibers consist of a cylindrical core and an encircling cladding, both usually made of silica. Refractive index of the core is slightly higher than the refractive index of the cladding. This is usually achieved by doping of the core (for example, with germanium). Sketches demonstrating principles of optical fibers are shown in **Figure 1.2**. Light through such kind systems

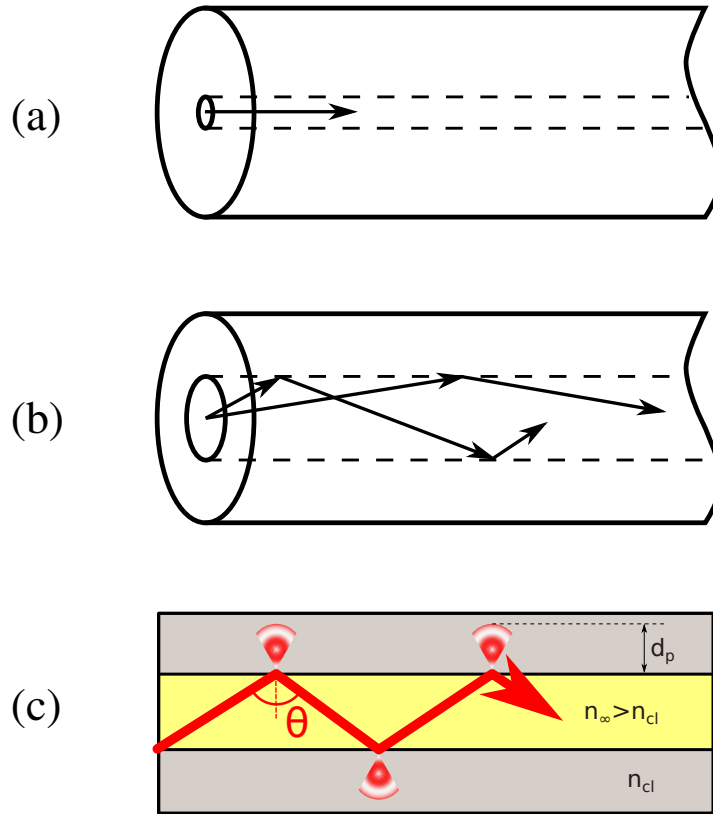


**Figure 1.2:** (a) Schematic of a step-index single mode optical fiber. Light transmission is carried out through a single path. (b) Sketch of a step-index multimode optical fiber. Usually, diameter of the core lies in the range from  $50 \mu\text{m}$  to  $200 \mu\text{m}$  and the total diameter – from  $125 \mu\text{m}$  to  $400 \mu\text{m}$ , respectively. Light can be transmitted through many different paths. Total internal reflection occurs when the angle of incidence is greater than the critical angle. (c) Schematic of the optical fiber longitudinal section. The thick arrow shows a single mode of light entering a multimode fiber at an incident angle  $\theta$ . Despite the fact that most of the light is transmitted, there is a tiny fraction known as the evanescent field that exponentially decays at the core-cladding interface. A distance where evanescent field decays exactly  $e \simeq 2.72$  times is denoted as  $d_p$ .

propagates by means of total internal reflection (TIR). Conventional optical fibers are designed to conduct light with minimal losses. These fibers have a uniform diameter, and the evanescent field quenches almost completely in the cladding. Therefore, interactions of the light propagating through such fibers with surroundings are eliminated.

To construct a sensor based on optical fibers some modifications of the system are required. One of the possible implementations is reducing the thickness of the cladding. Interaction of a device with the environment (or sensing media) may be achieved by exposing the object of study to the evanescent field. Sensing distance of such a device is characterized by a so-called penetration depth, which is the distance from the cladding where the evanescent field decreases by  $e \simeq 2.72$  times (see **Figure 1.2**):

$$E(x) = E_0 \exp\left(-\frac{x}{d_p}\right). \quad (1.1)$$

Here,  $x$  is the distance from the fiber core ( $x = 0$  at the core-cladding interface);  $E_0$  is the amplitude of the electric field at the interface and  $d_p$  is the penetration depth. The latter is defined by the following expression:

$$d_p = \frac{\lambda}{2\pi \sqrt{n_{co}^2 \sin^2 \theta - n_{cl}^2}}, \quad (1.2)$$

where  $\lambda$  is the light source wavelength,  $\theta$  is the incident angle of the light at the core-cladding interface,  $n_{co}$  and  $n_{cl}$  are the refractive indices of the core and cladding, respectively.

Interactions of the evanescent field with the analyte and following detection can be performed in several configurations [29]. Sketch representations of the optical fiber devices used for sensing are shown in **Figure 1.3**. Most common sensing approaches include detecting the changes in output power due to changes in refractive index; evanescent field absorption; fluorescence and surface plasmon resonance. In the simplest sensor design, the cladding is removed

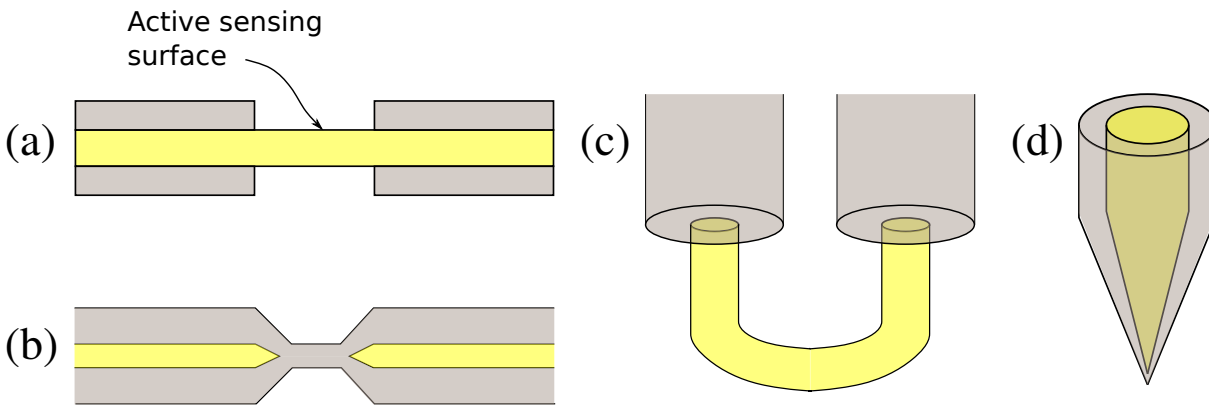


**Figure 1.3:** Optical fibers configurations used for sensing purposes: (a) optical fiber with removed cladding; (b) tapered fiber; (c) U-shape probe; (d) tapered tip.

from the part of the fiber that is in direct contact with the sensing media. Refractive index difference between the core and the sensing media determines the quantity of the propagating evanescent field. Changes in the intensity of the evanescent field can be detected by measuring the changes in output power in the fiber. The sensitivity of this approach can be increased by using tapered fibers. Adjusting geometrical parameters such as radius, length and/or taper ratio allows tuning the sensitivity of biosensor devices based on optical fibers. Bending of tapered fibers allows intensifying the evanescent field strength in the sensing region and thus further increases the sensitivity.

In one of the sensing scenarios, antibodies, immobilized on the surface of the waveguide, selectively bind specific target antigens and are further incubated with fluorophore-marked detecting antigens. Fluorophores are specific substances which can emit specific optical signals when being irradiated at a particular wavelength. Fluorescent molecules close to the fiber surface are excited by the evanescent field, and a part of their energy is going inside the fiber. Background signals from unbound species have a little effect on the total fluorescent measured

signal.

Fiber optics biosensors can also be used to measure other various biological objects including proteins, DNAs and cells. Detection of these species is performed by conducting infrared, visible and/or ultra-violet irradiation through optical fibers. Specific bindings with target species can be detected either indirectly by means of fluorescent optical labels or directly by measuring changes in refractive index or reflectivity. The latter allows label-free biosensing.

### **Colorimetric biosensors**

Colorimetric biosensors represent another common type of optical biosensors. They are used to determine the concentration of colored compounds in solution. Colorimetric biosensors are widely used for the detection of such common substances as glucose and urea. Colored chemical reactions either between glucose and concentrated sulfuric acid alone or in combination with anthrone,  $\alpha$ -naphthol, thymol or chromotropic acid are utilized for determination of glucose concentration. The most common colorimetric reagents for urea detection are diacetyl monoxime phthalaldehyde, naphthylethylenediamine, and chromotropic acid. However, these techniques have some drawbacks. They are difficult to conduct and require precise control of temperature and pH of the sensing media, which significantly slows down the analysis time. Moreover, in the real samples there is a big amount of interfering compounds, which may lead to inaccurate analysis results. On the other hand, additional purification steps such as adsorption, extraction, dialysis, deproteinization, etc. can be used to remove interfering substances and improve the sensing capabilities of colorimetric biosensors. Modern assays employing colorimetric approach can be used for the detection of target DNA hybridization in picomolar concentrations.

Gold nanoparticles (Au NPs) are often involved as transducers in colorimetric biosensors. Their unique optical properties, including localized surface plasmon resonance, high absorption coefficient, fluorescence, luminescence, ease of surface functionalization make them very attractive for applications in biosensing. Properties of Au NPs strongly depend on their size and geometry [30], e.g., the wavelength of the absorbed light increases as a function of nanoparticle size [31]. Another very important property of gold nanoparticles is that the interparticle plasmon coupling during Au NP aggregation or redispersion causes color change: red-to-purple or purple-to-red, respectively (see **Figure 1.4**) [32]. Analyte induces aggregation of Au NPs either directly or by means of biochemical reactions. This aggregation combines the surface plasmons of Au NPs, and the entire aggregate can then be considered as a single large particle. Qualitative analysis can be performed even with a naked eye since the color change is usually pronounced. When a quantitative analysis is required, absorption spectra are first recorded by a spectrophotometer, and then the ratio of the absorbances at the wavelength corresponding to dispersed particles and the one corresponding to aggregated particles is used to quantify the color change

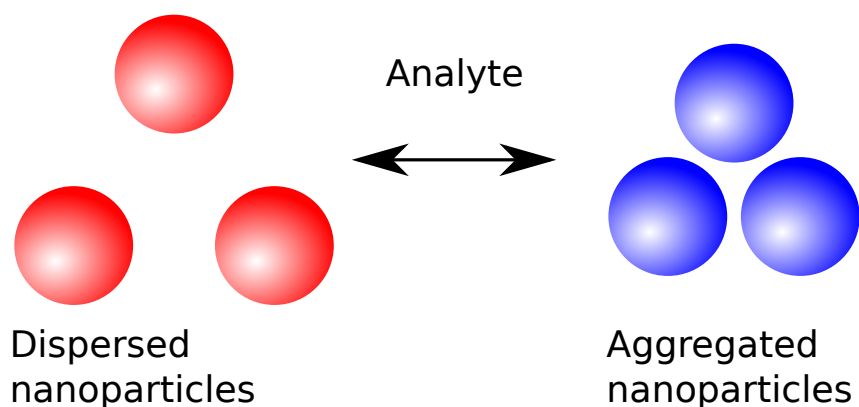


**Figure 1.4:** Schematic of the sensing principle of colorimetric biosensors based on analyte induced aggregation and dispersion of Au NPs.

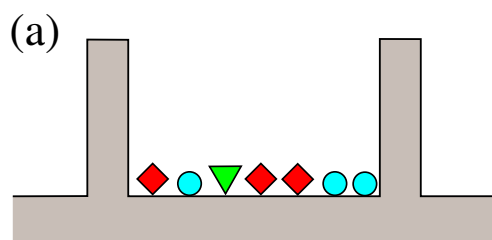
and hence the analyte concentration. Because of high extinction coefficients of gold nanoparticles, Au NP-based colorimetric biosensors can achieve very high sensitivity, approaching that of conventional assays [32].

### Enzyme-linked immunosorbent assay technique

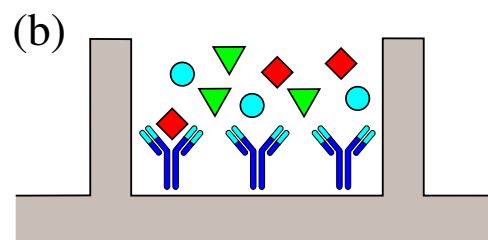
Immunosorbent analysis is widely used for diagnosis of various infectious diseases and cancer processes (mainly using specific proteins and peptides); determining concentrations of different low molecular weight compounds, such as toxins, medications, etc. One of the most widely used immunosorbent analysis techniques nowadays is called enzyme-linked immunosorbent assay (ELISA). It is a plate-based immunological assay technique, designed to measure (detect and quantify) antibodies, antigens, proteins and glycoproteins in biological samples. ELISA is based on the analysis of antigen-antibody binding reactions. Detection of formed complexes is usually performed using a fluorescent enzymatic marker for signal recording. In the past, primary polyclonal antibodies were used to bind target molecules. Development and application of monoclonal antibodies have led to a significant improvement in specificity of the immunoassay.

Applications of ELISA include a wide range of bio-objects – from low molecular weight compounds: peptides and steroid hormones, pharmacological preparations and pesticides to viruses, bacteria and even to other antibodies. Due to a huge variety of studied objects, there are different options/techniques to conduct ELISA analysis. The first step in ELISA is always immobilization (capture) of the antigen in a sample to the wall of the wells of a microtiter plate. This step can be performed either directly or indirectly. In the direct immobilization method (see **Figure 1.5** (a)) the antigens are bound by direct adsorption to the assay plate. This is a straightforward and fast approach, however, since the antigen capture is not specific, higher background noise may be observed in comparison to the indirect ELISA. This is generally because all proteins in the sample, including the target protein, will bind to the plate. In the indirect method (see **Figure 1.5** (b)), the plate is coated with antigen-specific antibodies prior

## Direct capture



## Indirect capture



## Designations:

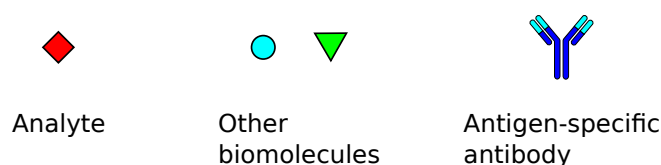


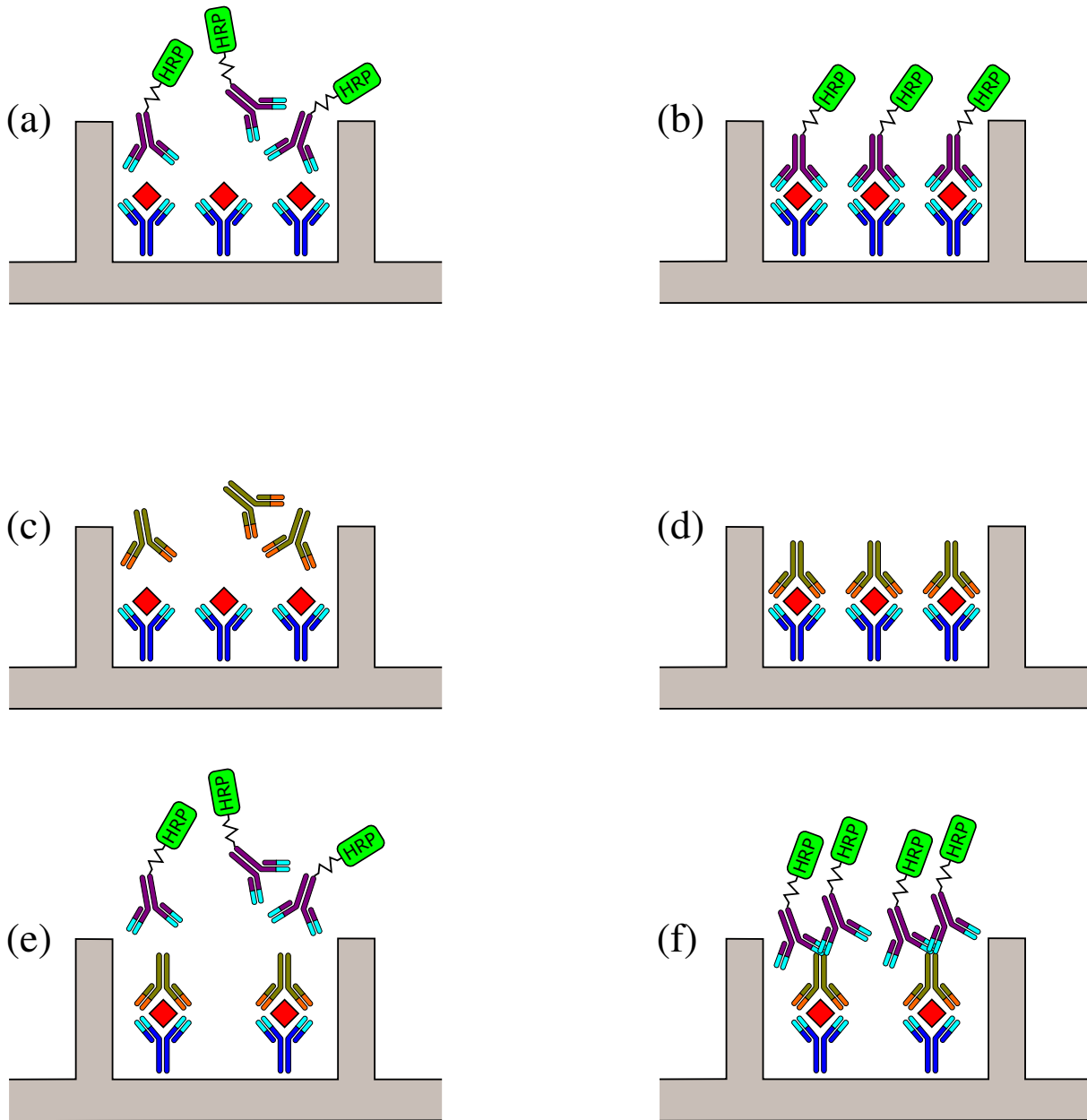
**Figure 1.5:** Schematic representations of ELISA immobilization techniques: (a) direct capture and (b) indirect capture.

to the antigen capture, thus implementing high selectivity. Regardless of the immobilization technique used, the antigen can then be detected either by “direct” or “indirect” approaches. Most commonly used detection techniques are briefly described in the paragraphs below.

“*Direct*” *ELISA*: Schematics of the “direct” detection approach are shown in **Figure 1.6** (a) and (b). A primary antibody that is conjugated to a reporter, such as horseradish peroxidase (HRP) is incubated with captured antigen. Once unbound antibodies are washed off, the enzyme substrate is added to detect the antigen-antibody interactions.

Direct ELISA is the simplest and the fastest among the other ELISA techniques since it requires a lower amount of steps and reagents. It is also less inclined to errors because cross-reactivity of secondary antibodies is excluded. However, this method has also several drawbacks. Direct ELISA is less flexible and more expensive since a specific conjugated primary antibody is needed for each target protein in the sample. This technique has lower sensitivity because secondary antibodies are not used, and thus no signal amplification is performed. Although the “direct” detection is not widely used in ELISA, it has some practical applications, most commonly when the immune response to an antigen has to be determined [33, 34].

“*Indirect*” *ELISA*: In the “indirect” approach, the detection is performed in two steps. An unlabeled primary antibody is firstly incubated with the target antigen. This primary antibody has several specific host species, which are able to bind other antibodies. At the second step, a primary antibody is recognized by secondary antibodies conjugated to the label (reporter). Because multiple secondary antibodies bind each primary antibody (at its host species), this approach allows multiple reporter molecules to localize to each antigen, thereby amplifying the signal and increasing the sensitivity of antigen detection.



Designations:

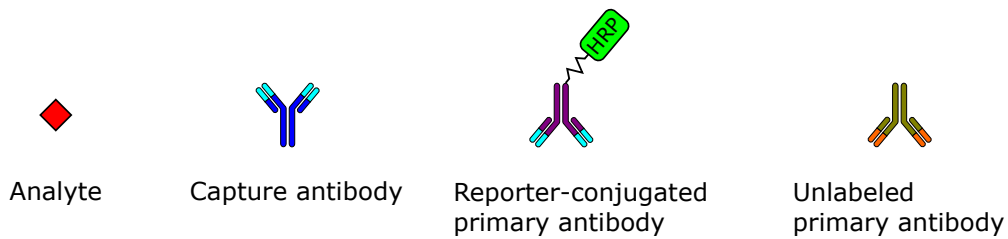


**Figure 1.6:** Schematic illustrations of ELISA detection approaches. Direct sensing: (a) incubation of labeled primary antibodies with captured antigen; (b) washing-off the unbound reporter-conjugated molecules. Indirect detection: (c), (d) incubation of unlabeled primary antibodies with captured antigen; (e), (f) introducing reporter-conjugated molecules that can bind primary antibodies in multiple places, thus allowing signal amplification.

The indirect ELISA approach possesses higher sensitivity due to an increased number of labeled markers that can bind the target. It is also more cost-efficient than direct ELISA technique because fewer labeled antibodies are required and it is more flexible since different primary antibodies can be used with a single labeled secondary antibody. It allows usage of different labels with the same primary antibody. Disadvantages of this method are its higher complexity and time, required for the analysis. Cross-reactivity of the secondary antibodies might also result in an increased level of background noise. Indirect ELISA is most commonly used for detection of the total antibody concentration in biological samples [35, 36].

*“Sandwich” ELISA:* The term “sandwich” ELISA is commonly used to refer the assay involving indirect immobilization of antigen (using a capture antibody) followed by addition of detection antibodies. The essential requirement for the successful application of “sandwich” ELISA is that capture and detection antibodies have to be specific for different and non-overlapping regions (or binding sites) of the antigen. The detection antibody can be either labeled or unlabeled, reflecting direct or indirect “sandwich” ELISA, respectively. For indirect “sandwich” configuration, a secondary reporter-conjugated antibody is required.

The main advantage of the “sandwich” ELISA is its increased sensitivity (up to 5 times higher than for direct or indirect ELISAs). It also possesses higher selectivity and flexibility, since two antibodies are used to detect the antigen. This technique, however, suffers more from cross-reactivity of secondary antibodies and demands thorough antibody optimization.

Most commercial ELISA kits are “sandwich” ELISAs that use indirect capture, indirect detection, and avidin-biotin chemistry. Avidin can strongly bind to biotin molecules. A biotinylated primary antibody is bound to the antigen, followed by avidin, streptavidin, or another biotin-binding molecule, that is conjugated to the reporter. Thus, multiple reporters are localized to the antigen, resulting in signal amplification [37].

*“Competitive” ELISA:* This the most sophisticated type of ELISA. Firstly, a reference sample with a known concentration of labeled antigen is prepared. Unlabeled antigen from the studied sample and the labeled antigen are competing for binding to a limited amount of capture antibodies. The concentration of target antigen is then determined by measuring interference between the reference and the measured sample. The obtained signal is inversely proportional to the concentration of antigen in the sample. Competitive detection technique can be adapted to any ELISA type described above. In practice, it is mostly used for the detection of small antigens that have only one antibody binding site [38].

*Drawbacks of the ELISAs:* Immunosorbent analysis is a complicated procedure that requires sophisticated laboratory equipment. High purity of the reagents and their superior specificity are vital prerequisites for reliable detection of biological substances using ELISA [39]. Failure to comply with these requirements may cause problems and affect the sensitivity and specificity of the assay [40]. The detection limit for most of conventional ELISA techniques

usually does not exceed nanomolar concentration level, which is often not enough to reach the clinical verge of many biomarkers, especially at the early disease stages [41]. Moreover, in contrast to other wet lab assay techniques, where the same reaction reservoir, e.g., a cuvette can be reused after a washing procedure, the ELISA plates are not easily reusable since the reaction products are immunosorbed on a part of the plate.

### 1.1.2 Techniques Based on Field-Effect Transistors

Biosensors on the basis of ion-selective field-effect transistors (ISFETs) are certainly an important class of potentiometric biosensors. This type of devices is very promising for practical applications in biosensing because they can be fabricated using well-developed semiconductor technologies, which once made huge progress in microelectronics. Recent advances in manufacturing planar and non-planar micro- and nanostructures on the basis of monocrystalline silicon, deep knowledge about mechanical and electrical properties of the latter gave a new pulse to this branch of analytical biotechnology. Moreover, integrated circuit technologies and mass production are the best way to reduce the cost of fabricated devices and allow combining sensing elements with electronic processing circuits.

#### Working Principles of ISFETs

Ion-selective field-effect transistor devices are similar to conventional metal-oxide-semiconductor (MOS) FETs. However, in contrast to their counterparts, in ISFETs the metal gate is replaced by an external reference electrode, which is connected to the gate dielectric through an electrolyte liquid solution (see **Figure 1.7**).

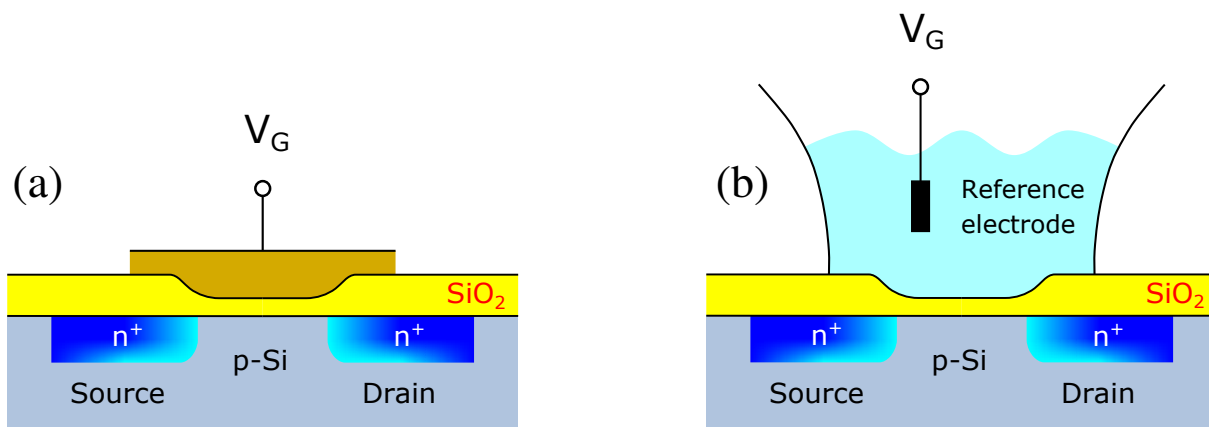


**Figure 1.7:** Schematic drawings of a  $n^+p\text{-}n^+$  MOSFET (a) and ISFET (b) devices. Source and drain regions of the devices are highly doped to form ohmic contacts. For a MOSFET the electric current through the device is controlled by a top metal gate electrode. In an ISFET the top metal gate is replaced by an electrolyte liquid solution and the electrical current between source and drain is controlled by an external reference electrode.

To understand the working principles of an ISFET let's first consider the operation of an inversion-type MOSFET as an example. These transistors are usually fabricated on the basis of silicon substrates with hole type conductivity (p-Si). Source and drain regions of the FET are highly doped with electron donor impurities, creating  $n^+$  regions. A metal gate electrode is placed over the conducting channel, which is pre-covered with a thin dielectric layer. Applying voltage bias to the gate allows precise control over the drain-source current of a MOSFET device. The gating effect can be explained well considering ideal MOS structures.

*Operation of a MOS structure:* A sketch of a MOS structure with oxide thickness  $d$  and applied voltage  $V$  is shown in **Figure 1.8**. The voltage sign is determined relatively to the ohmic contact potential ( $V > 0$ , if the potential of the metal plate is greater than the one of the ohmic contact). A MOS structure can be considered ideal if the following requirements are fulfilled:

- At zero voltage applied ( $V = 0$ ), there is no difference between electron work functions of the metal and semiconductor,  $\varphi_{ms} = 0$ :

$$\begin{aligned}\varphi_{ms} &= \varphi_m - (\chi + E_g/2 - \varphi_b) = 0 \quad \text{for } n\text{-type semiconductor;} \\ \varphi_{ms} &= \varphi_m - (\chi + E_g/2 + \varphi_b) = 0 \quad \text{for } p\text{-type semiconductor.}\end{aligned}\tag{1.3}$$

Here,  $\varphi_m$  denotes the metal electron work function;  $E_g$  is the bandgap width;  $\varphi_b$  is the difference between the Fermi level  $E_F$  and the Fermi level in an intrinsic semiconductor  $E_i$  (the middle of the bandgap);  $\chi$  is the electron affinity of the semiconductor.

- The charge, which occurs in the structure when the voltage bias is applied consists of the charge in the semiconductor and the equivalent charge of the opposite sign on the metal surface that is separated from the semiconductor by the insulator.
- There is no charge transfer through the dielectric layer when only a constant voltage is applied, which means that the resistance of the insulator is infinitely high.

A band structure of such a metal / dielectric / semiconductor system at the absence of external gate voltage is shown in **Figure 1.9**. The Fermi level is the same for the metal and semiconductor, and the conductivity of the subsurface area of the semiconductor does not differ from its bulk conductivity.

If a positive or negative voltage bias is applied to an ideal MOS structure there can be three different cases, shown in **Figure 1.10**. For certainty, let's consider the  $p$ -type semiconductor. If a negative voltage bias is applied to the metal ( $V < 0$ , **Figure 1.10 (a)**), the upper boundary of the valence band bends upwards and approaches the Fermi level. Since in the ideal MOS structure the through-current equals zero, the Fermi level in the semiconductor remains constant. According to the fact that the concentration of holes exponentially depends on the difference

in energy ( $E_F - E_v$ ), such bending of the zones leads to an increase in the number of major carriers (holes) close to the surface of the semiconductor. This operation mode is called the accumulation regime. If a small positive voltage bias is applied to the  $p$ -MOS structure ( $V > 0$ , **Figure 1.10** (b)), the zones bend downwards, which leads to depletion of the near-surface region with major charge carriers and its enrichment with the minor ones.

While the voltage and bending of zones are such that the Fermi level does not cross the intrinsic level  $E_i$ , the concentration of the major charge carriers exceeds the concentration of the minor ones. At the voltage when the Fermi level on the surface coincides with the intrinsic level  $E_i$ , the concentrations of the major and minor charge carriers in the near-surface region are equal (intrinsic semiconductor). With a further increase of the positive voltage bias, the intersection point of  $E_F$  and  $E_i$  levels is removed from the surface (**Figure 1.10** (c)), and the surface concentration of minor charge carriers (electrons) exceeds the concentration of the major ones (holes). This situation is called the inversion regime. Often this inversion is divided into a weak inversion when the concentration of minor carriers in the near-surface region is greater than the concentration of the major ones but it is smaller than the equilibrium major carrier concentration; and the strong inversion when the concentration of the minor carriers near the surface exceeds the major carrier concentration in the volume. Similar considerations can be made for the MOS structures on the basis of  $n$ -type semiconductors. In this case, the voltage polarity must be changed to the opposite.

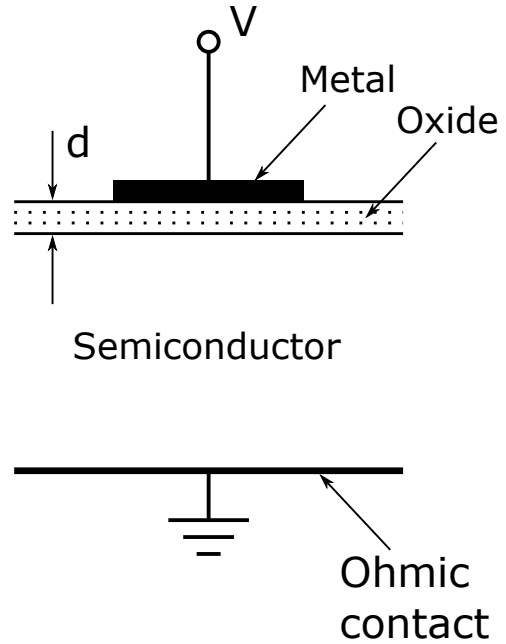


**Figure 1.8:** Sketch of an ideal MOS device.

The number of charge carriers, and thus, the conductivity of the near-surface layer strongly depend on the applied voltage. This mechanism explains the gating-field effect and is used for

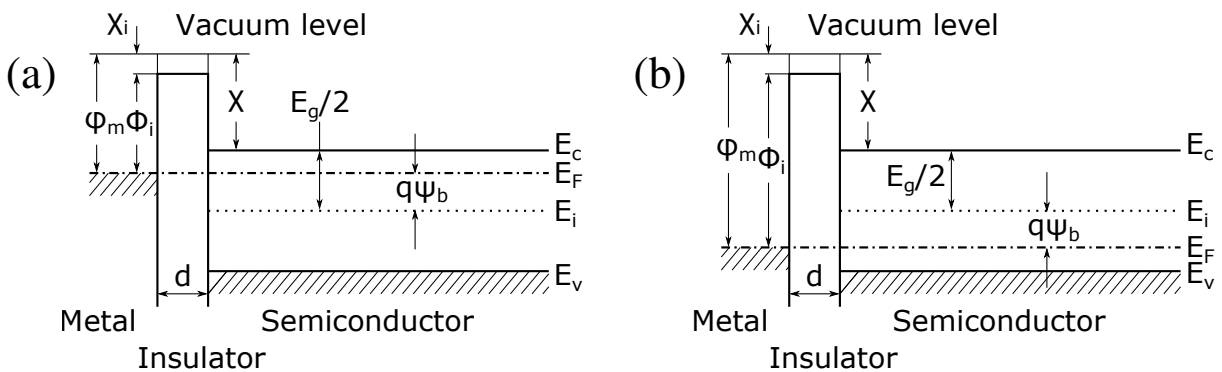


**Figure 1.9:** Band diagrams of ideal MOS structures at the absence of gate voltage: (a)  $n$ -type semiconductor; (b)  $p$ -type semiconductor.

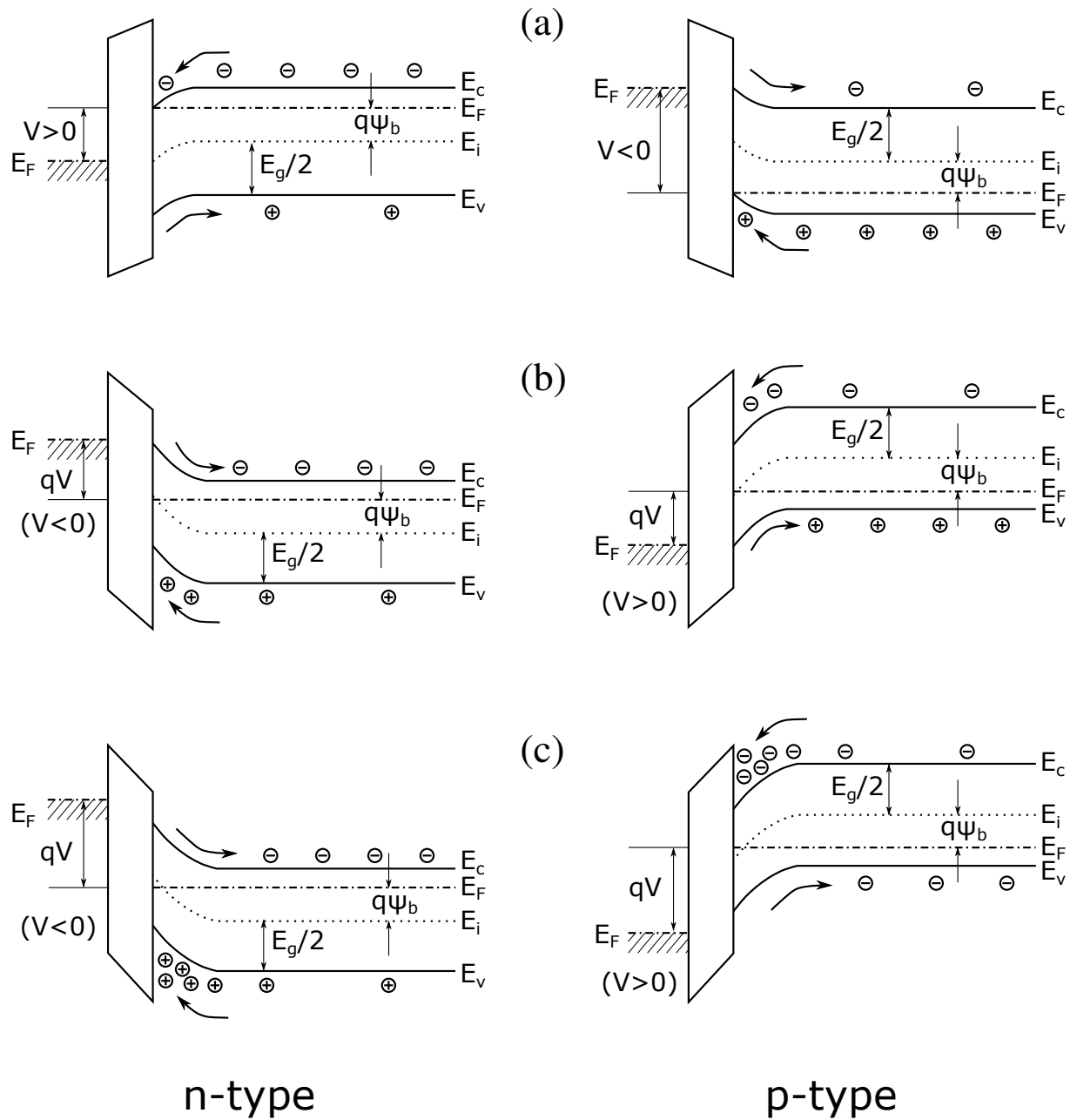


**Figure 1.10:** Band diagrams of *n*-type (left) and *p*-type (right) MOS structures at  $V \neq 0$ : (a) accumulation regime; (b) depletion regime; (c) inversion regime.

controlling the drain-source current  $I_D$  of MOSFET structures. The gate voltage at what the electron density in the near-surface inversion layer of a  $p$ -MOSFET is the same as the volume density of holes in the body is called the threshold voltage  $V_{Th}$  (the definition for  $n$ -MOSFET can be done by analogy). Taking into account the geometry of a simple planar MOSFET one can derive model equations for the drain current in different operation regimes:

$$I_D = \begin{cases} 0, & V_G \leq V_{Th}; \\ C_{Ox}\mu\frac{W}{L} [(V_G - V_{Th})V_{DS} - \frac{1}{2}V_{DS}^2], & V_G > V_{Th}, V_{DS} \leq V_G - V_{Th}; \\ \frac{\mu C_{Ox}}{2} \frac{W}{L} (V_G - V_{Th})^2 (1 + \lambda(V_{DS} - V_{DSsat})), & V_G > V_{Th}, V_{DS} > V_G - V_{Th}. \end{cases} \quad (1.4)$$

Here,  $C_{Ox}$  is the specific capacitance of the oxide (dielectric);  $W$  and  $L$  are the width and length of the channel, respectively;  $\mu$  is the electron mobility;  $V_G$  is the gate voltage;  $V_{DS}$  is the drain-source bias;  $\lambda$  is the channel-length modulation parameter;  $V_{DSsat}$  is the saturation drain-source voltage. When the geometrical factor  $\beta = \mu C_{Ox}W/L$  is constant, drain-source bias and threshold voltage do not change, then drain current is a unique function of the gate voltage. For the described configuration of a MOSFET, parameter  $\beta$  is a constant value defined by the manufacturing process,  $V_{DS}$  can also be fixed manually by applying a certain voltage between the source and drain contacts. The threshold voltage  $V_{Th}$  depends on FET fabrication technology and thus it is constant in each particular case. Therefore, the gate voltage  $V_G$  is the only input variable, responsible for the transistor operation.

The threshold voltage of an ISFET ( $V_{Th}$ ) can be modified changing surface potential on the electrolyte / dielectric interface. To make an ISFET sensitive to biochemical species, a special selective membrane has to be applied to the gate dielectric surface. Binding of charged target molecules to the membrane leads to the accumulation of charge on the gate surface. The accumulated charge works as an additional gate potential, altering the conductivity of the FET channel. After proper calibration, registered changes of the conductivity (or the drain current) can be correlated with the concentration of the target species.

Most of the membranes that are sensitive to  $H^+$  ions are at the same time effective barriers, which resist the diffusion of different molecules. Therefore, they are frequently used as a top layer of the gate dielectric of an ISFET and as an encapsulating substance. To make an ISFET selective to other types of biochemical species, different ion-selective membranes and biomatrices can be immobilized on top of the gate dielectric surface.

### Applications of ISFET Biosensors

One of the key advantages of ISFET biosensors over optical systems is their usability in miniaturized measurement systems. This opens broad perspectives for the development of lab-on-a-chip (LOC) biosensor devices for fast and reliable biochemical analysis. One of the first and the most widespread applications of ISFET sensors is, however, the pH sensing. When an ISFET

device is exposed to an electrolyte liquid solution, there exists an anisotropic ion accumulation at the gate oxide / electrolyte interface [42]. These ions have different size and charge, which leads to the formation of a well-confined electric double layer in the vicinity of the oxide surface. There also exists a diffuse layer of outer charges between the Helmholtz planes and the neutral bulk of the solution. If the gate insulator is  $\text{SiO}_2$ , the silanol groups ( $\text{Si-OH}$ ) are formed on its surface. These groups are in electrodynamic equilibrium with ions in the solution ( $\text{H}^+$  and  $\text{OH}^-$ ). The silanol groups on the surface can be protonated and deprotonated in an electrolyte solution. Thus, changing of pH leads to changes of the gate oxide surface potential and the drain current of an ISFET device. The pH sensing principle is analogous for other common types of gate insulators. For example, if gate dielectric is the silicon nitride then the surface potential is determined by the  $\text{H}^+$  ion exchange between the solution and the binding sites of the  $\text{Si}_3\text{N}_4$  surface:  $\text{Si-OH}$  and  $\text{Si-NH}_2$ . An analytical model, describing the response of an ISFET based pH sensors can be found in [43].

Nowadays, applications of ISFETs cover detection of a wide range of biochemical species including proteins [44], enzymes [45] and cells [46]. Authors of [47] applied a glucose oxidase coating to an ISFET based biosensor for determination of glucose level in blood serum. ISFET biosensors are also promising for DNA detection [48, 49]. For this purpose, the sensing surface of an ISFET based biosensor is firstly coated either with DNA or with specifically designed peptide nucleic acid (PNA) probe, and then a solution containing target DNA is added. When there is a match between the target DNA and probe, hydrogen ions ( $\text{H}^+$ ) are released, changing the pH of the sensing solution. The ISFET responds to these pH changes based on the rule of DNA extension, thus allowing quantitative detection and even sequencing of DNA.

## 1.2 Nanowire-Based Biosensors

Rapid development of fabrication technology has led to the emergence of a big variety of nanostructures and nanodevices on their basis. Not only their reduced size is appealing for the advancement of electrical circuitry and operation speed but also for the novel physical and chemical properties of nanomaterials [50]. Therefore, nanostructures have an immense potential application scope: from micro- / nanoelectronics to biosensing and bioengineering.

For a modern biosensor device, it is important to implement the following qualities: high sensitivity, low limit of detection (LOD), exceptional specificity to the target, rapid response, high device reproducibility, and low fabrication cost. Generally, optical techniques are highly sensitive and selective, nevertheless, they are often time-consuming and require expensive laboratory equipment for analysis. In contrast, the ISFET based sensors have lower fabrication cost and can provide rapid response. However, the sensitivity of conventional ISFET biosensors is

often not sufficient to detect very low concentrations of analyte, which can be crucial for the early stage disease determination. One possibility to overcome this issue is using nanomaterials as ISFET active sensing elements. This allows increasing the sensitivity and lowering down the LOD, at the same time maintaining the benefits of conventional ISFET biosensors [51].

Semiconductor nanowire-based devices are attracting substantial attention nowadays. They can be fabricated in FET configurations and utilized similarly to ISFETs. Their increased surface-to-volume ratio makes them extremely sensitive to changes in the surface charge. Furthermore, the dimensions of these nanostructures are comparable to those of the target biochemical species. Consequently, even binding of small amount of the analyte will cause considerable changes in the device response. Therefore, nanowire devices can serve as exceptional primary transducers for various sensing applications, including chemical sensing and biosensing [52–55].

Structures based on thin metal films, nanowires, and nanodots are also attracting considerable attention as promising objects for sensing applications. Among these structures, metallic nanowires are the most relevant since they can be easily designed and tailored for the desired functionality [56]. For example, a single metallic nanowire that contains gold and nickel parts could be used for surface functionalization and magnetic guidance control. A huge variety of chemical groups able to bind to the surface of metals (and thus, to the surface of metal nanowires) due to their high chemical affinity. Shrinking down the dimensions of these structures enhances their surface-to-volume ratios and increases the impact of each adsorbed molecule to the entire conductance change. This allows achieving ultimately high sensitivity, which in favorable cases approaches even the single molecule level [25].

Important technological aspects of nanowire fabrication and several common approaches for the development of NW-based biosensors are discussed below.

### 1.2.1 Current Fabrication Technologies

*Semiconducting nanowires:* Semiconductors such as Si, InAs, GaN, ZnO, SnO<sub>2</sub>, and In<sub>2</sub>O<sub>3</sub> have been utilized as materials for fabrication of nanowire FET sensors. Devices based on silicon nanowires have certain advantages over the other listed semiconductors. Si NWs benefit from the achievements of silicon industry: well-developed processing techniques, ultimate scalability and shape control, and possibilities of mass production. State of the art technologies allow fabrication of high-quality monocrystalline Si NWs with diameters as small as 2-3 nm.

At present, two main approaches are utilized to fabricate nanowire structures: “bottom-up” (growing) and “top-down” (etching). Usually, the “bottom-up” fabrication process contains the following steps:

- growing the nanowires;

- transfer of NWs onto a substrate;
- creating electrical contacts;
- passivation and surface modification.

The growth of nanowires is performed catalytically in a chemical vapor deposition (CVD) chamber through the vapor-liquid-solid (VLS) mechanism. Formed nanowires are dispersed in a solvent (e.g., ethanol) and deposited onto a substrate. To improve the orientation of nanowire structures, the deposition step can be performed using microfluidics [57], contact printing [58], electric-field [59], or other alignment techniques. Contacting of nanowire structures can be carried out using photolithography, metalization, and lift-off procedures. Electrical contacts and feed lines are then covered with a passivation layer (a thick insulator) to prevent current leakage during operation. To make the device specific to the recognition of the target biochemical species a surface functionalization of probe molecules is applied, thus creating a bioselective membrane. The functionalization procedure often involves covalent binding of target-specific molecules to Si or naturally grown SiO<sub>2</sub> layer through a chain of small linker molecules. Nanowires fabricated using “bottom-up” approach usually have a cylindrical shape, however current technologies allow for different cross-sectional structures of nanowires (e.g., square, triangular) to be achieved.

The “bottom-up” approach allows fabrication of high-quality quasi 1D nanowire structures with diameters of 20 nm or less. However, this technique has also certain disadvantages. One of its major drawbacks is that the nanowire alignment methods mentioned above are not CMOS compatible. This obstructs mass production of “bottom-up” fabricated nanowire sensors. Control of some important technological parameters, including doping concentration, is also quite a challenging task. Among other disadvantages are high integration complexity, demand in transferring to other substrates, difficulties in the positioning of individual nanowire structures and in making reliable ohmic contacts. All these weak points make the development of high-density sensor arrays on the basis of “bottom-up” fabricated devices a very difficult task.

Contrarily to the “bottom-up” technique, the “top-down” approach offers many opportunities to control nanowire orientation and position. Typical fabrication flow for manufacturing “top-down” nanowire FETs demands following steps:

- selection of a proper substrate;
- definition of the source and drain areas;
- etching of mesa structure;
- nanowire patterning;
- passivation and surface modification.

Fabrication is usually performed on the basis of commercially available silicon-on-insulator (SOI) wafers. Choosing *p*- or *n*-type SOI wafers with a defined level of impurities determines the doping level of nanowires and their further performance as FET biosensors. Source and drain areas should have small resistances to be able to form ohmic contacts. They are usually defined by photolithography and a subsequent heavy doping procedure. Then, the mesa structure, including the pattern for source and drain areas as well as areas reserved for nanowires, is defined using RIE. Nanosized nanowire structures are patterned by means of electron beam lithography, followed either by RIE or wet chemical etching procedures. Finally, passivation and surface modification steps are performed as in the “bottom-up” approach.

One of the key advantages of the “top-down” fabrication technology is its high CMOS compatibility. It also provides a precise control over the orientation of nanowires. State of the art electron beam and focused ion beam lithographies allow patterning of nanoscale objects with sizes as low as 10 nm. However, they are relatively expensive and not well suited for large scale serial production. Recent advances in fabrication techniques, e.g., nanoimprint lithography, allow reliable and cost-efficient nanostructure patterning, which facilitates large scale rapid fabrication of nanowires with a high yield rate. Nevertheless, the nanowire diameters are usually bigger compared to those fabricated using “bottom-up” techniques.

*Metallic nanowires:* Similarly to semiconducting nanowires, metallic nanowires can also be fabricated using “bottom-up” and “top-down” approaches. The “bottom-up” method, however, is used the most often. It has many variations that in general can be classified into template-assisted and template-free approaches [56].

Template-assisted electrodeposition is a simple technique to create metallic nanowires. At first, a proper template is selected on the basis of the following considerations:

- high mechanical and chemical stability;
- desired size and shape of the pores;
- suitable template material.

The pores of the template can be filled with the desired materials to form the NWs. The schematic of such a NW formation process is shown in **Figure 1.11**. Many porous materials are suitable for the role of templates including porous silicon [60], zeolites [61], and carbon nanotubes [62]. The most commonly used materials are, however, the templates on the basis of anodic alumina oxide and ion track-etched polycarbonate. Anodization of pure-aluminum films in acidic environments allows parallel channels formation of almost-cylindrical shape. Formed pores are highly uniform and densely packed ( $10^9 - 10^{11}$  pores  $\text{cm}^{-2}$ ). Pore diameters (usually in the range 10–200 nm) can be efficiently controlled by anodization conditions. Polycarbonate templates are formed by ion bombardment of polycarbonate thin films and subsequent chemical

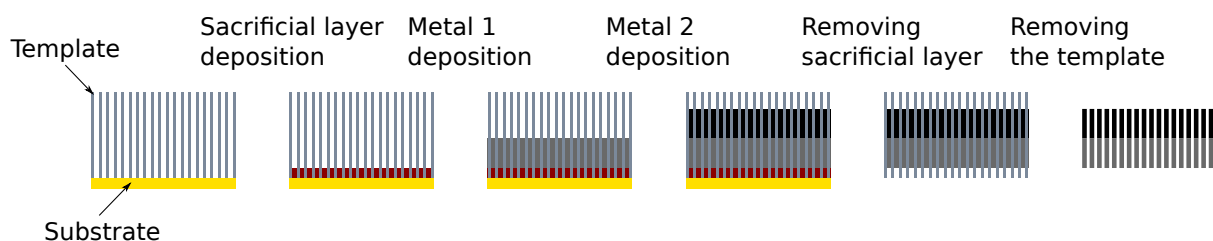


**Figure 1.11:** Schematic of a two layer metal nanowire fabrication process by the template-assisted method.

etching of the ion tracks. The pore density, achieved by this approach reaches  $10^9$  pores  $\text{cm}^{-2}$ . The pore distribution, in this case, is less uniform compared to the one of anodic alumina because of the random nature of the ion bombardment process. Size and shape of the formed pores can be adjusted by altering the ion bombardment conditions. Several approaches can be used to fill the template:

- Electrochemical deposition. The process is performed in an electrolyte liquid solution. Three electrodes are implied: Ag/AgCl reference electrode, Pt counter-reference electrode, and the template, one side of which is coated with a metal and serves as the working electrode. Metal ions from an electrolyte solution are reduced within the pores of the template, thus growing the nanowires starting from the metal pre-coated side;
- Electroless plating. Several simultaneous reactions occur in the electrolyte solution resulting in metal deposition inside the pores. Unlike the previous case, the process is carried out without the use of external electrical power. Another difference is that nanowires start growing from pore sidewalls towards their middle.
- Template filling. In this case, the template is filled with a liquid precursor. Nanowire growth occurs by solidification of the precursor on the inside walls of the pores.

When the pores are filled, the template is removed to achieve free nanowires. Although the template-assisted techniques allow fabrication of nanowire structures with controlled parameters, there are also certain drawbacks connected to difficulties with template removal and a relatively large amount of steps required for the fabrication.

Template-free techniques are developed to solve the problems of template-assisted approach and ease-up the fabrication process. They include chemical synthesis, assembling nanowires from nanoparticles, chemical vapor deposition, etc.

Growing nanowires using the chemical approach requires an electrodic surface that acts as a support for the growth. To achieve nanowires, the support is repeatedly dipped into a solution with the reagents required for NW synthesis and dried. The chemical approach is a very simple and versatile technique. Varying temperature, solution composition, and stirring speed allow tuning the properties of formed nanowire structures.

Metallic nanoparticles can be utilized as building blocks to construct nanowires. For this purpose, the nanoparticles are dispersed in an organic solvent and stirred thoroughly. The intense movement of nanoparticles in the solvent reduces their mutual electrostatic repulsion. This facilitates conjunction of the nanoparticles into long chains, thus forming nanowires.

Nanowire structures can be also produced using chemical vapor deposition approach. The CVD process involves deposition of the solid materials from a gas phase onto a solid substrate. Silicon or silica wafers and metal sheets are the most commonly-used substrates. The gaseous precursor flows through the reaction chamber and then hits the heated substrate. The solid phase forms on the substrate either as the result of a chemical reaction with the precursor or by the decomposition of the latter. This technique allows large scale nanomaterial formation and is promising for future applications in different fields [63, 64].

*Tunable cross-section structures:* Metallic nanostructures with tunable cross-sections are considered as very promising objects for biochemical investigations. One of the most developed techniques to achieve such structures is the mechanically controlled break junction (MCBJ) approach. Fabrication flow of MCBJ structures implies the “top-down” method. Nanosized metallic junctions are produced on the basis of bendable substrates. Bronze, spring steel, or flexible plastic are typical suitable substrate materials since they provide sufficient elasticity without breaking or irreversible bending [65]. One or several layers of flexible polymers, typically polyimide, are spin-coated onto substrates to create a uniform insulation layer. Nanosized junctions are then defined using electron beam lithography, metalization, and lift-off processes. The last and very important step is the isotropic etching of the polyimide film to create freestanding metallic constrictions. High-precision cross-section tuning of such structures is implemented by the controlled bending of the substrate.

Other common approaches to create tunable metallic nanowires are using scanning tunneling microscopy (STM) and conductive-mode atomic force microscopy (C-AFM). STM devices are based on the quantum tunneling phenomena. In the conventional operation mode, the nanosized metallic STM tip is retained at a tiny distance (around 1 nm) from the conductive (usually metallic) scanning surface. If an electrical bias is applied between these components, the electrons can tunnel from the tip through the vacuum barrier. Gimzewski and Möller thoroughly studied the formation of point contacts in STM and described the transient processes that occur in the system [66]. The strong dependence of the tunneling current on the distance between the tip and scanning surface allows registering tiny changes in this distance (even smaller than the size of an atom). However, when the STM tip is getting in contact with the scanning surface, it may form atomic-scale metallic wires. Cross-section of these wires can be tuned by adjusting the force, which is applied to the tip.

Conducting-mode atomic force microscopy is one of the variations of the AFM and STM techniques that utilizes electric current to obtain profile images of the scanning surface. C-

AFM, however, can also be utilized to form atomic-size metallic contacts. For this purpose, the tip approaches the substrate with a certain force, and then it rises upwards forming a conductive metal wire, the geometry of which changes during the raising process.

The aforementioned techniques allow studying the electrical properties of tiny metal constrictions. More importantly, they can be utilized to measure size, shape, electrical and nano-mechanical properties of various biochemical molecules at the single-molecule level [65, 67].

## 1.2.2 Advantages and Applications of Nanowire Biosensors

When characteristic sizes of a material shrink down to the nanometer scale, its physical and chemical properties become considerably different from those of a bulk material due to increased surface-to-volume ratio, and quantum effects.

Among a variety of nanomaterials, semiconducting nanowires have been shown to be very promising candidates for biomedical applications [68]. As mentioned above, nanowire based devices can be configured to work in an electrolyte liquid environment and operate as nanoscale ISFETs. However, in contrast to conventional ISFET biosensors, most of the sensing surface area of a nanowire FET device will be affected by the target species. This allows for a drastic improvement in the biosensor sensitivity to be achieved.

*Protein detection:* Detection of various proteins in biological samples has proven to be promising for biomedical applications. One of the first works describing the sensitive and selective determination of the protein concentration was reported by Cui et al. in 2001 [13]. Authors used boron-doped silicon nanowires for real-time detection of streptavidin. Specificity to the analyte was implemented by modification of Si NW biosensors with biotin molecules. The limit of detection for the reported NW structures was in the picomolar range.

In addition to the increased sensitivity, Si NW FET biosensors have several other advantages. Their high CMOS-compatibility allows fabrication of individually-addressable high-density nanowire arrays. Modification of distinct NW structures with the molecules specific to different analytes opens prospects for future applications in genomics and proteomics. Zheng and coauthors developed Si NW array-based biosensor capable of multiplexed detection of cancer biomarkers [17]. Another valuable advantage of semiconductor technology is the possibility of manufacturing complementary nanowire FETs. Thus, simultaneous processing of the readout signals from *p*- and *n*-type devices allows avoiding erroneous responses and enables highly-sensitive detection of multiplexed analytes in real-time [69].

*DNA sensing:* Compared to other techniques, nanowire sensors show a significant improvement in the limit of detection when sensing DNA. The sensing principle is similar to the one described above for protein sensing. Tracking of the device conductance change upon binding

of target DNA allows its selective detection in the 10 fM range [70]. This value is 2 to 5 orders of magnitude lower than the LOD reported for DNA sensing with SPR and quartz-crystal microbalance (QCM) [71–73]. Another advantage of this approach is that unlike other techniques, it does not require amplification step, e.g., polymerase chain reaction (PCR) to implement sufficient sensitivity.

The main difference in sensing approaches for proteins and DNAs is that successful DNA-complementary DNA detection requires buffers with high ionic strength. The reason behind this is that phosphate backbones of nucleic acids carry large amounts of negative charges. Therefore, the high salt concentration is needed to reduce the repulsion between the DNA strands. However, the Debye screening length decreases with increasing the ionic strength, thus limiting the biosensor performance [74]. To overcome this issue, the DNA probe can be substituted with synthetic PNA molecules, which possess similar functionality, i.e., selectively bind target DNA but do not have heavily charged backbones [75]. The PNA molecules are not charged at neutral pH and therefore, the PNA-target DNA bindings can be carried out in low ionic strength buffers.

*Other biological objects:* Semiconductor nanowire structures represent a versatile class of devices that can be utilized for various biosensing purposes. The range of possible targets is not limited to biological molecules but also extends to more complex analytes, such as viruses, cells, and even cellular networks.

Viruses are dangerous substances that often cause diseases, and in some cases, deaths. In this regard, information on the existence of viruses and their concentration in patients' blood is very valuable for the early diagnostics and proper medical treatment. Usually, the surface of nanowires is covered by virus-specific antibodies to implement exclusive selectivity to the target species. Similarly to the cases described above for proteins and DNAs, attachment/detachment of viruses on the sensing surface induce conductance modulation of the FET nanowire structure. Concentrations of the viruses in the sample can be achieved after appropriate calibration. One of the pioneering works for virus detection using Si NW FETs was performed by Patolsky et al. in 2004 [19]. Authors demonstrated a possibility of rapid electrical detection of influenza A virus with silicon nanowire arrays. Monoclonal anti-influenza A antibodies were immobilized on the nanowire surface to create a bioselective layer. The Si NW biosensors showed a distinct response to the target influenza A virus with the sensitivity approaching the single virus level. Moreover, no response was observed when adding non-specific paramyxovirus or adenovirus.

Measuring electrical responses from single cells and tissues *in vitro* is important both for fundamental biological studies and for practical applications, e.g., medical monitoring [76]. Nanowire FETs interfacing cells or tissues can be applied for extracellular signal recordings, which can help to understand cellular responses and provide insight into cell physiology. Compared to planar field-effect transistors, nanowire FETs showed an improved signal-to-noise ratio (SNR) when sensing spontaneous activity of cardiac muscle HL-1 cells [9]. Moreover, in such

kind measurements, the signal shape can be evaluated and attributed to different membrane currents. Si NW array sensors can be utilized for long-term sensitive and noninvasive measurements of single cardiomyocytes and cardiac tissues as well as for detection of membrane excitation of aortic smooth muscle cells [77]. Such measurement abilities open prospects for applications in investigating responses of living systems to biochemical compounds, and thus, potentially, in drug screening against cardiac diseases [51].

Another important research objects are neuronal cells. Deep knowledge about neurons and neural networks may help to struggle against neurodegenerative disorders such as Alzheimer's and Parkinson's diseases, essential tremor and dystonia. Thus, understanding neuronal electrical activity is of fundamental importance. In this respect, semiconducting nanowires can serve as a promising tool for recording signals from individual neurons and mapping of neural networks with high spatial resolution [10, 78].

*Sensing with metallic NWs:* Great surface activity of nanosized structures has facilitated a considerable interest for fabrication of novel type nanomaterial-based gas sensors [79]. It has been shown that the electrical conductivity of metals and some other conducting materials can change upon exposure to different organic and inorganic gases [13, 80, 81]. Adsorption of gases by bulk metals causes decreasing of their conductivity due to the increased electron scattering on the adsorbates. This situation, however, might change considerably when utilizing metallic nanostructures. Favier et al. developed a palladium nanowire hydrogen sensor that showed a rapid (less than 75 ms) response to the target gas concentration change [82]. The authors reported a reversible increase in the conductance of the Pd nanowire-array sensor over the H<sub>2</sub> concentration range from 2 % to 10 %. The sensing mechanism was attributed to the closing of nanosized gaps in the wires caused by the extension of palladium grains due to H<sub>2</sub> absorption.

Metallic nanowires can be used for electrochemical sensing of different organic and inorganic molecules including ascorbic acid, hydrazines, carbohydrates, alcohols, and drugs [56]. One of the promising applications is the detection of hydrogen peroxide. The H<sub>2</sub>O<sub>2</sub> is an oxidizing agent that acts either as a mediator or as a product in a variety of fields, including pharmacy, environment, and industry [83, 84]. The hydrogen peroxide as a human metabolite can serve as one of the illness indicating factors. It can also be used for food quality control since increased H<sub>2</sub>O<sub>2</sub> concentrations signify product decomposition. Thus, rapid and sensitive H<sub>2</sub>O<sub>2</sub> detection is very important. Authors of [84] implied highly-dense silver nanowires to create an enzyme-free chemical sensor for hydrogen peroxide detection. The nanowire structures demonstrated good electrocatalytic activity for the H<sub>2</sub>O<sub>2</sub> reduction and efficiently assisted the electron transfer. Additional covering with the chitosan film for holding the NWs on the surface of the working electrode allowed good stability of the fabricated sensor.

The exceptional advantages of metallic nanowires, in particular, ease of the chemical surface modification and oriented functionalization are also beneficial for applications in biosens-

ing. Biosystems are often very sophisticated and require the interaction of several different biomolecules in a confined space. The possibility to construct nanowires of different metals opens prospects for the development of differentiated and oriented biofunctionalization and represents a selective functionalization strategy for each metal in the nanowire [56].

Different kinds of biorecognition molecules including antibodies and aptamers can be immobilized on the surface of metallic nanowires, thus implementing exceptional specificity to the target analytes. Integration of the NWs and these target-specific species allows creating immunosensors and DNA sensors. One of the most common sensing targets is, however, glucose. The metal nanowire-based glucose sensing is usually carried out either by deposition of the NW suspension on the electrode by drop-casting and following drying or by the electrodeposition of the NWs on the electrode [85, 86]. Afterward, the surface functionalization with glucose oxidase is performed. Interaction of glucose and glucose oxidase leads to the production of hydrogen peroxide, which is the final molecule that the electrode measures.

### 1.2.3 Main Challenges

Despite all of the advantages described above, the nanowire-based techniques have also certain limitations [87]. Nanowire FETs fabricated using the “bottom-up” approach have two major drawbacks: (1) complexity of high-density fabrication and integration; and (2) large deviation in electrical characteristics of individual devices. These factors significantly obstruct the high-yield production of multiplexed NW FET array sensors.

As in the case of conventional ISFETs, the sensitivity of nanowire FET devices depends on the ionic strength of the measured solution. Therefore, measurement of complex bioliquids with high concentrations of salts (e.g., blood or blood serum) might be problematic and will require a desalting step prior to the measurement to achieve better sensitivity. In general, improving the nanowire FET biosensor performance and decreasing the LOD require increase in the analyte-induced surface charge change. The latter can be achieved by increasing the number of the bound analyte molecules at equilibrium, increasing the electric charge that is carried by each individual molecule, decreasing the double layer capacitance, and reducing the gate dielectric capacitance.

Another important point to be addressed when considering the LOD of NW FET biosensors is the electrical noise. Indeed, the lowest detectable signal change that can be expressed as  $\Delta I/I$  is limited by the smallest resolvable response, i.e., the sensor current noise  $\delta i$ . In this respect, ultimate scaling down the sizes of biosensor devices does not only bring the benefits of increased surface-to-volume ratio but enhances the current noise fluctuations. Therefore, improving the sensitivity and LOD demands a thorough understanding of the noise sources and advancement of the quality of the sensing surfaces and interfaces. Moreover, the performance of nanoscale biosensors can be advanced by improving the fabrication processes and optimizing

working regimes [88].

However, further advances in fabrication / synthesis technology will enhance stability, uniformity, reproducibility, and manufacturability of nanowires. Overall, nanowire-based devices are expected to make a significant contribution to the development of chemical, biological and medical sensors in the near future.

## 1.3 Noise Spectroscopy Techniques

Measurements of biosensor responses in the frequency domain complement ordinary DC measurements and can provide additional information about the dynamic activity of studied bio-objects. The interaction of the analyte with the sensing surface of the biosensor may influence the intrinsic noise sources such as mobility fluctuations or carrier fluctuations, which can then be reflected in the noise spectra. Thus, time and frequency domain measurements represent a powerful tool for studying the analyte-binding kinetics. Moreover, measurements of the current noise allow direct determination of the biosensor LOD and its comparison across various process parameters, biasing conditions, and device geometries [87]. In this regard, investigations of noise behavior are very important. Introduction to the electrical noise, its basic theoretical background, and applications in biosensing are described below.

### 1.3.1 What is Electrical Noise?

Theoretical and practical backgrounds of the electrical noise and noise spectroscopy techniques are discussed in details in [89, 90]. Random fluctuations of voltage (or current) level on the contacts of electronic systems are called the electrical noise. These fluctuations can have different sources. The most interesting is the noise that is not caused by defect contacts or any other parasitic effects but is characteristic for the system itself. It appears due to the random behavior (at the microscopic level) of charge carriers inside electronic components of the system.

Usually, the electrical noise is considered as an unwanted effect. This is true, for example, for high-quality sound amplifiers, where the minimum input power is mainly determined by the intrinsic noise level of the amplifier input stage. However, noise is not always an undesired phenomenon. It can be used to study the electrical properties of electronic devices [90]. Noise spectroscopy allows investigating the dynamics of charge carriers in the tested device, and thus complements the standard DC analysis. In this respect, noise spectroscopy represents a versatile characterization tool, which is becoming especially useful at the nanoscale, where the relative noise level increases with shrinking down the sizes of device components.

### 1.3.2 Theoretical Background

The correlation function can be determined using the following equation:

$$\Phi_x(\tau) = \overline{\langle x(t) \cdot x(t + \tau) \rangle}. \quad (1.5)$$

Here, angle brackets  $\langle \dots \rangle$  denote averaging over the complete ensemble of possible values while a bar on top stands for time averaging. The total power of a random process  $x(t)$  can be determined by the correlation function at  $\tau = 0$ :

$$\overline{x^2(t)} = \Phi_x(0). \quad (1.6)$$

In the theoretical analysis, it is convenient to operate with so-called “mathematical” (two-sided) spectra  $S_x(\omega)$ , which are defined both for positive and negative angular frequencies  $\omega \in (-\infty; +\infty)$ . The spectrum and correlation function  $\Phi_x(\tau)$  are Fourier-conjugated functions:

$$\begin{aligned} S_x(\omega) &= \int_{-\infty}^{+\infty} \Phi_x(\tau) \exp(-j\omega\tau) d\tau, \\ \Phi_x(\tau) &= \int_{-\infty}^{+\infty} S_x(\omega) \exp(j\omega\tau) \frac{d\omega}{2\pi}. \end{aligned} \quad (1.7)$$

Both correlation function and spectral density are even functions:

$$\begin{aligned} S_x(-\omega) &= S_x(\omega), \\ \Phi_x(-\tau) &= \Phi_x(\tau). \end{aligned} \quad (1.8)$$

By taking  $\tau = 0$ , we can obtain from Equations (1.7) and (1.6):

$$\overline{\langle x^2(t) \rangle} = \int_0^{\infty} 2S_x(\omega) \frac{d\omega}{2\pi}. \quad (1.9)$$

Therefore, the spectrum is a frequency decomposition of the total power of the random process.

In measurements, a so-called “physical” (one-sided) spectrum  $\langle x^2 \rangle_f$  is used. It is defined for a linear frequency  $f = \omega/2\pi$ ,  $f \geq 0$ . Considering Equation (1.9), we can write for the “physical” spectrum:

$$\overline{\langle x^2(t) \rangle} = \int_0^{\infty} \langle x^2 \rangle_f df. \quad (1.10)$$

The connection between the “mathematical” and “physical” spectra can then be represented as follows:

$$\langle x^2 \rangle_f = 2S_x(2\pi f), \quad f \geq 0. \quad (1.11)$$

The power of the process, which is accumulated within the frequency range  $[f_1, f_2]$  can be

calculated using the following expression:

$$\langle x^2(\Delta f) \rangle = \int_{f_1}^{f_2} \langle x^2 \rangle_f df, \quad \Delta f = f_2 - f_1. \quad (1.12)$$

### 1.3.3 Noise Components

Two most common noise components are, probably, the *thermal* and *shot* noise. Thermal noise is the result of random fluctuations of the charge carriers (either electrons or holes) velocity in a resistive material. This mechanism can be attributed to the Brownian motion of charge carriers, which is caused by the thermal energy in the system, i.e., dissipation on the crystal lattice. Thermal noise is present in a system that is in the state of thermal equilibrium with the surrounding environment. It was experimentally discovered by Johnson and Nyquist in 1928 [91, 92], and therefore it is often identified as the Johnson-Nyquist noise. Shot noise takes its origin in the discrete nature of the electrical charge. It was first discovered by Schottky in 1918 [93]. Shot noise is caused by the current flow through a system with a barrier(s), and therefore it can be considered as a non-equilibrium process. It can often be observed in semiconductor-based devices when the electric current has to pass through a potential barrier, e.g., a depleted region of a *p-n* junction.

The physical background of thermal and shot noises is different, however, their structure is similar. Both signals can be presented as a sequence of random pulses that have a similar shape and are randomly distributed in time. These signals are considered to be independent of each other and can be described by the Poisson distribution function. In this respect, if the noise signal is represented by a function  $x(t)$  and a shape of a single pulse – by a function  $f(t)$ , then the random pulse sequence is a linear superposition:

$$x(t) = \sum_k a_k f(t - t_k). \quad (1.13)$$

Here,  $a_k$  is the amplitude of the  $k$ -th pulse in this sequence, and  $t_k$  is the moment of time, in which the  $k$ -th event is occurring. The  $t_k$  sequence follows the Poisson distribution. In the case of the electrical current, Equation (1.13) transforms into:

$$i(t) = -q \sum_{k=1} f(t - t_k), \quad (1.14)$$

where  $q \approx 1.6 \times 10^{-19}$  C is the elementary charge. The spectral density of the signal, described by Equation (1.13), can be presented as follows:

$$\overline{S_x(\omega)} = 2\nu \overline{a^2} |F(j\omega)|^2. \quad (1.15)$$

Here,  $\omega$  is the angular frequency,  $F(j\omega)$  is the Fourier transform of the  $f(t)$  function,  $\nu$  is the average event frequency, and  $\overline{a^2}$  is the average square of amplitudes of the pulses. Equation (1.15) is also known as Carson theorem.

In the particular case when the components of the pulse sequence are infinitely small, the shape of each component can be represented by a pulse of an infinitely small width. In this case, the spectral density can be expressed as:

$$\overline{S_x(\omega)} = 2\nu\overline{a^2}. \quad (1.16)$$

As can be seen from Equation (1.16), the spectrum of the impulse process is constant for all frequencies, i.e., it is frequency independent. Such kind of spectrum is sometimes called “white”.

Pulses that originate from discrete events causing thermal or shot noise exhibit constant spectral densities. Every system at the state of thermal equilibrium possesses a thermal energy  $E_T = kT$ , where  $k = 1.38 \times 10^{-23} \text{ J K}^{-1}$  is the Boltzmann constant and  $T$  is the absolute temperature. Therefore, the voltage spectral density of the thermal noise can be written as follows:

$$\overline{S_v(\omega)} = 4kTR. \quad (1.17)$$

Here,  $R$  is the resistance of the sample. Equation (1.17) can also be written in terms of the current noise spectral density:

$$\overline{S_i(\omega)} = 4kTG, \quad (1.18)$$

where  $G = 1/R$  is the sample conductance.

The mean value of the direct current generated by the shot noise can be described by the following expression:

$$-I \equiv \overline{i(t)} = -qv, \quad (1.19)$$

where  $v$  denotes the electrons mean emission speed. The correlation function and current noise power spectral density for this case can be written as:

$$\Phi_i(\tau) = qIf(\tau) + I^2; \quad (1.20)$$

$$\overline{S_i(\omega)} = 2qI + 4\pi I^2 f(\omega), \quad (1.21)$$

respectively. The first term in Equation (1.21) is the current noise spectral density of the shot noise for the average current  $I$ :

$$\overline{S_i(\omega)} = 2qI, \quad (1.22)$$

This result can also be derived from Equation (1.16), if assume that the average number of pulses per unit of time equals  $I/q$  and that all pulses have the same amplitude  $q$ , which gives  $\overline{a^2} = q^2$ .

**Generation-recombination (GR)** or **Lorentzian-shaped** noise is another important noise component. This type of noise can usually be observed in semiconductor devices. It is caused by the random processes of generation and recombination of free charge carriers:

- *recombination*: an electron and a hole can recombine to form a neutral atom;
- *generation*: due to the thermal (or another type) ionization, a neutral atom generates an electron-hole pair.

Schematic representation of the GR processes is shown in **Figure 1.12**. These processes can be either direct (single stage generation-recombination) or indirect (trap-assisted). Main sources of the GR noise are:

- band-to-band generation-recombination;
- carriers exchange with shallow levels in the bandgap;
- GR processes through deep levels.

The corresponding band diagrams are shown schematically in **Figure 1.13**.

Characteristics of GR noise contain information concerning the existing generation and recombination fluxes and therefore about lifetimes of the free charge carriers; energy levels and zones, between which these fluxes are flowing. This information is mainly about the param-

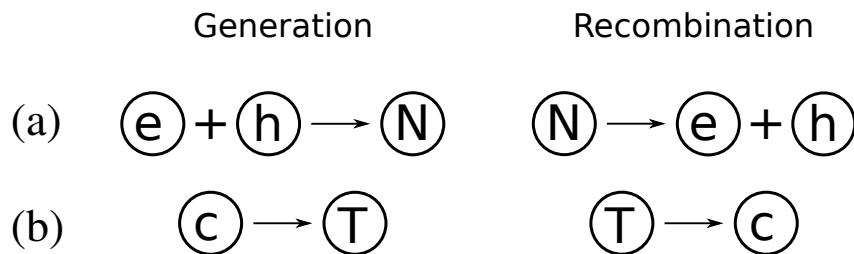


**Figure 1.12:** Schematics of generation-recombination processes: (a) direct, and (b) involving traps. Here,  $e$  denotes an electron,  $h$  is a hole,  $N$  is a neutral atom,  $c$  stands for a charge carrier (either electron or hole), and  $T$  is a trap.

ters of different local centers including their concentrations, capture cross-sections, and energy depths. Investigation of GR noise in semiconductor devices allows to detect various defects in the semiconductor and to find their parameters, i.e., to perform noise spectroscopy of the energy levels caused by these defects. Studies of GR noise can provide useful information about the nature of the characteristic physical processes, which are responsible for the conduction of a semiconductor.

Another fundamental noise type is the **flicker noise**. It is often called  $1/f$  noise, because its spectral density is inversely proportional to frequency as  $|f|^{-\alpha}$ , where coefficient  $\alpha$  usually lies

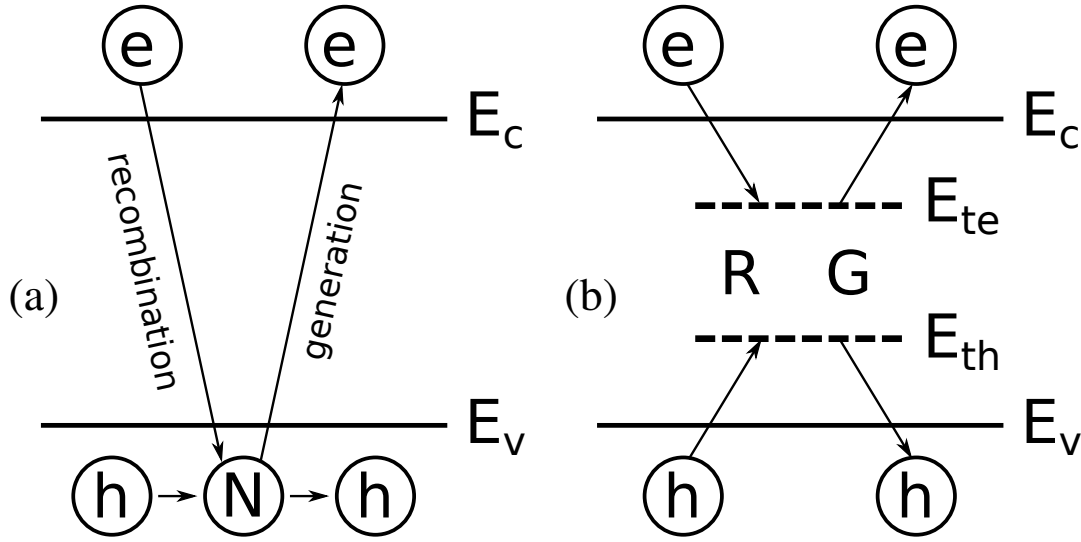


**Figure 1.13:** Band diagrams of generation-recombination processes: (a) band-to-band GR process, and (b) trap-assisted GR process. Here,  $E_c$  denotes bottom of the conduction band;  $E_v$  is the valence band ceiling;  $E_{te}$  and  $E_{th}$  are the energy levels of traps for electrons and holes, respectively.

in the range from 0.8 to 1.2. This dependency can be experimentally observed even at frequencies as high as  $10^6$  Hz. The upper limit of this dependence is difficult to find since at higher frequencies flicker noise amplitude rapidly decays, and thus it can no longer be distinguished due to the presence of thermal noise or other noise components. Although the flicker noise is an essential noise component that can be found in almost every electrical system, to the moment there is no comprehensive theoretical explanation of this phenomenon. Though, several applicable models are developed for particular cases, e.g., for the carrier capture-decapture in the oxide layer of MOSFET devices.

The  $1/f$  noise can also be represented as a sequence of random pulses. To have the  $1/f$  spectral density, the shape of these pulses has to be defined as:

$$f(t) = t^{-1/2}u(t), \quad (1.23)$$

where  $u = 1$  for  $t > 0$  and  $u = 0$  for  $t < 0$  is a step function. The Fourier transform of the function  $f(t)$  from Equation (1.23) can be written as follows:

$$F(j\omega) = \frac{\sqrt{\pi}}{|\omega|^{1/2}} \exp(\mp j\pi/4), \quad (1.24)$$

where the “-” sign corresponds to positive frequencies  $\omega > 0$ , and the “+” corresponds to the negative ones  $\omega < 0$ . By substituting this expression into Carson’s theorem (Equation (1.15))

we can get for the spectral density:

$$\overline{S_x(\omega)} \propto 1/|\omega|. \quad (1.25)$$

As it can be seen from Equation (1.25), the desired  $1/\omega$  dependence can be obtained analytically. However, in practice, it is difficult to find physical mechanisms, which could result in pulses that can be described by Equation (1.23).

Fluctuations of the resistance in the homogeneous materials that exhibit  $1/f$  spectra can be related either with fluctuations of the *number of charge carriers* or with fluctuations of their *mobility*.

The *number* of the charge carriers can vary due to the carrier exchange either with an external source, or with internal localized energy states, e.g., traps, or generation-recombination centers. For metals and semiconductors, the carrier exchange with an external source can be excluded since the condition of neutrality has to be fulfilled. Thus, the physical source of the  $1/f$  noise in these materials has to be related to capture-decapture processes of charge carriers to or from traps.

One of the most common models for  $1/f$  noise in semiconductor devices is based on the trapping and detrapping processes to/from traps with a wide range of the carriers lifetime. When a free charge carrier is trapped, it is not participating in the electrical conduction of the sample for a certain time. This results in modulation of the sample resistance. If such a capture process follows Poisson's statistics, then modulation of a single capture event has the random telegraph signal (RTS) shape, which possesses a relaxation type spectrum. If the sample has a set of such kind traps with a certain distribution of capture times, the total spectrum will be a sum of the relaxation spectra from each trap. This sum can result in the  $1/f$  dependence in a limited frequency range, which is defined by the interval of carriers lifetime.

The spectral density of fluctuations caused by traps of a certain type has the following form:

$$\frac{4\tau_z}{(1 + \omega^2\tau_z^2)}.$$

Here,  $\tau_z$  is the trap capture time. The capture time  $\tau_z$  can be described by a distribution function  $\rho(\tau_z)$ , which fulfills the normalization condition:

$$\int_0^\infty \rho(\tau_z) d\tau_z = 1. \quad (1.26)$$

The spectral density of the total number of fluctuations  $n(t)$  can be described by the following expression:

$$\overline{S_n(\omega)} = 4\overline{\varphi_n(0)} \int_0^\infty \frac{\tau_z \rho(\tau_z)}{(1 + \omega^2\tau_z^2)} d\tau_z, \quad (1.27)$$

where  $\overline{\varphi_n(0)}$  is the mean square of  $n(t)$ .

McWhorter suggested that the capture time distribution is defined by the tunneling of free charge carriers to/from traps, located in the gate dielectric layer and at the Si/SiO<sub>2</sub> interface. If the trap is located at the distance  $w$  from the surface, then the expression for the time constant can be written as follows:

$$\tau_z = \tau_0 \exp(\gamma w), \quad (1.28)$$

where  $\tau_0$  and  $\gamma \simeq 10^8 \text{ cm}^{-1}$  are constants. For the uniform distribution of traps in the distance range  $w_1 - w_2$ , which corresponds to the time constants  $\tau_1$  and  $\tau_2$ , from Equation (1.28) we can get:

$$\rho(\tau_z) d\tau_z = \begin{cases} \frac{d\tau_z/\tau_z}{\ln(\tau_2/\tau_1)}, & \text{for } \tau_1 \leq \tau_z \leq \tau_2, \\ 0 & \text{otherwise.} \end{cases} \quad (1.29)$$

If we substitute expression (1.29) into Equation (1.27), then we can get the following expression for the spectral density of fluctuations:

$$\overline{S_n(\omega)} = \frac{\overline{4\varphi_n(0)}}{\ln(\tau_2/\tau_1)} \int_{\tau_1}^{\tau_2} \frac{d\tau_z}{(1 - \omega^2 \tau_z^2)} = \frac{\overline{4\varphi_n(0)}}{\ln(\tau_2/\tau_1)} \frac{(\arctan \omega \tau_2 - \arctan \omega \tau_1)}{\omega}, \quad (1.30)$$

The dependence, defined by Equation (1.30), can be approximated with the  $1/|f|$  law well in the frequency range where  $\omega \tau_2 \gg 1$  and  $0 \ll \omega \tau_1 \ll 1$ .

Fluctuations of *mobility* can also cause flicker noise in materials. Hooge suggested that  $1/f$  fluctuations in all homogeneous materials can be represented by the empirical relation [94]:

$$\frac{\overline{S_r(\omega)}}{R_0^2} = \frac{\alpha_H}{N_{tot} |f|}, \quad (1.31)$$

where  $N_{tot}$  is the total number of free charge carriers in the sample,  $R_0$  is the average value of the sample's resistance,  $\overline{S_r(\omega)}$  is the spectral density of the resistance fluctuations and  $\alpha_H \simeq 2 \times 10^{-3}$  is the “universal” constant, which has a weak dependence on temperature. The fact that the noise spectral density, defined by Equation (1.31), does not depend on the sample size and the concentration of charge carriers indicates the “volumetric” nature of noise.

Equation (1.31) describes the  $1/f$  noise behavior well when the charge dissipation on the crystal lattice is dominating over dissipation on impurities, and dissipation on the edges is small. For the cases when the dissipation on impurities is significant, the constant  $\alpha_H \simeq 2 \times 10^{-3}$  has to be reduced by a factor

$$\left( \frac{\mu_{imp}}{\mu_{lat} + \mu_{imp}} \right)^2.$$

Here,  $\mu_{imp}$  and  $\mu_{lat}$  are the carrier mobilities, related to the dissipation on impurities and crystal lattice, respectively. It has been shown, that the Hooge's parameter can significantly vary from the stated value of  $\alpha_H \simeq 2 \times 10^{-3}$ , however it can still be used to compare noise levels in

different materials and devices [87, 90, 95].

It can be shown that the noise power spectral density is inversely proportional to the total number of free carriers that experience independent mobility fluctuations. In this case, the parameter  $\alpha_H$  in Equation (1.31) for the  $1/f$  noise is proportional to:

$$\alpha_H \sim (\mu/\mu_{lat}), \quad (1.32)$$

where  $\mu$  is the measured mobility.

However, this explanation of the flicker noise has certain drawbacks. To describe experimentally obtained  $1/f$  dependencies, mobility fluctuations must have inexplicably large characteristic times (greater than 1 s). Most of the known physical processes, have much lower characteristic times, e.g., the mean free time  $\approx 10^{-12}$  s, or even the average carrier transit time  $< 10^{-3}$  s. Therefore, it is difficult to find a reasonable physical background, which could explain the flicker noise in a wide frequency range by such an approach.

*Random telegraph signal (RTS) noise:* For a variety of semiconductor devices, it was observed that with scaling the sizes down to sub-micrometer scale the  $1/f$  noise decomposes into separate GR components, arbitrarily distributed by frequency. As with shrinking down the sizes, the defect quantity also decreases, in an extreme case a single defect can take control over the charge transport. In this particular case, the electrical current will have an RTS shape (see **Figure 1.14**). Such fluctuations have Lorentzian-type spectra:

$$S_I(\omega) = \frac{4\Delta I^2\tau^2}{(\tau_c + \tau_e)[1 + \omega^2\tau^2]}, \quad (1.33)$$

where  $\Delta I$  is the current switching amplitude,  $\tau$  is the time constant, defined by mean values of the capture time ( $\tau_c$ ) and emission time ( $\tau_e$ ):  $\tau^{-1} = \tau_c^{-1} + \tau_e^{-1}$  [96].

Analysis of the RTS noise behavior at different temperatures and applied voltages allows

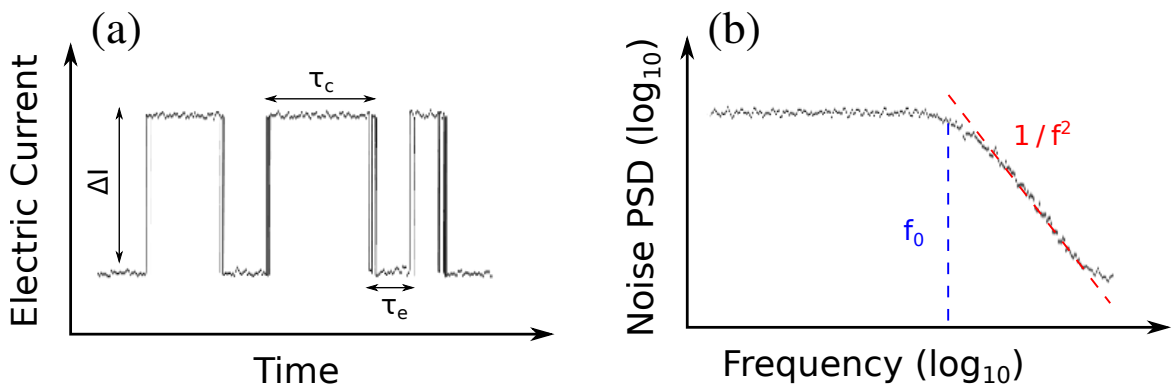


**Figure 1.14:** Schematic drawings of (a) two-level RTS current fluctuations, and (b) corresponding noise power spectral density spectrum.

studying of single electrically active traps in the dielectric layer (or at the Si/SiO<sub>2</sub> interface), determine their spatial position and physical origin [97–99].

### 1.3.4 Noise Spectroscopy for Biosensing

Low-frequency noise spectroscopy is a powerful, highly sensitive and non-destructive analysis technique that can provide useful information about the sample performance and operation regime. It provides insight into the dynamics of the charge carriers in the device being tested and, thus complements standard current-voltage measurements [100]. In this respect, studies of the noise origin in order to find possible ways to increase the SNR are important to improve the sensing capabilities of nanobiosensors.

In most cases, the electrical noise is considered as an unwanted effect limiting the performance of electronic devices. Its negative impact becomes especially pronounced at the nanoscale, since shrinking down the sizes of electronic components inevitably leads to an increase of the relative contribution of noise to the resulting signal. In nanobiosensors, where the signals usually have very small amplitudes, the low-frequency electrical noise becomes a critical issue affecting the sensitivity and determining the limit of detection. Thus, reducing the noise level is one of the main goals in modern biosensing field.

On the other hand, noise can also be used as a sensing signal, which can be used for detection of different biochemical species [52, 101–103]. For example, in nanowire FET biosensors binding and unbinding of target biological molecules may induce a two-level random telegraph signal noise [104, 105]. Such fluctuations exhibit a Lorentzian shape power spectral density (PSD) with a characteristic frequency  $f_0$ . Frequency domain analysis of such fluctuations demonstrated a novel promising approach for the detection of biomolecules in ultralow concentrations.

Two-level fluctuations of the drain current can appear also due to intrinsic properties of Si NW FET devices. Such behavior is usually attributed to capture / emission processes of a charge carrier into / from the single electrically active trap, located close to the Si/SiO<sub>2</sub> interface [106, 107]. This RTS noise causes the dynamic variability of devices and considerably affects reliability, productivity, and quality of electronic devices. However, it turns out that parameters of such an RTS noise are highly sensitive to changes in the gate surface potential, which opens prospects for its applications in biochemical sensing. Authors of [108] fabricated liquid gated Si NW FETs with characteristic dimensions  $W \times L = 100 \times 500 \text{ nm}^2$ , which exhibited RTS fluctuations of the drain current in the linear operation regime, and tested their sensitivity in 0.1 M phosphate-buffered saline (PBS) solutions with different pH values. Obtained results demonstrated a 400% sensitivity gain when using the RTS noise caused by a single trap as a sensing signal in comparison to the conventional  $I_D - V_G$  shift approach. This technique can be further extended to detect various biomolecules. One of the biggest chal-

allenges for practical applications, however, is that the RTS noise is a completely casual effect, which appears in nanodevices due to the random distribution of traps at the conducting channel / insulator interface. The dynamics of the carrier exchange with a single trap greatly depends on the trap position and charge state. Therefore, to utilize single trap phenomena for sensing purposes it is important to understand and control the single trap parameters. Recently, several novel approaches to tune the characteristics of a single trap were reported. Zadorozhnyi and Li et al. applied an external influence to fabricated silicon nanowire devices containing a single electrically active trap [52]. The authors have shown that modulation dynamics of the drain current by the single trap can be effectively tuned by a small dose gamma irradiation treatment. Furthermore, not only an external influence but also device configuration and operation can be used to control parameters of the single trap. Studies on the liquid-gated two-layer Si NW FETs with pronounced RTS noise shown that the capture time constant can be precisely modified by applying the back-gate voltage in dual-gate configuration [103].

Characteristic  $1/f^2$  noise dependencies resulting from RTS noise were observed also in tunable metallic nanoconstrictions modified by organic molecules. It has been shown that a number of thiol-terminated metal-molecule-metal systems can express very high noise levels [109, 110]. Such noise behavior was explained by vibrations, breaking and reestablishing of the bonds between the molecule and metal electrodes. In the cases of more stable metal-molecule-metal systems (without bond breaking) it was revealed that noise originates from the current-induced reconfigurations of the molecule [111]. In this respect, noise fluctuations can provide very useful information about the strengths of molecular and atomic bindings as well as mechanisms of transport formation in the structures.

Another noise components can also be efficiently used for biomolecule detection. Guo et al. revealed that the inverse flicker noise amplitude of liquid-gated Si NW FETs demonstrates strong gate coupling effect in the inversion operation regime [101]. This phenomenon can be used to detect target molecules that bind silicon nanowires even in the cases of low signal-to-noise ratios.

## 1.4 Summary

The high demand in the performance improvement of medical diagnostics has facilitated rapid development of biosensing field. At present, many different methods have been developed for qualitative and quantitative determination of various biochemical targets. Optimization of an existing approach or/and the development of a new biosensor for the specific analyte always require:

- selecting most efficient type of transducer;
- selecting most suitable immobilization technique.

Often these choices are made without a thorough analysis of different signal conversion systems, specific features of transducers and bioselective membranes. In this chapter, therefore, several most promising sensing approaches, their advantages, drawbacks, and practical applications are discussed.

Nanowires modified with specific biorecognition species represent a powerful sensing platform for rapid, label-free, selective and highly-sensitive detection of proteins, DNAs, and viruses. Nanowire-based devices have proven to be promising candidates for extracellular recordings from different electrogenic cells and cellular networks. Moreover, the advances of semiconductor fabrication technology allow multiplexed detection of various analytes simultaneously. Therefore, nanowires represent a versatile class of biochemical sensors.

The aim of this work is the development of high-quality nanowire-based devices suitable for biochemical sensing purposes. In this respect, single Si NW FETs are fabricated on the basis of *p*-type SOI substrates in different configurations and geometries. The patterning of the NW structures is carried out using optimized thermal nanoimprint lithography. Optimization of the fabrication technology is performed to achieve good reproducibility and reliability of the NW structures. The fabricated devices are specifically designed for measurements in bioliquids, and thus they can be tested for lab-on-a-chip applications. The Si NW FETs are characterized using current-voltage (I-V) technique, and low-frequency noise spectroscopy – a powerful non-destructive characterization approach.

Electrical properties of metallic nanowires can be strongly affected by molecular adsorbates. Thus, metal-NW structures can be utilized for sensing applications. In this regard, this work also describes investigations of transport and noise properties of ultrathin ( $\sim 2$  nm in diameter) gold nanowire bundles, produced by wet chemical synthesis, and “top-down” fabricated tunable gold nanoconstrictions ( $< 100$  nm in cross-section). The impact of adsorbed organic molecules on the electrical properties of the fabricated gold nanowire structures is studied using low-frequency noise spectroscopy. The results obtained are promising for understanding the electrical behavior of metal-molecule systems, molecular layers, and single molecules.

# **OPTIMIZATION OF Si & Au NWs FABRICATION TECHNOLOGY**

At present, a variety of patterning techniques are developed for fabricating micro- and nanostructures. Silicon nanowire (Si NW) field-effect transistors (FETs) can be fabricated using well-developed complementary metal-oxide-semiconductor (CMOS) compatible technology. This allows for good scalability, reproducibility and low device-to-device variation of electrical characteristics to be achieved. Patterning techniques used in the processing define the resolution, the complexity of the fabrication, and the cost of the fabricated devices. One of the most common ways to pattern nanostructures is using the electron beam lithography (EBL). However, this technique is quite expensive and time-consuming. Indeed, there are different patterning techniques, which allow reducing the fabrication cost including nanoimprint lithography (NIL), extreme ultraviolet lithography (EUV), nanosphere / colloidal lithography, etc. Among the alternative solutions, NIL is one of the first choices because of its high CMOS-compatibility and possibility of high-resolution nanopatterning.

Metallic nanowires and nanojunctions are other interesting devices for the sensing applications. They can be fabricated on the basis of flexible substrates. By a controlled bending of the substrate, one can tune cross-sections of such structures, and therefore, their physical characteristics. Devices of this kind are promising for studying the properties of molecular layers and even single molecules.

## **2.1 Fabrication of Si NW Biosensors**

All technological steps needed for the fabrication of Si NW FETs devices are performed using the Helmholtz Nanoelectronic Facility (HNF) of Forschungszentrum Jülich GmbH (FZJ). Si NW FETs are fabricated using cost-efficient nanoimprint technology. Fabrication of nanowire biosensors using NIL consists of two main steps: fabrication of mold – a reusable master for patterning the nanowire structures and subsequent fabrication of Si NW FETs – active transducer elements of the sensor. Optimization of every technological process is crucial for the performance of the devices, and thus it has to be done carefully. Main steps needed to fabricate the Si NW FET devices are described below.

### 2.1.1 Fabrication of Si NW Mold

The master structure should allow low-roughness high-resolution nanopatterning. It should also have good mechanical properties, e.g., stiffness, to be suitable for multiple time usage. In this respect, silicon can be considered as a perfect substrate material for mold fabrication. They possess high mechanical stability, and they can be processed using well-developed CMOS compatible technologies. When patterning nanostructures, anisotropic wet etching techniques allow for almost atomically-flat etching profiles to be achieved, which is crucial for the device performance. It is known that (Si  $\langle 110 \rangle$ ) substrates give well-defined vertical etching profiles when exposed in potassium hydroxide (KOH) or tetramethylammonium hydroxide (TMAH). Therefore, silicon (Si  $\langle 110 \rangle$ ) wafers are chosen as substrates for mold structures. Main technological steps used to create the mold are described below.

#### Substrate cleaning

The purity of the wafer surface is a crucial requirement for the successful fabrication of silicon structures. Thus, before further processing, substrates have to be cleaned to remove any organic or metallic contaminants. For the cleaning purpose, RCA standard cleaning procedure is used. It consists of three steps: PIRANHA cleaning, alkaline standard clean one (SC-1), and acidic standard clean two (SC-2). Each cleaning step is carried out for 10 min. In between these steps, a short time 1 % HF dip is performed to remove the thin native oxide layer.

PIRANHA solution used is a mixture of concentrated sulfuric acid ( $\text{H}_2\text{SO}_4$ , 96 % wt.) and hydrogen peroxide ( $\text{H}_2\text{O}_2$ , 30 % wt.) in a volume proportion  $\text{H}_2\text{SO}_4 : \text{H}_2\text{O}_2 = 1 : 1$ . This mixture is prepared by slowly adding the peroxide to the acid. The solution is highly exothermic (sometimes it heats up to 130 °C) and very corrosive. Therefore, it must be prepared carefully. PIRANHA is a powerful oxidizing agent, which removes most of the organic residuals from the wafer surface. However, substrates have to be well cleaned and completely free from organic solvents (possibly from the previous cleaning steps) before exposing into PIRANHA. Failure to comply with these requirements can lead to the severe bubbling of the solution, the release of reaction gases in huge amount and even to an explosion.

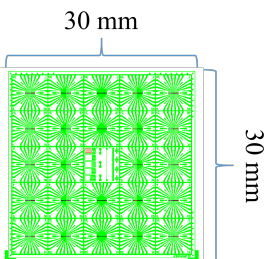
After the PIRANHA, SC-1 and SC-2 procedures are performed to clean the surface from metallic contaminants. Both cleaning procedures are performed at a constant temperature of 60 °C. SC-1 is used for further cleaning of organic residuals and from group 1B and group 2B metals, as well as some other materials (including Au, Ag, Cu, Ni, Cd, Zn, Co, and Cr) [112]. This step is performed by immersing the substrates into a solution containing 30 % wt. ammonia water, deionized (DI) water and hydrogen peroxide in a proportion  $\text{NH}_4\text{OH} : \text{H}_2\text{O} : \text{H}_2\text{O}_2 = 1 : 20 : 4$ . SC-1 is also efficient for particle removal. The procedure results in a surface modification of the substrate and particles, changing their zeta potentials, which causes the

particles to repel [113]. After the procedure is performed, substrates are extensively rinsed in highly filtered DI water. SC-2 cleaning is performed by immersing the substrates into a mixture of hydrochloric acid (30 % wt. HCL), DI water and hydrogen peroxide in a proportion: HCL : H<sub>2</sub>O : H<sub>2</sub>O<sub>2</sub> = 1 : 20 : 1. The process results in the cleaning of alkali ions and Al<sup>3+</sup>, Fe<sup>3+</sup> and Mg<sup>2+</sup> cations. This procedure also helps to remove the metal ions that are not completely removed by SC-1, e.g., gold.

### Formation of the hard mask

Before further processing, including dry and wet etching steps, a thin silicon dioxide layer is thermally grown on the surface of the substrates. This layer later serves as a hard mask for structure patterning. The oxidation is performed directly after the RCA cleaning using the Tempress Omega Junior oxidation furnace at the temperature of 950 °C for 30 min. The process allows for a uniform 30 nm SiO<sub>2</sub> film to be achieved. Oxidized substrates are spin-coated with the electron beam sensitive polymer poly(methyl methacrylate) (PMMA) 649.04 at the spin speed of 4000 rpm and then soft-baked at 180 °C for 5 min. Both: nanowire structures and feed lines are defined using EBL. Sets of nanowire structures with different geometrical parameters are designed. Widths and lengths of the nanowires are listed in **Table 2.1**. Large feedlines

**Table 2.1:** Designed single Si NW Structures

Row number	Width, $W$ nm	Length, $L$ $\mu$ m	
1	50-500	20	
2	100	16-21	
3	50-500	5	
4	50-500	4	
5	250	2-22	

pattern is written coarse with the resolution of 50 nm and the dose of 270  $\mu$ C cm<sup>-2</sup>. However, when e-beam writing very small and narrow structures, different size-dependent effects, e.g., line broadening become critical. Thus, they have to be considered to achieve good control over the parameters of the fabricated biosensor devices. As a result, patterning the nanowires of different geometry requires the use of different doses. Therefore, dose tests are performed to find optimal writing parameters for every nanowire structure. All the designed nanowires are written with the fine resolution of 2.5 nm and the optimized doses, ranging from 208  $\mu$ C cm<sup>-2</sup> to 547  $\mu$ C cm<sup>-2</sup>. After the e-beam exposure, development procedure is performed in AR600-55 developer for 1 min, followed by stopping in isopropanol for 30 s and drying under a nitrogen flow. Finally, the pattern is transferred from the resist layer to the silicon dioxide using reactive ion etching (RIE). Firstly, resist residuals are removed from the surface using short-time oxygen plasma treatment. Silicon dioxide is then selectively etched down to the silicon through the

openings in the resist layer using  $\text{CHF}_3$  / Ar plasma. Finally, the residuals of the resist mask are stripped-off using high-power  $\text{O}_2$  inductively coupled plasma.

### Wet etching in KOH

After the hard mask is defined, the pattern has to be transferred into the silicon layer using etching techniques. Low roughness of the mold is a key prerequisite for its long-term application and reproducibility of the imprinted pattern. In this respect, wet etching processes have an advantage over the plasma-based techniques since they can provide much smoother etching profiles. [114, 115]. Chemicals like TMAH or KOH are widely used in the semiconductor industry for the silicon etch purposes. They provide not only smooth but also highly anisotropic etching profiles [116, 117].

Parameters of the etching process, such as etchant concentration and temperature have to be optimized and kept constant during the etching procedure to have reproducible etching results. To achieve smooth etching profiles, high etchant concentration and low-temperature processes are beneficial [118].

The mold etching process is performed using 45% wt. stock KOH solution at 30 °C. At first, tests are performed to determine the exact etching rate of the silicon  $\langle 110 \rangle$  at these conditions. For this purpose, patterned Si /  $\text{SiO}_2$  test samples are prepared using photolithography and RIE. The samples are dipped in the KOH solution for a different amount of time. After the silicon etching, the oxide mask is removed using buffered oxide etch (BOE) (BOE 7 : 1) solution. Depth of the etched pattern is measured for each sample using Dektak 150 profilometer and plotted versus the etching time in **Figure 2.1**. The etching rate of  $78.27 \pm 1.7 \text{ nm min}^{-1}$  is

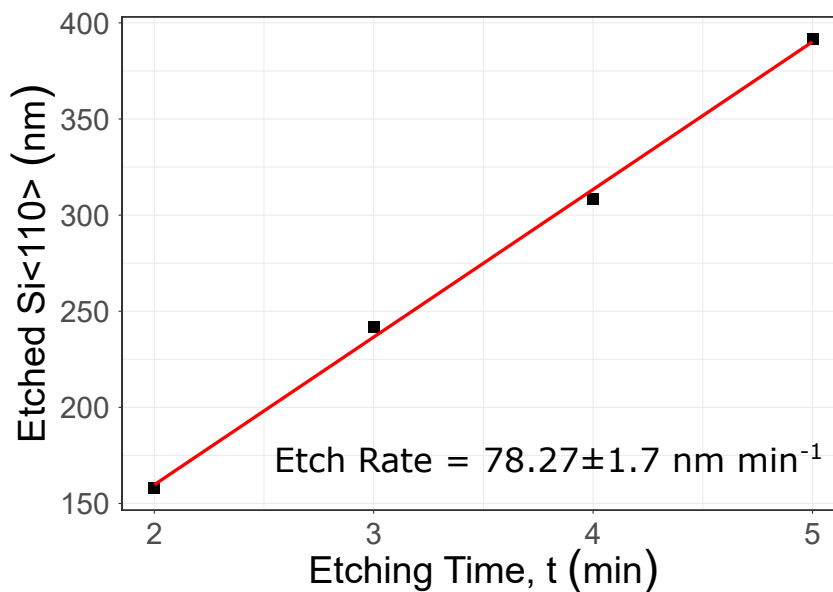


**Figure 2.1:** Depth of the etched Si  $\langle 110 \rangle$  versus the etching time in the 45 % wt. KOH solution at 30 °C. Etching rate, extracted by fitting of the data is  $78.27 \pm 1.7 \text{ nm min}^{-1}$ .

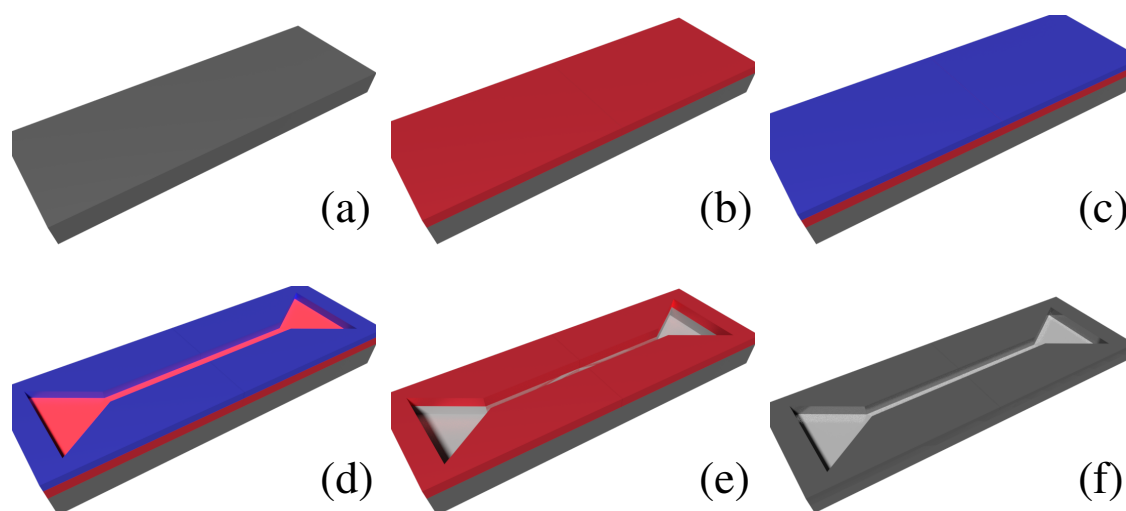


**Figure 2.2:** Sketches of the technological steps, needed to fabricate nanoimprint mold: (a) Si $\langle 110 \rangle$  substrate; (b) hard mask thermal oxidation; (c) spin-coating of e-beam sensitive polymer; (d) electron beam lithography and development; (e) RIE and KOH etching; (f) HF mask oxide stripping.

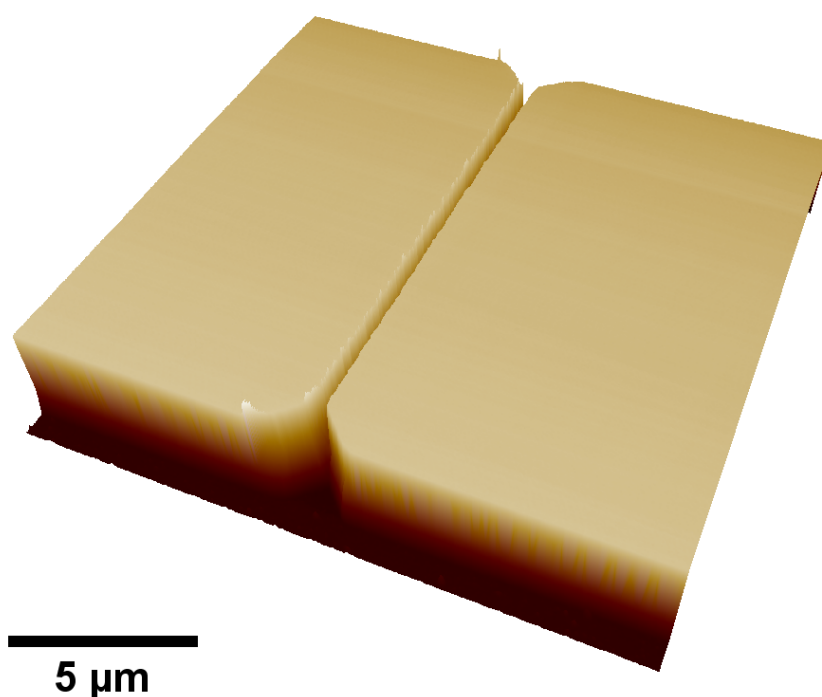


**Figure 2.3:** A typical atomic force microscopy micrograph of the fabricated mold nanowire structure, showing low roughness of the surface (about 2 nm) and therefore – the high quality of the fabricated device.

extracted from the data obtained. The optimized silicon etching time for mold is 1 min 40 s. The procedure allows for a 130 nm deep smooth and well-defined pattern to be achieved. Sketches, of the nanoimprint mold fabrication process are shown in **Figure 2.2**.

Typical AFM image of the fabricated mold nanowire structure is shown in **Figure 2.3**. After the etching, substrates are additionally cleaned using SC-2 cleaning procedure to get rid of the possible contamination with potassium ions.

### **Anti-sticking functionalization**

The imprint process is usually performed at high pressures and elevated temperatures [119]. To establish a stable and reproducible imprint operation, the mold should be able to retract easily from the sample after the imprinting procedure. Thus, an appropriate surface treatment should be applied to improve the anti-sticking properties of the mold [120]. For this purpose, the surface of the mold is functionalized with 1H, 1H, 2H, 2H-Perfluorooctyltriethoxysilane (FOTCS) molecules. Firstly the mold surface is activated by oxygen plasma treatment in a GIGAbatch system. Using the oxygen plasma with optimized parameters for power  $P = 80$  W, pressure  $p = 0.8$  mbar and time  $t = 5$  min results in formation of the hydroxyl (-OH) groups on the SiO<sub>2</sub> surface. Directly after the plasma activation, FOTCS molecules are deposited on the sample surface from a gas-phase inside a desiccator at the constant pressure of 45 mbar for 1 h. This process is performed in an oxygen-free environment inside the argon-filled Glove Box. Silane molecules covalently bind the -OH groups on the mold surface, forming a monolayer. The excess amount of molecules, which didn't bind the surface, is removed by extensive rinsing with ethanol. The silanization procedure is repeated three times in a row to achieve a good quality of the FOTCS layer. Each deposition step is followed by heating-up to 140 °C for 3 min. This surface functionalization allows achieving better anti-adhesive properties, and thus facilitates the demolding process. Once the anti-sticking functionalization is done, the mold is ready to use for the imprint purposes.

### **2.1.2 Si NW FET Fabrication**

Fabrication of the silicon nanowire biosensors is done on the basis of 100 mm *p*-type silicon-on-insulator (SOI) wafers, purchased from Soitec. The substrates have 70 nm of a *p*-type active silicon  $\langle 100 \rangle$  layer, which is separated from the highly-doped base silicon by a 145 nm thick buried oxide (BOX) layer. Concentrations of the impurities in the boron-doped active silicon and base silicon layers are  $10^{15}$  cm<sup>-3</sup> and  $10^{17}$  cm<sup>-3</sup> respectively.

## Substrate Preparation

The technological processes are optimized for the fabrication of 50 nm high structures with widths and lengths of nanowires as listed in **Table 2.1**. At first, a complete RCA cleaning is performed (as described in section 2.1.1) to purify the surface of the substrate from any organic and metallic contaminants. Cleaned substrates are then given for dry thermal oxidation. The process is performed in the Centrotherm CLV 200 oxidation furnace at 950 °C for 55 min. As result, a uniform 30 nm thick SiO<sub>2</sub> film is formed.

The hard mask oxidation reduces the thickness of the active silicon down to  $\sim 57$  nm. After the patterning process, the oxide mask has to be removed. This is done by dipping the sample into diluted 1 % HF solution. The drawback of this procedure is that the BOX layer is etched as well. This might cause some undesirable effects, e.g., under-etching of the nanowire structures and appearance of leakage currents. To prevent this issue, the thickness of the mask is decreased to  $\sim 15$  nm by etching in 1 % HF solution prior to the patterning. This reduces the mask removal time and under-etching of the BOX at further fabrication steps<sup>1</sup>.

## Optimization of the Imprint Procedure

Thermal resists of mr-I 70xx R series are purchased from [microresist technology](#) and used for the patterning purpose. These resists have the glass transition temperature of 55 °C. Parameters of the process, such as aspect ratios of the mold grooves (width / depth), the initial thickness of the resist layer, as well as the imprint pressure and temperature should be optimized to achieve well-defined and reproducible results [121]. For this purpose, the patterning procedure is firstly developed on flat Si / SiO<sub>2</sub> test samples. The mold structure used in all tests was 130 nm in depth. To achieve different polymer thickness the Si / SiO<sub>2</sub> substrates are spin-coated with mr-I 70xx R resists at different spin speeds, and then soft-baked for 1 min at 100 °C. The two stage thermal imprint procedure is performed to transfer the pattern into the resist layer. Firstly, the temperature and pressure are gradually increased to 140 °C and 450 PSI, respectively. After this, the pressure is increased to 575 PSI and kept constant at the same temperature of 140 °C for 4 min. Applying high pressures at the temperatures above the glass transition temperature forces the resist to fill in the grooves of the mold. Then the chamber is slowly cooled down below the glass transition temperature while keeping the pressure ( $P = 575$  PSI) constant. When the temperature reaches 45 °C, the chamber pressure is slowly released. The mold is then removed from the sample with patterned resist film. For this purpose a sharp razor blade is slowly introduced between the sample and the mold.

The pattern transfer is analyzed for every test sample using optical microscopy. The results are presented in **Figure 2.4** for the values of the initial resist thickness ranging from 100 nm to

---

<sup>1</sup>The author thanks Ihor Zadorozhnyi for this valuable suggestion and for many useful discussions of technological processes.

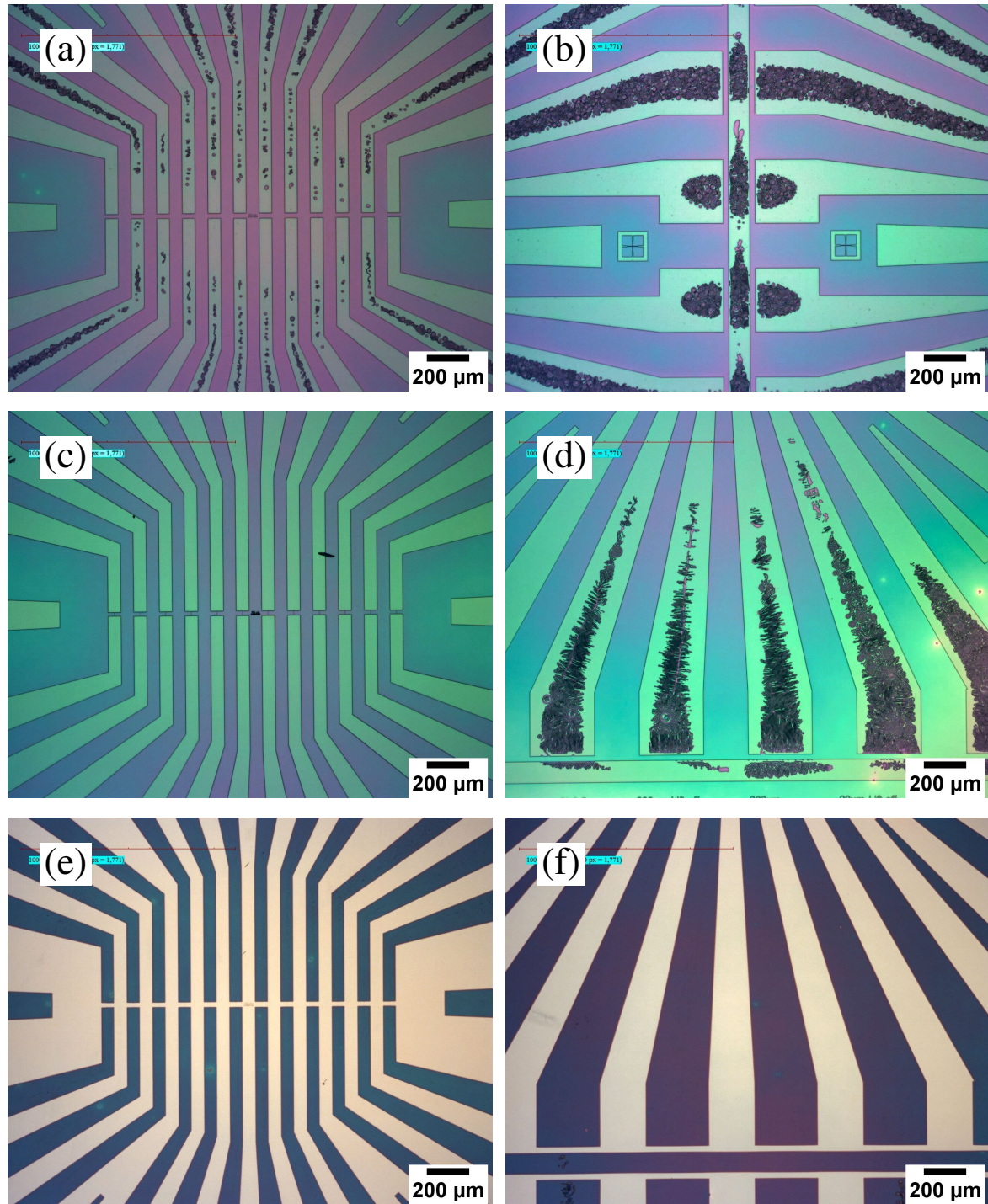


**Figure 2.4:** Optical microscopy images of the test samples, used for the optimization of the resist thickness for the nanoimprint patterning procedure. Micrographs (a) and (b), (c) and (d), (e) and (f) correspond to the nanowire and feed line patterns for the resist thicknesses of 100 nm, 130 nm, and 185 nm, respectively. Increasing the resist film thickness results in a significant improvement of the large feed line pattern while the tiny nanowire structures are imprinted well for almost any of the tested resist thicknesses.

185 nm. At low thicknesses of the resist film, a lot of cracks are formed in the resist layer. This is particularly pronounced in the feed line region, where the pattern is large. At the same time, the tiny nanowire structures and adjoining contact lines are imprinted well almost for any of the tested resist thicknesses. This observation is in a good agreement with previously reported literature [122]. The feed line pattern is more uniform on the samples with thicker resist layer. On the other hand, the thicker is the initial resist film, the thicker is the residual layer on the surface of the sample after the demolding process. The optimized resist thickness is  $\sim 180$  nm for the described imprint conditions.

One of the major drawbacks of this technique is, however, that a thin residual resist layer is inevitably present everywhere on the sample including the patterned regions, which should not be covered by the resist. This residual layer has to be removed prior to the etching procedure to achieve the best patterning results.

### Etching of Nanowire Structures

After the imprinting procedure the pattern is transferred to the top silicon dioxide layer using reactive ion etching. The procedure is performed in three steps. At first, the resist residual layer is removed using isotropic etching in pure oxygen plasma. Nanowire pattern is then etched through the silicon dioxide using  $\text{CHF}_3$  / Ar plasma. Finally, the resist film is completely stripped-off using high power  $\text{O}_2$  inductively coupled plasma (ICP).

The nanowire pattern, defined in the  $\text{SiO}_2$  hard mask, is then transferred to the active silicon layer of the SOI substrate using wet chemical etching in TMAH solution. The patterned SOI pieces are immersed into 5% TMAH solution at  $60^\circ\text{C}$  for 15 s. TMAH etching is highly anisotropic depending on the crystal orientation: the etch rate for Si  $\langle 100 \rangle$  plane is almost 13 times higher than for the Si  $\langle 111 \rangle$  plane ( $0.33 \mu\text{m min}^{-1}$  compared to  $0.026 \mu\text{m min}^{-1}$ , respectively) at the aforementioned etching conditions. Resulting nanowires have a trapezoidal cross-section, with angles of  $54.7^\circ$  at the base corresponding to the Si  $\langle 111 \rangle$  plane (see **Figure 2.5**).

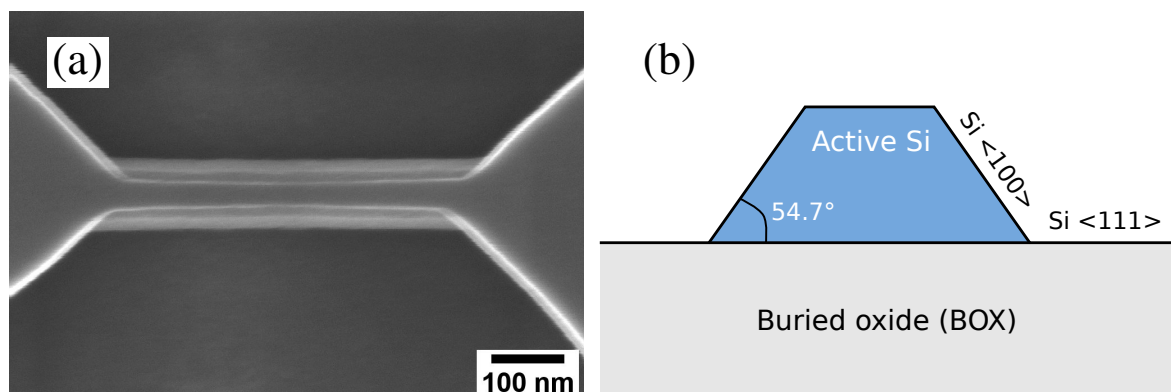


**Figure 2.5:** Scanning electron microscopy (SEM) image of a typical single Si NW after the TMAH etching (a), and a sketch of the nanowire cross-section (b).

The etching procedure allows for a smooth and almost atomically flat surface of nanowire sidewalls to be achieved, thus significantly reducing the noise of the fabricated devices, which is of critical importance for biosensing applications.

### Defining the Drain, Source and Gate Electrodes

The next step after the nanowire etching is the definition of the source and drain electrodes. For this purpose, feed line regions and access parts to nanowires are highly implanted with either boron or arsenic impurities and then thermally annealed. Depending on the impurity type two types of transistor structures can be achieved:  $p^+-p-p^+$  for boron and  $n^+-p-n^+$  for arsenic ions, respectively. Photolithography is firstly performed to protect the NW structures and open the feed lines and access parts to the nanowires. Impurity ions are implanted using the Optima HDx ion implantation system. After the implantation, the residual resist layer is removed using PIRANHA ( $\text{H}_2\text{SO}_4 : \text{H}_2\text{O}_2 = 3 : 1$ ) cleaning. The impurities are then activated using thermal annealing in a forming gas atmosphere. The process parameters are summarized in **Table 2.2**.

**Table 2.2:** Parameters for the ion implantation process

Impurity type	Exposure parameters		Annealing parameters	
	Energy [keV]	Dose [ $\text{cm}^{-2}$ ]	Temp. [ $^{\circ}\text{C}$ ]	Time [s]
Boron	6	$10^{15}$	1000	5
Arsenic	8	$5 \times 10^{14}$	950	30

After the annealing, an 8 nm thin uniform layer of silicon oxide is thermally grown on the surface of nanowires and contact feed lines. The process is performed at  $820^{\circ}\text{C}$  for 68 min using the Tempress Omega Junior oxidation furnace. The high quality of the nanowire structures are confirmed using focused ion beam milling (see **Figure 2.6**). This  $\text{SiO}_2$  film serves as a front

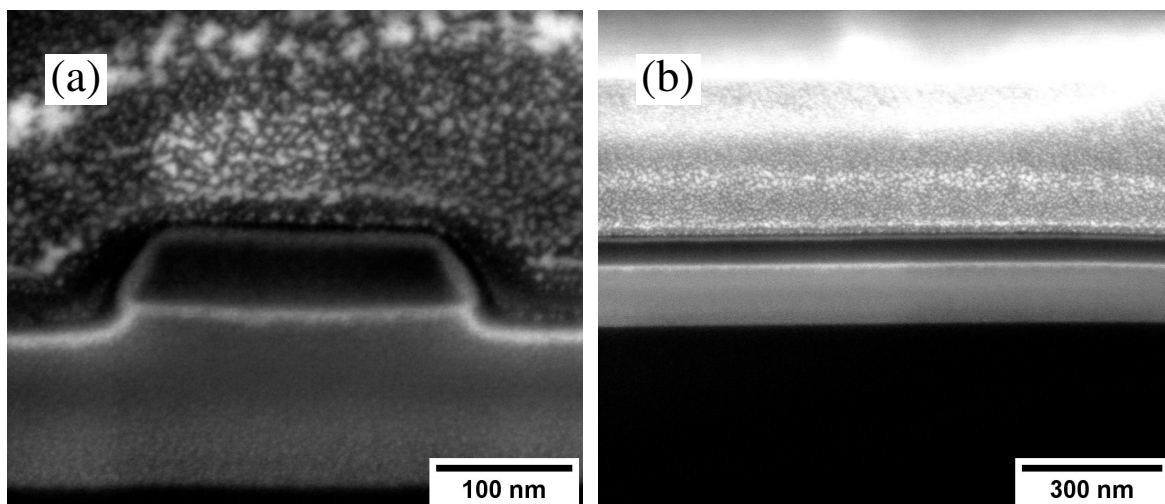


**Figure 2.6:** Focused ion beam (FIB) micrographs of a cross-section (a) and longitudinal section (b) of a typical fabricated silicon nanowire structure.

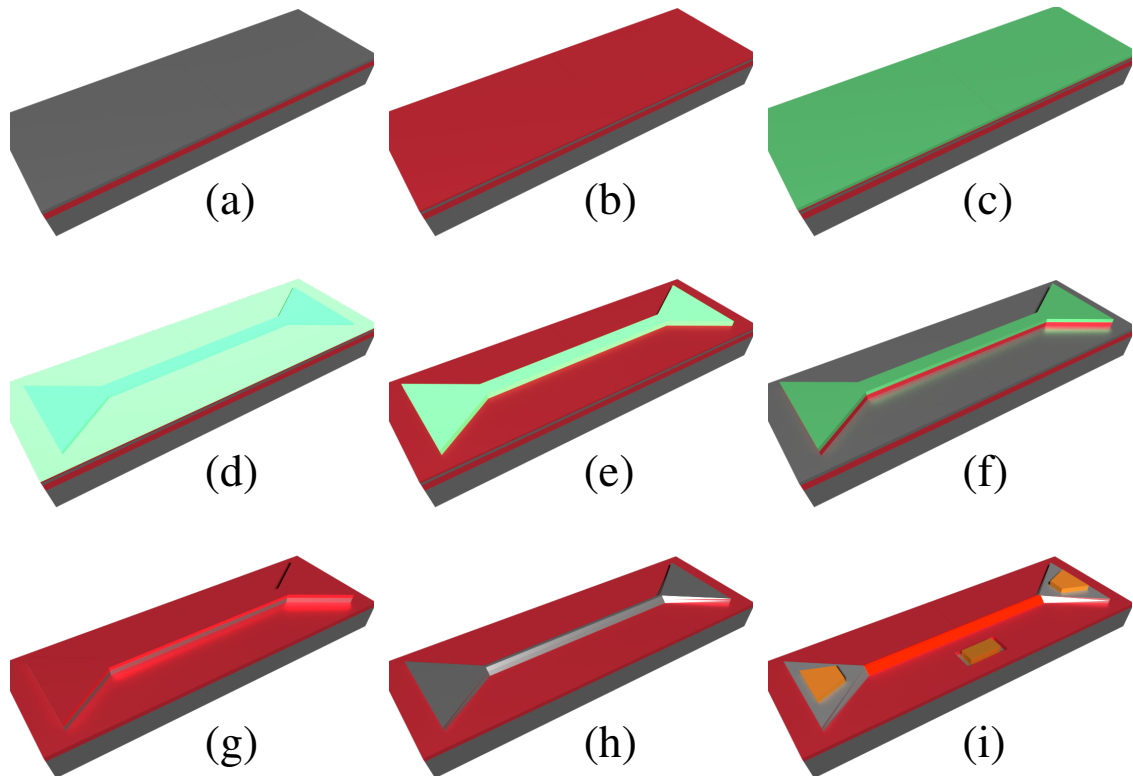


**Figure 2.7:** Sketches of the technological steps, needed to fabricate silicon nanowire FETs: (a) SOI substrate; (b) hard mask thermal oxidation; (c) nanoimprint resist coating; (d) thermal imprint process; (e) and (f) stripping of the resist residuals and hard mask patterning by RIE; (g) TMAH etching of nanowire (NW) structures; (h) HF mask oxide stripping; (i) gate oxidation, back gate opening, and metallization.

gate dielectric layer when exposed to an electrolyte. Small openings in the BOX layer are then obtained using photolithography and etching in a buffered oxide etch (BOE 7 : 1) solution. These openings serve as contacts to the substrate and are utilized as back gate electrodes.

At last, the metal contacts to source, drain, and back gate electrodes are created. For this purpose, a metalization procedure is performed. Firstly, the openings in appropriate places on the chip are defined using photolithography. A 300 nm thin aluminum film is then evaporated on the substrate, and the lift-off procedure in acetone is performed. Then, the substrates are annealed at 550 °C for 30 min in a forming gas atmosphere to achieve ohmic behavior of the contact pads. Sketches of the Si NW FET fabrication processes are shown in **Figure 2.7**.

### Passivation of NW FETs

After the metal contact pads are defined, a passivation layer is introduced to protect feed lines from the electrolyte liquid environment. This procedure is performed in several steps. Firstly VM 652 adhesion promoter is spin-coated on the substrate at the spin speed of 3000 rpm and baked at 140 °C for 1 min to improve the adhesive properties of the substrate. Then, a layer of

polyimide (PI) precursor PI 2545 is spin-coated on the substrates at 5000 rpm and soft-baked for 1 min at 140 °C. Since the polyimide used is not photostructurable, an additional layer of AZ nlof 2020 photo-resist is subsequently applied on top of the polyimide precursor at 4000 rpm and soft-baked for 1 min at 110 °C. Openings in the resist and polyimide film in the NW regions and contact pads are defined by photolithography. Substrates are aligned with a mask using the Karl Süss Mask Aligner VI and exposed with UV light (365 nm, exposure time 1.5 s, dose 7 mW cm<sup>-2</sup>). Developing in a basic developer, such as MIF 326, results in removing the parts of the resist that were not exposed by the UV light, as well as the PI precursor underneath these openings. Afterward, the residual nlof 2020 resist layer is removed by rinsing the substrate in acetone and isopropyl alcohol. Finally, the polyimide film is hard-baked in a process furnace. For the purpose of uniform polyimide baking, samples are heated in a nitrogen atmosphere using the following temperature ramping program:

- pre-heating: from 60 °C to 200 °C, 4 °C min<sup>-1</sup>, followed by a 30 min hold time;
- hard-baking: from 200 °C to 350 °C, 4 °C min<sup>-1</sup>, followed by an 30 min hold time;
- cooling-down: from 350 °C to 40 °C, 6 °C min<sup>-1</sup>.

The curing procedure removes the solvent and converts the polyimide precursor into an insoluble polyimide film.

### **Fabrication of On-Chip Pseudo-Reference Electrodes**

The devices are designed to be operated in a liquid environment. When conducting measurements in (bio)liquids, an external reference electrode is utilized to set the device working regime and to control the current flow through the nanowire channel. Usually, commercial Ag/AgCl reference electrodes are used for this purpose. However, these electrodes are usually bulky and are not suitable for point-of-care (POC) applications. To overcome this issue, platinum pseudo-reference electrodes are microfabricated directly on the chip using photolithography, metalization of platinum and lift-off procedures. Afterward, all contact pad regions, including those on pseudo-reference electrodes are covered with a thin 10 nm titanium – 200 nm gold stack to be suitable for wire bonding and flip-chip contacting techniques. After the gold metalization, initial 30 × 30 mm<sup>2</sup> SOI pieces are cut into 5 × 5 mm<sup>2</sup> chips.

### **Encapsulation and Using the Fabricated NW FET Biosensors**

Fabricated chips are glued to special chip-carriers and bonded using either wire bonding or alternatively flip-chip technique. To make the devices suitable for measurements in liquids, the encapsulation procedure is performed as follows:

- Polydimethylsiloxane (PDMS) is prepared by mixing the precursor with the curing agent in proportion 10 : 1. This mixture is a viscous gel at normal conditions, and it becomes solid after curing. Baked PDMS is a biocompatible material with good dielectric properties, and it is, therefore, perfectly suitable for the biosensors encapsulation purpose.
- A small glass ring (the inner diameter 3 mm and the outer diameter 4 mm; height 1.5 mm) is glued to the top of the chip using the prepared PDMS mixture, leaving open the nanowire structures, and separating them from contact pads and electrical wiring.
- A bigger glass ring (the inner diameter 19 mm and the outer diameter 20 mm; height 10 mm) is glued to the chip-holder to create a vessel, which is utilized as a cell for measurements in liquid environments.
- The space between these rings is then filled with PDMS and hard-baked inside a commercial processing oven for 1 h at a constant temperature of 110 °C.

The procedure results in a basin, where the contact pads and electrical wiring are insulated by a thick PDMS layer, and only nanowire structures inside the inner ring are opened and can be exposed to the liquid environment. The encapsulated chips are ready to use for measurements in bioliquids.

### 2.1.3 Fabrication of Nanoribbons and Patterned NW Structures

Since the geometry of designed Si NWs can have a crucial effect on the sensitivity of fabricated biosensor devices, nanoribbon structures with the same length as for nanowires but much greater widths are patterned using conventional photolithography for comparison. Parameters of the designed nanoribbons are listed in **Table 2.3**. Except for the patterning of SiO<sub>2</sub> mask

**Table 2.3:** Designed single Si Nanoribbons

Row number	Width, $W$ $\mu\text{m}$	Length, $L$ $\mu\text{m}$
1	0.5-5	20
2	1	16-21
3	0.5-5	5
4	0.5-5	4
5	2.5	2-22

(photolithography instead of nanoimprint lithography), the fabrication process for the nanoribbon FETs includes the same steps as the one described above for fabrication of Si NW FETs.

Increased surface-to-volume ratio (SVR) is one of the key features of nanowire FET biosensors. This allows for higher sensitivity and lower detection time to be achieved. One of the

possible ways to increase SVR is to use patterning techniques. Authors of [123] used honeycomb nanowire structures for the detection of human cardiac troponin (cTn) with high specificity to target molecules and low detection limit. However, usual ways to produce patterned nanostructures (e.g., EBL, FIB milling, etc.) are quite expensive and therefore are not well suited for practical use. One of the promising techniques to fabricate such a nanostructured pattern in a cost-efficient way is nanosphere lithography (NSL). The idea of NSL is to use self-assembled monolayers of spheres (typically made of polystyrene) as evaporation masks. It allows for a monolayer of hexagonally-packed (or similar patterned) nanoscale objects to be achieved.

To fabricate hollow nanowire structures using NSL, the nanoribbon pattern is firstly defined in a SiO<sub>2</sub> mask as described above. Then an additional polystyrene beads deposition step is applied.

### Deposition of Polystyrene Beads

A water solution of polystyrene beads (380 nm in diameter, 4 % wt.) is purchased from [Bangs Laboratories, Inc.](#) A deposition solution is prepared as follows. Firstly, polystyrene beads are diluted with highly filtered DI water in a proportion 1 : 1. Then an equal amount of ethanolic solution of surfactant Triton X-100, 0.02 % wt. is added to the solution and stirring is performed. After thorough mixing, the nanoparticle solution is additionally sonicated for 1 min to achieve more homogeneous particle dispersion, and to avoid clusters formation.

Before the deposition, the sample surface is cleaned and activated by oxygen plasma treatment using a GIGAbatch plasma oven. The procedure is carried out for 5 min at the oxygen pressure of 0.8 mbar, and power of 80 W. Plasma treatment creates the silanol (Si-OH) groups on the SiO<sub>2</sub> surface, making it more hydrophilic. It also facilitates the deposition procedure.

The deposition is performed using the Langmuir-Blodgett technique. Firstly, a big glass beaker is filled with highly filtered DI water, and a special sample holder is placed inside (see **Figure 2.8** (a)). Then activated samples are placed on top of the holder and fixed so that the entire construction, including the holder and samples, stands under the water surface. The sample holder used is designed in a way that samples are slightly tilted (approximately 10°) relative to the water surface. This allows for a higher quality monolayer to be formed during the particle deposition. Cleaned and activated laboratory glass slice is fixed on a tripod and placed close to an edge of the beaker with one of its ends dipped in water at the angle of approximately 30°. It is used to introduce polystyrene beads to the water surface. Small portions of the prepared nanoparticle solution (10 µl each) are then continuously applied onto the glass slice close to its top by drop-casting. The droplets slowly spread on the glass surface until they hit the water at the other end of the slice. Most of the polystyrene beads stay at the water-air interface, kept there by the surface tension forces. Droplets of the solution are applied until a

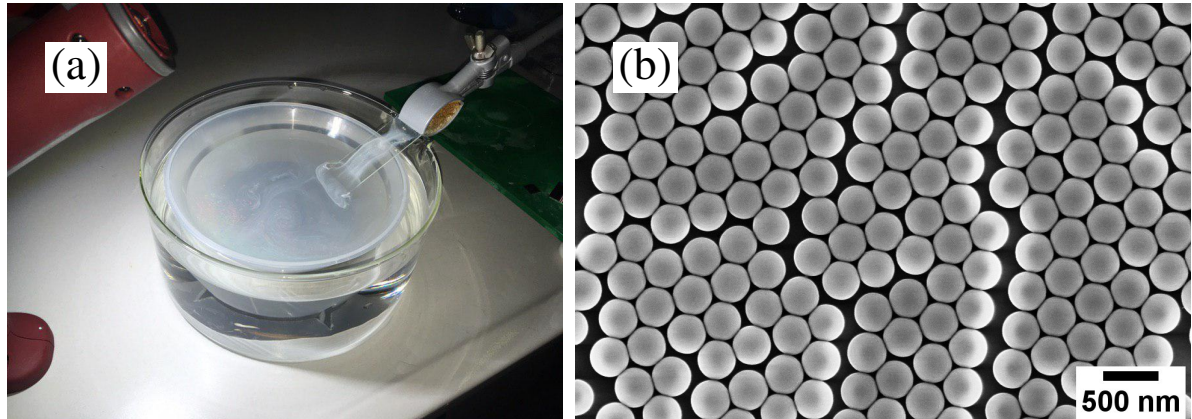


**Figure 2.8:** Photo of the polystyrene beads deposition setup (a); and a typical SEM micrograph of a 380 nm polystyrene beads monolayer on a flat SiO<sub>2</sub> substrate (b).

dense layer of polystyrene beads is formed at the water surface. The laboratory glass is then gently removed, and water is slowly sucked-out from the bottom of the beaker using a rubber tube. The water level and consequently the level of polystyrene beads are slowly decreasing. When the beads layer hits the sample, nanoparticles start assembling on the sample surface, forming a nice hexagonal shaped lattice (see **Figure 2.8** (b)). After the deposition, samples are left undisturbed overnight for drying.

### “Drilling” Holes in the Nanoribbons

Although the formed polystyrene layer forms the desired hexagonal pattern, it is very dense and closely packed. Therefore, to create the evaporation mask for hollow nanoribbons, the sizes of the particles are firstly reduced using RIE. After this procedure, a 30 nm thin layer of chromium is deposited on top using Balzers PLS 500 e-beam evaporator. Finally, the nanoparticle lift-off procedure is performed to define the hollow pattern. Most of the particles are removed using adhesive tape stripping. Then samples are dipped into acetone and gently wiped with cotton sticks to remove the rest of the particles and clean the sample surface up. By choosing the initial particle size and by adjusting the RIE time, one can tune the parameters of the pattern, such as hole diameter and lattice constant (see **Figure 2.9** and **Figure 2.10**).

Polystyrene nanoparticles of 380 nm in diameter are chosen for the fabrication purpose. To find optimal etching time, test samples with deposited nanoparticles are etched using RIE for different amounts of time. Particle analysis is then performed on obtained micrographs to find the etching rate. The average hole diameter vs etching time data are summarized in **Table 2.4**. The etching rate of  $36.1 \pm 0.8 \text{ nm min}^{-1}$  is extracted from the data using the linear fitting.

After the particle lift-off procedure is done, samples are spin-coated with AZ 5214E photoresist at 4000 rpm, and photolithography is performed to protect nanowire contact pads. The SiO<sub>2</sub> mask is then etched down to the active silicon layer by immersing the samples into

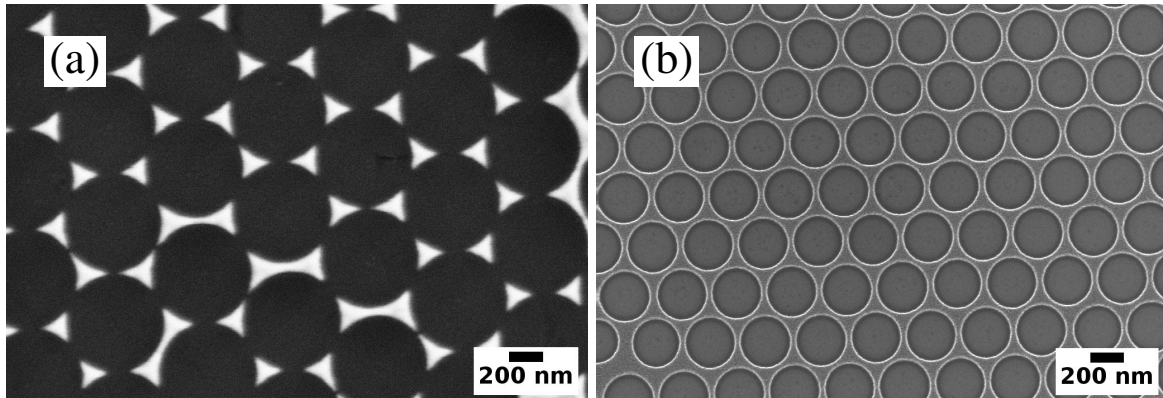


**Figure 2.9:** SEM images of the Cr patterning masks on a flat SiO<sub>2</sub> surface obtained using (a) unaffected 570 nm polystyrene beads, and (b) 380 nm beads with sizes reduced by RIE.

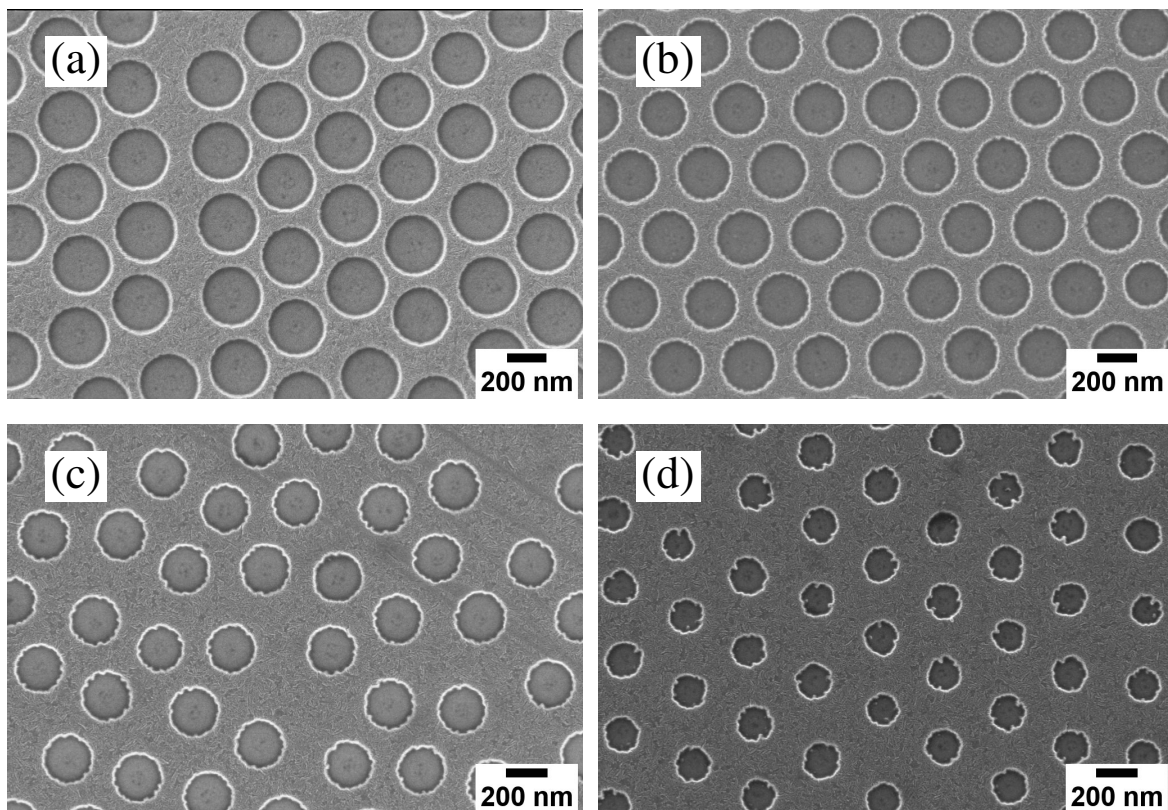


**Figure 2.10:** SEM micrographs of the evaporation masks, obtained on test flat Si / SiO<sub>2</sub> samples using different plasma etching times: (a) 4 min, (b) 5 min, (c) 6 min and (d) 8 min.

1 % HF solution for 3 min to pattern holes in the nanoribbon regions. After the patterning,

**Table 2.4:** Polystyrene etching rate test

Etching time (min)	Hole Diameter (nm)
4	$337.33 \pm 4.96$
5	$303.32 \pm 12.29$
6	$269.54 \pm 6.01$
8	$193.22 \pm 7.25$

the residual photoresist mask is removed by rinsing the sample in acetone and isopropyl alcohol for 2 min in each. Then the chromium mask is removed by etching in commercial chrome-etch solution (time = 45 s; Cr etching rate  $\sim 80 \text{ nm min}^{-1}$ ). To purify the sample surface from possible chromium or other contaminants, the SC-2 cleaning is performed. Etching of the hollow nanowire structures can then be performed using either RIE or TMAH etching. Scanning electron microscopy image of a typical hollow nanoribbon structure after the TMAH etching step is shown in **Figure 2.11**. The estimated increase in the SVR for the pre-

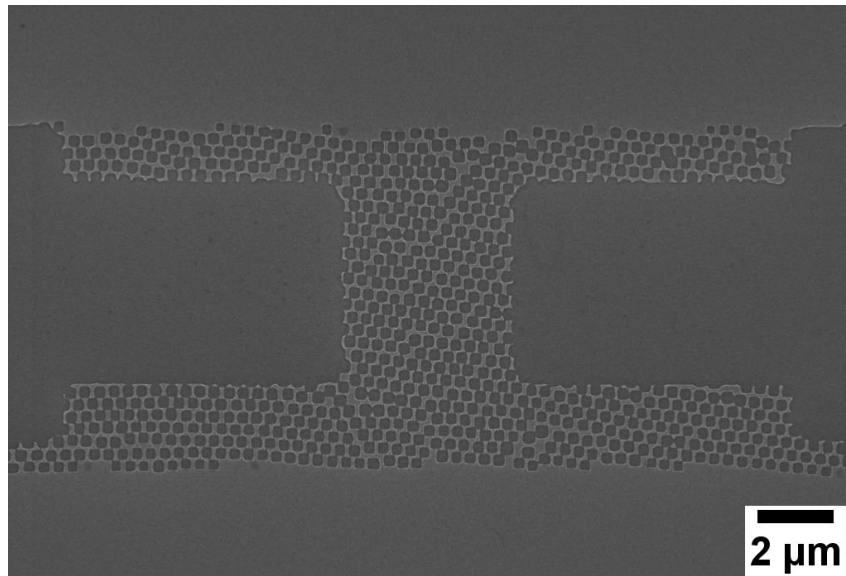


**Figure 2.11:** SEM image of a hollow nanowire structure, fabricated using photolithography and nanosphere lithography.

sented hollow nanowire structure in comparison with non-patterned nanoribbon structure is  $SVR_{Hollow\ NR}/SVR_{Normal\ NR} \approx 250\ %$ . Such patterned devices are promising for creating nanowire-based biosensors with enhanced sensitivity.

## 2.2 Fabrication of Tunable Nanoconstrictions

The fabrication of tunable gold nanoconstriction devices is performed on the basis of rectangular shaped stainless steel substrates with the geometry for the width, length and thickness  $w \times l \times t = 1 \times 5 \times 0.25 \text{ cm}^3$ , respectively (see **Figure 2.12** (a)). Before further processing,

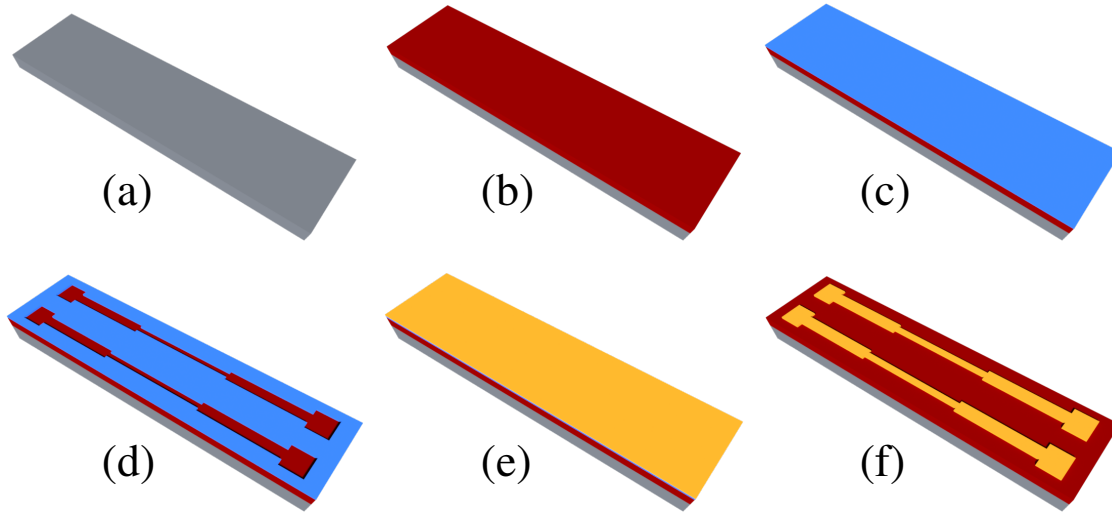


**Figure 2.12:** Sketches of the technological steps, needed to fabricate tunable metal nanoconstriction devices: (a) metallic substrate; (b) polyimide passivation; (c) spin-coating e-beam sensitive polymer; (d) electron beam lithography and development; (e) metal deposition; (f) lift-off and RIE.

substrates are cleaned in acetone and then in isopropyl alcohol for 5 min in each. To improve the cleaning quality, this procedure is performed in an ultrasonic bath. This allows purifying the substrates from oil and other organic residuals. Then the passivation layer is created to insulate substrates. For this purpose, two layers of the polyimide PI 2611 are subsequently spin-coated on the sample surface with spin speeds of 3000 rpm and 4000 rpm for the first and the second layer, respectively. Each coating step is followed by the hard baking procedure. To achieve a good quality of the passivation film, the baking is performed in a process furnace using a temperature ramping program: heating up from 40 °C to 350 °C with a step of 4 °C, holding at 350 °C for 30 min, and subsequent cooling down to the room temperature with a step of 5 °C min<sup>-1</sup>. The sketch of a passivated substrate is shown in **Figure 2.12** (b). After this, two layers of the e-beam sensitive polymers PMMA 649.04 and PMMA 679.04 are subsequently spin-coated at 4000 rpm on top of the passivation layer. Each coating step is followed by the two-step soft-baking: firstly 5 min at 80 °C and then for 10 min at 150 °C. The e-beam writing is performed in two steps. The coarse pattern (including large contact pads and feed lines) is written with the dose of 300  $\mu\text{C cm}^{-2}$ , beam current of 150 nA and resolution of 50 nm; fine pattern (nanoconstriction) – with the e-beam dose of 400  $\mu\text{C cm}^{-2}$ , beam current of 100 pA, and 2 nm resolution, respectively. The development procedure is then performed by immersing the

samples into AR 600-55 developer for 1 min 30 s, followed by stopping in isopropyl alcohol for 30 s and drying under a nitrogen flow. As a result, exposed parts of the resist film are removed, and a positive-type structure pattern is formed. After drying under a nitrogen flow, structures are additionally baked at 80 °C for 10 min to get rid of any solvent residuals on the surface. Sketches of a PMMA-coated substrate before and after the e-beam writing/development procedures are shown in **Figure 2.12** (c) and (d), respectively. Metalization is then performed to form contact pads, feed lines, and nanoconstrictions simultaneously. For this purpose, 10 nm of titanium and 60 nm of gold are subsequently evaporated on the substrates using Pfeiffer PLS 570 e-beam evaporator. Evaporation speeds are 0.1 nm s<sup>-1</sup> and 0.5 nm s<sup>-1</sup> for Ti and Au, respectively (see **Figure 2.12** (e)). After the metalization, the lift-off procedure is performed in acetone: nanoconstrictions, feed lines, and contact pads stay on the polyimide, while the sacrificial resist layer and titanium/gold layer above it are removed (see **Figure 2.12** (f)). The last and very important fabrication step is the reactive ion etching. The metal structure pattern serves as a hard mask, and the polyimide layer is isotropically etched down using the ICP oxygen plasma with the parameters listed in **Table 2.5**. As a result, in the narrowest part of the structure, the

**Table 2.5:** RIE parameters for etching tunable nanoconstriction devices

Gas	Flow (sccm)	RF (W)	ICP (W)	Temperature (°C)	Time (s)
O <sub>2</sub>	30	50	500	10	120

polyimide layer is completely removed, and a freestanding metal nanoconstriction is formed. A typical scanning electron microscopy image of a fabricated tunable nanoconstriction device is shown in **Figure 2.13**. The optimized fabrication technology allows the production of high-quality structures capable of single-molecule measurements. It should be noted that oxygen plasma etching oxidizes the top gold layer. Thus, the samples have to be treated with a reducing

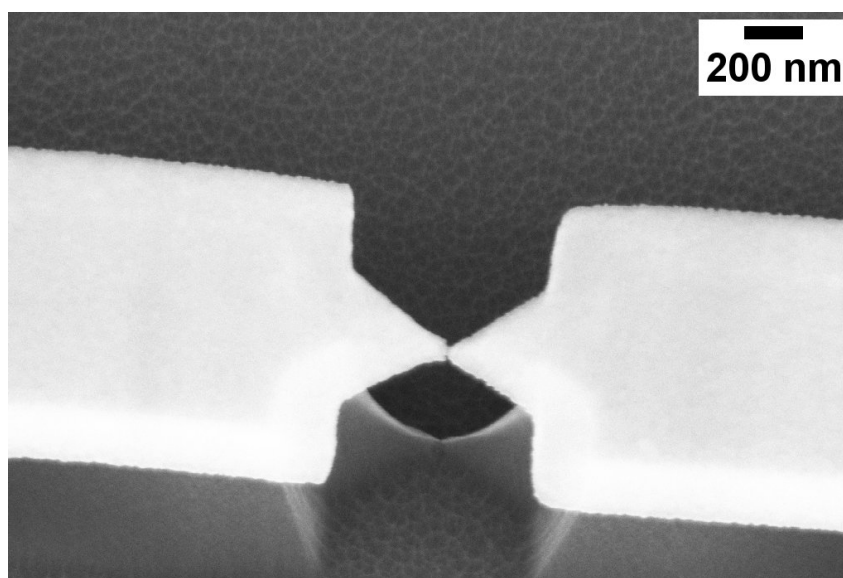


**Figure 2.13:** Typical SEM micrograph of a fabricated tunable gold nanoconstriction device.

agent before use.

## 2.3 Summary

Silicon nanowire field-effect transistors are fabricated on the basis of  $p$ -type SOI substrates using advanced cleanroom technology. Cost-efficient CMOS-compatible thermal nanoimprint lithography is used as an alternative to EBL high-resolution approach for simultaneous patterning of the tiny nanowire structures and large feed lines. For this purpose, low-roughness nanoimprint molds are fabricated on the basis of Si  $\langle 110 \rangle$  substrates using electron beam lithography, RIE, and wet etching techniques. The geometrical parameters (widths and lengths) of the designed nanowire structures are summarized in **Table 2.1**. The fabricated molds are suitable for multiple time use.

The pattern is transferred to the SOI substrate, coated with mr-I 70xxR resist, using optimized two-step imprint procedure with the parameters for the temperature  $T_{1,2} = 140$  °C, pressure  $P_{1,2} = 450, 500$  PSI, and time  $t_2 = 4$  min, respectively<sup>2</sup>. The mesa and NW structures are defined by wet etching in TMAH solution, which allows for a smooth profile of nanowire sidewalls to be achieved. The high quality of the fabricated devices is confirmed by AFM and SEM imaging as well as by FIB sectioning.

Samples with tunable nanoconstrictions are fabricated on the basis of rectangular-shaped stainless steel pieces ( $w \times l \times h = 1 \times 5 \times 0.25$  mm<sup>3</sup>) covered by 15  $\mu$ m thick polyimide insulating film. The structures are formed using EBL, metalization, and lift-off techniques. The suspended gold nanojunctions ( $< 100$  nm in cross-section) are formed using reactive ion etching. The optimized RIE process parameters are presented in **Table 2.5**. The high quality of the fabricated devices is confirmed by scanning electron microscopy.

---

<sup>2</sup>The time of the first pre-imprint step is defined by the time of the gradual increase of the pressure and temperature to their nominal values  $T_1$  and  $P_1$ .

# MODERNIZATION OF TRANSPORT CHARACTERIZATION SETUPS

Electrical characterization of the fabricated nanowire devices is essential for the successful development of NW-based sensors. Enhancing the performance and finding optimal operation regimes of NW devices requires advanced data collection and analysis. In this respect, improving the measurement capabilities of experimental setups and automation of data acquisition/analysis is beneficial for enhancing the measurement accuracy and speed, and thus it facilitates the advancement of nanowire biosensors.

## 3.1 Automation of Experimental Setups

Studies of the electrical transport and noise properties of fabricated nanowire structures are of extreme importance for their performance characterization. To implement the possibility of advanced transport measurements and to have precise control over the measurement conditions, the setups for current-voltage (I-V) and noise measurements are modernized and automated.

Stable, multithreading software to operate the measurement setups described below is developed in house using the C# programming language. The software allows error-free continuous data acquisition in automated mode even for several weeks of continuous measurement. Using the Windows Presentation Foundation (WPF) framework allowed to create user-friendly graphical user interface (GUI). R and MATLAB scripts are developed and used for advanced processing of the acquired data.

A brief overview of measurement setups and developed software used for the characterization of fabricated devices is given below.

### 3.1.1 Transport Characterization

The electrical properties of nanostructures often define the range of their possible applications. In the case of silicon nanowire (Si NW) field-effect transistors (FETs), studies of electrical transport can determine important parameters such as dopand type, carrier concentration and mobility, interface quality, trap density, contact resistance, etc. [124]. Studies on metallic nanowires allow determining their intrinsic properties as well as external effects including molecular adsorption, wire oxidation, and contamination.

## Transport Characterization of FET Structures

Measurements of the electrical characteristics of FET structures are performed using the Keithley 2602A two-channel source-measurement unit (SMU). Both channels are used for the electrical biasing of FET devices and measuring their response (see **Figure 3.1**). One channel is used to apply the drain-source bias, and the other – to apply the gate potential, respectively. Two possibilities of I-V measurements are implemented:

- measurement of transfer curves (drain current  $I_D$  versus gate voltage  $V_G$  at a constant drain bias  $V_{DS} = \text{const.}$  applied);
- measurements of output curves (drain current  $I_D$  versus drain voltage  $V_D$  at a constant gate bias  $V_G = \text{const.}$  applied).

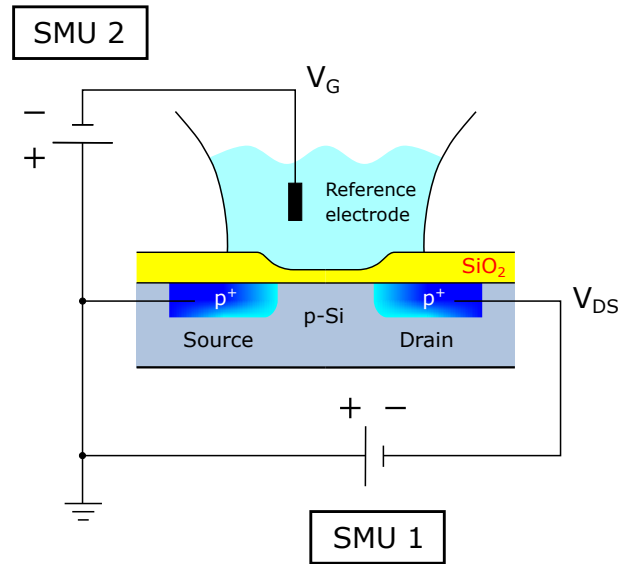


**Figure 3.1:** Bio-FET biasing schematic.

One channel always acts as the “sweeping” type SMU while the other is used to apply constant bias. Depending on the measurement type, sets of transfer or output curves can be measured by configuring one SMU as bias “sweep” and the other – as bias “step” (voltage “sweep” is performed to obtain I-V curves each time “step” voltage changes, see **Figure 3.2**). Important parameters, such as initial and final values for “sweep” and “step” biases, current compliance and integration time (defines measurement accuracy) can be set by the user from the interface. The screenshot of the developed software is shown in **Figure 3.3**. Acquired data are saved as text files, containing information about measured curves and leakage currents data. The measurement results can be easily imported using standard data processing software, e.g., Origin, R, Matlab, etc., and further analyzed.

## Single-Molecule Characterization

Electrical measurements of single molecules are performed on the fabricated tunable gold nanoconstrictions (see section 2.2) using the mechanically controlled break junction (MCBJ) technique. An advanced three-point bending system developed in house is used to tune the cross-section of metal nanoconstrictions in a controlled manner. A schematic of the bending apparatus is shown in **Figure 3.4** (a) and a photo of the real device – in **Figure 3.4** (b). The sample is placed on the pushing rod and fixed on top with two counter supports. Vertical movement of the pushing rod leads to bending of a sample, elongation of suspended gold nanoconstrictions and narrowing their cross-sections. Vertical movement of the pushing rod ( $\Delta Z$ ) is driven by the

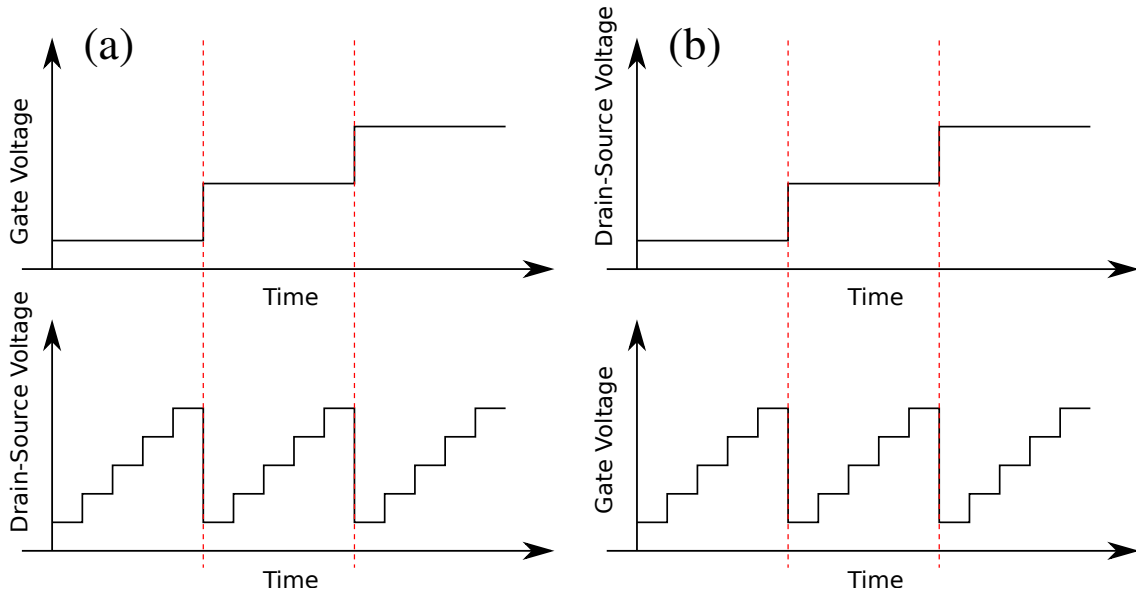


**Figure 3.2:** Configurations of SMUs for I-V FET measurements: (a) output curves (bias step on  $V_G$  and bias sweep on  $V_{DS}$ ), and (b) transfer curves (bias step on  $V_{DS}$  and bias sweep on  $V_G$ ).

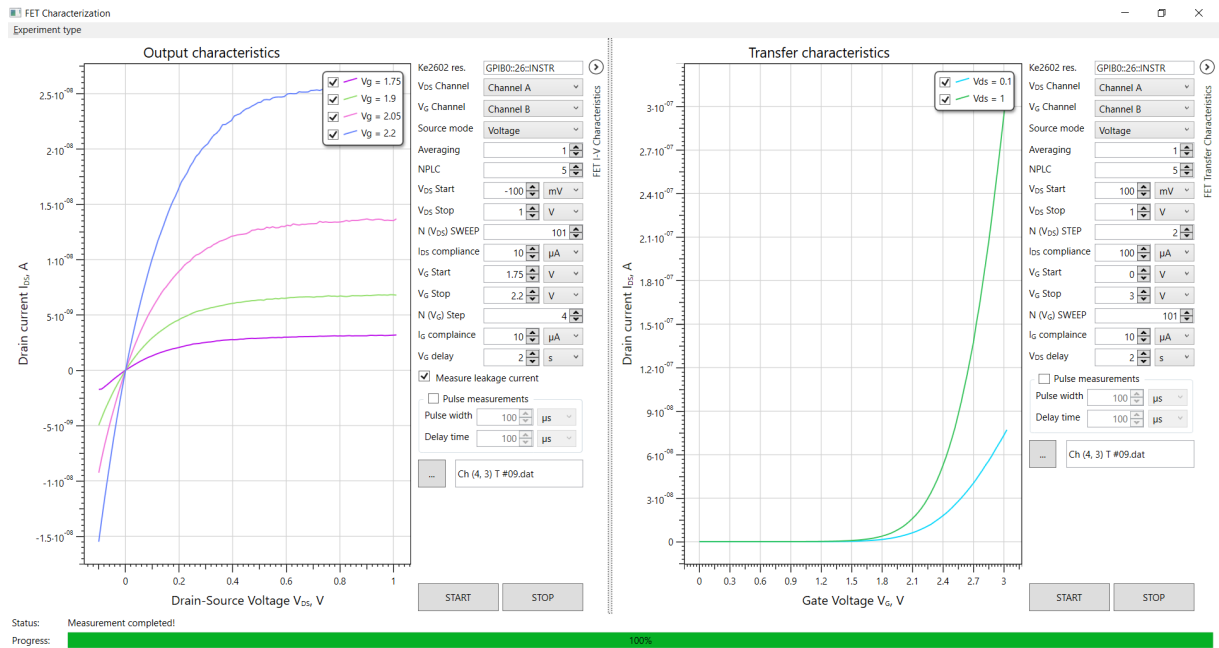


**Figure 3.3:** Screenshot of the developed program for measurement of FET output and transfer curves.

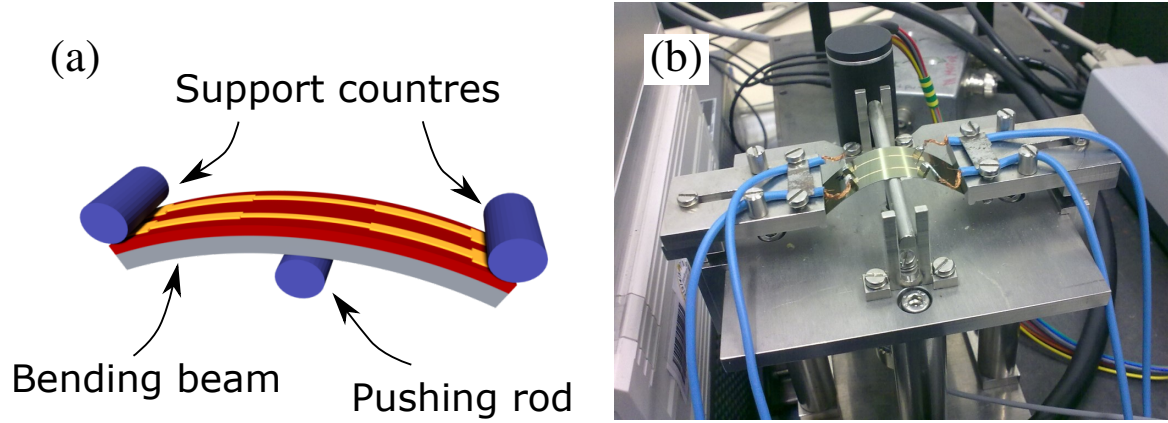


**Figure 3.4:** A schematic (a), and a photo (b) of the developed in house three-point bending apparatus for tuning the metal nanoconstrictions.

motion control system (MCS) described below. It is connected with the width of the nanogap ( $\Delta x$ ) by the following equation:

$$\alpha = \Delta x / \Delta Z = 6utL^{-2}, \quad (3.1)$$

where  $\alpha$  is the attenuation factor,  $u$  is the width of the under-etched bridge,  $t$  is the thickness of the substrate, and  $L$  is the distance between two counter supports. The attenuation factor is defined by the setup geometry [125]. At some point constrictions break, forming nanoscale gaps. If samples are additionally modified with molecules, which can bind gold electrodes, after breaking of the metallic nanoconstriction these molecules can be anchored within the formed nanogaps. In this case, the molecules determine the electrical transport in the system. However, to be able to anchor and measure single molecules one has to have ultimate control over the formed nanogap size.

The width of the under-etched bridge in our typical fabricated nanoconstriction device, estimated by analyzing scanning electron microscopy (SEM) micrographs is  $u \approx 600 \mu\text{m}$ , the thickness of the sample substrate is  $t = 0.25 \text{ mm}$ , and the distance between support counters is  $L = 3.7 \text{ mm}$ . Therefore, the attenuation factor calculated using Equation (3.1) is  $\alpha \approx 3 \times 10^{-7}$ . In our setup, a micrometer screw plays the role of a pushing rod. A metal bar is placed on top of the screw to apply force and bend the sample homogeneously (see **Figure 3.4** (b)). A personal computer (PC)-controlled stepper motor (Faulhaber Brushless Minimotor SA 2036U012V with a low-outclassing lubricant and the 1526 : 1 mechanical gear) is connected with the micrometer screw using a gear train. This motor is used to rotate the screw either clockwise or counter-clockwise, and therefore, to provide movement of the pushing rod up or down, respectively. This system allows vertical displacement ( $\Delta Z$ ) control with a sub-micrometer precision, which allows tuning of the nanogap width ( $\Delta x$ ) with sub-angstrom accuracy.

Measurements of electrical characteristics are performed using Keithley 2602A two channel

source-measurement unit. Schematic of the electrical connection is shown in **Figure 3.5**. Sev-

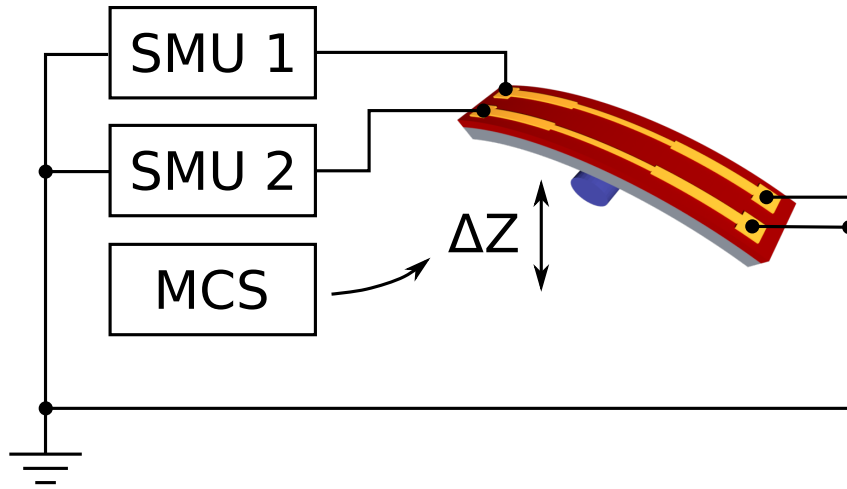


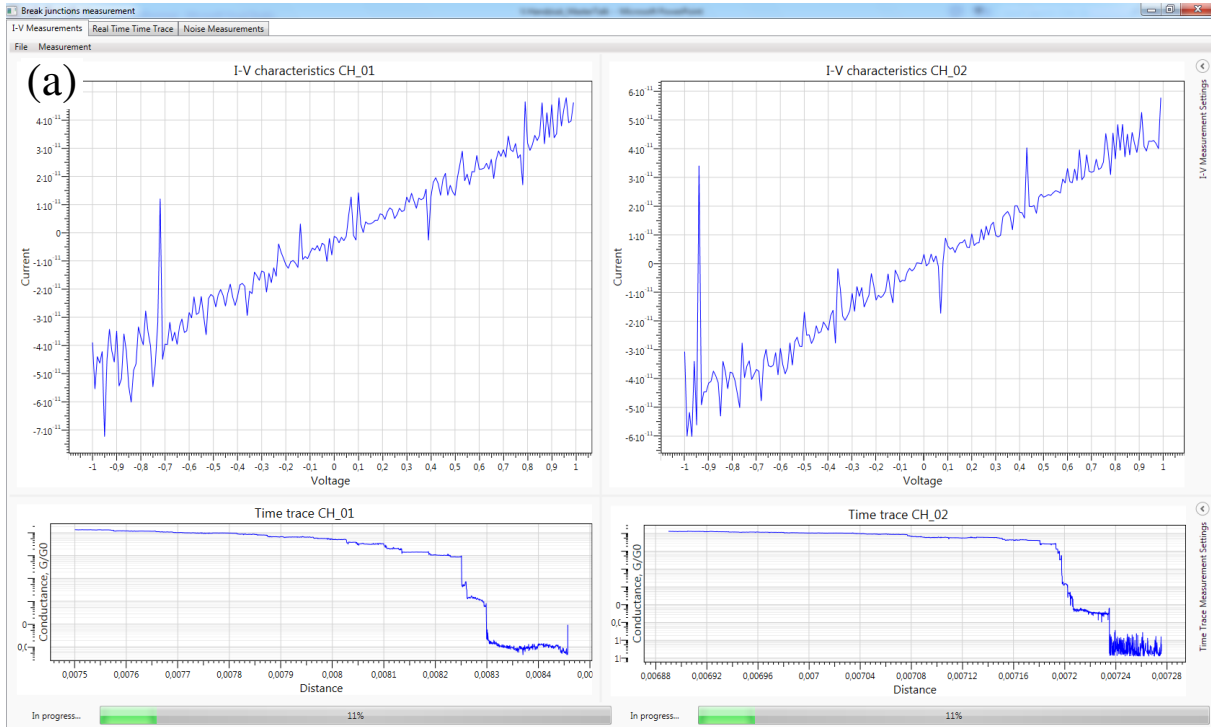
**Figure 3.5:** Schematic of the electrical connections for transport measurements of tunable nanoconstrictions. Here, SMU 1 and SMU 2 are the source-measurement unit channels of the Keithley 2602A device, and MCS is the motion control system.

eral types of experiments are developed and automated to measure the transport characteristics of single molecules. They are briefly described below.

*Conductance-traces acquisition:* The conductance of the studied molecule is one of the most important characteristics to study. It can give a first insight into the peculiarities of transport in studied molecules. Conductance trace is the dependence of the system conductance on the displacement of the pushing rod, measured while stretching the nanojunction.

The nanoconstriction is repeatedly “opened” and “closed” using the three-point bending apparatus while the system conductance is recorded using the Keithley 2602A SMUs at a constant bias applied. The range of the pushing rod displacement is chosen in a way that at the lower position the constriction is completely closed ( $G \gg G_0$ ), and in the upper position it is completely opened ( $G \ll G_0$ ). To have precise control over the displacement of the pushing rod and therefore – over the size of the formed nanogap, measurement is performed by sequential moving of the motor and measuring the conductance. The user defines the number of data points to acquire for 1 mm vertical displacement of the pushing rod. At each point, the bending system stops and conductance measurement is performed. After the conductance measurement is done, the bending system moves to the next point. Screenshot of the developed software is shown in **Figure 3.6**. The user can set the following parameters using the software GUI to control the experiment:

- power supply mode: constant voltage or current;
- voltage (or current) constant bias value;
- number of data points for 1 mm pushing rod displacement (measurement resolution);



**(b)**

Source Mode

Voltage Mode

Current Mode

1-st Channel Parameters

Start Value: 0.0000 [None]

End Value: 1.0000 [None]

Step: 0.0100 [None]

Data file name: IV\_MeasurementChannel\_01.dat [Browse ...]

2-nd Channel Parameters

**(c)**

1-st Channel Parameters

Source Mode

Voltage Mode

Current Mode

Value through str.: 0.0200 [None]

Data file name: TimeTraceMeasurementChannel\_01\_dat [Browse ...]

2-nd Channel Parameters

**(d)**

Motion Parameters

Points per millimeter: 2000

Motion speed, [mm/min]

Going UP: 2.5000

Going DOWN: 3.0000

Distance: Distance (Repetitive) Time Fixed R

Moving direction:  Up  Down [Move to initial]

Motion start pos.: 0.0000

Motion current pos.: 0.0000

Motion final dest.: 5.0000

**Figure 3.6:** (a) Graphical user interface of the developed software for measurements of tunable nanoconstriction devices. User-defined measurement parameters for acquisition of I-V-curves (b), and time-traces (c), (d).

- maximum moving up/down speed of the bending system;
- pushing rod displacement range and number of breaking cycles.

The GUI also has indicators of the pushing rod movement direction (up/down) and its current position as well as the experiment progress-bar indicator. Several measurement modes to acquire conductance traces are implemented:

- “Normal” mode: the motion system is moving the pushing rod up and down continuously within the entire user-defined displacement range and data are acquired using the Keithley 2602A both on the “opening” and “closing” stages of the movement. However, when trying to acquire data with a good spatial resolution and high accuracy, this measurement mode becomes very time-consuming.
- “Eliminate Closing” mode is developed to increase the speed of data acquisition. Measurement is performed in a similar way as in “Normal” mode, however, since useful information about the molecule conductance is contained only in “opening” but not “closing” curves, sample conductance is measured only at the breaking stage of the pushing rod movement. When “closing”, motion system goes to its start position at high speed without any additional measurements. The “Eliminate Closing” mode allows reducing the measurement time almost twice in comparison to the “Normal” approach.
- “Smart” mode is developed to further improve data acquisition quality and speed. Both the “Normal” and “Eliminate Closing” modes anticipate the movement of the bending system up and down within the entire user-defined displacement range while measuring sample conductance. This leads to the acquisition of a huge amount of data in ranges that do not contain molecule conductance data, including regions before “opening” of the nanoconstriction and after its complete breaking. In the “Smart” mode, instead, the user defines lower and upper limits of the pushing rod movement, as well as the conductance values, within which the measurement should be performed. Usually the latter correspond to conductance values close to breaking of the nanoconstriction ( $G \approx 5G_0$ ) and right after its complete breaking ( $G \approx 5 \times 10^{-6}G_0$ ). the lower conductance limit is defined by the measurement accuracy of the SMU used. Once the measured conductance runs out of the defined range, a PC-controlled feedback system changes the pushing rod movement direction, thus acquiring data only in a narrow range and including data about molecular conductance. Measurement in “Smart” mode allows for a tremendous increase in acquisition speed to be achieved in comparison to “Normal” and “Eliminate Closing” modes.

*Current-Voltage measurements:* Studies of electrical characteristics of single molecules are important for understanding their fundamental transport mechanisms and for designing metal-molecule systems with predefined properties.

Before measuring I-V curves of single molecules, a conductance-trace experiment is performed to determine their conductance values. Then a molecule-modified nanoconstriction is slowly tuned using a three-point bending apparatus while continuously measuring conductance. In contrast to conductance-traces measurements, motion and measurement systems work more independently. Pushing rod does not stop to wait for the conductance measurement. However, it gradually changes its speed and, sometimes, its moving direction depending on the current conductance value to implement smooth tuning of a nanoconstriction. When a breaking event occurs, molecules bridge to two formed nanoelectrodes. A PC-controlled feedback loop then adjusts and stabilizes the conductance of the system to match the single-molecule conductance. After the stabilization, either voltage or current bias sweep is performed, and the response of the metal-molecule system is measured. The software developed in house allows performing this kind of experiments in a completely automated way. All the parameters needed to control the experiment can be defined using user-friendly GUI. Main parameters are listed below:

- Scanning bias: value of voltage or current, which is applied to the structure while tuning conductance of a nanoconstriction;
- Set conductance (or alternatively Set resistance): value of conductance/resistance to be stabilized;
- Deviation: allowed conductance/resistance deviation while tuning;
- Start and stop bias values for the I-V sweep;
- Minimum and maximum allowed motion speed and position;
- Stabilization time.

Acquired data are saved as text files that can be easily imported and analyzed by standard data analysis software.

### 3.1.2 Low-Frequency Noise Spectroscopy

The noise measurement setup was originally developed by Dr. Viktor Sydoruk, Dr. Mykhailo Petrychuk, and Prof. Dr. Svetlana Vitusevich. Schematically, the setup is shown in **Figure 3.7**. It allows simultaneous measurement of the low-frequency noise spectra in the frequency range from 1 Hz to 102.4 kHz and time-traces of the voltage fluctuations on the terminals of a studied sample with the sampling rate up to 500 kHz.

*Noise setup description:* A lead-acid battery is used to apply the drain-source voltage to the sample. The value of the voltage bias is tuned using an Inelta motorized potentiometer of 2 k $\Omega$ ,

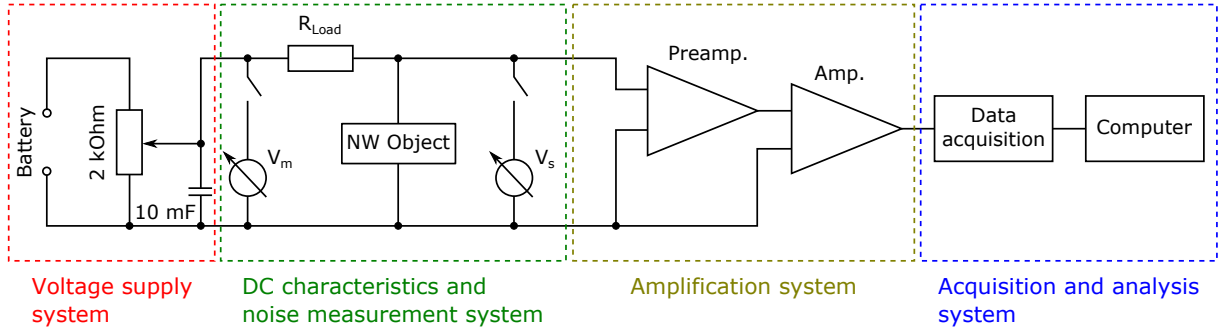


**Figure 3.7:** Schematic of the noise measurement setup.

which can be controlled by applying an external voltage to the control terminals. A large capacitor of  $9400 \mu\text{F}$ , connected in parallel to the variable resistor, decreases the value of the resistance to  $< 16.7 \Omega$  at 1 Hz. This, in turn, reduces the level of intrinsic thermal noise. The voltage bias is applied to the serial connection of the sample and the load resistance,  $R_{Load}$ . The load resistance is given by the high-precision low inductance resistance box decade, fabricated by [IET Labs Inc.](#) The decade allows changing the  $R_{Load}$  in the range from  $1 \Omega$  to  $10 \text{ k}\Omega$ . However, using an external load resistance of any value is also possible. The automated voltage supply system allows precise electrical biasing of studied structures with the accuracy approaching  $1 \text{ mV}$  or  $2 \text{ mV}$  when using  $6.7 \text{ V}$  or  $12 \text{ V}$  lead-acid batteries, respectively.

When measuring three-terminal FET devices, two voltage supply units are used to apply an electrical bias to the drain-source and gate electrodes, respectively. However, the gate bias is applied directly to the gate electrode without the use of the load resistance.

Applying DC voltage bias to the sample is necessary for specifying the working point of the device. In the automated setup the multimeters  $V_S$  and  $V_M$  allow measuring voltages applied to the sample ( $R_{sample}$ ) and to the whole working circuit ( $R_{sample} + R_{load}$ ), respectively. The DC current in the circuit can be calculated as  $I_S = (V_M - V_S)/R_{Load}$ . The multimeters are represented by the Agilent U2542A simultaneous data acquisition (SDA) analog input channels (in polling mode configuration). They are connected to the measurement circuit before and after the noise spectra acquisition. This allows checking the stability of studied samples: electrical parameters before and after the noise spectra measurement should not show significant deviation. During the noise measurements and acquisition of time-traces, the multimeters are disconnected from the measurement circuit to avoid the influence of their intrinsic noise on the measured spectra.

Fluctuations of current on the drain-source terminals of the studied sample are firstly amplified by the homemade ultra-low noise preamplifier ( $k_{preamp.} = 178$ ) and then – by the variable gain commercial low noise Stanford SR560 amplifier. The first amplification step is very important since it determines the precision of the measurement. Therefore, it should be optimized to have the lowest possible instrumental noise. Our homemade preamplifier has the intrinsic noise value  $S_V = 2.2 \times 10^{-18} \text{ V}^2 \text{ Hz}^{-1}$  at  $100 \text{ Hz}$ , which is one order of magnitude lower than the

noise level of the Stanford SR560 amplifier ( $S_V = 2.4 \times 10^{-17} \text{ V}^2 \text{ Hz}^{-1}$ ) [126]. The amplified noise signal is then recorded using the Agilent U2542A SDA device. To calculate the noise power spectrum from the measured time trace, the Fast Fourier Transform (FFT) of the data is used. The power spectrum is then calculated using the following equation:

$$S_V(f) = \frac{FFT^*(signal) \times FFT(signal)}{N^2}, \quad (3.2)$$

where  $N$  denotes the number of points in the signal array and  $*$  represents a complex conjugate.

Because of the capacitance ( $\sim 350 \text{ pF}$ ) of the cable connection, at large values of the load resistance, measured spectra can have a roll-off in the high-frequency range. For example, at  $R_{Load} = 5 \text{ k}\Omega$ , the cutoff frequency is  $f_{cutoff} \approx 91 \text{ kHz}$ . Therefore, an appropriate spectra correction should be performed when analyzing the measured data. A detailed description of the noise measurement setup can also be found in [100, 127].

*Investigation of FET Structures:* Constant voltage biases are applied to the drain-source and gate contacts of a nanowire FET to set its working point. Studies of the noise spectra in different operation regimes of the device can provide useful information about the dynamics of charge transport in the structure, and therefore, complement the DC characterization. Analysis of the generation-recombination (GR) processes can provide important information about various local centers including their concentrations, capture cross-sections, and energy levels [90]. Studies of the flicker noise component allow quantitative determination of the dimensionless Hooge parameter  $\alpha_H$  that can be used to compare the performance of various electronic devices in different operation regimes.

*Investigation of tunable metal nanoconstriction devices:* When measuring tunable nanoconstrictions, the voltage bias is only applied to the drain and source contacts. Cross-section of the nanoconstriction and, therefore, its resistance are precisely tuned using the home-developed PC-controlled feedback system (similarly as for time-traces acquisition described above). The setup allows stabilization of the desired system resistance values, corresponding either to multiples of quantum conductance (for the formed tunable gold nanowire without breaking) or single/multiple molecular conductances (when studied molecules are bridging the electrodes (lock-in state, soft breaking in the molecule-modified system)), or the conductance of a formed nanogap (complete breaking, vacuum tunneling).

*Experiments automation:* Noise measurement setup described above allows acquiring noise spectra and I-V characteristics of studied structures in an automated way. The user defines the following parameters of the measurement:

- Sets of drain-source and gate (only applicable for the measurements of three-terminal devices) voltages to be measured;

- Voltage deviation – allowed variation of the real voltage bias applied to the terminals of the structure from the desired one (biasing precision);
- Stabilization time – the delay between the end of the DC characteristics measurement and beginning of the noise spectra acquisition needed to stabilize the noise trace;
- Spectra averaging – the number of spectra to be measured for specified bias conditions;
- $k_{preamp.}$  – amplification coefficient of the ultra-low noise homemade preamplifier used ( $k_{preamp.} = 180$ );
- $k_{amp.}$  – amplification coefficient of the commercial low noise Stanford SR 560 variable gain amplifier ( $k_{amp.} = 1 - 10^5$ );
- Temperature values at the beginning and at the end of the noise spectra measurement:  $Temperature_0$  and  $Temperature_E$ , respectively.

The version of the software developed for measurements of tunable nanoconstriction devices has additional settings:

- Sets of the sample conductances normalized by the quantum conductance  $G/G_0$  (or, alternatively, resistances) to be stabilized;
- Conductance deviation – allowed variation of the sample conductance at what the measurement is considered stable;
- Bending setup control: maximum and minimum speed of the pushing rod, and its displacement limits.

Implemented automation allows to significantly shorten the time required for measurements. The screenshot of the developed software is shown in **Figure 3.8**.

After the measurement, the fitting procedure can be performed to decompose measured spectra into sets of uncorrelated noise components: thermal, flicker and Lorentzian-shape. Spectra fitting is performed using a program, previously developed by Dr. Sergii Pud [11]. The software allows precise determination of the components parameters. In addition, it allows to distinguish up to four Lorentzian-shaped components and to obtain their parameters with an error not exceeding 10 %.

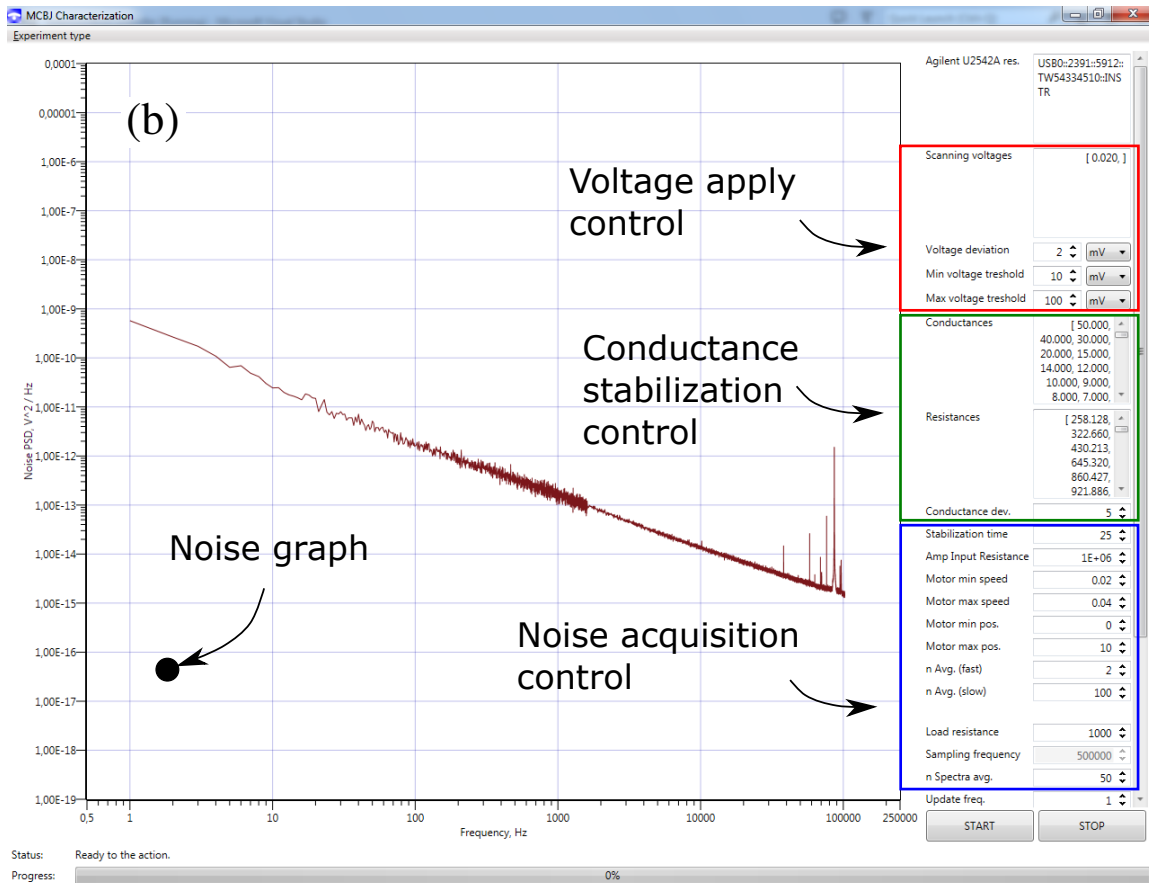
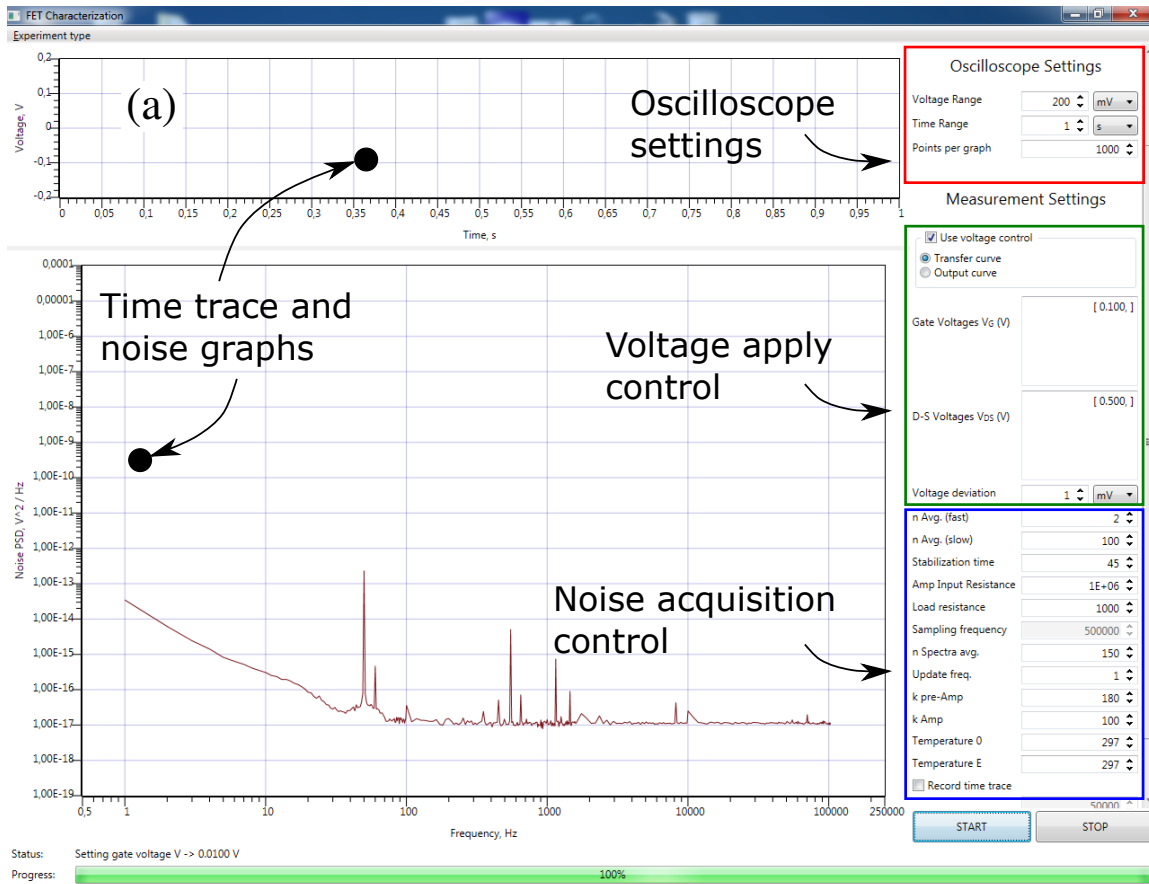


**Figure 3.8:** Graphical user interface of the developed software for noise measurements of (a) FET and (b) MCBJ noise characteristics.

## 3.2 Development of Microfluidics for FET Biosensors

The ability to perform measurements of bioliquids is often essential for the functioning of biosensor devices. Therefore, fabricated Si NW FETs are designed to operate in an electrolyte liquid environment (see section 2.1). Bioliquids of interest can be filled into a basin formed by two glass rings of an encapsulated chip. To set the device working point, an electrical bias is applied to the drain and source contacts while the gate potential is set using either an external Ag/AgCl reference electrode or a Pt on-chip pseudo-reference electrode. The analyte-induced response of our biosensor device can be tracked by shifts of the transfer curves or changes in the noise spectra (shifts in the noise amplitude or characteristic GR frequencies, etc.).

The volume of studied bioliquids affects biosensor detection precision and speed. The lower is the volume, the faster and the more accurate is the sensing. Furthermore, when working with biosamples, it is rarely possible and not cost-efficient to use large analyte amounts. Therefore, reducing working volumes while maintaining high biosensor performance is considered as one of the greatest challenges of the biosensing field. One of the possible solutions is to use microfluidics – sub-millimeter bioliquid supply channels used to geometrically constrain the fluid transport to the active area of the device.

The microfluidics used are made of polydimethylsiloxane. The PDMS mixing and baking are performed in the same way as for the chip encapsulation procedure, described in section 2.1. Prepared mixture is poured into a special heat-resistant mold and then baked. The resulting specimen is then cut into cylindrically-shaped billets for individual microfluidics using a 6 mm biopsy puncher. Next, the tubing for pumping bioliquids through the channel is prepared. For this purpose, two holes are punched in the billets using a tiny syringe needle, and then 1.5 mm inlet and outlet nylon tubes are inserted.

To align the prepared microfluidic over the nanowire region of a Si NW chip and to fix it, a special holder is designed using Autocad 2013 Autodesk software and then printed using a 3D printer. The cross-section of the developed holder is shown in **Figure 3.9**. It can hold a prepared cylindrical shaped polydimethylsiloxane (PDMS) microfluidic in a tight position with the studied Si NW chip, thus avoiding leakage of the liquid while pumping.

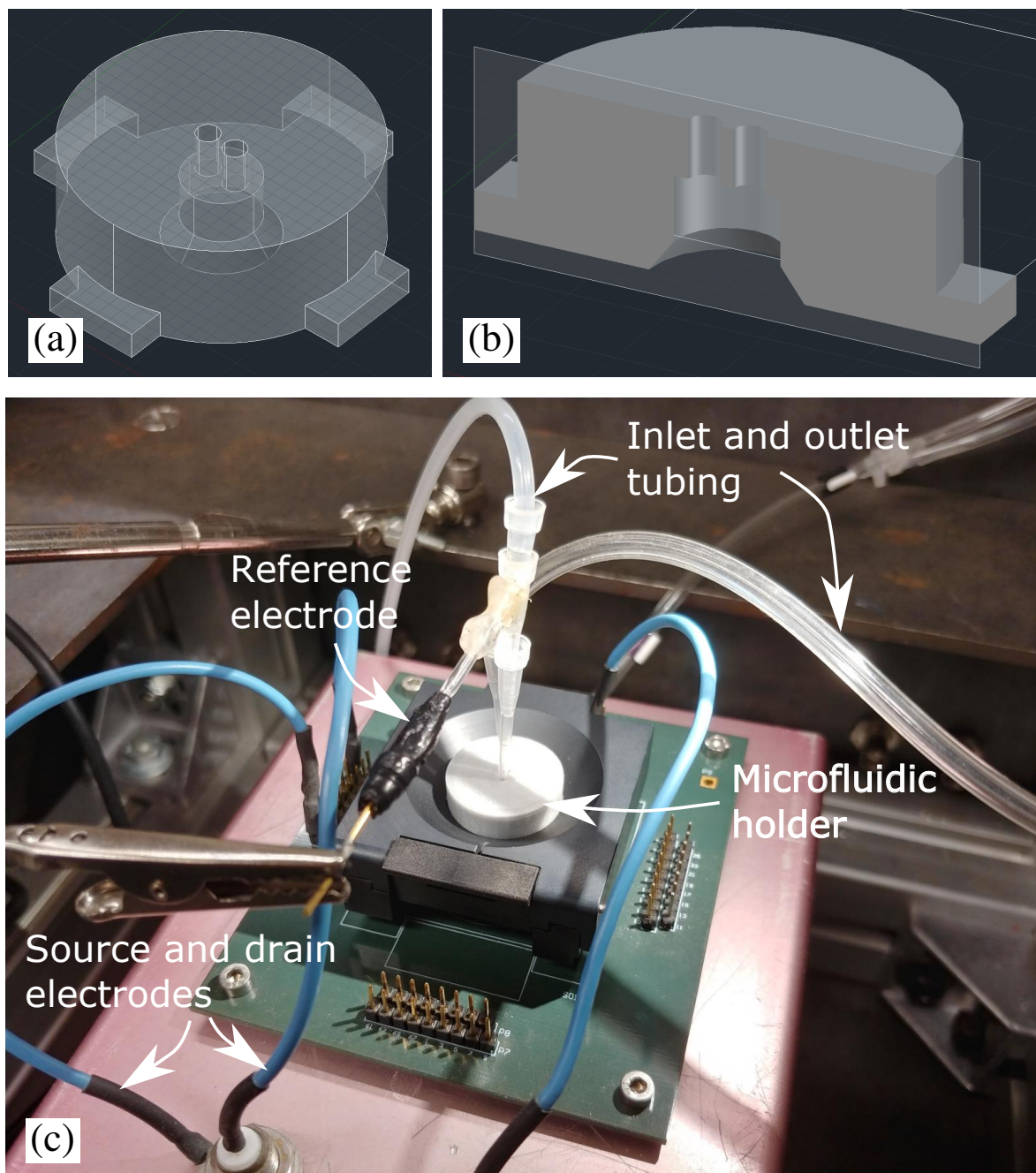


**Figure 3.9:** (a) Wire frame drawing of the designed microfluidic holder, and (b) its cross-section. (c) Photo of the measurement setup with implemented microfluidic system.

### 3.3 Summary

Knowledge about transport and noise properties of nanowire-based devices are crucial for their applications as biochemical sensors. It allows to find optimal operation regimes with the lowest possible device noise and superior signal-to-noise ratios (SNRs). Moreover, optimization of measurement techniques and detailed studies of the structures may reveal novel physical effects, e.g., single trap phenomena [52, 103, 108, 128], that can significantly enhance the sensing capabilities of nanowire biosensors.

Such studies, indeed, demand collection and analysis of large amounts of experimental data. In this regard, automation and modernization of measurement setups can significantly simplify the data acquisition processes, enhance measurement accuracy and speed, reduce the probability of incorrect results, and avoid possible human-related errors. For this purpose, setups for measuring transport and noise characteristics of nanowire structures: silicon nanowire FETs and tunable metal nanoconstriction devices are modernized and automated. A microfluidic fluid supply system is developed and optimized to reduce the volume of studied bioliquids when measuring Si NW FETs. Stable multithreading GUI-based user-friendly software is developed using the C# programming language to operate the measurement setups and acquire data in an automated way. The implemented hardware/software improvements of the noise measurement setup including advancements of the voltage apply units and time-traces/spectra acquisition system greatly enhance its measurement capabilities.



## DEVELOPMENT OF Si NW-BASED BIOSENSORS

Nanowires (NWs) represent a versatile class of nanoscale devices with a broad range of possible applications. Silicon nanowire (Si NW) field-effect transistors (FETs) are attracting considerable attention nowadays both in theoretical and practical studies. Their remarkable properties, in particular, high sensitivity to surface charges make them very attractive for various sensing applications [52–55].

Within the past few decades selective detection of various biological molecules, such as deoxyribonucleic acids (DNAs), proteins, enzymes, etc. is attracting considerable attention in current research [129]. It involves the development of different techniques for the detection of target biomolecules by utilizing their characteristic properties, e.g., size, mass, electrical charge, and/or chemical structure. In this respect, silicon nanowire-based devices are promising for the role of excellent transducers for label-free, efficient, rapid, selective, and highly-sensitive signal conversion from the biological to the electrical domain.

### 4.1 Characterization of Si NW FETs

Constant quality control of the silicon nanowire FET structures is an essential requirement for the development of robust and reliable Si NW-based biosensors. Thus, appropriate performance characterization tests have to be performed at each of the development stages from device fabrication to encapsulation and calibration. The optimization of the fabrication procedure is discussed in section 2.1. The high quality of the Si NWs is confirmed by atomic force microscopy (AFM) and scanning electron microscopy (SEM) imaging as well as by focused ion beam (FIB) sectioning. The studies on the electrical performance of the fabricated Si NW FET structures including current-voltage measurements and low-frequency noise spectroscopy investigations are described below.

#### 4.1.1 Electrical Transport Studies

The DC electrical transport in the fabricated Si NW FET devices is investigated using current-voltage (I-V) measurements. The characteristics are measured using a Keithley 2602A two-channel source-measurement unit (SMU) and the software developed in house (see section 3.1).

## Transfer and Output Curves

The FET transfer curves are the dependencies of the drain current  $I_D$  on the applied gate voltage  $V_G$  at a fixed value of the drain-source bias. They reflect the controllability of the current flow in the NW channel. Transfer curves, measured on an accumulation mode  $p$ -type single Si NW FET with the width of 250 nm and the length of 6  $\mu\text{m}$ , are shown in **Figure 4.1** (a). The fabricated devices show typical transistor-type behavior of the electrical characteristics and

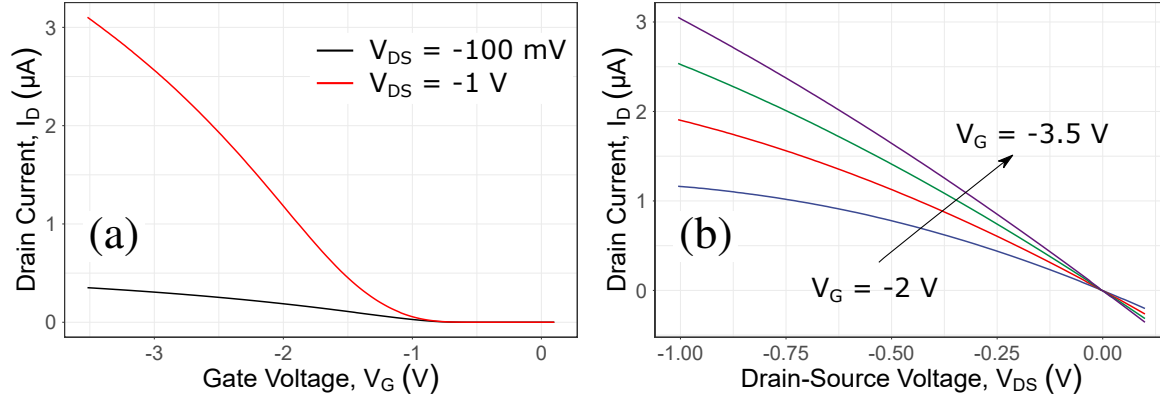


**Figure 4.1:** (a) Transfer curves, measured on a single silicon nanowire FET structure with the width of 250 nm and the length of 6  $\mu\text{m}$ . The characteristics are measured at different values of the drain-source voltage applied:  $V_{DS} = -100 \text{ mV}$  (linear regime), and  $V_{DS} = -1 \text{ V}$  (saturation regime). (b) Sets of the output curves, measured on the same NW FET device, obtained at different values of the liquid gate voltage in the range from  $-2 \text{ V}$  to  $-3.5 \text{ V}$  with the step of  $-0.5 \text{ V}$ .

stable operation in the electrolyte-liquid environment. It should be noted that the registered leakage current  $I_G \leq 1 \text{ nA}$  is at least three orders of magnitude lower than the drain current  $I_D$  within the entire range of the liquid gate voltages applied. This confirms the high quality of the fabricated nanowire FET structures.

Set of the transfer curves measured on single silicon nanowire FETs with the width of 250 nm and the lengths in the range from 6  $\mu\text{m}$  to 22  $\mu\text{m}$  are shown in **Figure 4.2**. Analysis of the NW FET transfer curves allows quantitative determination of such important parameters as the threshold voltage  $V_{Th}$ , the subthreshold swing  $SS$ , and the carrier mobility  $\mu$ . The first two parameters can be extracted from the transfer curves directly while the other can be estimated using the following considerations. The expression for the drain current in MOSFET and ISFET structures (in non-saturation operation regime) can be approximated as [130]:

$$I_D = C_{ox}\mu\frac{W}{L} \left[ (V_G - V_{Th}) V_{DS} - \frac{1}{2} V_{DS}^2 \right]. \quad (4.1)$$

Here,  $C_{ox}$  is the gate oxide capacitance per unit area,  $\mu$  is the carrier mobility in the NW FET channel,  $W$  and  $L$  are the width and length of the NW channel, respectively. In the linear

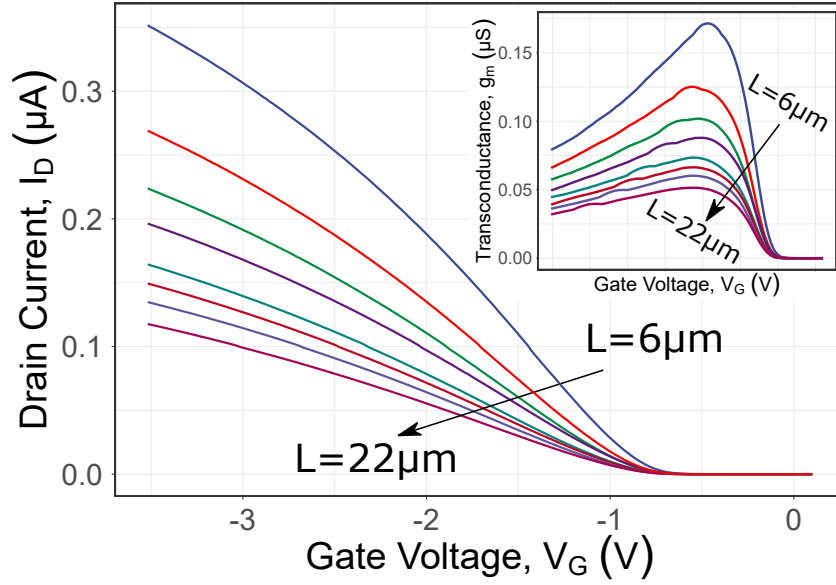


**Figure 4.2:** Set of transfer curves, measured at  $V_{DS} = 100$  mV on the accumulation mode  $p$ -type single Si NW FET structures with the width of 250 nm and the lengths in the range from 6  $\mu\text{m}$  to 22  $\mu\text{m}$ . The corresponding transconductance curves are shown in the inset.

operation regime (small  $V_{DS}$ ) Equation (4.1) can be simplified to:

$$I_D = C_{ox}\mu \frac{W}{L} (V_G - V_{Th}) V_{DS}. \quad (4.2)$$

Taking into account the expression for the drift current, Equation (4.2) can be represented as follows:

$$I_D = en\mu E_{DS} = \frac{N}{WLH} e\mu E_{DS}WH = eN\mu \frac{V_{DS}}{L^2}. \quad (4.3)$$

Here,  $n$  is the carrier concentration,  $N$  is the number of the charge carriers,  $H$  is the channel height,  $E_{DS} = V_{DS}/L$  is the electric field between the source and drain electrodes, and  $e$  is the elementary charge. Taking the derivative of the  $I_D$  vs.  $V_G$  dependence allows estimation of the FET transconductance  $g_m$ :

$$g_m = \left. \frac{\partial I_D}{\partial V_G} \right|_{V_{DS}=\text{const.}} = \mu C_{ox} \frac{W}{L} V_{DS} \quad (4.4)$$

Equations (4.3) and (4.4) allow estimation of the mobility and concentration of the charge carriers in the NW channel:

$$\mu = \frac{g_m L}{WC_{ox} V_{DS}}, \quad (4.5)$$

$$n = \frac{I_D C_{ox}}{e g_m H}. \quad (4.6)$$

Typical parameters of the fabricated Si NW FET structures, extracted from the transfer curves are summarized in **Table 4.1**. The obtained values are in good agreement with the data reported

**Table 4.1:** Parameters of NW FETs

Parameter name		Value
Threshold voltage	$V_{Th}$	-0.8 V
Subthreshold swing	$SS$	130 mV dec <sup>-1</sup>
Carrier mobility	$\mu$	95 cm <sup>2</sup> V <sup>-1</sup> s <sup>-1</sup>

in the literature [131]. It should be noted that the above considerations are valid for large planar structures and they do not take into account the effect of the charge distribution in the NW channel. However, this approach describes the macroscopic I-V characteristics of Si NW FETs well until ultimately low sizes ( $\lesssim 20$  nm in each dimension) [11].

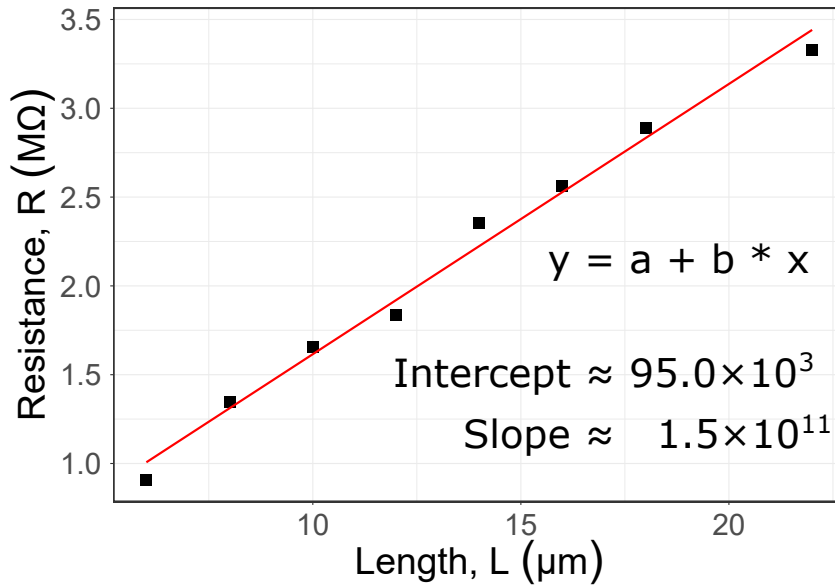


**Figure 4.3:** The resistance of the fabricated Si NW FET structures extracted from **Figure 4.2** as a function of the nanowire length. The red line represents linear fitting of the data.

Data from **Figure 4.2** also allow estimation of the contact resistance – another important parameter of the Si NW FET devices. For this purpose, the resistance values are obtained from the linear region of the transfer curves using the Ohm’s law and plotted vs. the nanowire length (see **Figure 4.3**). The value of the contact resistance can be extracted by fitting the data to linear model. It should be emphasized that this value ( $2R_c \simeq 95$  k $\Omega$ ) is much lower than the nanowire channel resistance  $R_{ch} \gtrsim 1$  M $\Omega$ . Thus, the influence of the contact resistance on the electrical characteristics of the fabricated Si NW structures can be neglected.

The FET output curves are the dependencies of the drain current  $I_D$  on the drain-source voltage  $V_{DS}$  at a fixed value of the gate voltage  $V_G$ . Sets of the output curves, measured on a single silicon nanowire FET with the width of 250 nm and the length of 6  $\mu$ m are shown in **Figure 4.1** (b). Analysis of the output curves can be applied for estimation of the NW channel differential resistance.

## Transconductance Studies

The FET transconductance is defined as the change in the drain current  $I_D$  induced by the small change in the gate voltage  $V_G$  (see Equation (4.4)). It represents a gain of the transistor circuit and carries information about the strength of the gate control over the drain current. Thus, transconductance measurements can be used to find the optimal operation regimes of silicon nanowire devices. Such studies become particularly important when the Si NW FETs are operated in dual-gate configuration and can be used for investigation of the front-to-back gate coupling in the structures [132, 133].

The transconductance curves, measured on a single Si NW FET device with the width of 250 nm and the length of 4  $\mu\text{m}$  at different back gate voltages applied are shown in **Figure 4.4** (a) and outlined in the form of the contour plot in **Figure 4.4** (b). Applying voltage to the back gate electrode shifts the threshold voltage of the Si NW FET devices due to the pronounced front-to-back gate coupling. This observation is in good agreement with previously reported results [132]. It should be noted that the back gate biasing also causes changes of the transconductance maximum (see **Figure 4.4** (b)). In this respect, the simultaneous utilization of both the front and the back gate electrodes is promising for tuning the NW FET's working point, for optimization of the  $g_m$  value, and thus for improving the device sensitivity.

### 4.1.2 Noise Spectroscopy Characterization

Despite the immense sensitivity of Si NW FET biosensors, they still have certain drawbacks. One of the most fundamental problems is the degeneration of their electrical characteristics while operating in an electrolyte liquid environment [134]. This undesirable effect is most often

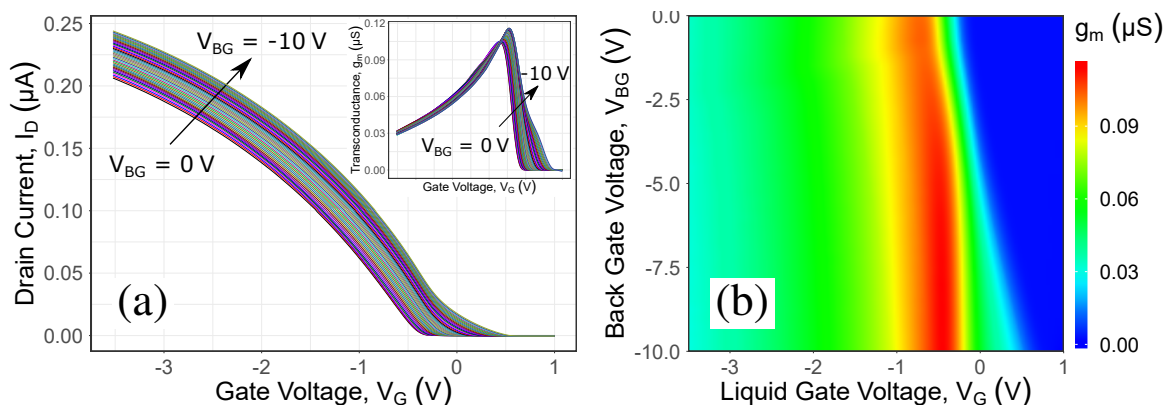


**Figure 4.4:** (a) Set of the transfer curves, measured on a single Si NW FET structure with the width of 250 nm and the length of 4  $\mu\text{m}$  at different values of the back gate voltage applied from 0 V down to  $-10$  V with the step of  $-250$  mV. The corresponding transconductance curves are shown in the inset. (b) Color map of the nanowire structure transconductance, obtained as numerical derivative of the transfer curves presented in (a).

caused by the damage of the thin gate oxide layer, which is in the direct contact with studied bioliquids during sensing experiments. Therefore, the quality of the gate insulator determines the performance of Si NW FET sensors and is one of the limiting factors for their repetitive use [51, 135]. In this respect, using techniques to continuously control the device performance and establishment of novel nondestructive sensing approaches are crucial for the development of reliable Si NW biosensor devices.

Ultimate downscaling of the electrical devices significantly obstructs the use of conventional characterization techniques such as capacitance-voltage measurements. Thus, an alternative approach has to be utilized to achieve knowledge about the conducting channel/insulator and insulator/electrolyte interfaces in nanoscale liquid-gated Si NW FETs. In this regard, low-frequency noise spectroscopy can provide useful information about the quality, electrical performance, and operating regimes of silicon nanowire sensors [52, 136]. It is a powerful, highly sensitive, and nondestructive approach. Therefore, it can substitute the capacitance-voltage measurements and complement the DC current-voltage characterization.

There are several known noise sources in transistor structures. They are generally determined by various types of carrier generation and recombination processes. In nanoscale FETs, noise usually comes from traps and defects that are randomly distributed in the gate oxide layer close to the conducting channel. At low frequencies, the flicker noise component is usually the most pronounced. In particular cases, Lorentzian-shaped generation-recombination (GR) components can appear on the noise spectra, reflecting the evidence of the random telegraph signal (RTS) noise corresponding to the capture/emission processes to/from a single electrically-active trap [52, 137].

The low-frequency noise measurements are conducted using the advanced noise measurement setup and the software developed in house (see section 3.1). Typical normalized current noise spectra, measured on the single silicon nanowire FET structure with the width of 250 nm and the length of 6  $\mu\text{m}$ , acquired at different values of the liquid gate voltage applied are shown in **Figure 4.5**. The measured spectra demonstrate a clear  $1/f$  dependence within the entire range of the gate voltages applied.

The input referred noise  $S_U$  dependencies are used to analyze the noise origin in the nanowire channel. It is obtained using the current noise power spectral density (PSD)  $S_I$ , and the transconductance values  $g_m$  calculated as numerical derivative of the NW FET transfer curve:

$$S_U = \frac{S_I}{g_m^2}. \quad (4.7)$$

The input-referred noise level, taken at the frequency of 100 Hz, is plotted as a function of the overdrive gate voltage  $V_{OV} = V_G - V_{Th}$  in **Figure 4.6**. At increased gate voltages  $|V_{OV}| > -0.5$  V, the  $S_U$  increases with the increase of the liquid gate overdrive. Such noise behavior indicates that the main noise source is the mobility fluctuation of the charge carriers in the

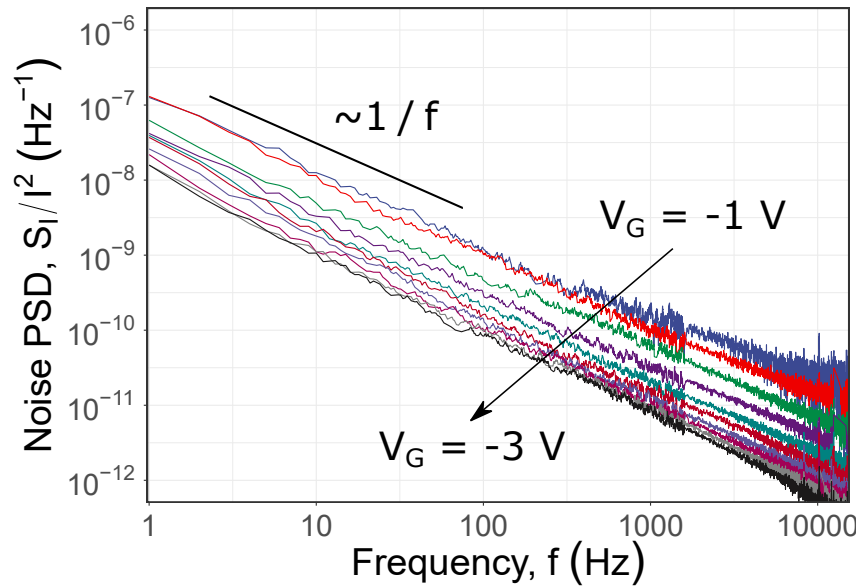


**Figure 4.5:** Typical normalized current noise spectra, measured on the single Si NW structure with the width of 250 nm and the length of 6  $\mu\text{m}$  at different values of the liquid gate voltage in the range from  $V_G = -1$  V to  $V_G = -3$  V applied.

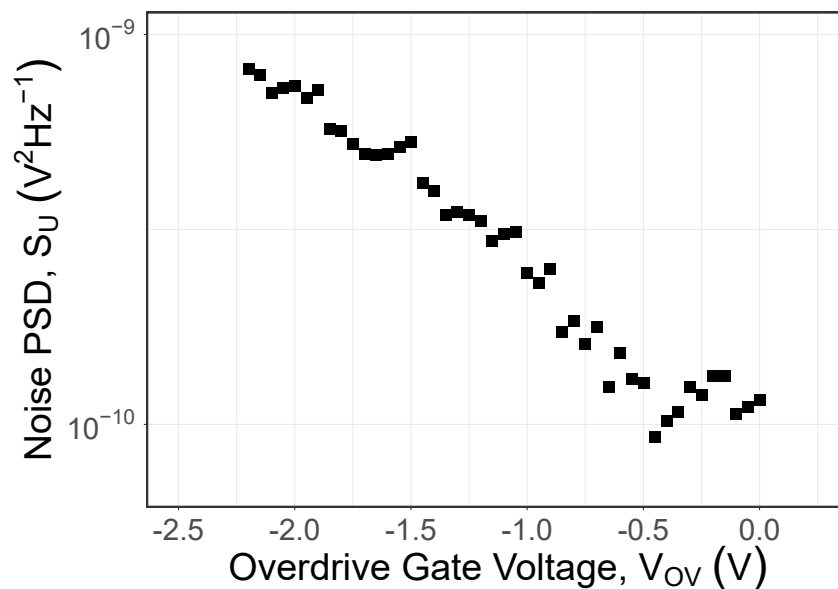


**Figure 4.6:** Input referred noise taken at the frequency of 100 Hz as a function of the overdrive liquid gate voltage.

nanowire channel, which can be described by the Hooge's model [138].

To compare the noise level of the fabricated devices with the one reported in literature, the dimensionless Hooge parameter is estimated using the following expression [139, 140]:

$$\alpha_H = \frac{f S_I}{I_D} \frac{L^2}{q \mu V_{DS}}. \quad (4.8)$$

Here,  $q = 1.602 \times 10^{-19}$  C is the electron charge. The obtained Hooge's parameter,  $\alpha_H$ , vs. the overdrive gate voltage dependence is shown in **Figure 4.7**. It should be noted that the  $S_U$

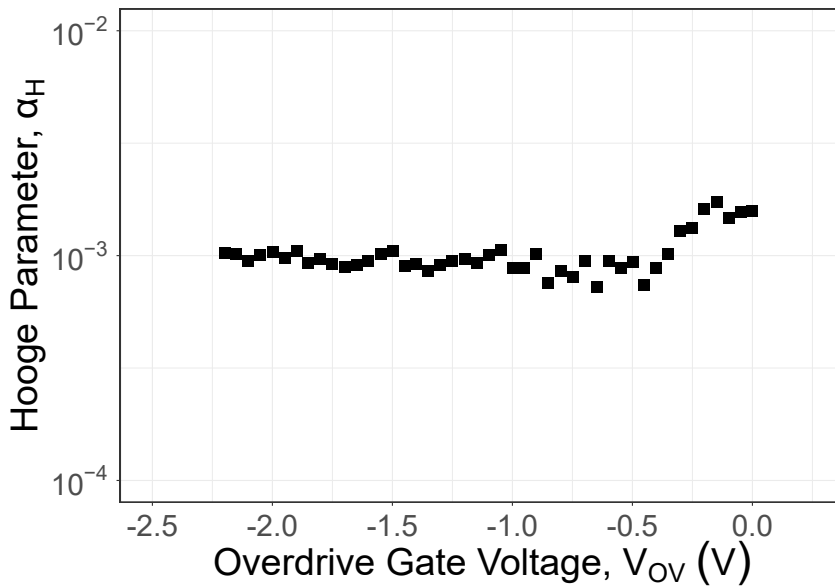


**Figure 4.7:** Hooge parameter  $\alpha_H$  as a function of overdrive liquid gate voltage.

and  $\alpha_H$  values in the liquid-gated NW structures fabricated using the optimized nanoimprint technology are comparable with those obtained for structures fabricated using electron beam lithography [141] for the same range of overdrive gate voltages. The results demonstrate the high quality of the liquid-gated NW FET structures, which can be used for biosensing and bio-medical monitoring of biological liquids.

## 4.2 Si NWs: Towards the Detection of Cardiac Biomarkers

Biosensors based on Si NW FETs have recently emerged as promising candidates for the role of reliable and robust electronic devices for sensing of various biological molecules [102, 142, 143] due to the unique and tunable electrical properties of silicon nanowires. The sensing mechanism for this type of sensors is usually based on monitoring the changes in current or conductance of the FETs upon attachment of target molecules to the nanowire surface. Being charged molecules, biomolecules induce a gating field effect, which leads to the depletion or accumulation of charge carriers in the channel resulting in conductance changes that can be

measured and correlated with the concentration of target biomolecules in studied solution. Increased surface-to-volume ratio of Si NWs allows for tremendous sensitivity of these devices to the changes in surface potential to be achieved. Moreover, bindings of target biomolecules do not only alter the conductance of Si NW FETs but also affect the dynamics of the charge transport in the structures. In this regard, noise spectroscopy can be utilized to reveal the nature of analyte-induced charge exchange processes.

Since molecular analysis of blood and other bioliquids is very important in disease diagnosis, Si NW FETs are also promising candidates for the role of biosensors that can rapidly deliver diagnostics. A fast, precise, and reliable analysis is essentially important in the treatment of cardiovascular diseases, where proper timing becomes a critical lifesaving issue. In this section, the studies on the quantitative determination of C-reactive protein (CRP) and cardiac troponin (cTn) I molecules are presented. The CRP and cTnI are the gold standard biomarkers indicating the presence of inflammation processes and/or damage of the cardiac tissue. Thus, rapid sensing of these molecules and continuous monitoring of their levels in bioliquids are promising for early prediction of acute myocardial infarctions (AMIs) and strokes.

#### 4.2.1 Sensing of the Human C-Reactive Protein

C-reactive protein molecules are a primary inflammation markers, which have recently emerged in clinical practice for monitoring the state of inflammations [144, 145]. The concentration of these molecules increases rapidly in response to inflammations and tissue damage [146]. Thus, monitoring of CRP levels in the blood allows prediction of the risk of different diseases, and helps to track the development of these diseases in order to apply appropriate medical treatment.

Here, the results of studies of Si NW FETs fabricated using optimized cost-efficient complementary metal-oxide-semiconductor (CMOS)-compatible nanoimprint technology are reported. The high quality of NW structures is confirmed by scanning electron microscopy and focused ion beam imaging. Fabricated by nanoimprint technology liquid-gated Si NW FETs are highly sensitive to the surface charges introduced by human C-reactive protein molecules of different concentrations in bioliquids.

##### Functionalization Procedure

At first, the sensing surface of Si NW structures are cleaned and activated using a Pico Diener plasma oven. Oxygen plasma treatment (pressure = 0.8 mbar, power = 80 W, time = 3 min) is used to produce silanol groups (Si-OH) on the gate silicon dioxide. Silicon nanowire FETs are then functionalized with 3-aminopropyl-triethoxysilane (APTES) molecules by deposition from the gas phase in a desiccator (pressure = 5 mbar, time = 1 h). The process is performed in an argon atmosphere inside a Glove Box. The following step is adding aldehyde bonds

by sample incubation in 2.5 % glutaraldehyde solution for 1 h at room temperature. Finally, structures are covered with anti-CRP antibodies and incubated for 2 h at room temperature. Since the distribution of the antibodies on the surface of the structures can be non-uniform, some aldehyde groups may not be covered with antibodies and thus remain active. Therefore, to prevent nonspecific bindings, free aldehyde groups are blocked with ethanolamine solution. Functionalized samples can be stored at 4 °C for up to 24 h prior to use.

### Setup for Liquid Gated FET Measurements

Current-voltage curves of fabricated Si NW FETs are measured using a Keithley 2602A two channel source-measurement unit (see section 3.1). The nanowire structures, surrounded by the gate oxide are exposed to 10 mM phosphate-buffered saline (PBS) pH = 7.4 solution. An external standard Ag/AgCl reference electrode is used to apply the gate potential while the drain-source bias is applied to the highly doped regions of the FETs (see **Figure 4.8**). The drain-source bias is kept constant at  $-0.1$  V for all sensing measurements in order to provide the linear working regime of the transistor structures. The measurements are performed at room temperature inside an electrically shielded cage. NW devices controlled by liquid-gate voltage show reproducible transistor I-V characteristics without leakage current.

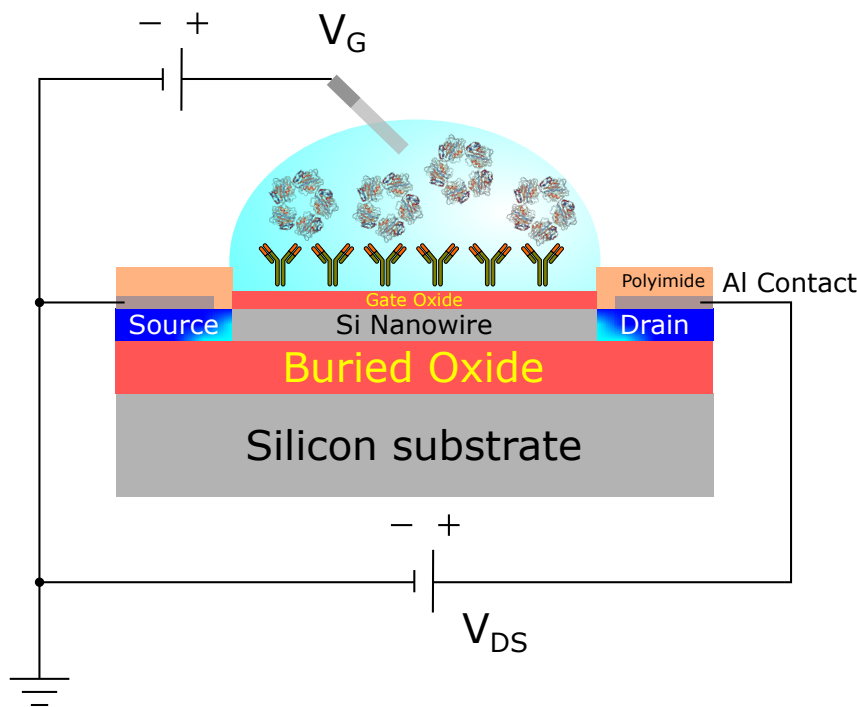


**Figure 4.8:** Sketch of a silicon nanowire biosensor. The drain-source current  $I_{DS}$  through the nanowire is measured with increasing CRP concentration at constant drain-source bias. A liquid-gate voltage  $V_{ref}$  (corresponds to  $V_{LG}$ ) is applied using Ag/AgCl reference electrode and back-gate electrode is grounded.

### CRP Antigen Detection

Single Si NW FETs with a width of 250 nm and length of 4  $\mu\text{m}$  are used for the measurements. The response of the sensors to the concentration of target CRP antigen molecules is measured by monitoring the concentration-dependent shift of transfer characteristics (drain current,  $I_{DS}$ , vs. liquid gate voltage,  $V_{LG}$ ). Firstly, reference measurements are performed in the pure 10 mM PBS pH = 7.4 solution and then in different concentrations of CRP antigen molecules in the range from 10  $\text{pg ml}^{-1}$  to 10  $\text{ng ml}^{-1}$ . After each concentration change transfer curves are measured. The results of the measurements are shown in **Figure 4.9**. With increasing of the antigen

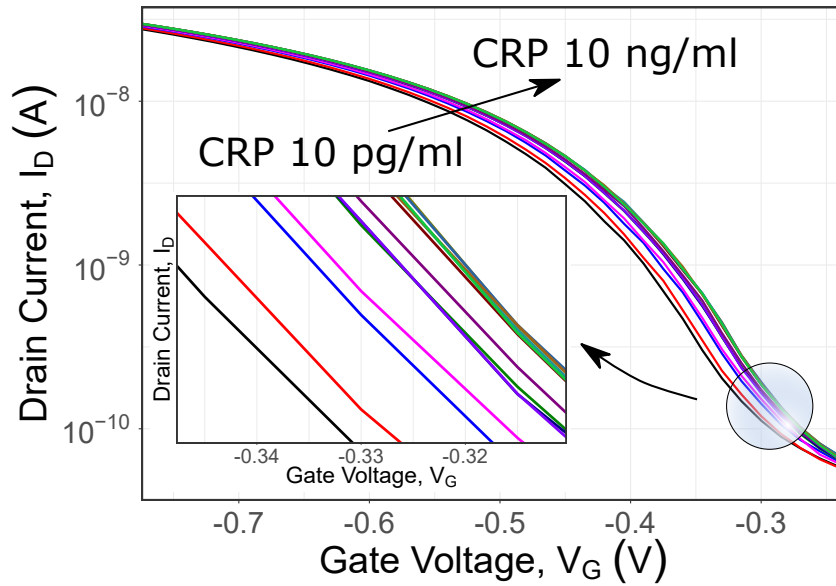


**Figure 4.9:** Transfer curves shift of the Si NW FET due to increase of CRP concentration. Enlarged for clarity curves are shown in the inset.

concentration transfer curves shift to the direction of higher currents. This indicates that the CRP concentration increase causes the negative charge increase on the gate oxide surface due to antigen-antibody bindings. The negative introduced charge is in good agreement with literature data [146] concerning the charge state of CRP molecules.

The biosensor calibration curve is extracted from the  $I_D - V_G$  data and replotted in terms of sensitivity [123]:

$$S = |I_D - I_{D0}| / I_{D0}, \quad (4.9)$$

which shows the normalized biosensor response to changes in the concentration of target molecules (see **Figure 4.10**). Here,  $I_{D0}$  is the reference drain current at zero CRP concentration. Fabricated Si NW FET biosensors show an almost linear response in a semi-logarithmic scale in the concentration range from 50  $\text{pg ml}^{-1}$  to 5  $\text{ng ml}^{-1}$ . This concentration range of CRP detection can be described by the following equation:

$$S = 0.23 \times \log_{10}(C_{CRP}) + 0.63. \quad (4.10)$$

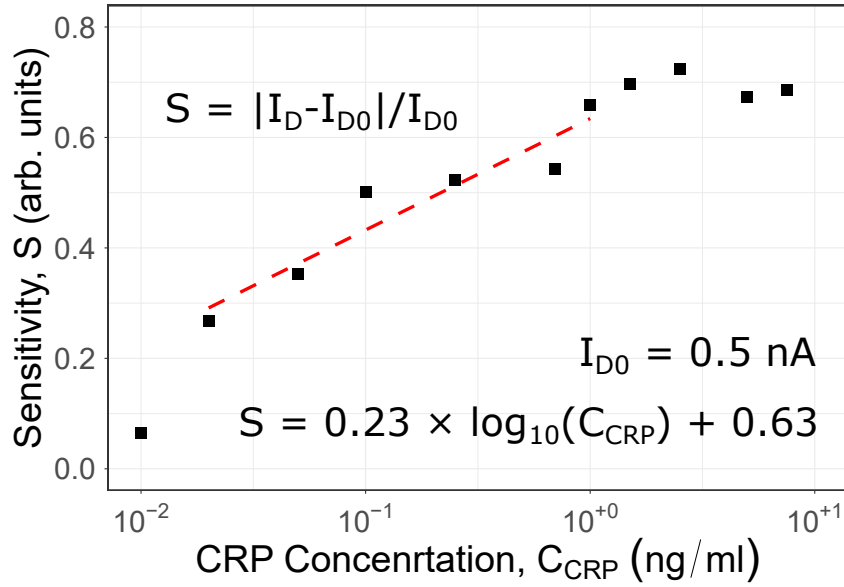


**Figure 4.10:** Sensitivity of Si NW FET biosensor vs. concentration of the target CRP molecules.

Starting from concentrations above  $5 \text{ ng ml}^{-1}$ , no further shift of transfer curves is observed with an increase of the antigen concentration. At this point, all the anti-CRP antibodies on the gate-oxide surface are bound to antigen molecules resulting in the formation of saturation region. The lowest determined CRP concentration was equal to  $10 \text{ pg ml}^{-1}$ . Using nanowire structures with different widths and lengths allows for this value to be tuned.

## 4.2.2 Human Cardiac Troponin I Sensing

Human troponin is represented by a complex of three regulatory proteins: troponin C, troponin I, and troponin T. It is involved in muscle contraction processes of cardiac and skeletal muscles. It should be noted that the protein exists in different isoforms: troponins T and I, expressed in cardiac muscle differ from those expressed in skeletal muscles. Troponin C has no cardiac-specific isoform. In contrast, cTnI is expressed only in the myocardium, and it has only one tissue-specific isoform. Elevated levels of cTnI in blood are, therefore, highly specific for myocardial injury [147, 148]. Thus, monitoring of cTnI levels can be used for diagnostics of AMI and stroke.

Here, the application of  $n^+ - p - n^+$ -type Si NW FETs as reusable biosensors for detection of cardiac troponin I is reported. An increase of the cTnI concentration leads to well-resolved shifts of the transfer curves, reflecting the binding of charged target molecules. Addition of non-specific C-reactive protein antigens to the sensing media does not change the drain current, which reflects the high specificity of the Si NW troponin biosensor.

Low-frequency noise spectroscopy is applied for performance characterization of Si NW

biosensor devices. Studies of the noise spectra and input referred noise revealed that changes in the dynamic processes are caused by the analyte-induced decrease of the effective gate voltage. Noise spectroscopy, therefore, can be utilized not only as a powerful characterization technique but also as a promising highly-sensitive and label-free sensing approach. The results of these studies are published in [102].

### Electrical detection of cTnI

The surface modification of the silicon nanowires is firstly performed to implement the exceptional specificity to the cardiac troponin I. The whole functionalization procedure is performed in a similar way as described above for CRP detection. In the last step, however, monoclonal anti-cTnI antibodies are applied to the sample instead of anti-CRP antibodies.

The target cTnI antigens are measured in 1 mM PBS solution with  $\text{pH} = 7.4$ . The response of Si NW FET biosensors to the changes in analyte concentration is traced by the shift of transfer curves. At first, a 100  $\mu\text{l}$  of bare PBS solution is introduced to the nanowire region of the chip, and a reference  $I_D - V_G$  curve is measured. Then, different concentrations of cTnI antigen are introduced using the direct on-chip dilution approach: measured portions of higher-concentrated stock solutions are consequently applied to the sensing media using a micropipette to achieve the desired troponin concentration. Each concentration change is followed by a 2 min delay and subsequent transfer curve measurement. The delay is required for the system to approach an equilibrium state, and thus to achieve reliable sensor readings. The measured  $I_D - V_G$  dependencies are shown in **Figure 4.11**. They shift to the direction of higher positive gate voltages

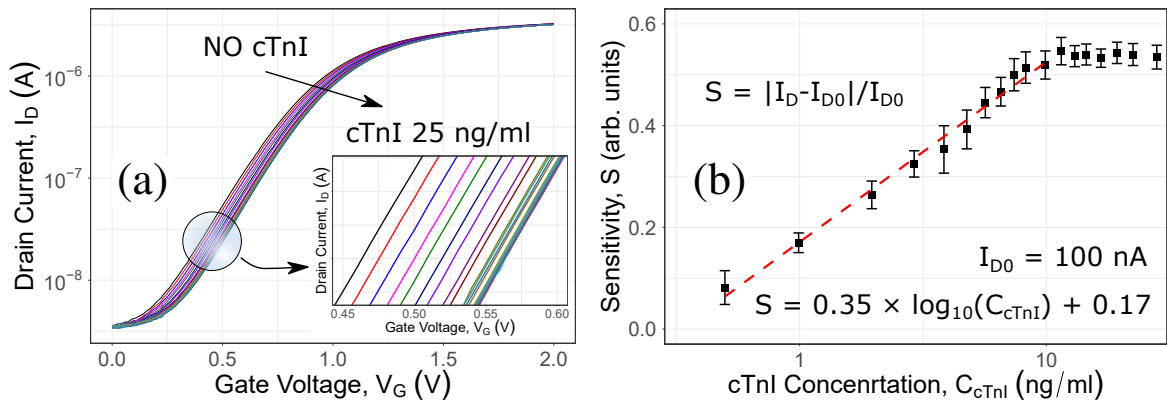


**Figure 4.11:** (a) Transfer curves of the Si NW FET troponin biosensor, shifting in response to the analyte concentration changes. (b) Normalized biosensor response extracted from the transfer curves at  $I_{D0} = 100 \text{ nA}$ .

with increasing of the cTnI concentration. This means that binding of analyte molecules leads to the accumulation of negative charges on the active sensing surface (gate oxide) and, accordingly, to the depletion of charge carriers in the  $n^+ - p - n^+$  NW FET channel. This observation can be explained by the electrostatic properties of cTnI antigens. The cardiac troponin I molecules

have the isoelectric point (pI) value of 5.2, and therefore, they are negatively charged in the PBS pH = 7.4 solution used. The obtained results are in good agreement with previously reported literature [123]. The response of the Si NW troponin biosensor is extracted from the transfer curves for  $I_{D0} = 100$  nA. The corresponding sensitivity, obtained using Equation (4.9) is plotted vs. the cTnI concentration in **Figure 4.11** (b). Two distinct regions could be resolved on the sensitivity curve. At concentrations from  $0.5 \text{ ng ml}^{-1}$  to  $10 \text{ ng ml}^{-1}$  the sensitivity depends linearly on the cTnI concentration in semi-logarithmic scale. This range defines the applicability of the Si NW sensor for cTnI detection. It can be approximated by the following analytical equation:

$$S = 0.35 \times \log_{10} [C_{cTnI}] + 0.17. \quad (4.11)$$

At concentrations higher than  $10 \text{ ng ml}^{-1}$  the saturation region is formed (no sensitivity change is measured with the increase of analyte concentration). This effect can be attributed to the complete occupancy of anti-cTnI antibodies on the sensing surface with troponin antigens. The achieved detection range (linear region of the sensitivity curve) comprises the biological range of elevated cTnI levels that occur within the first hours of the AMI development. Therefore, such kind sensors can be utilized to track the current disease state and to prevent aggravations. However, the detection range can be tuned if needed using the Si NW devices with different geometries or configurations.

### Biosensor reusability

The biosensor field is experiencing a significant development breakthrough within the last few decades. Nevertheless, the ability to repeatedly use the sensor still remains one of its great challenges. Si NW-based biosensors, unfortunately, are not an exception. While these devices are proven to be exceptional transducers for sensing of various biological objects, yet only a few studies report on the biosensor reusability [149–151]. There are several approaches to regenerate the sensors. Depending on the type of the analyte and measurement configuration, different approaches can be considered. In general, to regenerate the biosensors the active sensing surface has to be cleaned from the bound analyte. This can be done by removing either the analyte itself or the entire analyte-receptor complex. In the first case, the care must be taken not to damage the receptors and maintain their full functionality. The second approach requires full re-functionalization and calibration.

For our Si NW FET biosensors, the first approach is selected since it is faster, i.e., demands fewer steps to regenerate the sensor, and it does not require the additional calibration stage. The mild 10 mM glycine-HCl in 1 mM PBS buffer solution (pH = 4.0) is used to wash-off the bound antigen molecules. This solution forces the dissociation of the antigen-antibody complexes, i.e., the release of cTnI antigens without denaturation of the receptors (anti-cTnI antibodies). The biosensor regeneration consists of the following steps:

- Replacement of the sensing media with the regeneration solution and incubation for 10 min at room temperature. This causes the separation of the bound antigens from anti-cTnI antibodies, thus reestablishing the biorecognition layer functionality.
- Rinsing the sensor with deionized water to wash-off the released cTnI antigens and regeneration buffer residuals.
- Refilling the sensing volume with an initial 1 mM PBS solution with  $\text{pH} = 7.4$  and repeating the  $I_D - V_G$  measurements.

The reference  $I_{D0} - V_G$  curve (black), taken before the cTnI measurement, is plotted in **Figure 4.12** (a) together with the  $I_D - V_G$  transfer curve, measured after the biosensor regeneration procedure. The dependence of the NW FET conductance on the cTnI concentration is shown in

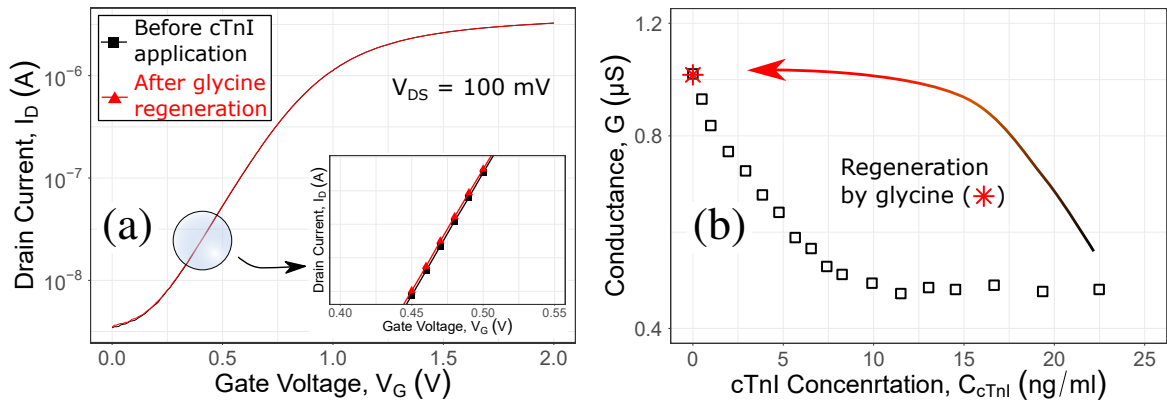


**Figure 4.12:** (a) Transfer curves of the Si NW FET troponin biosensor: reference curve (black) and  $I_D - V_G$  dependence measured after the sensor regeneration procedure (red). (b) Conductance of the Si NW FET biosensor as a function of cTnI concentration for the values of  $I_{D0} = 100$  nA (black squares). The conductance value obtained after the biosensor regeneration is shown as a red star.

**Figure 4.12** (b). The NW transfer curve measured after the glycine-HCl treatment (red) follows the reference curve (black), and the NW conductance (red star) returns to its initial value. This signifies the successful regeneration and high quality of the developed Si NW FET troponin biosensor.

### Noise Spectroscopy Analysis

Noise spectroscopy has proven to be a powerful approach for nanowire devices characterization [152, 153]. It is a highly-sensitive and non-destructing technique that can provide information about the dynamics of the charge transport in the structures. The carrier exchange processes at the semiconductor/insulator interface are among the most common noise sources in semiconductor FET devices. They induce perturbations in the gate surface potential and therefore, in the

drain-source current. Another noise sources, however, always exist and contribute to the overall noise behavior. When Si NW FETs are operated in a liquid environment, extra noise can come from the charge exchange processes occurring at the gate insulator/electrolyte interface [154]. In this regard, binding of the target analyte molecules can considerably affect the noise of Si NW FET biosensors.

To analyze the impact of analyte binding on the noise behavior of the liquid gated troponin biosensors the noise spectra of the functionalized Si NW FETs are recorded before and after the cTnI application. The devices are measured in the 1 mM PBS pH = 7.4 solution at the drain-source voltage  $V_{DS} = 100$  mV applied (linear working regime). The acquired normalized current noise PSD dependencies are shown in **Figure 4.13**. The measured spectra demonstrate a

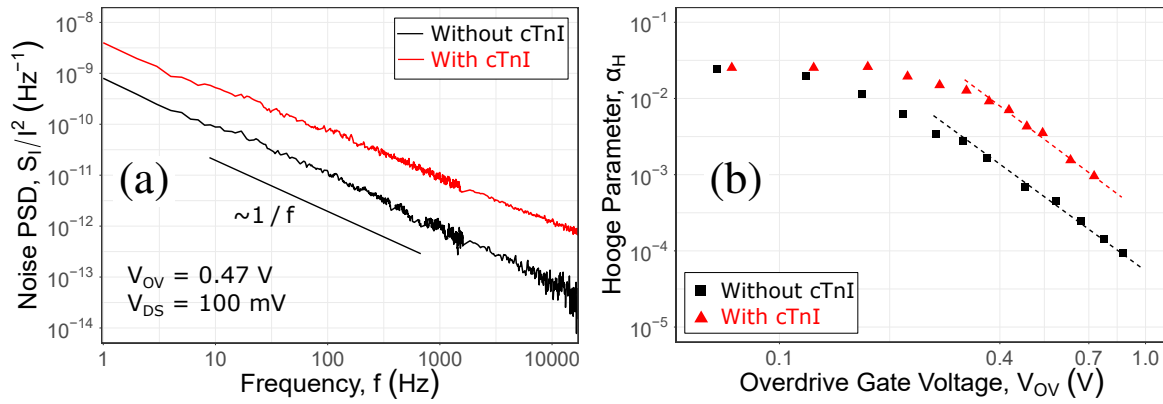


**Figure 4.13:** (a) Normalized current noise PSD dependencies, measured on the functionalized Si NW FETs before (black curve) and after (red curve) the cTnI application. (b) Hooge parameter  $\alpha_H$ , extracted from the noise spectra by fitting vs. the overdrive gate voltage  $V_G - V_{Th}$ . Black and red points correspond to the cases before and after the cTnI application, respectively.

clear  $1/f$  dependence both before and after the cTnI application. In the latter case, however, the normalized noise amplitude is increased almost one order of magnitude (see **Figure 4.13** (a)). Though, such behavior is in good agreement with previously reported results [101].

To further confirm the evidence of the antigen impact, the dimensionless Hooge parameter  $\alpha_H$  is extracted from the noise spectra by fitting and plotted vs. the overdrive gate voltage  $V_G - V_{Th}$  in **Figure 4.13** (b). The  $\alpha_H$  value decreases with the gate voltage increase, and approaches the value  $\alpha_H \simeq 10^{-4}$  at  $V_G - V_{Th} = 0.9$  V. This reflects the high quality of the Si NW FET biosensor. Moreover, there is a pronounced difference in the behavior of the device before and after the addition of cTnI antigens. At the overdrive gate voltages above  $V_G - V_{Th} = 0.3$  V, the Si NW sensor shows almost one order of magnitude higher  $\alpha_H$  when measured in cTnI containing solution than in bare PBS buffer. This indicates the influence of the analyte on the noise performance of the device.

To identify the source of the excess noise, the input-referred noise  $S_U = S_I/g_m^2$  characteristics are calculated and analyzed (see **Figure 4.14**). When no analyte molecules are present in the

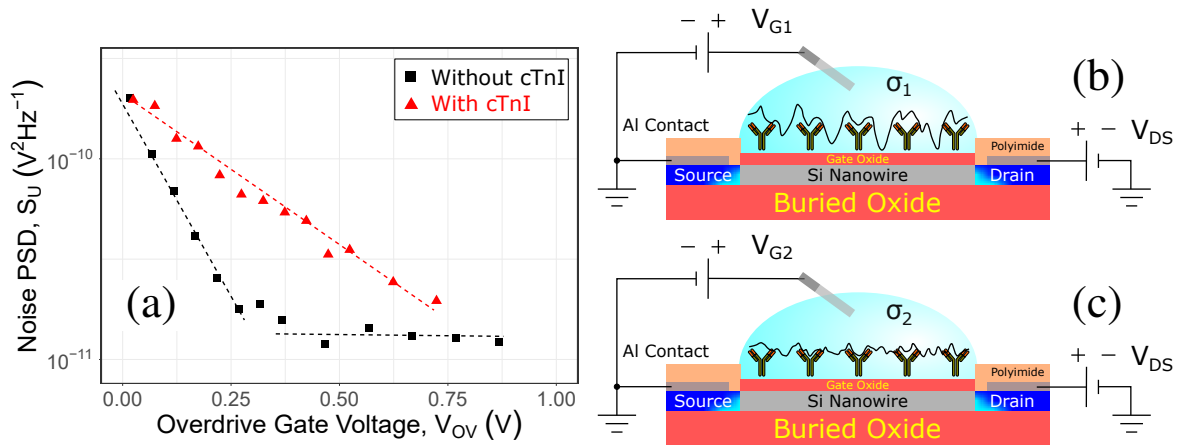


**Figure 4.14:** (a) The equivalent input-referred noise  $S_U$  at 30 Hz, estimated for Si NW FET troponin biosensor before (black squares) and after (red triangles) the cTnI addition, plotted vs. the overdrive gate voltage  $V_G - V_{Th}$ . (b), (c) Schematic images reflecting the fluctuation change  $\sigma_2 < \sigma_1$  with the increase of the liquid gate voltage  $V_{G2} > V_{G1}$ . Here,  $\sigma_1$  and  $\sigma_2$  are the fluctuation dispersion values, corresponding to the gate voltages  $V_{G1}$  and  $V_{G2}$ , respectively.

sensing solution, the  $S_U$  remains constant at the overdrive gate voltages above  $V_G - V_{Th} > 0.3$  V. This verifies that the noise of the Si NW FET biosensor can be described by the carrier fluctuation model when operated in bare PBS solution [155, 156]. Adding the cTnI antigens considerably changes the  $S_U$  behavior. Analyte binding results in the increase of the equivalent input-referred noise level, which indicates the presence of an additional noise source. Moreover, the noise behavior in this case significantly deviates from the McWhorter model [156]. Thus, the obtained results prove that the excess noise is caused by the analyte-induced changes in the dynamic processes at the gate oxide/functional layer/electrolyte interfaces (see **Figure 4.14** (b), (c)). These changes can be attributed to the ion movement through the membrane, formed by the anti-cTnI antibodies and bound antigens. Such interpretation is in good agreement with Donnan's theory, which predicts the possibility of antigen-antibody binding detection even in the cases when the antibody size exceeds the Debye screening length, assuming that antibodies form a membrane on the gate dielectric [157, 158]. Changes in the analyte concentration can significantly alter the ion transparency of this membrane, and thus change the effective charge delivered by the analyte molecules, modulate the gate surface potential, and therefore affect the noise behavior of the Si NW FET biosensors.

### 4.3 Summary

Detection of cardiac biomolecules/biomarkers is of extreme importance for the perspectives of fast medical diagnostics of cardiovascular diseases. Silicon nanowire field-effect transistors are perfect candidates for (bio)sensing studies due to their tremendous sensitivity to changes in surface charge.

Liquid-gated single Si NW FETs are fabricated using cost-efficient optimized nanoimprint technology, compatible with CMOS technology. The fabricated nanowire FETs are characterized using the DC current-voltage approach and low-frequency noise spectroscopy. Important performance characteristics including the threshold voltage, subthreshold swing, and carrier mobility are estimated by analyzing the NW FET transfer curves and summarized in **Table 4.1**. The obtained values are in good agreement with reported literature. Analysis of the noise spectra measured on a *p*-type accumulation mode Si NW FET device revealed that the main noise source in the fabricated structure is connected to the mobility fluctuations of the charge carriers in the nanowire channel. The estimated values of the Hooge's parameter were close to  $\alpha_H \approx 1 \times 10^{-3}$ , which is comparable with or even lower than those reported for most traditional fabrication technologies including electron beam lithography [88, 141, 159].

The fabricated Si NW FET structures are tested for the detection of human C-reactive protein, – a biomolecule which has recently emerged as a reliable biomarker used in clinical practice for prediction and tracking the state of tissue inflammations. The response of the sensor to different concentrations of target molecules is studied. Binding of CRP antigen molecules to the antibodies, immobilized on the gate oxide, causes the drain current increase. The NW sensor demonstrates linear response (in semi-logarithmic scale) in the drain current shift to changes in CRP concentration in the range from  $10 \text{ pg ml}^{-1}$  to  $5 \text{ ng ml}^{-1}$ . This concentration range should be used for quantitative detection of the analyte in CRP containing solutions. The concentration of CRP antigens can be estimated from the device response using Equation (4.10). The results obtained are promising for cost-efficient lab-on-a-chip monitoring of target analytes in bioliquids.

The electrical detection of human cardiac troponin I is performed using silicon nanowire array structures, patterned by electron beam lithography. The transport and noise properties of the Si NWs and the absence of leakage currents indicate the excellent performance of the Si NW FET biosensors. Attachment of the target antigen molecules effectively modulates the channel conductance and affects the normalized current noise level. The device shows linear response in the semi-logarithmic scale to changes in cTnI antigen concentrations in the range from  $0.5 \text{ ng ml}^{-1}$  to  $10 \text{ ng ml}^{-1}$ . The linear region of the dependence obtained should be used for rapid label-free electrical detection of the cTnI molecules. The unknown concentration of the analyte can be estimated from the biosensor response using the calibration curve fitting (Equation (4.11)).

Investigations of the noise spectra revealed that the addition of the cTnI antigens leads to increase of the normalized noise level. It should be emphasized that after washing the antigens off using the low-pH glycine-HCl buffer the Si NW FETs return to their initial characteristics (before introducing the antigens). This indicates the possibility of biosensor repetitive use.

# **Au NW STRUCTURES FOR SINGLE MOLECULE SENSING**

Rapid technology development leads to continuous shrinking down the sizes of active elements of electrical circuits. The ultimate downscaling demands understanding the properties of nano-sized materials and one-dimensional (1D) channels. Metallic nanowires and tunable metallic nanoconstriction devices represent a versatile platform for investigation of ultrathin 1D conductors. Moreover, metallic nanowire structures are promising candidates for the use in chemical sensing and biosensing applications since physicochemical properties of these devices change considerably upon binding of various organic and inorganic molecules. This opens prospects for investigation of metal-molecule systems, molecular layers, and even single molecules.

## **5.1 Ultrathin Au NW Structures**

Unique transport properties of ultrathin gold nanowires (Au NWs) make them highly attractive for both theoretical and experimental studies [160–168]. However, in most current technologies, the ultrathin nanowires (NWs) can only be fabricated with short lengths, and usually they are not stable [162, 166]. Therefore, they demand complex storage conditions, e.g., high vacuum, and are functional only for short periods of time. Recently, a new approach for the chemical synthesis of ultrathin Au NWs has been developed [164]. It allows fabrication of chemically stable cylindrical shape NWs with diameters around 2 nm and lengths approaching several microns. Such nanowires can be applied for studies of transport and noise properties of one-dimensional metallic conductors. Moreover, this ultrathin Au NWs are promising candidates for the role of electrical contacts between functional elements in nanoscale electronics.

The chemical synthesis procedure often requires the use of organic molecules that assist and direct the nanowire growth. As a result, these molecules can attach to the surface of NWs, and thus affect their performance. Indeed, the molecular adsorption considerably alters both the conductance and mechanical properties of the synthesized nanowires [169]. This can cause considerable challenges for the development of nanowire-based electronic devices since the existence of organic interfaces between NWs and contacts can have a strong impact on the electrical properties of the system [160].

The immense surface sensitivity of ultrathin Au NWs can be also applied for biosensing purposes [169] and for studying the junction properties of molecular layers. Thus, investigations on

electrical transport and noise characteristics of these devices are very important. The transport characterization of such Au NW structures at room [167, 168] and low [160] temperatures has already been reported. The direct current (DC) analysis provided allows thorough investigations of conduction mechanisms in the structures to be performed. However, this approach has certain limitations since it only allows investigation of the static electrical characteristics. Thus, understanding the features of the charge carrier dynamics demands using other characterization approaches.

Here, the studies on chemically-synthesized 2 nm Au NW bundles are presented. The influence of molecular interfaces on the electrical properties of the NWs is examined. The studies are performed using the low-frequency noise spectroscopy technique, – a powerful characterization approach for investigation of the dynamic processes in the nanostructures.

Analysis of the experimental data revealed that the noise spectra of the studied gold nanowire bundles contain several components: thermal, flicker and generation-recombination. The generation-recombination (GR) components are attributed to the presence of a layer of organic molecules at the nanowire/contact interface that affects the transport and noise properties of the system. The presented studies are published in [100].

### 5.1.1 Synthesis and Contacting of Ultrathin Au NWs

The chemical synthesis of the Au NWs is described in details in [160, 170]. A brief overview of the fabrication procedure is given below. Firstly, 7.4 mg AuCl is dissolved in 10 ml oleylamine and 1 ml hexane. The reaction is carried out at room temperature for 24 h. Afterward, the temperature of the reaction is increased to 80 °C and O<sub>2</sub> (99.998 % from Praxair) bubbling into the solution is performed for 6 h. The Au NWs are then precipitated by adding ~5 ml ethanol and subsequent centrifugation at 12 000 rpm for 20 min. Lastly, the supernatant is removed, and the Au NW containing precipitate is dispersed in hexane. To achieve higher yield, the centrifugation step is repeated three times. The chemicals used are purchased from Sigma-Aldrich (unless otherwise stated) and used as received without delay in time.

The electrical contacting of the synthesized nanowires is performed as follows [160]. The Au NWs are firstly dispersed in hexane and sonicated for 10 – 15 s. Then the nanowire bundles are formed by delivering ~20 µl of the sonicated solution through a microfluidic channel aligned over the metal electrodes, and subsequent drying.

The scanning electron microscopy (SEM) image of a typical fabricated Au NW structure is shown in **Figure 5.1**. The produced nanowires have an average diameter of 2 nm and a length of several micrometers.

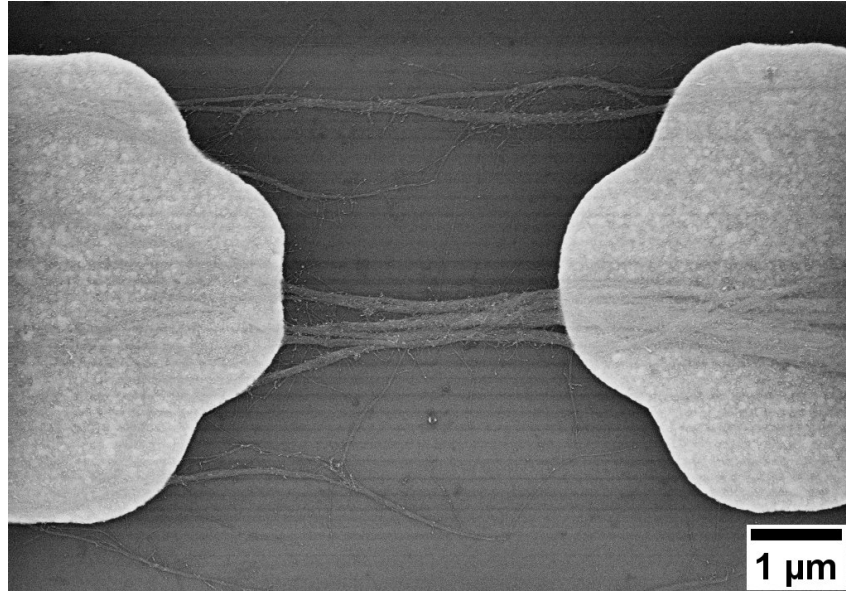


**Figure 5.1:** Scanning electron microscopy image of investigated Au NW structure.

### 5.1.2 Features of the Noise Behavior

The current-voltage curve of the studied sample is shown in **Figure 5.2** (a). It follows a linear behavior in the entire measured voltage range from 0 V to 1 V. This observation can be explained by a considerable decrease of the role of thermally-activated processes in charge transport at room temperature [160]. A typical voltage noise power spectral density dependence, measured for the Au NW structure at room temperature is shown in **Figure 5.2** (b).

The acquired noise spectra can be represented as a superposition of thermal, flicker ( $1/f$ ), and GR ( $1/f^2$ ) noise constituents. Thus, the individual noise components can be extracted from the spectra by fitting:

$$S_V(f) = \frac{A}{f} + \frac{B/F_0}{1 + (f/f_0)^2} + 4k_BTR, \quad (5.1)$$

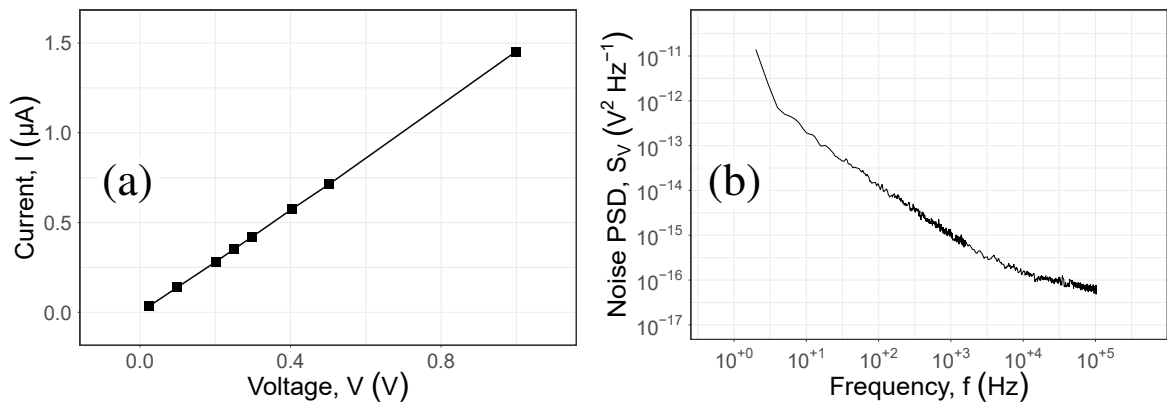


**Figure 5.2:** (a) Current-voltage (I-V) curve of investigated Au NW structure and (b) typical voltage noise spectral density dependency, measured at  $V_{DS} = 0.4$  V.

where  $f_0$  is the characteristic frequency,  $A$  is the amplitude of the flicker noise taken at 1 Hz,  $B$  is the amplitude of the  $1/f^2$  noise at low frequencies ( $f < f_0$ ),  $k_B$  is the Boltzmann constant,  $T$  is the absolute temperature, and  $R$  is the equivalent resistance, which is represented by the load resistance ( $R_{Load}$ ) connected in parallel to the Au NW resistance at AC regime. The time scale of the physical process responsible for  $1/f^2$  fluctuations is given by  $\tau_0 = 1/(2\pi f_0)$  [171].

The amplitude of the normalized current power spectral density (PSD) of the  $1/f$  noise is plotted vs. the current squared in **Figure 5.3** (a). This dependence is directly proportional,

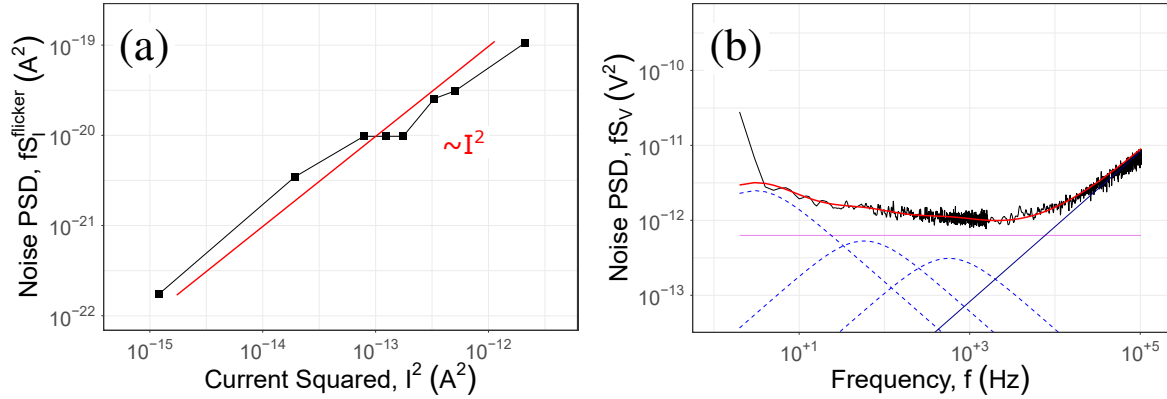


**Figure 5.3:** (a) Current PSD of the flicker noise component multiplied by frequency as a function of current squared; (b) voltage noise PSD multiplied by frequency is used for the analysis of noise components. Noise spectra of the studied Au NW structure are decomposed into different components: thermal, flicker and GR.

which indicates the ohmic behavior of the Au NW structures. Fitting of the noise spectra revealed several generation-recombination components (see **Figure 5.3** (b)). The characteristics of the Lorentzian-shaped noise components are defined by the parameters of the centers responsible for the capture-emission processes [90], and thus reflect different fluctuation properties of the studied structure [172]. It should be noted that the presence of GR components is not typical for pure gold nanowires [161, 163]. However, at least two well resolved Lorentzian-shaped noise components can be found on the measured noise spectra. The characteristic frequencies of the Lorentzians (3 Hz and 58 Hz, respectively) are independent of the drain bias, which excludes self-heating of the NWs [90]. Thus, the observed GRs can be attributed to the interaction of the layer of oleylamine, used for the growth of the nanowires and adsorbed onto their surface, with the charge carriers. Similar low-frequency noise behavior has been observed in studies of benzene-1,4-dithiol (BDT)-modified single-molecule junctions [171, 173]. As stated in these works, the  $1/f^2$  fluctuations in metal-BDT-metal junctions are caused by the dynamic reconfigurations of the molecule-to-metal coupling with the characteristic relaxation time. The dynamic processes in the studied Au NW structures may also be determined by the oleylamine organic molecules, implied in their chemical synthesis. However, contrarily to the situation considered in [171, 173], where only a single molecule was bridging the metal electrodes, here several molecules or a molecular layer can be present at the nanowire/contact interface

in different states with their characteristic relaxation times. To confirm the evidence of oleylamine molecules, the high-resolution transmission electron microscopy (HRTEM) imaging is performed. The micrograph of an ultrathin Au NW on a graphene sheet is shown in **Figure 5.4**, where the single-crystalline 2 nm thick gold nanowire and the blurred objects (marked with white arrows) associated with oleylamine molecules on the nanowire can be clearly resolved. Hence, one or two layers of oleylamine molecules can be found on the nanowire surface as a re-

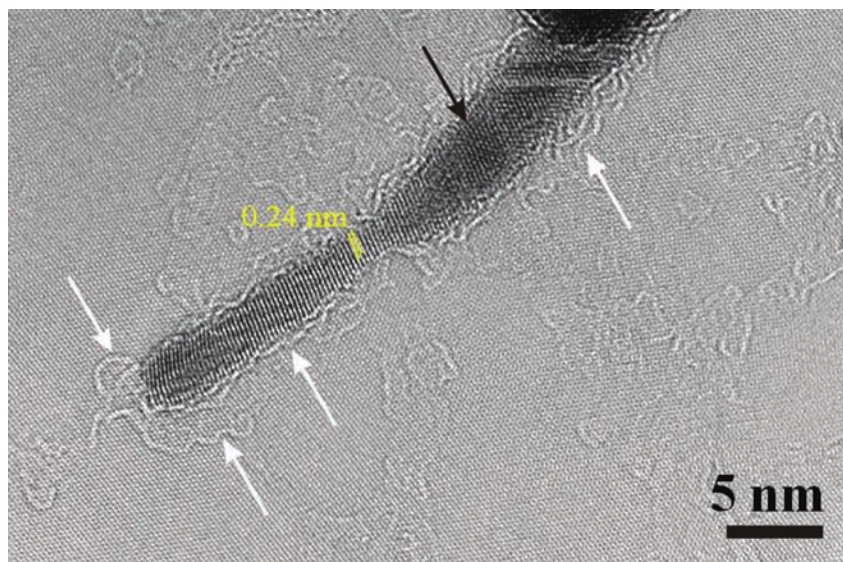


**Figure 5.4:** High-resolution transmission electron microscopy image of an ultrathin Au NW on a graphene sheet. The black arrow corresponds to the Au NW, while the white arrows indicate oleylamine molecules.

sult of the chemical synthesis [160]. These molecules form an insulating barrier at the interface between the NW and contact pads, and thus obstruct the electron transport in the system.

Oleylamine is a versatile reagent that can be used either alone or in combination with other organic and/or inorganic compounds to produce nanostructures, e.g., nanoparticles and nanowires [174, 175]. It is an amphiphilic molecule that can form channeled micellar structures and facilitate the growth of nanowires. However, the oleylamine residuals remain on the surface of the grown structures (see Figure 5.4). As a result, they are inevitably present at the Au NW/contact pad interfaces after the nanowire assembly. Moreover, in such contact systems, molecules can be found in different conformational states. Thus, the evidence of oleylamine layers affects the electrical properties of the Au NW structures, which results in the appearance of Lorentzian-shaped components in the noise spectra.

To verify the mechanism of the GR noise formation in the studied system, additional investigations of oleylamine-free and oleylamine-modified gold nanowires are performed. The test nanowire structures are fabricated without the use of oleylamine and have the diameters from 3 nm to 5 nm. The noise spectra are measured firstly on bare-gold nanowires, and then, – on those modified with oleylamine molecules. Typical normalized current noise PSD dependencies for a test NW with and without oleylamine are shown in **Figure 5.5**. In the case of a bare-gold

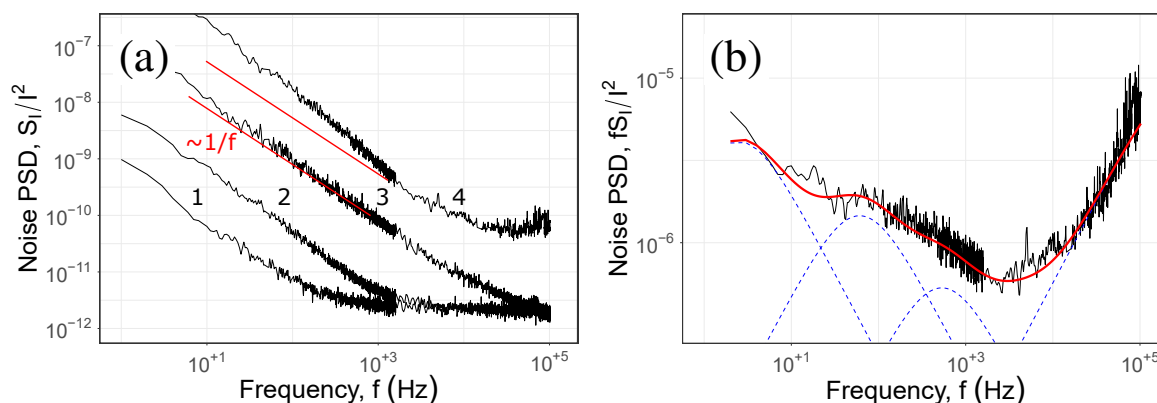


**Figure 5.5:** (a) Typical normalized current noise PSD, measured for a set of Au NWs with diameters ranging from  $\sim 3$  nm to 5 nm: (curves 1–3) correspond to bare Au NWs, reflecting only  $1/f$  excess noise component; (curve 4) corresponds to  $\sim 5$  nm diameter Au NW with oleylamine deposited on the nanowire surface, reflecting well resolved deviation from  $1/f$  behavior. (b) Normalized current noise PSD multiplied by frequency for the oleylamine-modified nanowire (curve 4 of figure (a), the flicker and thermal noise components are subtracted from the spectrum for clarity). Dashed blue lines reflect the fitting procedure by taking into account Lorentzian-shaped components. The characteristic frequencies extracted by fitting for two well resolved GR components are 2.5 Hz and 60 Hz.

NW, the noise spectra follow exclusively  $1/f$  behavior (**Figure 5.5** (a), curves 1-3). However, the sample modification with oleylamine leads to the appearance of several Lorentzian-shaped components in the noise spectra (see **Figure 5.5** (a), curve 4 and **Figure 5.5** (b)). The characteristic frequencies of the GR noise components obtained for the test samples modified with oleylamine are in good agreement with those achieved for chemically-synthesized 2 nm gold nanowires (see **Figure 5.3** (b)). Moreover, the obtained frequencies are specific and consistent. Thus, the presence of the additional GR noise components only in the noise spectra measured on oleylamine-modified samples indicates that these noise features are related to the oleylamine molecule attachments.

## 5.2 Investigations of Single (Bio)Molecules

The rapid technology development leads to continuous shrinking down the sizes of active elements of electrical circuits. Modern devices, e.g., processors, graphics cards, etc., are already working on sub-10 nm transistors. As the sizes of electronic devices continue decreasing, knowledge about the transport and noise in one-dimensional conductors and atomic-sized functional components becomes extremely important. Further downscaling will demand utilizing the atomic and molecular complexes or even single molecules in electrical circuits. Therefore, acquiring information on transport mechanisms in individual molecules and further ability to manipulate the electrical properties of molecular systems are essential for the development of

sub-nanometer functional devices. For the first time, the possibility to use a single organic molecule as an electronic device was reported by Aviram and Ratner in 1974 [176]. Designing the molecular electronics circuits demands investigations of single-molecule junctions (metal-molecule-metal systems) since they can provide valuable information about the molecule electrical performance.

Here, the results on transport and noise investigations of molecule-free and molecule-modified tunable cross-section gold nanoconstrictions are presented. Several approaches for characterization of single molecules and metal-molecule-metal systems including conductance traces measurements are presented. The low-frequency noise spectroscopy is applied as a versatile characterization tool that allows features of the electrical transport to be examined. The peculiarities of the flicker noise behavior in gold nanoconstrictions with bare surface and those modified by BDT molecules are analyzed for a broad range of sample resistances from  $10\ \Omega$  to  $10\ \text{M}\Omega$ . Thus, the noise features are studied not only in the diffusive but also in ballistic and tunneling transport regimes. Moreover, the effect of the adsorbed BDT molecular layer on the noise properties of the system is considered. The obtained results on the noise studies of molecule-free and molecule-modified tunable gold nanoconstrictions are published in [177].

### 5.2.1 Features of Transport

The studied nanojunctions are full-metal structures fabricated on the basis of flexible substrates as described in section 2.2. They contain tiny ( $< 100\ \text{nm}$  in cross-section) suspended gold nanoconstrictions in their middle part, which are electrically led to the large contact pads located at the both ends of the sample via feed lines.

A homemade PC-controlled three-point (pushing rod and two counter supports) bending setup is used for precise tuning of the cross-sections of the suspended gold nanojunctions. The attenuation factor  $\alpha$ , calculated using Equation (3.1) is  $\alpha \approx 3 \times 10^{-7}$ . Thus, adjusting the position of the pushing rod ( $\Delta Z$ ) in micrometer range allows altering the horizontal displacement ( $\Delta x$ ) with the sub-angstrom precision. Such a precise mechanical tuning allows for fine rearrangement of the gold atoms in the nanoconstriction being elongated.

At low resistances ( $R \lesssim (4G_0)^{-1}$ ,  $G_0 \simeq 77.5\ \mu\text{S}$  is the quantum conductance), narrowing the cross-section of the suspended nanoconstriction leads to a gradual increase of the sample resistance while at higher ones the abrupt resistance changes can be clearly resolved. This observation indicates the fact that only few gold atoms are connecting the bulky electrodes at higher resistances, and it can be explained by the quantum nature of the charge transport in the formed atomic-size wire. At low voltages applied this system behaves like a nanoscale conductor. Typical current-voltage curves measured on a bare-gold tunable nanoconstriction device at different values of the resistance from  $R = (50G_0)^{-1}$  to  $R = 1G_0^{-1}$  are shown in **Figure 5.6** (a). All the measured I-V curves demonstrate linear behavior, which reflects the ohmic

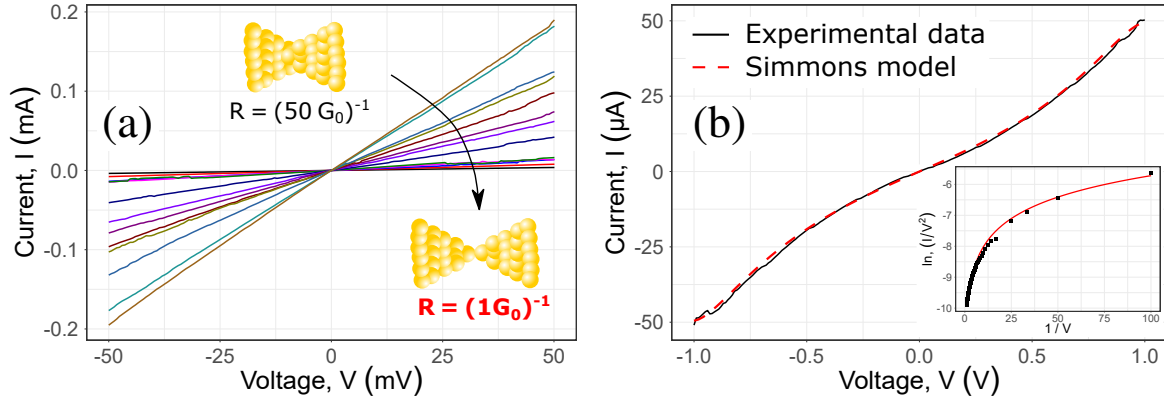


**Figure 5.6:** Current-voltage curves, measured on a bare-gold tunable nanoconstriction structure before breaking at different values of the resistance in the range (a) from  $R = (50G_0)^{-1}$  to  $R = 1G_0^{-1}$ . (b) I-V-curve, measured after the breaking of the nanoconstriction. Black curve corresponds to experimental data, and red dashed curve represents the Simmons fitting. Inset: the measured I-V-curve plotted as  $\ln(I/V^2)$  vs.  $1/V$ .

transport in the structure. After the complete breaking of the electrodes ( $R > 12.9 \text{ k}\Omega$ ) the electrical transport is governed by the quantum tunneling through a nanosized gap. The width of the gap determines the resistance of the sample in this regime. The current-voltage curves of the tunable nanoconstriction device acquired after the breaking are shown in **Figure 5.6** (b). The red dashed curve represents fitting of the data to Simmons model [178]:

$$J = \frac{e}{4\pi\hbar d^2} \left[ \left( \phi_B - \frac{eV}{2} \right) \exp \left( -\frac{2\sqrt{2m_e}}{\hbar} \alpha \sqrt{\phi_B - \frac{eV}{2}} d \right) - \left( \phi_B + \frac{eV}{2} \right) \exp \left( -\frac{2\sqrt{2m_e}}{\hbar} \alpha \sqrt{\phi_B + \frac{eV}{2}} d \right) \right]. \quad (5.2)$$

Here,  $e = 1.602 \times 10^{-19} \text{ C}$  and  $m_e = 9.11 \times 10^{-31} \text{ kg}$  are the electron charge and mass, respectively,  $\hbar = 1.05 \times 10^{-34}$  is the reduced Planck constant. The effective barrier height  $\phi_B = 9.16 \times 10^{-20} \text{ J}$  and the distance between electrodes  $d = 0.67 \text{ nm}$  are extracted by fitting the experimental data to the model. The analysis of  $\ln(I/V^2)$  vs.  $1/V$  dependence further confirms that the charge transport in the tunable nanoconstriction structure after breaking is defined by the direct tunneling mechanism.

## 5.2.2 Conductance Traces of Tunable Nanoconstrictions

A typical conductance traces (or breaking curves) measurement experiment is performed as follows. The constant voltage bias of  $0.13 \text{ V}$  is applied to the terminals of the sample, and then the conductance is measured continuously while driving the pushing rod up and down to mechanically break and form the nanocontact. Acquiring a sufficiently large number of such

curves (usually several hundreds or thousands) allows for statistical analysis to be performed. Typical conductance traces and the conductance histogram for the bare-gold nanoconstriction device are shown in **Figure 5.7** (a) and (b), respectively. The breaking curves show a clear

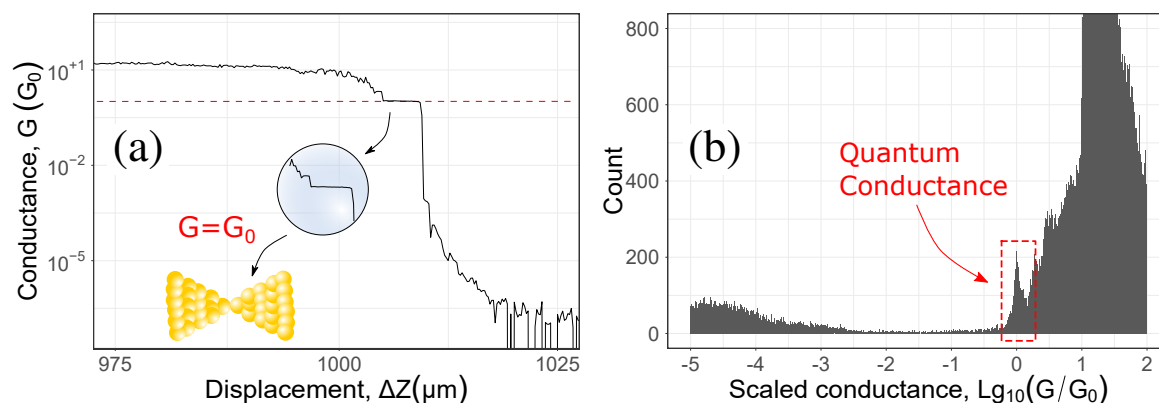


**Figure 5.7:** (a) Typical conductance trace of the bare-gold sample with tunable nanoconstriction vs. the displacement of the pushing rod and (b) conductance histogram, obtained by the conductance traces statistical analysis.

plateau at the conductance corresponding to the quantum conductance  $G_0 \simeq 77.5 \mu\text{S}$ . Several less pronounced plateaus corresponding to the multiples of  $G_0$  can also be resolved on some curves. These plateaus appear as “bumps” on the conductance histograms.

To measure electrical properties of single molecules, an appropriate chemical modification procedure must be performed. The protocol used for BDT molecules is described below. At first, the samples are cleaned by rinsing with pure ethanol for 2 min. A  $10^{-2}$  M stock solution is prepared by dissolving 7.2 mg BDT (99% GC, from Sigma Aldrich) in 5 ml ethanol. Then, 200  $\mu\text{l}$  of  $10^{-4}$  M BDT solution, obtained by dilution of the stock solution, are applied to the nanoconstriction region of the samples by drop-casting. After 2 h incubation, the samples are rinsed in ethanol for 1 min to remove the BDT residuals that did not bind gold covalently.

Typical conductance vs. displacement of the pushing rod dependence and conductance histogram, obtained for the sample modified with BDT are shown in **Figure 5.8** (a) and (b), respectively. It should be noted that the obtained results differ considerably from those achieved on bare-gold nanoconstrictions (see **Figure 5.7**). The BDT-modified samples show an extra conductance plateau around  $10^{-1} G_0$  that can be attributed to the BDT conductance. The mean molecular conductance value can be extracted by fitting the conductance histogram to Gaussian distribution. The obtained value is equal to  $G_{BDT} \approx 0.11 G_0$ , which is in good agreement with the previously reported data [179, 180].

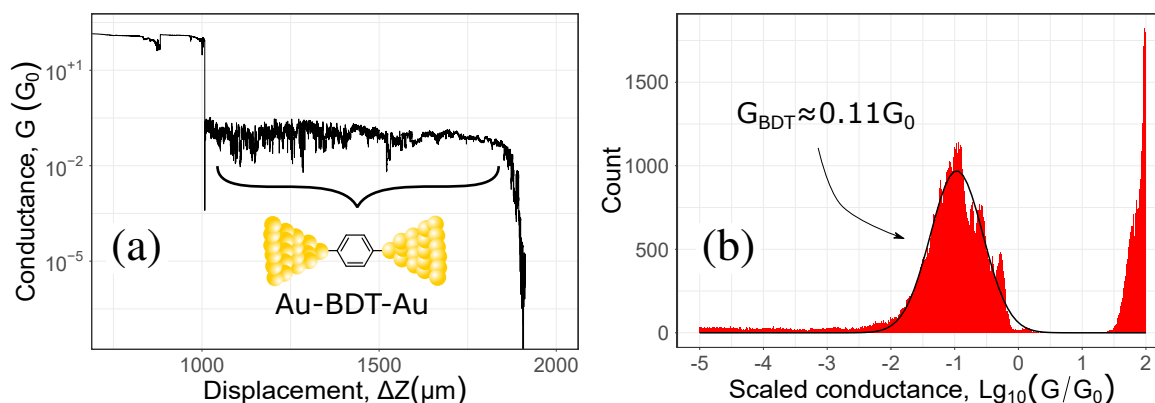


**Figure 5.8:** (a) Typical conductance change of the sample with nanoconstriction as a function of the displacement of pushing rod, and (b) conductance histogram, measured on a bare gold sample.

### 5.3 Noise Spectroscopy of Molecular Junctions

Stable electrical contacts are an essential prerequisite for the development of sub-nanometer molecular devices. Currently, the most prevalent contacting technique is anchoring the molecule of interest within a nanogap, formed by nanoscale metal electrodes. The molecule couples the electrodes with special chemical linker groups by covalent bonding. The mechanisms of electrical transport formation and low-frequency noise behavior in thin metal films and nanowires have been thoroughly investigated over the course of several decades [100, 160, 173, 181–193]. Nevertheless, electrical and noise measurements of single molecules and metal-molecule systems are still challenging.

#### 5.3.1 Peculiarities of the Flicker Noise Behavior

Studies of the noise behavior revealed that in the case of bare-gold metallic nanoconstrictions the normalized flicker noise power spectral density demonstrates a power dependence on the resistance [173]:

$$\frac{S_I}{I^2} \propto R^m. \quad (5.3)$$

Here,  $S_I$  denotes the current noise PSD, and  $m$  is the exponent. It was shown that the magnitude of the exponent  $m$  equals 3 at low sample resistances (diffusive regime), and it was estimated as  $m = 1.5$  at higher resistances (assumed as ballistic regime) [173].

Understanding the charge transport and noise of molecular systems determines the scope of their practical use and future perspectives in molecular electronics applications. The electrical properties of nanosized metallic structures and nanoconstrictions are extremely sensitive to the surface adsorbates. Thus, investigations of molecule-free and molecule-modified metallic nano-

junctions in different transport regimes can provide valuable information for the development of nanoscale functional devices with tailored properties.

The flicker noise behavior of the tunable bare-gold and BDT-modified nanoconstrictions in diffusive, ballistic, and tunneling transport regimes is analyzed and discussed below.

### Noise measurements

The electrical transport and noise measurements are performed at room temperature (297 K) under high vacuum ( $10^{-6}$  mbar) in an electrically shielded environment. The low-frequency noise spectra are measured in the low-bias regime the constant voltage  $V = 20$  mV applied. The presented measurements are repeated on 10 tunable nanoconstriction devices to ensure the high results accuracy. All the studied BDT-modified samples show a molecular conductance peak at  $G_{BDT} = 0.11 G_0$  (see **Figure 5.8**). The BDT-modified samples demonstrate approximately 6 times lower normalized flicker noise level than the bare ones at resistances in the range from  $(4G_0)^{-1}$  to  $G_0^{-1}$ . It should be noted that the parasitic capacitance of the cable connection is  $C = 300$  pF, which results in the minimal cut-off frequency  $f_{cutoff} = 106$  kHz in the configuration of our setup [100]. The  $f_{cutoff}$  value lies outside the investigated frequency range (from 10 Hz to 1 kHz). Accordingly, the parasitic capacitance does not affect the measurement results. Furthermore, the cut-off correction and subtraction of the thermal noise component are performed on the measured noise spectra before the analysis.

The noise spectroscopy technique is used to characterize the nanoconstriction transport properties in different regimes. The noise spectra are measured for a wide range of sample resistances (from  $10 \Omega$  to  $10 M\Omega$ ) including regions before and after the mechanical breaking of the constriction. Tuning the resistance of the system by shrinking the nanoconstriction's cross-section causes changes in the nature of its dominant transport mechanism from diffusive at low resistances, ballistic at intermediate ones, followed by quantum tunneling in the case of a broken nanoconstriction. The sample resistance is stabilized before every noise spectra measurement using the PC-controlled feedback loop, developed in house.

The conductance and noise measurements are performed on bare tunable gold nanoconstrictions and on those modified with BDT molecules. Typical noise spectra are shown in **Figure 5.9**. The  $1/f$  flicker noise is the dominant excess noise component in the entire range of investigated sample resistances. The normalized current noise PSD level (taken at the frequency of 100 Hz) is plotted vs. the system resistance in **Figure 5.10**. Black points correspond to the data measured on bare gold nanoconstriction devices, red points reflect the data corresponding to the BDT-modified nanoconstrictions. Narrowing of the nanoconstriction due to the bending process leads to the growth of its resistance and to the increase in the relative flicker noise level, which can be described by Equation (5.3). The exponent has the value  $m = 2$  at low resistances ( $R < 300 \Omega - R \approx 3 \text{ k}\Omega$ ), and it decreases with the further resistance increase. This effect can be

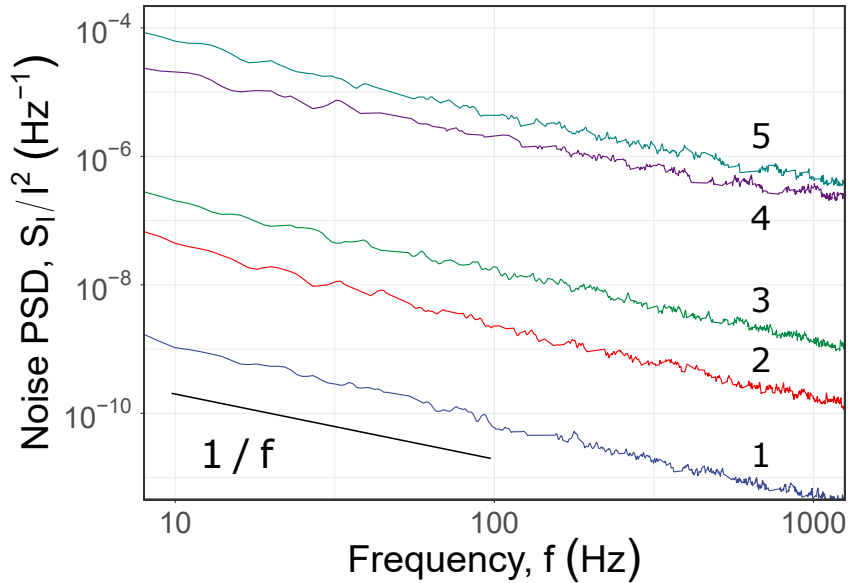


**Figure 5.9:** Normalized current noise PSD vs. frequency dependencies measured before (1–3) and after (4, 5) the breaking of a bare-gold nanoconstriction. The presented spectra correspond to the following values of the resistance  $R$ : 1- 360  $\Omega$ ; 2- 770  $\Omega$ ; 3- 2.02 k $\Omega$ ; 4- 223.00 k $\Omega$ ; 5- 642.6 k $\Omega$ , respectively.

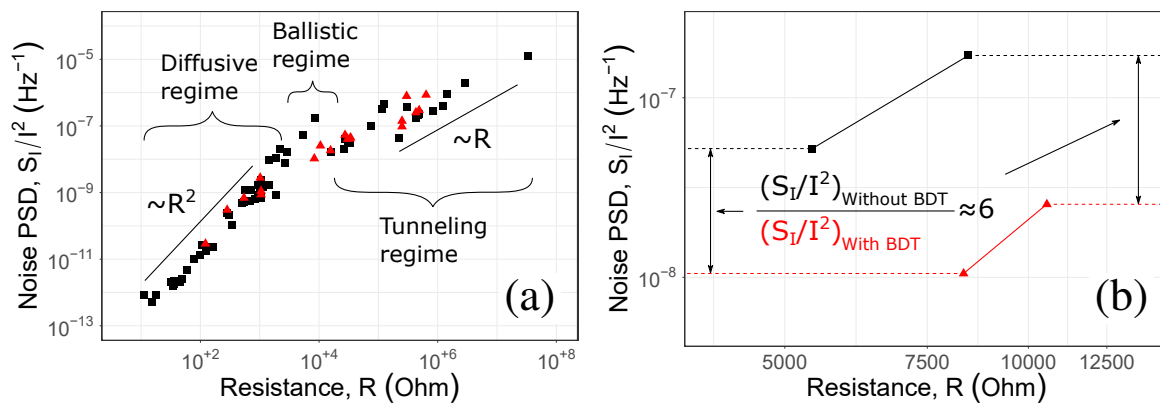


**Figure 5.10:** (a) Normalized flicker noise PSD, taken at 100 Hz vs. the nanoconstriction resistance. Black squares show the data obtained for a bare nanojunction, red triangles correspond to the case of the presence of BDT molecules. (b) Enlarged section of the transition from diffusive to tunneling regime, including ballistic region.

attributed to the changes in transport properties of the sample due to shrinking the characteristic size of the nanoconstriction down to the mean free path of charge carriers ( $\lambda_e \approx 4$  nm in gold at room temperature [194]).

### Noise behavior in the diffusive regime

At low resistances and moderate voltages applied, the diffusive regime determines the charge transport in the studied nanoconstriction devices. The flicker (or  $1/f$ ) noise results from the conductivity fluctuations. For the resistance and noise calculations our system is considered as a variable resistor, in which the resistance can be altered by tuning the cross-section of the nanoconstriction. The 2D case is considered for simplicity of the mathematical calculations. The power dissipation induced by the current flow can be determined using the following equations:

$$\begin{aligned} RI^2 &= \int_{Area} R_{sh} J^2 dA; \\ GV^2 &= \int_{Area} \frac{E^2 dA}{R_{sh}}. \end{aligned} \quad (5.4)$$

Here,  $R_{sh}$  [ $\Omega$ ] is the sheet resistance,  $J$ , [ $A\ cm^{-1}$ ] is the current density,  $G$  [S] is the conductance,  $E$  [ $V\ cm^{-1}$ ] is the electric field strength, and  $dA$  [ $cm^2$ ] is the elementary area. Power spectral density of the flicker noise is proportional to  $\int J^4$  [195–200]:

$$S_R = \frac{C_{us} R_{sh}^2}{f I^4} \int_{Area} J^4 dA, \quad (5.5)$$

where  $C_{us}$  [ $cm^2$ ] is the  $1/f$  noise parameter. The ratio  $C_{us}/R_{sh} \approx 5 \times 10^{-21}$  for uniform gold layers or poly-silicon [200]. The integrals in 2D can be calculated using different numerical approaches such as solving finite-difference equations [201, 202] and conformal mapping [203, 204]. Yet, an analytical approach has more advantages, e.g., it allows evaluation of some important parameters of the system by fitting the experimental data to the model.

Typical SEM micrograph of the sample top view is shown in **Figure 5.11** (a), and its schematic image – in **Figure 5.11** (b). Since elongation of the gold occurs only in the narrowest region of the tunable nanoconstriction, calculations of the resistance and noise can be performed independently for two parts of the system:

- trapezoidal access part, which does not change during the tuning process;
- tunable inner part (narrow neck).

At first, the model of trapezoidal access parts is discussed.

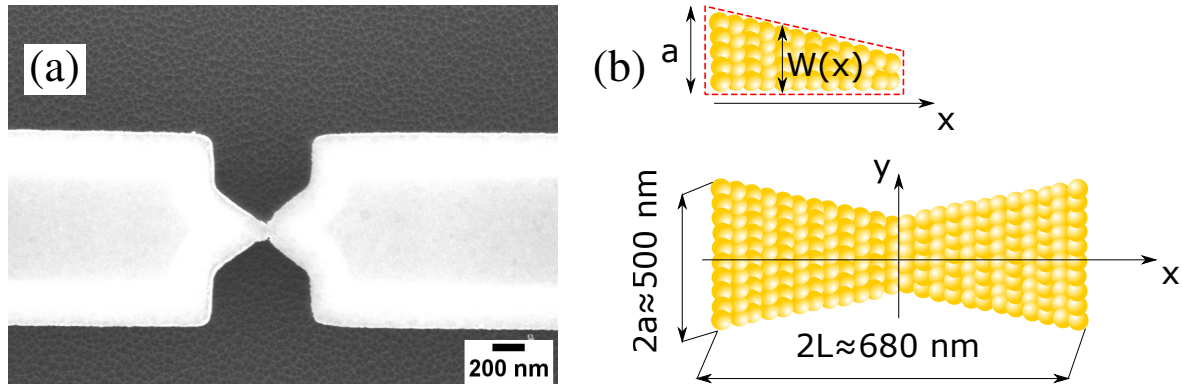


**Figure 5.11:** (a) Typical SEM micrograph of the top view of the sample. (b) Schematic of the access part. Top: Geometrical model of the trapezoidal access part to the narrow neck as a quarter of the complete access part for the calculations of resistance and noise. Bottom: Trapezoidal access parts with the dimensions shown in the figure, without the narrow neck part.

*The resistance and noise estimation of the access parts:* To estimate the resistance and flicker noise level of the trapezoidal access parts, a technique based on approximated equipotentials is used. This method has certain benefits because it allows partial cancellation of the  $R$  and  $S_R$  calculation errors [195].

The equipotentials are considered as straight lines perpendicular to the  $x$ -axis (shown as thick lines in **Figure 5.11** (b)). In the context of the suggested model, the resistance and noise of the access parts are assumed to remain constant while tuning the nanoconstriction since their geometry does not change during the bending process. As shown in **Figure 5.11** (b), the access part has sizes along the  $x$  and  $y$  axes  $2L$  and  $2a$ , respectively. The studied system is symmetrical along both axes. Thus, for ease of calculations, the resistance  $R$  and noise  $S_R$  are firstly estimated for a quarter part (see **Figure 5.11** (b), on the top). The total access resistance  $R_{\otimes}$  and noise  $S_{R_{\otimes}}$  are calculated by the proper addition of four equally contributing parts, two of which are connected in series and two – in parallel.

The change of the  $W$  of the access part along the  $x$ -axis can be described as follows:

$$W(x) = -\frac{a-b}{L}x + a. \quad (5.6)$$

The current density at the point  $x$  can be written as:

$$J(x) = \frac{I}{W}(x) = I / (x(-(a-b)/L) + a).$$

The resistance of a quarter access part of the nanoconstriction can be estimated using Equation (5.4):

$$R = R_{sh} \frac{L}{a-b} \ln \frac{a}{b} \quad (5.7)$$

The expressions for the resistance noise and relative resistance noise can be obtained using

Equations (5.5, 5.7):

$$S_R = \frac{C_{us} R_{sh}^2 L}{2f} \frac{(a/b)^2 - 1}{a^2 (a-b)}, \quad (5.8)$$

$$\frac{S_R}{R^2} = \frac{C_{us}}{2f} \frac{a-b}{La^2} \frac{(a/b)^2 - 1}{(\ln a/b)^2}.$$

The resistance  $R_{\otimes}$ , resistance noise  $S_{R_{\otimes}}$  and relative noise  $S_{R_{\otimes}}/R_{\otimes}$  of the complete access part can therefore be described by following expressions:

$$R_{\otimes} = 2R/2 = R = R_{sh} \frac{L}{a-b} \ln \frac{a}{b} \quad (5.9)$$

$$S_{R_{\otimes}} = \frac{1}{4} S_R \Rightarrow S_{R_{\otimes}} = \frac{1}{4} \frac{C_{us} R_{sh}^2 L}{2f} \frac{(a/b)^2 - 1}{a^2 (a-b)} \quad (5.10)$$

$$\frac{S_{R_{\otimes}}}{R_{\otimes}^2} = \frac{1}{4} \frac{S_R}{R^2} \Rightarrow \frac{S_{R_{\otimes}}}{R_{\otimes}^2} = \frac{C_{us}}{8f} \frac{a-b}{La^2} \frac{(a/b)^2 - 1}{(\ln a/b)^2} \quad (5.11)$$

The value of the relative noise level of the access parts can be estimated using Equation (5.11) and taking into account parameters of the real sample:  $S_R/R^2|_{access} \approx 2 \times 10^{-14}$  at 100 Hz.

*Resistance and noise estimation of the narrow neck:* Elongation of the narrow neck due to the sample bending results in its plastic deformation and subsequent breakage. Resistance and noise estimations are based on the current crowding due to shrinking of the cross-section of the nanoconstriction, treated as a bending sector (see **Figure 5.12** with  $2b = W$ , the characteristic radius  $r_1$  a small fraction of  $W$ :  $r_1 = pW$ ;  $p \ll 1$  and  $r_2 = r_1 + W_{eff} \Rightarrow r_2/r_1 = 1 + W_{eff}/pW$ ). Width and length of the tunable inner part before deformation are equal to  $W = 2b$ .

The analytical solution for the resistance and noise is based on approximated current lines around the trim-cut, caused by damage as shown in **Figure 5.12**. Since the narrow neck is the sample's tiniest part, it is the region of the increased electrical field, which is the highest for the radius  $r$  close to the smallest rounding-off radius  $r_1$ . The biggest radius of the sector is equal to  $r_2 = r_1 + W_{eff}$  and hence,  $r_2/r_1 = 1 + W_{eff}/r_1$ . The electrical field strength and current

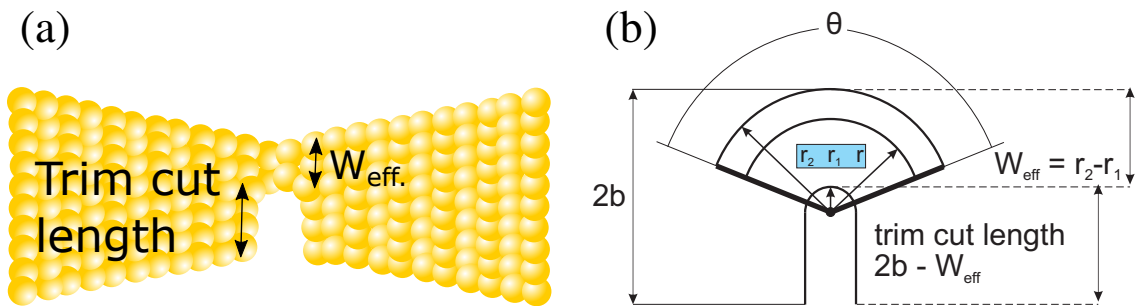


**Figure 5.12:** Sketch of the damaged nanoconstriction (a) and bending sector around the trim-cut (b), caused by the damage, showing the circular current lines between radii  $r_1$  and  $r_2$ . The bending of current lines due to a trim-cut is shown over an angle  $\theta < \pi$ . Assumed equipotentials are drawn as thick lines.

density within the sector with radii  $r$  and  $r + dr$  equal the voltage drop  $V$  over the assumed equipotential lines:  $E(r) = V/(\theta r)$  and  $J(r) = V/(R_{sh}r\theta)$  [204]. Calculations, performed using Equations (5.4) and (5.5), give following results for the resistance and resistance noise:

$$R = \frac{\theta R_{sh}}{\ln(1 + W_{eff}/r_1)} \quad (5.12)$$

$$S_R = \frac{R_{sh}^2 C_{us} \theta}{2f \left( \ln \left( 1 + \frac{W_{eff}}{r_1} \right) \right)^4} \left[ \frac{1}{r_1^2} \right] \left[ \frac{\left( \frac{W_{eff}}{r_1} \right)^2 + 2 \frac{W_{eff}}{r_1}}{\left( \frac{W_{eff}}{r_1} + 1 \right)^2} \right] \propto R^4 \text{ for } \frac{r_1}{W_{eff} + r_1} < 1 \quad (5.13)$$

To find the dependence of the relative current noise level on the system resistance, we use the general relation between relative values of current and resistance noise levels [90]:

$$\frac{S_I}{I^2} = \frac{S_R}{R^2} \quad (5.14)$$

Using Equations (5.13, 5.14), the following expression for the relative current noise can be obtained:

$$\begin{aligned} \frac{S_I}{I^2} = \frac{S_R}{R^2} &= \frac{C_{us}}{2\theta f \left( \ln \left( 1 + \frac{W_{eff}}{r_1} \right) \right)^2} \left[ \frac{1}{r_1^2} \right] \left[ \frac{\left( \frac{W_{eff}}{r_1} \right)^2 + 2 \frac{W_{eff}}{r_1}}{\left( \frac{W_{eff}}{r_1} + 1 \right)^2} \right] \Rightarrow \\ &\Rightarrow \frac{S_I}{I^2} \propto \begin{cases} R^2, & \text{for } \frac{r_1}{W_{eff} + r_1} < 1 \\ R, & \text{for } \frac{W_{eff} + r_1}{r_1} \downarrow 1 \end{cases} \end{aligned} \quad (5.15)$$

As can be seen from Equation (5.15), there are two cases of the relative flicker noise level scaling with the sample resistance depending on the relation between the values of  $r_1$  and  $W_{eff}$ .

### Noise in the Ballistic Regime

Shrinking down the characteristic sizes of the nanoconstriction to the mean free path of electrons  $\lambda_e$  or below leads to changes in the nature of the electrical transport in the system. At this stage no scattering events occur in the narrow neck part of the nanojunction in a passage. At resistances corresponding to the ballistic regime only a few gold atoms are connecting two bulky electrodes. Thus, the resistance of the system is mostly determined by the quantum resistance of the interconnecting atoms, forming a wire.

*Model for bare-gold nanoconstrictions:* The proposed model is based on the assumption that elongation of the suspended nanojunction in its narrowest part due to the bending causes a rearrangement of gold atoms keeping constant the area of the nanoconstriction  $A_{constr.} = c \times d = \text{const}$  (see **Figure 5.13**). The resistance of the sample in the ballistic conductance regime

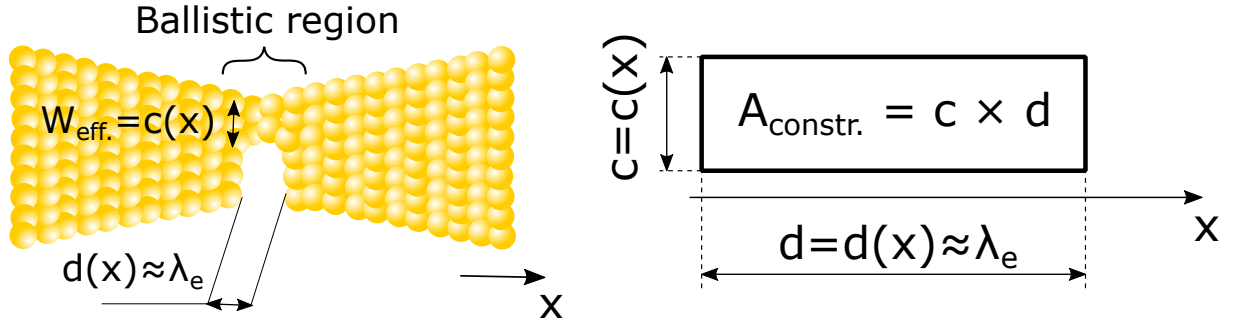


**Figure 5.13:** Schematic representations of the nanoconstriction's inner part in the ballistic regime of conductance.

is determined by the Sharvin resistance:

$$R_S = \frac{4\rho\lambda_e}{3\pi r_c^2}, \quad (5.16)$$

where  $\rho$  is the resistivity of the sample material, and  $r_c = c/2$  is the ballistic contact radius. The resistivity can be written as  $\rho = m_e v_F / (n e^2 \lambda_e)$  [205], where  $m_e$  is the electron mass,  $v_F$  is the Fermi velocity,  $n$  is the free electron density and  $e$  is the electron charge. Therefore, from Equation (5.16) we can obtain following expression for the resistance:

$$R_S = \frac{(4m_e v_F / 3\pi n e^2)}{r_c^2} = \frac{C_1}{r_c^2}, \quad (5.17)$$

where constant  $C_1 = 3.58 \times 10^{-16} \Omega \text{ m}^2$  for gold [205].

Dimensions of the narrow neck part (width  $c$  and length  $d$ ) are changing during the bending process. Accordingly, they depend on the current value of the displacement between the electrodes  $x$ :

$$\begin{aligned} d &= f(x) = d_0 + x \\ c &= f(x) = A_{constr.}/d(x) \end{aligned} \quad (5.18)$$

Thus, the resistance of the constriction is defined by the following expression:

$$R_S = \frac{4C_1}{c^2(x)} = \frac{d^2(x) 4C_1}{A_{constr.}^2} \Rightarrow d = \sqrt{A_{constr.}^2 \frac{R_S}{4C_1}}. \quad (5.19)$$

The flicker noise level and its dependence on the sample resistance can be estimated using the Hooge formula:

$$S_I = \frac{\alpha_H e I}{\tau f}, \quad (5.20)$$

where  $S_I$  is the current noise spectral density,  $\alpha_H$  is the dimensionless Hooge parameter, and  $\tau$  is the characteristic time. In the context of our model,  $\tau$  signifies the time that electron spends for passing the distance between bulky electrodes separated by the ballistic region. In the quasi-

ballistic regime, the velocity of electrons is determined by the thermal velocity:

$$\nu_T = \sqrt{\frac{kT}{m_e}}, \quad (5.21)$$

where  $\nu_T$  is the thermal velocity of electrons,  $k$  is the Boltzmann constant,  $T$  is the temperature, and  $m_e$  is the electron mass. Electrons motion from one electrode to another under the influence of the electric field can be described by the following equation:

$$x(t) = x_0 + \nu_0 t + \frac{a_e t^2}{2}, \quad (5.22)$$

where  $x_0 = 0$  is the initial position of an electron,  $\nu_0 = \nu_T$  is the speed of the electron at its initial position, and  $a_e$  is its acceleration in electric field. In experiments carried out, a constant voltage is applied to the sample:

$$V = U_0; I = U_0/R. \quad (5.23)$$

Thus, the formula for the acceleration  $a_e$  can be deduced using the expression for the electric force and Newton's law as follows:

$$\begin{aligned} F = eE, E = U_0/d \Rightarrow a_e = \frac{F}{m_e} = \frac{eU_0}{m_e d} \\ F = m_e a_e \end{aligned} \quad (5.24)$$

By solving Equation (5.22), considering that  $x(t = \tau) = d$  we can obtain the expression for  $\tau$ :

$$\tau = d \frac{m_e}{eU_0} \left( \sqrt{\nu_T^2 + 2eU_0/m_e} - \nu_T \right) = C \cdot d; C = \frac{m_e}{eU_0} \left( \sqrt{\nu_T^2 + 2eU_0/m_e} - \nu_T \right). \quad (5.25)$$

The equation for the current noise spectral density can be obtained from Equations (5.20), (5.23) and (5.25):

$$S_I = \frac{1}{f} \frac{2\alpha_H e U_0}{A_{constr.} C \sqrt{1/C_1}} R_S^{-3/2} \sim R_S^{-3/2} \quad (5.26)$$

The expression for the relative current noise can be deduced using Equations (5.23) and (5.26):

$$\frac{S_I}{I^2} = \frac{1}{f} \frac{2\alpha_H e}{A_{constr.} C \sqrt{1/C_1} U_0} R_S^{-1/2} \sim \sqrt{R_S}. \quad (5.27)$$

Therefore, accordingly to our model, the ballistic transport regime can be characterized by the square root dependence of the normalized current noise PSD on the junction resistance. The experimental results are in good agreement with theoretically predicted dependencies described by Equation (5.27). Thus, the flicker noise dependencies can be utilized as the characteristic features confirming the evidence of the ballistic transport in the system.

*Model considering the influence of molecular layer on noise properties of the system:* The conductance of metallic nanostructures usually consists of the bulk conductance and surface conductance components. For very thin metal films and nanowires the impact of the surface conductance is significantly increased. Therefore, the total conductance of the nanoconstriction can be strongly modified by organic adsorbates, i.e., the layer of molecules deposited onto the metal nanoconstriction can influence the transport and noise properties of the system:

$$\begin{aligned} G &= G_{bulk} + G_{surface}; \quad G_{surface} \propto A_{eff}. \\ S_G &= S_{G_{bulk}} + S_{G_{surface}} \end{aligned} \quad (5.28)$$

Here,  $G_{bulk}$  denotes the bulk gold conductance,  $G_{surface}$  is the surface conductance of gold modified by a molecular layer, and  $A_{eff}$  is the effective area of a molecular layer influencing the conductance of the system. Normalized current noise level in this case is defined by:

$$\frac{S_I}{I^2} = \frac{S_G}{G^2} = \frac{S_R}{R^2} = \frac{S_{G_{bulk}} + S_{G_{surface}}}{(G_{bulk} + G_{surface})^2} \quad (5.29)$$

At low resistance values  $G_{surface} \leq G_{bulk} \Leftrightarrow S_{G_{surface}} \leq S_{G_{bulk}}$ , i.e., molecular layer has no considerable impact on the noise behavior of the system  $S_I/I^2 \approx S_{G_{bulk}}/G_{bulk}^2 \sim R^m$ . This case is already described above. At higher values of the resistance, before the nanoconstriction breaks,  $G_{surface} \geq G_{bulk} \Leftrightarrow S_{G_{surface}} \geq S_{G_{bulk}}$ , and therefore:

$$\frac{S_I}{I^2} \approx \frac{S_{G_{layer}}}{G_{layer}^2} \propto \frac{1}{A_{eff}} \propto R \quad (5.30)$$

Thus, the change in the flicker noise behavior from  $S_I/I^2 \sim R^2$  to  $S_I/I^2 \sim R$  at the resistances corresponding to the ballistic transport regime can indicate the presence of molecular layers in tunable metallic nanoconstrictions.

### Noise Behavior in the Tunneling Regime

Further bending of the system can lead to the complete electrode separation (electrodes are not connected neither by gold atoms nor by BDT molecules). In this case, the electrical current in the system is determined by the tunneling processes through a nanoscale gap. Thus, the source of the flicker noise in this system can be associated with the scattering processes of the tunneling electrons on the bulky electrodes.

Since after the breaking the deposited molecules do not affect the charge transport mechanisms of the system, the bare and BDT-modified samples show the same normalized flicker noise level (see **Figure 5.10**). To model the relative noise behavior in the tunneling regime, a similar approach as in calculations for the ballistic regime is used. Hooge formula for the flicker noise and the  $\tau$  vs.  $R$  dependence are used to determine the relative noise level. Solving the

Equation (5.22) and taking the initial velocity  $v_0 = 0$  we can obtain for  $\tau$ :

$$\tau = d\sqrt{\frac{2m_e}{eU_0}}, \quad (5.31)$$

where  $\tau$  is the time that electron spends to pass the distance between the bulky electrodes separated by a nanogap, and  $d$  is the width of the nanogap.

The electric current exponentially decays with the distance between electrodes in the tunneling regime [206]:

$$I_{DT} \sim A_{emitter}e^{-\beta d}, \quad (5.32)$$

where  $\beta = 2\sqrt{2m_e\Phi}/\hbar$  is the constant that depends on the metal work function, and  $A_{emitter}$  is the effective electrode emitting area.

Since only the constant voltage  $V = U_0$  is applied to the sample, the resistance of the system can be estimated using the Ohm's law:

$$R = \frac{V}{I} = \frac{U_0}{I} \sim \frac{1}{A_{emitter}}U_0e^{\beta d}. \quad (5.33)$$

Solving Equation (5.33) for  $d$  gives:

$$d \sim \left(\ln \frac{R}{U_0}\right) / \beta \sqrt{\frac{2m_e}{eU_0}} \quad (5.34)$$

The expression for the flicker noise level can be obtained considering Equation (5.20):

$$\frac{S_I}{I^2} = \frac{1}{f} \frac{\alpha_H e \beta A_{emitter}}{U_0 \sqrt{2m_e/eU_0}} \frac{R}{\ln R/U_0} \sim \frac{1}{f} \frac{R}{\ln R} \quad (5.35)$$

Thus, the flicker noise power has a weaker dependence on the resistance ( $S_I/I^2 \sim R/\ln(R)$ ) in the tunneling regime of sample conductance in comparison to diffusive regime.

### Comparison of Model and Experiment for Different Transport Regimes

The measured noise data and corresponding fitting to the developed models are shown in **Figure 5.14**. Data, obtained on the bare-gold and BDT-modified samples are shown as the black squares and red triangles, respectively. Colored dashed lines represent fitting of the data to the developed models for different transport regimes. The parameters of the models are described below.

The noise behavior of the system in diffusive regime ( $R \leq 300 \Omega$ , **Figure 5.14**, black curve) is simulated using Equations (5.12) and (5.15) with  $\theta = 160^\circ$ ,  $r_1 = 3 \text{ nm}$ ,  $0.5 \leq W_{eff}/r_1 \leq 500$ ,  $R_{sh} = 40 \Omega$ , and  $C_{us}/f = 10^{-7} \text{ nm}^2 \text{ Hz}^{-1}$ . The normalized current noise of the access parts ( $\approx 2 \times 10^{-14}$  at 100 Hz) is much lower than the noise, of the tunable narrow neck, and thus

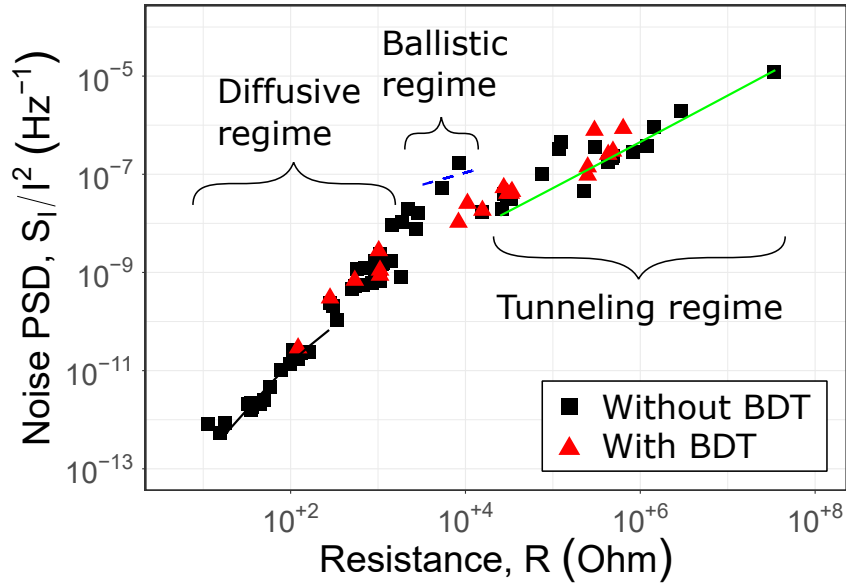


**Figure 5.14:** Comparison of experimental data from **Figure 5.10** with theoretical dependencies obtained for different transport regimes. Black curve represents calculated data for the diffusive transport regime, blue one – for the ballistic transport regime, respectively. Green curve represents the results of simulations for the tunneling regime using the expression for tunneling transport.

it can be neglected. Fitting of the spectra allows determination of the angle  $\theta$  and the effective width of the nanoconstriction  $W_{eff}$ . The developed model based on changing of the normalized flicker noise level due to the geometry change of the narrow neck describes noise behavior well in the defined resistance range.

With further resistance increase ( $R \geq 300 \Omega$ ), the nanoconstriction shrinks in its dimensions rapidly, and eventually, a ballistic or even a one-dimensional quantum channel could be formed. This leads to a formation of a transitional region where both the diffusive and ballistic transport mechanisms contribute to the charge transfer processes.

Fitting of the normalized noise level in the ballistic transport regime is plotted in blue for the resistance range from  $R = (4G_0)^{-1}$  to  $R = G_0^{-1}$ . The suggested model allows estimation of the dimensionless Hooke parameter  $\alpha_H$  and the effective area of nanoconstriction that demonstrates ballistic properties. The corresponding values of  $\alpha_H = 2.5 \times 10^{-5}$  and  $A_{constr.} = 2 \text{ nm}^2$  are extracted from the measured noise spectra by fitting. It should be noted that the obtained results are in good accordance with physical considerations about the system and reported literature [194, 207]. Presence of organic molecules on the sample surface leads to the decrease in the normalized flicker noise level. This phenomenon can be quantitatively characterized by the effective area  $A_{eff}$ . (see Equation (5.30)) of the molecular layer that contributes to the total system conductance.

Computations for the normalized flicker noise level in tunneling regime ( $R = 25 \text{ k}\Omega - 10 \text{ M}\Omega$ ) are shown as green curve in **Figure 5.14**. Fitting of the experimental data allows estimation of

the effective barrier height  $\Phi$  and/or the effective electron emitting area ( $A_{emitter} \approx 20 \text{ nm}^2$ ).

**Table 5.1:** Characteristic dependencies of the flicker noise in studied tunable nanoconstrictions.

Dominant transport regime	Approximate resistance range, [ $\Omega$ ]	Characteristic flicker noise behavior	Model parameters	
Diffusive	$\leq 300$	$S_I/I^2 \sim R^2$	$W_{eff.}$	Effective width of the nanoconstriction
			$\theta$	Angle characterizing current crowding in the nanoconstriction
Ballistic (BR1)	3000 – 12900	$S_I/I^2 \sim \sqrt{R}$	$\alpha_H$	Dimensionless Hooge parameter
			$A_{constr.}$	Effective ballistic area of the nanoconstriction
Ballistic (BR2)	3000 – 12900	$S_I/I^2 \sim R$ , lower amplitude than in BR1 case	$A_{eff.}$	Effective area of molecular layer covering the ballistic nanoconstriction
Tunneling	$> 12900$	$S_I/I^2 \sim \ln(R)/R$	$\Phi$	Effective barrier height
			$A_{emitter}$	Effective electron emitting area

## 5.4 Summary

Studies are performed on the ultrathin gold nanowire structures and tunable gold nanoconstrictions. Bundles of ultrathin gold nanowires (2 nm in diameter) are chemically synthesized and subsequently assembled onto electrodes. The fabricated devices are characterized using I-V measurements and noise spectroscopy. The measured I-V curves demonstrate quasi-linear behavior, and the flicker noise power spectral density is proportional to the current squared, which indicates ohmic behavior in Au NW structures. In addition to the flicker noise, several GR noise components with characteristic frequencies of  $f_1 = 2.5 \text{ Hz}$  and  $f_2 = 60 \text{ Hz}$  are revealed in the noise spectra. They are attributed to the result of the participation of the oleylamine molecules adsorbed on the NW surface in transport phenomena. The presence of organic molecules at the NW surface is confirmed by high-resolution transmission electron microscopy imaging. The

adsorbed molecules play an important role in the charge transport, and therefore they considerably affect the electrical and noise properties of the Au NWs.

Tunable cross-section nanoconstriction devices are fabricated on the basis of flexible substrates using cleanroom technology. Transport and noise properties of the fabricated devices are studied using the low-frequency noise spectroscopy technique. Normalized current noise power spectral density dependencies are measured and analyzed for a wide range of sample resistances from  $R = 10 \Omega$  to  $R = 10 \text{ M}\Omega$ . The features and physical background of the flicker noise behavior in the low-bias regime are investigated. Modification of the sample surface with benzene-1,4-dithiol molecules results in a decrease of the normalized flicker noise PSD level in the ballistic regime of the sample conductance. Furthermore, the characteristic power dependence of the normalized noise PSD as a function of the system resistance is revealed. Models describing the flicker noise behavior for bare-gold and BDT-modified samples are developed and compared with the experimental data for the diffusive, ballistic, and tunneling transport regimes. The obtained analytical dependencies for the flicker noise level are summarized in **Table 5.1**. Parameters extracted by fitting of experimental data to the models are used for the characterization of nanoconstriction devices.



## CONCLUSIONS AND OUTLOOK

This thesis is devoted to the development of nanowire-based nanosensors for the detection of biochemical species. It describes the optimization of the nanofabrication technology, electrical and noise characterization of the fabricated single silicon nanowire (Si NW) field-effect transistor (FET) devices, finding their optimal operation regimes, and optimization of the devices for *in vitro* sensing of biochemical species. The nanoimprint technology is chosen as the alternative to electron beam lithography (EBL) patterning technique to reduce the fabrication costs of the sensors. The high quality of the fabricated Si NW structures is confirmed by the atomic force microscopy (AFM), scanning electron microscopy (SEM), and focused ion beam (FIB) imaging. The devices can be operated using the front liquid gate and the back-gate electrodes. They show typical transistor-type behavior of electrical characteristics and stable operation in electrolyte liquid environments without leakage currents. The device performance parameters including threshold voltage  $V_{Th} \simeq 0.8$  V, subthreshold swing  $SS \simeq 130$  mV dec<sup>-1</sup>, and carrier mobility  $\mu = 95$  cm<sup>2</sup> V<sup>-1</sup> s<sup>-1</sup> are extracted from the transfer curves analysis. The values obtained reflect the high quality of Si NW FETs. Noise spectroscopy analysis revealed that the excess noise is caused by the mobility fluctuations of the charge carriers in the NW channel. The calculated values of the Hooge's parameter are in the order of  $\alpha_H \approx 1 \times 10^{-3}$ , which further confirms the high quality of the devices. The fabricated silicon nanowire structures are utilized for the electrical detection of the cardiac diseases biomarkers: human C-reactive protein (CRP) and cardiac troponin (cTn)I.

The CRP sensing experiments are performed on  $p^+ - p - p^+$  single silicon nanowire structures. Electrical characteristics of the fabricated nanowire biosensors are highly-sensitive to small changes in human C-reactive protein concentration. Binding of CRP antigen molecules to the antibodies, immobilized on the gate oxide, causes the drain current increase. Shifts of the drain current show linear dependence on concentration in semi-logarithmic scale in the range of CRP concentrations from 50 pg ml<sup>-1</sup> to 5 ng ml<sup>-1</sup>. The results are promising for biosensing applications, including monitoring and prediction of inflammations at the very early stages, where a healthy state can be easily recovered by applying the appropriate medical treatment.

Human cardiac troponin I is a gold standard biomarker that can be used for the early acute myocardial infarction (AMI) diagnosis. Thus, the rapid determination of the cTnI concentration in biological media is promising for future applications in medical diagnosis. The selective detection of cTnI molecules is performed on the  $n^+ - p - n^+$  Si NW array FET structures, fabricated using EBL. The performance of the fabricated devices is characterized using current-voltage (I-V) and noise measurements. Addition of the cTnI antigens induces shifts of the thresh-

old voltage to the positive voltage direction, which indicates the negative charge of the target molecules. The Si NW biosensor shows linear response in the semi-logarithmic scale to changes in the analyte concentration in the range from  $0.5 \text{ ng ml}^{-1}$  to  $10 \text{ ng ml}^{-1}$ . This concentration range should be used for the quantitative determination of cTnI concentration in bioliquids. A thorough analysis of the noise spectra revealed that the addition of the target cTnI molecules increases the noise level, thus indicating the presence of an additional noise source. The characteristics of this noise deviate considerably from the typical transistor noise behavior. Therefore, this excess noise is attributed to the charge fluctuations of troponin molecules originating from the antigen-antibody binding events. It should be emphasized that the Si NW sensor can be regenerated to its initial state by the addition of the low-pH glycine-HCl buffer, which opens prospects for biosensor reusability. Thus, the fabricated Si NW FET structures can serve as label-free reusable biosensors for rapid detection of cardiac biomarker molecules, and they are promising for applications in diagnostics and medicine.

This thesis also describes investigations of unique chemically synthesized ultrathin metallic nanowires and lithographic tunable metallic nanoconstrictions. While most conventional technologies allow fabrication of nanowire structures with sizes exceeding 10 nm, wet chemical synthesis allows producing of NWs with diameters of 2 nm or below. Moreover, tunable metallic nanoconstrictions allow the formation of atomic size wires. Studies of such kind systems are important for the fundamental understanding of transport in one-dimensional conductors and quantum channels and for applications in molecular electronics.

Bundles of ultrathin ( $\sim 2 \text{ nm}$  in diameter) gold nanowires (Au NWs) are fabricated by wet chemical synthesis and subsequently assembled and contacted to gold electrodes. The electrical performance of the fabricated devices is investigated using I-V measurements and noise characterization. I-V curves of the studied samples demonstrate quasi-linear behavior. Furthermore, the measured flicker noise power spectral density (PSD) is directly proportional to the current squared, which confirms the ohmic nature of the charge transport in Au NWs.  $1/f$  flicker noise is the dominant component in the entire frequency range from 1 Hz to 100 kHz. However, several generation-recombination (GR) components are revealed in the noise spectra in the case when NWs were covered with oleylamine molecules. The characteristic frequencies of these components extracted by fitting lie in the range  $f_0 = 3 - 570 \text{ Hz}$  ( $\tau_0 = 0.3 - 53 \text{ ms}$  respectively). The organic monolayers, assembled on the surface of the nanowires considerably affect the electrical transport and noise behavior of the gold nanowires. Thus, the high sensitivity of the noise properties of Au NWs to the surface chemical modification can be used as a powerful platform for molecular layer investigations.

Tunable metallic nanoconstriction devices are fabricated using advanced cleanroom technology involving lithography and etching techniques. Electrical transport and noise properties of bare-gold and molecule-modified nanoconstrictions are studied during the resistance tuning process for a wide range of sample resistances from  $10 \Omega$  to  $10 \text{ M}\Omega$  before and after constrict-

tion breaking. A comprehensive analysis of the flicker noise behavior is performed for different regimes of the sample conductance: from diffusive to tunneling, including ballistic regime. The specific to the transport regime dependence of the normalized flicker noise level on the system resistance  $S_I/I^2 \sim R^m$  is revealed. In the diffusive conductance regime ( $R \leq 300 \Omega$ ), the normalized noise PSD scales proportionally to  $R^2$ . At higher resistances, corresponding to the ballistic region, the magnitude of the exponent  $m$  decreases for bare-gold as  $S_I/I^2 \sim \sqrt{R}$  and for molecule-modified nanoconstrictions as  $S_I/I^2 \sim R$ . Surface modification of the sample by benzene-1,4-dithiol (BDT) molecules causes a decrease of the normalized flicker noise level in comparison with bare gold samples. Such behavior is attributed to the molecular layer influence on the total sample conductance at relatively high resistances and to the confinement of the configurational freedom of the gold atoms by the constriction stabilizing with the covalently bound BDT molecules. Analytical models are developed to describe the features and physical background of the  $1/f$  flicker noise behavior in diffusive, ballistic, and tunneling transport regimes. Parameters, extracted by fitting the experimental data to the models are useful for the characterization of such kind devices.

The fabricated Si NW FETs and metallic nanowires show high sensitivity to the target molecules, and thus are promising for biochemical applications. At the same time, further improvements can be achieved with careful choices of materials and thicknesses. In particular, high-k dielectric coatings, e.g.,  $\text{Al}_2\text{O}_3$  or  $\text{Ta}_2\text{O}_5$ , can be used to further enhance the performance, stability, and reliability of the Si NW FETs in electrolyte liquid environments. Furthermore, different nanowire geometries and configurations that can be obtained by different patterning techniques could be used to find optimal patterns with high surface-to-volume ratios (SVRs) and excellent signal-to-noise ratios (SNRs). Another important step to be done is the integration of the developed Si NW FETs with ultimate CMOS circuits. This will allow simultaneous multiplexed detection of various analytes on a single chip and facilitate the development of point-of-care (POC) devices for applications in future personal diagnostics.

Ultrathin gold nanowires and tunable gold nanoconstrictions can be used to further investigate the electrical and noise properties of quasi one-dimensional quantum systems as well as various organic molecules and molecular complexes. In particular, these structures can be used to model/build the basic functional components of molecular electronics circuits. Another important direction is the investigation of small biomolecules, e.g., peptides. Knowledge of electrical transport and noise in these molecules can provide insight into the charge transfer mechanisms that occur in big biomolecules, e.g., antibodies, and molecular machines.



## LIST OF ABBREVIATIONS

- AC** alternating current. 98
- AFM** atomic force microscopy. 3, 24, 25, 45, 46, 60, 77, 119
- AMI** acute myocardial infarction. 1, 85, 88, 90, 119
- APTES** 3-aminopropyl-triethoxysilane. 85
- AST** aspartate aminotransferase. 1
- Au NP** gold nanoparticle. 9, 10
- Au NW** gold nanowire. viii, 95–100, 116, 117, 120, 121
- BDT** benzene-1,4-dithiol. viii, 98, 101, 103, 105, 106, 113, 114, 117, 121
- BOE** buffered oxide etch. 44, 51
- BOX** buried oxide. 46, 47
- CK** creatine kinase. 1
- CMOS** complementary metal-oxide-semiconductor. vii, 2, 21, 22, 25, 41, 42, 60, 85, 94, 121
- CRP** C-reactive protein. viii, 1, 3, 85–89, 94, 119
- cTn** cardiac troponin. viii, 1, 3, 54, 85, 88–94, 119, 120
- CVD** chemical vapor deposition. 21, 23, 24
- DC** direct current. 29, 69–71, 77, 82, 94, 96
- DNA** deoxyribonucleic acid. 2, 4, 9, 19, 25, 26, 28, 40, 77
- e-beam** electron beam. 22, 43, 45, 58–60
- EBL** electron beam lithography. 3, 22, 24, 41, 43, 45, 54, 58, 60, 84, 94, 119
- ELISA** enzyme-linked immunosorbent assay. 1, 2, 10–14
- EUV** extreme ultraviolet lithography. 41
- FET** field-effect transistor. vii, viii, 2, 3, 14, 15, 18, 20–22, 25, 26, 28, 34, 38–41, 51, 53, 60–63, 69, 70, 72, 73, 75, 77–82, 84–94, 119–121

- FFT** Fast Fourier Transform. 70
- FIB** focused ion beam. xii, 3, 22, 50, 54, 60, 77, 85, 119
- FOTCS** 1H, 1H, 2H, 2H-Perfluorooctyltriethoxysilane. 46
- FZJ** Forschungszentrum Jülich GmbH. xi, 41
- GR** generation-recombination. viii, 33, 34, 37, 70, 73, 82, 96–100, 116, 120
- GUI** graphical user interface. 61, 65–68, 72, 75
- HNF** Helmholtz Nanoelectronic Facility. xii, 41
- HRP** horseradish peroxidase. 11
- HRTEM** high-resolution transmission electron microscopy. 99, 116
- I-V** current-voltage. vii, 40, 61–63, 66, 68, 70, 77, 80, 82, 86, 94, 97, 101, 102, 116, 119, 120
- ICP** inductively coupled plasma. 44, 49, 59
- ISFET** ion-selective field-effect transistor. 14, 15, 18–20, 25, 28, 78
- KOH** potassium hydroxide. 42, 44
- LDH** lactate dehydrogenase. 1
- LG** liquid-gated. vii, 3, 39, 84
- LOC** lab-on-a-chip. 18, 40, 94
- LOD** limit of detection. 19, 20, 25, 26, 28, 29, 38
- MB** myocardial band. 1
- MCBJ** mechanically controlled break junction. 24, 62, 72
- MCS** motion control system. 64, 65
- MOS** metal-oxide-semiconductor. 14–18, 34, 78
- NIL** nanoimprint lithography. vii, 22, 40, 41, 60
- NSL** nanosphere lithography. 54, 57
- NW** nanowire. vii, viii, 2, 3, 20–29, 38, 40, 41, 43, 45–55, 57, 60, 61, 70, 73, 75, 77–82, 84–86, 88, 89, 91, 94–96, 98–100, 104, 113, 116, 119–121

- PBS** phosphate-buffered saline. 38, 86, 87, 89–93
- PC** personal computer. 2, 64, 70, 101, 105
- PCR** polymerase chain reaction. 26
- PDMS** polydimethylsiloxane. 53, 73
- PI** polyimide. 52, 58, 60
- pI** isoelectric point. 90
- PMMA** poly(methyl methacrylate). 43, 58, 59
- PNA** peptide nucleic acid. 19, 26
- POC** point-of-care. 52, 121
- PSD** power spectral density. 37, 38, 82, 92, 97–100, 104–107, 112, 116, 117, 120, 121
- QCM** quartz-crystal microbalance. 26
- RIE** reactive ion etching. 3, 22, 43–45, 51, 55–60
- RTS** random telegraph signal. 35, 37–39, 82
- SAM** self-assembled monolayer. 6
- SDA** simultaneous data acquisition. 69, 70
- SEM** scanning electron microscopy. xii, 3, 49, 55–57, 59, 60, 64, 77, 85, 96, 97, 107, 108, 119
- Si NW** silicon nanowire. vii, viii, 2, 3, 20, 25–27, 38–41, 43, 49–51, 53, 60, 61, 73, 75, 77–94, 119–121
- SMU** source-measurement unit. 62, 63, 65, 67, 77, 86
- SNR** signal-to-noise ratio. 26, 38, 39, 75, 121
- SOI** silicon-on-insulator. vii, 22, 40, 46, 49, 51, 60
- SPR** surface plasmon resonance. 4–6, 8, 9, 26
- STM** scanning tunneling microscopy. 24
- SVR** surface-to-volume ratio. vii, 2, 20, 25, 28, 53, 54, 57, 85, 121
- TIR** total internal reflection. 7

**TMAH** tetramethylammonium hydroxide. 42, 44, 49, 51, 57, 60

**VLS** vapor-liquid-solid. 21

**WHO** World Health Organization. 1

**WPF** Windows Presentation Foundation. 61

## REFERENCES

- [1] S. Mythili and N. Malathi. “Diagnostic markers of acute myocardial infarction”. *Bio-medical reports* 3.6 (2015), pp. 743–748.
- [2] “Nomenclature and criteria for diagnosis of ischemic heart disease. Report of the Joint International Society and Federation of Cardiology/World Health Organization task force on standardization of clinical nomenclature.” *Circulation* 59.3 (1979), pp. 607–609.
- [3] E. Antman et al. “Myocardial infarction redefined - A consensus document of The Joint European Society of Cardiology/American College of Cardiology Committee for the redefinition of myocardial infarction”. *Journal of the American College of Cardiology* 36.3 (2000), pp. 959–969.
- [4] W. K. Lagrand et al. “C-reactive protein as a cardiovascular risk factor more than an epiphenomenon?” *Circulation* 100.1 (1999), pp. 96–102.
- [5] R. M. Lequin. “Enzyme immunoassay (EIA)/enzyme-linked immunosorbent assay (ELISA)”. *Clinical Chemistry* 51.12 (2005), pp. 2415–2418.
- [6] E. L. Chiswick et al. “Detection and Quantification of Cytokines and Other Biomarkers”. In: *Leucocytes: Methods and Protocols*. Ed. by R. B. Ashman. Totowa, NJ: Humana Press, 2012, pp. 15–30.
- [7] J. A. Nemzek, J. Siddiqui, and D. G. Remick. “Development and optimization of cytokine ELISAs using commercial antibody pairs”. *Journal of Immunological Methods* 255.1-2 (2001), pp. 149–157.
- [8] X.-J. Huang and Y.-K. Choi. “Chemical sensors based on nanostructured materials”. *Sensors and Actuators B: Chemical* 122.2 (2007), pp. 659–671.
- [9] J. F. Eschermann et al. “Action potentials of HL-1 cells recorded with silicon nanowire transistors.” *Applied Physics Letters* 95.8 (2009), p. 83703.
- [10] F. Patolsky et al. “Detection, stimulation, and inhibition of neuronal signals with high-density nanowire transistor arrays”. *Science* 313.5790 (Aug. 2006), pp. 1100–1104.
- [11] S. Pud. “Silicon nanowire structures for neuronal cell interfacing”. Monography. RWTH Aachen University, 2014, p. 151.
- [12] P. Feng et al. “Gas sensors based on semiconducting nanowire field-effect transistors”. *Sensors* 14.9 (2014), pp. 17406–17429.
- [13] Y. Cui et al. “Nanowire Nanosensors for Highly Sensitive and Selective Detection of Biological and Chemical Species”. *Science* 293.5533 (2001), pp. 1289–1292.

- [14] Z. Gao et al. “Silicon Nanowire Arrays for Label-Free Detection of DNA”. *Analytical Chemistry* 79.9 (2007), pp. 3291–3297.
- [15] G.-J. Zhang et al. “DNA Sensing by Silicon Nanowire: Charge Layer Distance Dependence”. *Nano Letters* 8.4 (2008), pp. 1066–1070.
- [16] A. Gao et al. “Silicon-nanowire-based CMOS-compatible field-effect transistor nanosensors for ultrasensitive electrical detection of nucleic acids”. *Nano Letters* 11.9 (2011), pp. 3974–3978.
- [17] G. Zheng et al. “Multiplexed electrical detection of cancer markers with nanowire sensor arrays”. *Nature Biotechnology* 23.10 (2005), pp. 1294–1301.
- [18] J. H. Chua et al. “Label-free electrical detection of cardiac biomarker with complementary metal-oxide semiconductor-compatible silicon nanowire sensor arrays”. *Analytical Chemistry* 81.15 (2009), pp. 6266–6271.
- [19] F. Patolsky et al. “Electrical detection of single viruses”. *Proceedings of the National Academy of Sciences* 101.39 (2004), pp. 14017–14022.
- [20] G. J. Zhang et al. “Silicon nanowire biosensor for highly sensitive and rapid detection of Dengue virus”. *Sensors and Actuators, B: Chemical* 146.1 (2010), pp. 138–144.
- [21] N. N. Mishra et al. “Ultra-sensitive detection of bacterial toxin with silicon nanowire transistor”. *Lab on a Chip* 8.6 (2008), pp. 868–871.
- [22] B. Ibarlucea et al. “Nanowire sensors monitor bacterial growth kinetics and response to antibiotics”. *Lab on a Chip* 17.24 (2017), pp. 4283–4293.
- [23] M. Dawber and J. F. Scott. “Models of electrode-dielectric interfaces in ferroelectric thin-film devices”. *Japanese Journal of Applied Physics, Part 1: Regular Papers and Short Notes and Review Papers* 41.11 B (2002), pp. 6848–6851.
- [24] K. Fuchs. “The conductivity of thin metallic films according to the electron theory of metals”. *Mathematical Proceedings of the Cambridge Philosophical Society* 34.1 (1938), pp. 100–108.
- [25] P. Shi et al. “Effect of molecular adsorption on the electrical conductance of single Au nanowires fabricated by electron-beam lithography and focused ion beam etching”. *Small* 6.22 (2010), pp. 2598–2603.
- [26] P. Damborský, J. Švitel, and J. Katrlík. “Optical biosensors”. *Essays in Biochemistry* 60.1 (2016). Ed. by P. Estrela, pp. 91–100.
- [27] B. Liedberg, C. Nylander, and I. Lunström. “Surface plasmon resonance for gas detection and biosensing”. *Sensors and Actuators* 4.C (1983), pp. 299–304.
- [28] J. Homola. “Surface plasmon resonance sensors for detection of chemical and biological species”. *Chemical Reviews* 108.2 (2008), pp. 462–493.

- [29] A. Leung, P. M. Shankar, and R. Mutharasan. "A review of fiber-optic biosensors". *Sensors and Actuators B: Chemical* 125.2 (2007), pp. 688–703.
- [30] S. Zeng et al. "A Review on Functionalized Gold Nanoparticles for Biosensing Applications". *Plasmonics* 6.3 (2011), pp. 491–506.
- [31] S. Link and M. A. El-Sayed. "Size and Temperature Dependence of the Plasmon Absorption of Colloidal Gold Nanoparticles". *The Journal of Physical Chemistry B* 103.21 (1999), pp. 4212–4217.
- [32] W. Zhao, M. A. Brook, and Y. Li. "Design of gold nanoparticle-based colorimetric biosensing assays". *ChemBioChem* 9.15 (2008), pp. 2363–2371.
- [33] J. Martínez et al. "Detection of serum immunoglobulins in wild birds by direct ELISA: A methodological study to validate the technique in different species using antichickens antibodies". *Functional Ecology* 17.5 (2003), pp. 700–706.
- [34] C. J. Landers et al. "Selected loss of tolerance evidenced by Crohn's disease-associated immune responses to auto- and microbial antigens". *Gastroenterology* 123.3 (2002), pp. 689–699.
- [35] M. Elvander et al. "Evaluation and application of an indirect ELISA for the detection of antibodies to bovine respiratory syncytial virus in milk, bulk milk, and serum". *Journal of Veterinary Diagnostic Investigation* 7.2 (1995), pp. 177–182.
- [36] T. Yun et al. "Development and application of an indirect ELISA for the detection of antibodies to novel duck reovirus". *Journal of Virological Methods* 220 (2015), pp. 55–59.
- [37] C. Kendall, I. Ionescu-Matiu, and G. R. Dreesman. "Utilization of the biotin/avidin system to amplify the sensitivity of the enzyme-linked immunosorbent assay (ELISA)". *Journal of Immunological Methods* 56.3 (1983), pp. 329–339.
- [38] T. G. Kingan. "A competitive enzyme-linked immunosorbent assay: Applications in the assay of peptides, steroids, and cyclic nucleotides". *Analytical Biochemistry* 183.2 (1989), pp. 283–289.
- [39] S. Paulie, P. Perlmann, and H. Perlmann. "Chapter 64 - Enzyme-Linked Immunosorbent Assay". In: *Cell Biology (Third Edition)*. Ed. by J. E. Celis. 3rd ed. Burlington: Academic Press, 2006. Chap. 64, pp. 533–538.
- [40] G. P. Rai and K. S. Venkateswaran. "Limitations and practical problems in enzyme-linked immunosorbent assays". *Defence Science Journal* 42.2 (1992), pp. 71–84.
- [41] S. Hosseini et al. "Advantages, Disadvantages and Modifications of Conventional ELISA". In: *Enzyme-linked Immunosorbent Assay (ELISA): From A to Z*. Singapore: Springer Singapore, 2018, pp. 67–115.

- [42] M. Yuqing, G. Jianguo, and C. Jianrong. “Ion sensitive field effect transducer-based biosensors”. *Biotechnology Advances* 21.6 (2003), pp. 527–534.
- [43] S. Kal and V. Bhanu Priya. “Design and modeling of ISFET for pH sensing”. In: *IEEE Region 10 Annual International Conference, Proceedings/TENCON*. IEEE, 2007, pp. 1–4.
- [44] S. Koch et al. “Protein detection with a novel ISFET-based zeta potential analyzer”. *Biosensors and Bioelectronics* 14.4 (1999), pp. 413–421.
- [45] B. H. van der Schoot and P. Bergveld. “ISFET based enzyme sensors”. *Biosensors* 3.3 (1987), pp. 161–186.
- [46] A. Offenhäusser and W. Knoll. “Cell-transistor hybrid systems and their potential applications”. *Trends in Biotechnology* 19.2 (2001), pp. 62–66.
- [47] S. V. Dzyadevich et al. “Application of enzyme field-effect transistors for determination of glucose concentrations in blood serum”. *Biosensors and Bioelectronics* 14.3 (1999), pp. 283–287.
- [48] G. Xu, J. Abbott, and D. Ham. “Optimization of CMOS-ISFET-based biomolecular sensing: Analysis and demonstration in DNA detection”. *IEEE Transactions on Electron Devices* 63.8 (2016), pp. 3249–3256.
- [49] A. Dinar, A. S. Mohd Zain, and F. Salehuddin. “Utilizing of CMOS ISFET sensors in DNA applications detection: A systematic review”. *Journal of Advanced Research in Dynamical and Control Systems* 10 (2018).
- [50] X. Cheng. “Nanostructures: Fabrication and applications”. In: *Nanolithography: The Art of Fabricating Nanoelectronic and Nanophotonic Devices and Systems*. Woodhead Publishing, 2013, pp. 348–375.
- [51] V. Pachauri and S. Ingebrandt. “Biologically sensitive field-effect transistors: from IS-FETs to NanoFETs”. *Essays In Biochemistry* 60.1 (2016), pp. 81–90.
- [52] I. Zadorozhnyi et al. “Effect of Gamma Irradiation on Dynamics of Charge Exchange Processes between Single Trap and Nanowire Channel”. *Small* 14.2 (2018), pp. 1–8.
- [53] B. Choi et al. “A bottom-gate silicon nanowire field-effect transistor with functionalized palladium nanoparticles for hydrogen gas sensors”. *Solid-State Electronics* 114 (Dec. 2015), pp. 76–79.
- [54] A. Gao et al. “Enhanced Sensing of Nucleic Acids with Silicon Nanowire Field Effect Transistor Biosensors”. *Nano Letters* 12.10 (Oct. 2012), pp. 5262–5268.
- [55] L. Mu et al. “Silicon Nanowire Field-Effect Transistors - A Versatile Class of Potentiometric Nanobiosensors”. *IEEE Access* 3 (2015), pp. 287–302.

- [56] M. García, P. Batalla, and A. Escarpa. “Metallic and polymeric nanowires for electrochemical sensing and biosensing”. *TrAC - Trends in Analytical Chemistry* 57 (2014), pp. 6–22.
- [57] Y. Huang et al. “Directed Assembly of One-Dimensional Nanostructures into Functional Networks”. *Science* 291.5504 (2001), pp. 630–633.
- [58] Z. Fan et al. “Wafer-scale assembly of highly ordered semiconductor nanowire arrays by contact printing”. *Nano Letters* 8.1 (2008), pp. 20–25.
- [59] M. Li et al. “Bottom-up assembly of large-area nanowire resonator arrays”. *Nature Nanotechnology* 3.2 (Feb. 2008), pp. 88–92.
- [60] L. Zhao et al. “Porous silicon and alumina as chemically reactive templates for the synthesis of tubes and wires of SnSe, Sn, and SnO<sub>2</sub>”. *Angewandte Chemie - International Edition* 45.2 (Jan. 2005), pp. 311–315.
- [61] P. Enzel, J. J. Zoller, and T. Bein. “Intrazeolite assembly and pyrolysis of polyacrylonitrile”. *Journal of the Chemical Society, Chemical Communications* 0.8 (Jan. 1992), pp. 633–635.
- [62] Y. Zhang et al. “Synthesis of alumina nanotubes using carbon nanotubes as templates”. *Chemical Physics Letters* 360.5-6 (July 2002), pp. 579–584.
- [63] C. Wang et al. “Controllable synthesis of Ni-catalyzed tetragonal tungsten nanowires via chemical vapor deposition”. *Progress in Natural Science: Materials International* 22.5 (Oct. 2012), pp. 514–519.
- [64] J. Benson et al. “Chemical vapor deposition of aluminum nanowires on metal substrates for electrical energy storage applications”. *ACS Nano* 6.1 (Jan. 2012), pp. 118–125.
- [65] J. C. Cuevas and E. Scheer. *Molecular Electronics an Introduction to Theory and Experiment*. WORLD SCIENTIFIC, 2010, p. 724.
- [66] J. K. Gimzewski and R. Möller. “Transition from the tunneling regime to point contact studied using scanning tunneling microscopy”. *Physical Review B* 36.2 (1987), pp. 1284–1287.
- [67] R. Frisenda et al. “Electrical properties and mechanical stability of anchoring groups for single-molecule electronics”. *Beilstein Journal of Nanotechnology* 6.1 (July 2015), pp. 1558–1567.
- [68] J. Coffey. *Semiconducting silicon nanowires for biomedical applications*. Woodhead Publishing, 2014.
- [69] A. Zhang and G. Zheng. “Semiconductor nanowires for biosensors”. In: *Semiconductor Nanowires: Materials, Synthesis, Characterization and Applications*. Woodhead Publishing, Jan. 2015, pp. 471–490.

- [70] F. Patolsky, G. Zheng, and C. M. Lieber. “Nanowire-Based Biosensors”. *Analytical Chemistry* 78.13 (2006), pp. 4260–4269.
- [71] K. K. Jensen et al. “Kinetics for Hybridization of Peptide Nucleic Acids (PNA) with DNA and RNA Studied with the BIAcore Technique”. *Biochemistry* 36.16 (1997), pp. 5072–5077.
- [72] L. He et al. “Colloidal Au-enhanced surface plasmon resonance for ultrasensitive detection of DNA hybridization”. *Journal of the American Chemical Society* 122.38 (2000), pp. 9071–9077.
- [73] X. Mao et al. “A nanoparticle amplification based quartz crystal microbalance DNA sensor for detection of Escherichia coli O157:H7”. *Biosensors and Bioelectronics* 21.7 (Jan. 2006), pp. 1178–1185.
- [74] E. Stern et al. “Importance of the debye screening length on nanowire field effect transistor sensors”. *Nano Letters* 7.11 (2007), pp. 3405–3409.
- [75] J. I. Hahm and C. M. Lieber. “Direct Ultrasensitive Electrical Detection of DNA and DNA Sequence Variations Using Nanowire Nanosensors”. *Nano Letters* 4.1 (2004), pp. 51–54.
- [76] T. Cohen-Karni et al. “Flexible electrical recording from cells using nanowire transistor arrays”. *Proceedings of the National Academy of Sciences* 106.18 (May 2009), pp. 7309–7313.
- [77] T. S. Pui et al. “CMOS-compatible nanowire sensor arrays for detection of cellular bioelectricity”. *Small* 5.2 (Dec. 2009), pp. 208–212.
- [78] Q. Qing et al. “Nanowire transistor arrays for mapping neural circuits in acute brain slices”. *Proceedings of the National Academy of Sciences* 107.5 (Feb. 2010), pp. 1882–1887.
- [79] X. Chen et al. “Nanowire-based gas sensors”. *Sensors and Actuators, B: Chemical* 177 (Feb. 2013), pp. 178–195.
- [80] F. A. Lewis. *The Palladium Hydrogen System*. Academic Press, 1967, p. 178.
- [81] M. Z. Atashbar and S. Singamaneni. “Room temperature gas sensor based on metallic nanowires”. In: *Sensors and Actuators B: Chemical*. Vol. 111-112. SUPPL. Elsevier, Nov. 2005, pp. 13–21.
- [82] F. Favier et al. “Hydrogen sensors and switches from electrodeposited palladium mesowire arrays”. *Science* 293.5538 (Sept. 2001), pp. 2227–2231.
- [83] L. Wang and E. Wang. “A novel hydrogen peroxide sensor based on horseradish peroxidase immobilized on colloidal Au modified ITO electrode”. *Electrochemistry Communications* 6.2 (Feb. 2004), pp. 225–229.

- [84] X. Gao et al. “A Nonenzymatic Hydrogen Peroxide Sensor Based on Silver Nanowires and Chitosan Film”. *Electroanalysis* 24.8 (July 2012), pp. 1771–1777.
- [85] L. Wang et al. “Amperometric glucose biosensor based on silver nanowires and glucose oxidase”. *Sensors and Actuators, B: Chemical* 176 (Jan. 2013), pp. 9–14.
- [86] D. Pradhan, F. Niroui, and K. T. Leung. “High-performance, flexible enzymatic glucose biosensor based on ZnO nanowires supported on a gold-coated polyester substrate”. *ACS Applied Materials and Interfaces* 2.8 (Aug. 2010), pp. 2409–2412.
- [87] N. K. Rajan, X. Duan, and M. A. Reed. “Performance limitations for nanowire/nanoribbon biosensors”. *Wiley Interdisciplinary Reviews: Nanomedicine and Nanobiotechnology* 5.6 (Nov. 2013), pp. 629–645.
- [88] N. K. Rajan et al. “1 / f Noise of Silicon Nanowire BioFETs”. *IEEE Electron Device Letters* 31.6 (2010), pp. 615–617.
- [89] M. J. Buckingham. *Noise in Electronic Devices and Systems*. Ellis Horwood series in electrical and electronic engineering. Horwood, 1985.
- [90] N. B. Lukyanchikova. *Noise Research in Semiconductor Physics*. Ed. by K. Jones. Amsterdam: Gordon and Breach Science Publishers, 1997.
- [91] J. B. Johnson. “Thermal Agitation of Electricity in Conductors”. *Phys. Rev.* 119.1 (Jan. 1927), pp. 97–109.
- [92] H. Nyquist. “Thermal Agitation of Electric Charge in Conductors”. *Phys. Rev.* 32.1 (1928), pp. 110–113.
- [93] W. Schottky. “Über spontane Stromschwankungen in verschiedenen Elektrizitätsleitern”. *Annalen der Physik* 362 (1918), pp. 541–567.
- [94] F. N. Hooge. “1/f noise is no surface effect”. *Physics Letters A* 29.3 (1969), pp. 139–140.
- [95] C. A. Richter et al. “Metrology for the electrical characterization of semiconductor nanowires”. *IEEE Transactions on Electron Devices* 55.11 (Nov. 2008), pp. 3086–3095.
- [96] E. Simoen and C. Claeys. “On the flicker noise in submicron silicon MOSFETs”. *Solid-State Electronics* 43.5 (1999), pp. 865–882.
- [97] E. Simoen and C. Claeys. “Random telegraph signal: A local probe for single point defect studies in solid-state devices”. In: *Materials Science and Engineering B: Solid-State Materials for Advanced Technology*. Vol. 91-92. Elsevier, Apr. 2002, pp. 136–143.
- [98] Z. Çelik-Butler, P. Vasina, and N. V. Amarasinghe. “A method for locating the position of oxide traps responsible for random telegraph signals in submicron MOSFETs”. *IEEE Transactions on Electron Devices* 47.3 (2000), pp. 646–648.

- [99] J. W. Lee et al. "Investigation of random telegraph noise in gate-induced drain leakage and gate edge direct tunneling currents of high- $\kappa$  MOSFETs". *IEEE Transactions on Electron Devices* 57.4 (2010), pp. 913–918.
- [100] V. Handziuk et al. "Features of noise in ultrathin gold nanowire structures". *Journal of Statistical Mechanics: Theory and Experiment* (2016), p. 054023.
- [101] Q. Guo et al. "Noise spectroscopy as an equilibrium analysis tool for highly sensitive electrical biosensing". *Applied Physics Letters* 101 (2012), p. 093704.
- [102] Y. Kutovyi et al. "Origin of noise in liquid-gated Si nanowire troponin biosensors". *Nanotechnology* 29.17 (Apr. 2018), p. 175202.
- [103] Y. Kutovyi et al. "Liquid-Gated Two-Layer Silicon Nanowire FETs: Evidence of Controlling Single-Trap Dynamic Processes". *Nano Letters* 18.11 (Oct. 2018), pp. 7305–7313.
- [104] G. Zheng, X. P. A. Gao, and C. M. Lieber. "Frequency Domain Detection of Biomolecules Using Silicon Nanowire Biosensors". *Nano Letters* 10.8 (Aug. 2010), pp. 3179–3183.
- [105] B. R. Goldsmith et al. "Monitoring Single-Molecule Reactivity on a Carbon Nanotube". *Nano Letters* 8.1 (Jan. 2008), pp. 189–194.
- [106] M. J. Kirton and M. J. Uren. "Capture and emission kinetics of individual Si:SiO<sub>2</sub> interface states". *Applied Physics Letters* 48.19 (1986), pp. 1270–1272.
- [107] K. S. Ralls et al. "Discrete Resistance Switching in Submicrometer Silicon Inversion Layers: Individual Interface Traps and Low-Frequency ( $1/f$ ?) Noise". *Phys. Rev. Lett.* 52.3 (1984), pp. 228–231.
- [108] J. Li et al. "Sensitivity Enhancement of Si Nanowire Field Effect Transistor Biosensors Using Single Trap Phenomena". *Nano Letters* 14.6 (June 2014), pp. 3504–3509.
- [109] C. Schinabeck et al. "Current noise in single-molecule junctions induced by electronic-vibrational coupling". *Physical Review B - Condensed Matter and Materials Physics* 90.7 (2014), pp. 1–16.
- [110] J. Brunner et al. "Random telegraph signals in molecular junctions." *Journal of physics. Condensed matter : an Institute of Physics journal* 26.47 (2014), p. 474202.
- [111] D. Xiang et al. "Noise characterization of metal-single molecule contacts". *Applied Physics Letters* 106.6 (2015), p. 063702.
- [112] W. Kern. "The Evolution of Silicon Wafer Cleaning Technology". *Journal of the Electrochemical Society* 137.6 (1990), pp. 1887–1892.
- [113] M. Itano et al. "Particle Removal from Silicon Wafer Surface in Wet Cleaning Process". *IEEE Transactions on Semiconductor Manufacturing* 6.3 (1993), pp. 258–267.

- [114] H. C. Liu, Y. H. Lin, and W. Hsu. "Sidewall roughness control in advanced silicon etch process". *Microsystem Technologies* 10.1 (Dec. 2003), pp. 29–34.
- [115] C. R. Yang, C. H. Yang, and P. Y. Chen. "Study on anisotropic silicon etching characteristics in various surfactant-added tetramethyl ammonium hydroxide water solutions". *Journal of Micromechanics and Microengineering* 15.11 (Nov. 2005), pp. 2028–2037.
- [116] M. Shikida et al. "Differences in anisotropic etching properties of KOH and TMAH solutions". *Sensors and Actuators, A: Physical* 80.2 (2000), pp. 179–188.
- [117] M. Kramkowska and I. Zobel. "Silicon anisotropic etching in KOH and TMAH with modified surface tension". *Procedia Chemistry* 1.1 (2009), pp. 774–777.
- [118] M. Noor, B. Bais, and B. Majlis. "The effects of temperature and KOH concentration on silicon etching rate and membrane surface roughness". *ICONIP '02. Proceedings of the 9th International Conference on Neural Information Processing. Computational Intelligence for the E-Age (IEEE Cat. No.02EX575)* (2002), pp. 524–528.
- [119] H. Schiff. "Nanoimprint lithography: An old story in modern times? A review". *Journal of Vacuum Science & Technology B: Microelectronics and Nanometer Structures* 26.2 (Mar. 2008), p. 458.
- [120] H. Schiff et al. "Controlled co-evaporation of silanes for nanoimprint stamps". *Nanotechnology* 16.5 (2005).
- [121] Y. Hirai et al. "Study of the resist deformation in nanoimprint lithography". *Journal of Vacuum Science & Technology B: Microelectronics and Nanometer Structures* 19.6 (2001), p. 2811.
- [122] N. Bogdanski et al. "Structure size dependent recovery of thin polystyrene layers in thermal imprint lithography". *Microelectronic Engineering* 84.5-8 (May 2007), pp. 860–863.
- [123] K. Kim et al. "Silicon nanowire biosensors for detection of cardiac troponin I (cTnI) with high sensitivity". *Biosensors and Bioelectronics* 77 (2016), pp. 695–701.
- [124] M. J. Deen and F. Pascal. "Electrical Characterization of Semiconductor Materials and Devices". In: *Springer Handbook of Electronic and Photonic Materials*. Ed. by S. Kasap and P. Capper. Cham: Springer International Publishing, 2017, p. 1.
- [125] Lucia Grüter. "Mechanical Controllable Break Junction in Liquid Environment: A Tool to Measure Single Molecules". PhD thesis. 2005, pp. 1–95.
- [126] V. Sydoruk. "Low-frequency noise and transport characteristics of nanostructures". PhD thesis. 2011, p. 168.
- [127] S. A. Vitusevich et al. "Excess low-frequency noise in AlGaN / GaN-based high-electron-mobility transistors". *Applied Physics Letters* 80.12 (2002), p. 2126.

- [128] S. Pud et al. “Single trap dynamics in electrolyte-gated Si-nanowire field effect transistors”. *Journal of Applied Physics* 115.23 (June 2014), p. 233705.
- [129] H. Seok and T. H. Park. “Integration of biomolecules and nanomaterials: Towards highly selective and sensitive biosensors”. *Biotechnology Journal* 6.11 (2011), pp. 1310–1316.
- [130] S. M. Sze and K. K. Ng. *Physics of semiconductor devices*. 3rd ed. Wiley-Interscience, 2006, p. 815.
- [131] E. Stern et al. “Label-free immunodetection with CMOS-compatible semiconducting nanowires”. *Nature* 445.7127 (2007), pp. 519–522.
- [132] S. Pud et al. “Liquid and back gate coupling effect: Toward biosensing with lowest detection limit”. *Nano Letters* 14.2 (Feb. 2014), pp. 578–584.
- [133] I. Zadorozhnyi et al. “Features of the gate coupling effect in liquid-gated Si nanowire FETs”. In: *2015 International Conference on Noise and Fluctuations, ICNF 2015*. IEEE, June 2015, pp. 1–4.
- [134] A. Hassibi, H. Vikalo, and A. Hajimiri. “On noise processes and limits of performance in biosensors”. *Journal of Applied Physics* 102.1 (2007).
- [135] G. D. Wilk, R. M. Wallace, and J. M. Anthony. “High- $\kappa$  gate dielectrics: Current status and materials properties considerations”. *Journal of Applied Physics* 89.10 (2001), pp. 5243–5275.
- [136] A. Motayed, S. Krylyuk, and A. V. Davydov. “Characterization of deep-levels in silicon nanowires by low-frequency noise spectroscopy”. *Applied Physics Letters* 99.11 (2011), pp. 1–4.
- [137] M. Schulz and A. Karmann. “Single, individual traps in mosfets”. *Physica Scripta* T35 (1991), pp. 273–280.
- [138] G. Ghibaudo et al. “Improved Analysis of Low Frequency Noise in Field-Effect MOS Transistors”. *physica status solidi (a)* 124.2 (1991), pp. 571–581.
- [139] L. K. J. Vandamme and F. N. Hooge. “What do we certainly know about 1/f noise in MOSTs?” *IEEE Transactions on Electron Devices* 55.11 (2008), pp. 3070–3085.
- [140] N. B. Lukyanchikova et al. “A study of noise in surface and buried channel SiGe MOS-FETs with gate oxide grown by low temperature plasma anodization”. *Solid-State Electronics* 46.12 (2002), pp. 2053–2061.
- [141] I. Zadorozhnyi et al. “Hooge’s parameter in Si NW FET with different widths”. In: *2017 International Conference on Noise and Fluctuations, ICNF 2017*. IEEE, 2017, pp. 1–4.
- [142] C.-C. Wu et al. “Label-free biosensing of a gene mutation using a silicon nanowire field-effect transistor”. *Biosensors and Bioelectronics* 25.4 (Dec. 2009), pp. 820–825.

- [143] K.-I. Chen, B.-R. Li, and Y.-T. Chen. “Silicon nanowire field-effect transistor-based biosensors for biomedical diagnosis and cellular recording investigation”. *Nano Today* 6.2 (Apr. 2011), pp. 131–154.
- [144] P. M. Ridker et al. “C-Reactive Protein and Other Markers of Inflammation in the Prediction of Cardiovascular Disease in Women”. *New England Journal of Medicine* 342.12 (Mar. 2000), pp. 836–843.
- [145] P. M. Ridker et al. “Comparison of C-Reactive Protein and Low-Density Lipoprotein Cholesterol Levels in the Prediction of First Cardiovascular Events”. *New England Journal of Medicine* 347.20 (Nov. 2002), pp. 1557–1565.
- [146] P. Salvo et al. “Sensors and Biosensors for C-Reactive Protein, Temperature and pH, and Their Applications for Monitoring Wound Healing: A Review”. *Sensors* 17.12 (Dec. 2017), p. 2952.
- [147] G. Boriani et al. “Evaluation of myocardial injury following repeated internal atrial shocks by monitoring serum cardiac troponin I levels”. *Chest* 118.2 (2000), pp. 342–347.
- [148] S. Korff, H. A. Katus, and E. Giannitsis. “Differential diagnosis of elevated troponins”. *Heart* 92.7 (2006), pp. 987–993.
- [149] T.-W. Lin et al. “Label-free detection of protein-protein interactions using a calmodulin-modified nanowire transistor.” *Proceedings of the National Academy of Sciences of the United States of America* 107.3 (Jan. 2010), pp. 1047–1052.
- [150] S. P. Lin et al. “A reversible surface functionalized nanowire transistor to study protein-protein interactions”. *Nano Today* 4.3 (June 2009), pp. 235–243.
- [151] P. L. Chiang et al. “Nanowire transistor-based ultrasensitive virus detection with reversible surface functionalization”. *Chemistry - An Asian Journal* 7.9 (Sept. 2012), pp. 2073–2079.
- [152] S. Vitusevich and I. Zadorozhnyi. “Noise spectroscopy of nanowire structures: fundamental limits and application aspects”. *Semiconductor Science and Technology* 32.4 (2017), p. 043002.
- [153] V. A. Sydoruk et al. “Electronic edge-state and space-charge phenomena in long GaN nanowires and nanoribbons”. *Nanotechnology* 28.13 (2017), p. 135204.
- [154] M. Kuscu and O. B. Akan. “Modeling and Analysis of SiNW FET-Based Molecular Communication Receiver”. In: *IEEE Transactions on Communications*. Vol. 64. 9. Sept. 2016, pp. 3708–3721.
- [155] I. Zadorozhnyi et al. “Single-trap kinetic in Si nanowire FETs: Effect of gamma radiation treatment”. In: *MRS Advances*. Vol. 1. 56. Materials Research Society, May 2016, pp. 3755–3760.

- [156] M. J. Kirton and M. J. Uren. "Noise in solid-state microstructures: A new perspective on individual defects, interface states and low-frequency ( $1/f$ ) noise". *Advances in Physics* 38.4 (Jan. 1989), pp. 367–468.
- [157] R. B. M. Schasfoort et al. "Possibilities and limitations of direct detection of protein charges by means of an immunological field-effect transistor". *Analytica Chimica Acta* 238.C (Jan. 1990), pp. 323–329.
- [158] M. Kaisti. "Detection principles of biological and chemical FET sensors". *Biosensors and Bioelectronics* 98 (2017), pp. 437–448.
- [159] K. Heo et al. "Large-scale assembly of silicon nanowire network-based devices using conventional microfabrication facilities". *Nano Letters* 8.12 (Dec. 2008), pp. 4523–4527.
- [160] S. Pud et al. "Features of transport in ultrathin gold nanowire structures". *Small* 9.6 (2013), pp. 846–852.
- [161] A. Bid, A. Bora, and A. K. Raychaudhuri. "1/F Noise in Nanowires". *Nanotechnology* 17 (2006), pp. 152–156.
- [162] P. Z. Coura et al. "On the structural and stability features of linear atomic suspended chains formed from gold nanowires stretching". *Nano Letters* 4.7 (2004), pp. 1187–1191.
- [163] F. Gasparyan. "Low-Frequency Noises in Nanotubes and Nanowires". *American Journal of Physics* 3.4 (2010), pp. 312–341.
- [164] A. Halder and N. Ravishankar. "Ultrafine single-crystalline gold nanowire arrays by oriented attachment". *Advanced Materials* 19.14 (2007), pp. 1854–1858.
- [165] M. Henny et al. "1/3-shot-noise suppression in diffusive nanowires". *Physical Review B* 59.4 (1999), pp. 2871–2880.
- [166] Y. Kondo and K. Takaynagi. "Synthesis and Characterization of Helical Multi-Shell Gold Nanowires". *Science* 289.5479 (2000), pp. 606–608.
- [167] Y. Lu et al. "Cold welding of ultrathin gold nanowires." *Nature nanotechnology* 5.3 (2010), pp. 218–224.
- [168] C. Wang et al. "Ultrathin Au nanowires and their transport properties". *Journal of the American Chemical Society* 130.28 (2008), pp. 8902–8903.
- [169] H. He and N. J. Tao. "Interactions of molecules with metallic quantum wires". *Advanced Materials* 14.2 (2002), pp. 161–164.
- [170] A. Kisner et al. "The Role of Oxidative Etching in the Synthesis of Ultrathin Single-Crystalline Au Nanowires". *Chemistry - A European Journal* 17.34 (Aug. 2011), pp. 9503–9507.

- [171] V. Sydoruk et al. “Noise and transport characterization of single molecular break junctions with individual molecule”. *Journal of Applied Physics* 112.1 (2012), p. 014908.
- [172] V. Mitin et al. *Noise and Fluctuations Control in Electronic Devices*. Ed. by A. Bajandin. American Scientific Publishers, 2002, pp. 11–30.
- [173] Z. Wu et al. “Scaling of  $1/f$  noise in tunable break junctions”. *Physical Review B - Condensed Matter and Materials Physics* 78.23 (2008), pp. 1–5.
- [174] S. Mourdikoudis and L. M. Liz-marza. “Oleylamine in Nanoparticle Synthesis”. *Chemistry of Materials* 25 (2013), pp. 1465–1476.
- [175] C. Bouet et al. “Flat colloidal semiconductor nanoplatelets”. *Chemistry of Materials* 25.8 (2013), pp. 1262–1271.
- [176] A. Aviram and M. A. Ratner. “Molecular Rectifiers”. *Chemical Physics Letters* 29.2 (1974), pp. 277–283.
- [177] V. Handziuk et al. “Noise spectroscopy of tunable nanoconstrictions: molecule-free and molecule-modified”. *Nanotechnology* 29.38 (2018), p. 385704.
- [178] J. G. Simmons. “Generalized Formula for the Electric Tunnel Effect between Similar Electrodes Separated by a Thin Insulating Film”. *Journal of Applied Physics* 34.6 (June 1963), pp. 1793–1803.
- [179] Y. Kim et al. “Benzenedithiol: A broad-range single-channel molecular conductor”. *Nano Letters* 11.9 (2011), pp. 3734–3738.
- [180] M. Tsutsui et al. “High-conductance states of single benzenedithiol molecules”. *Applied Physics Letters* 89.16 (2006), pp. 16–19.
- [181] F. N. Hooge. “Discussion of recent experiments on  $1/f$  noise”. *Physica* 60.1 (1972), pp. 130–144.
- [182] F. N. Hooge. “ $1/F$  Noise”. *Physica B+C* 83.1 (1976), pp. 14–23.
- [183] F. N. Hooge and A. M. H. Hoppenbrouwers. “Contact noise”. *Physics Letters A* 29.11 (1969), pp. 642–643.
- [184] A. M. H. Hoppenbrouwers and F. N. Hooge. “ $1/f$  noise of spreading resistances”. *Philips Research Reports* 25.2 (1970), pp. 69–80.
- [185] F. N. Hooge and A. M. H. Hoppenbrouwers. “ $1/f$  Noise in Continuous Thin Gold Films”. *Physica* 45 (1969), pp. 386–392.
- [186] L. K. J. Vandamme. “ $1/f$  noise of point contacts affected by uniform films”. *Journal of Applied Physics* 45.10 (1974), pp. 4563–4565.
- [187] L. K. J. Vandamme. “Noise as a diagnostic tool for quality and reliability of electronic devices”. *Electron Devices, IEEE Transactions on* 41.11 (1994), pp. 2176–2187.

- [188] M. Celasco et al. “Electrical conduction and current noise mechanism in discontinuous metal films. II. Experimental”. *Physical Review B* 17.6 (1978), pp. 2564–2574.
- [189] M. B. Ketchen and J. Clarke. “Temperature fluctuations in freely suspended tin films at the superconducting transition”. *Physical Review B* 17.1 (1978), pp. 114–121.
- [190] F. N. Hooge. “The relation between  $1/f$  noise and number of electrons”. *Physica B: Physics of Condensed Matter* 162.3 (1990), pp. 344–352.
- [191] J. K. E. Tunaley. “Conduction in a random lattice under a potential gradient”. *Journal of Applied Physics* 43.11 (1972), pp. 4783–4786.
- [192] G. P. Zhigal’skii. “ $1/f$  noise and nonlinear effects in thin metal films”. *Physics-Uspekhi* 40.6 (1997), pp. 599–622.
- [193] Y. V. Sharvin. “A possible method for studying fermi surfaces”. *Soviet Physics JETP* 21.3 (1965), pp. 655–656.
- [194] N. Agrait, A. L. Yeyati, and J. M. van Ruitenbeek. “Quantum properties of atomic-sized conductors”. *Physics Reports* 377.2-3 (2003), pp. 81–279.
- [195] L. K. J. Vandamme. “On the Calculation of  $1/f$  Noise of Contacts”. *Applied Physics* 11.1 (1976), pp. 89–96.
- [196] G. Coppus and L. K. J. Vandamme. “Spreading Resistance and  $1/f$  Noise of Embedded Ellipsoidal Electrodes in a Conductor”. *Applied Physics* 20 (1979), pp. 119–123.
- [197] L. K. J. Vandamme and J. C. F. Groot. “ $1/f$  noise and resistance between circular electrodes”. *Electron Lett.* 14.2 (1978), pp. 30–32.
- [198] L. K. J. Vandamme and A. H. de Kuijper. “Conductance noise investigations on symmetrical planar resistors with finite contacts”. *Solid State Electronics* 22.11 (1979), pp. 981–986.
- [199] C. Liang et al. “Resistance and  $1/f$  noise between circular contacts on conductive thin films” (2012).
- [200] L. K. J. Vandamme. “Characterization of contact interface film, sheet resistance and  $1/f$  noise with circular contacts”. *Fluctuation and Noise Letters* 10.04 (2011), pp. 467–484.
- [201] W. Ulbrich. “Resistor geometry comparison with respect to current noise and trim sensitivity”. *Electrocomponent Science and Technology* 4.2 (1977), pp. 63–68.
- [202] T. M. Chen and J. G. Rhee. “The effects of trimming on the current noise of thick film resistors”. *Solid State Technology* (1977), pp. 49–53.
- [203] A. P. J. Van Deursen and L. K. J. Vandamme. “Conductance noise on a square sample, calculation of the geometrical factor  $f(Q)$ ”. *Fluctuation and Noise Letters* 7.2 (2007), pp. L101–L110.

- 
- [204] H. Yoshida. “The Effect of Resistor Geometry on Current Noise”. *IEEE Transactions on Components, Hybrids, and Manufacturing Technology* 16.3 (1993), pp. 344–349.
- [205] R. S. Timsit. “Electrical conduction through small contact spots”. *IEEE Transactions on Components and Packaging Technologies* 29.4 (2006), pp. 727–734.
- [206] D. Xiang et al. “Gap size dependent transition from direct tunneling to field emission in single molecule junctions.” *Chemical communications (Cambridge, England)* 47.16 (2011), pp. 4760–4762.
- [207] G. P. Zhigal’skii and B. K. Jones. *Physical Properties of Thin Metal Films*. 1st ed. CRC Press, 2003, p. 232.



# PERSONAL PUBLICATION LIST

## Peer-reviewed journals

- [1] I. Zadorozhnyi, H. Hlukhova, Y. Kutovyi, **V. Handziuk**, N. Naumova, A. Offenhaeusser, and S. Vitusevich. “Towards pharmacological treatment screening of cardiomyocyte cells using Si nanowire FETs ”, **Biosensors and Bioelectronics**, (2019)  
[DOI: 10.1016/j.bios.2019.04.038](https://doi.org/10.1016/j.bios.2019.04.038)
- [2] Y. Kutovyi, I. Zadorozhnyi, **V. Handziuk**, H. Hlukhova, N. Boichuk, M. Petrychuk, and S. Vitusevich. “Temperature-Dependent Noise and Transport in Silicon Two-Layer Nanowire FETs”, **Physica Status Solidi B**, 1800636 (2019)  
[DOI: 10.1002/pssb.201800636](https://doi.org/10.1002/pssb.201800636)
- [3] Y. Kutovyi, I. Zadorozhnyi, **V. Handziuk**, H. Hlukhova, N. Boichuk, M. Petrychuk, and S. Vitusevich. “Liquid-Gated Two-Layer Silicon Nanowire FETs: Evidence of Controlling Single-Trap Dynamic Processes”, **Nano Letters**, 18(11), 7305-7313 (2018)  
[DOI: 10.1021/acs.nanolett.8b03508](https://doi.org/10.1021/acs.nanolett.8b03508)
- [4] **V. Handziuk**, F. Gasparyan, L. K. J. Vandamme, M. Coppola, V. Sydoruk, M. Petrychuk, D. Mayer, and S. Vitusevich. “Noise Spectroscopy of Tunable Nanoconstrictions: Molecule-Free and Molecule-Modified”, **Nanotechnology**, 29, 385704 (2018)  
[DOI: 10.1088/1361-6528/aad0b7](https://doi.org/10.1088/1361-6528/aad0b7)
- [5] Y. Kutovyi, I. Zadorozhnyi, H. Hlukhova, **V. Handziuk**, M. Petrychuk, A. Ivanchuk, and S. Vitusevich. “Origin of noise in liquid-gated Si nanowire troponin biosensors”, **Nanotechnology**, 29(17), 175202 (2018) [DOI: 10.1088/1361-6528/aaaf9e](https://doi.org/10.1088/1361-6528/aaaf9e)
- [6] I. Zadorozhnyi, J. Li, S. Pud, H. Hlukhova, **V. Handziuk**, Y. Kutovyi, M. Petrychuk, and S. Vitusevich. “Effect of Gamma Irradiation on Dynamics of Charge Exchange Processes between Single Trap and Nanowire Channel”, **Small**, 14(2), 1702516 (2018)  
[DOI: 10.1002/sml.201702516](https://doi.org/10.1002/sml.201702516)
- [7] D. S. Zhulai, S. A. Bugaychuk, G. V. Klimusheva, T. A. Mirnaya, V. N. Asaula, **V. I. Handziuk**, and S. A. Vitusevich “Structural characteristics of different types of nanoparticles synthesised in mesomorphic metal alkanoates”, **Liquid Crystals**, (2017)  
[DOI: 10.1080/02678292.2016.1276979](https://doi.org/10.1080/02678292.2016.1276979)
- [8] **V. Handziuk**, S. Pud, M. Coppola, A. Kisner, and S. Vitusevich “Features of noise in ultrathin gold nanowire structures”, **Journal of Statistical Mechanics: Theory and Experiment**, 054023 (2016) [DOI: 10.1088/1742-5468/2016/05/054023](https://doi.org/10.1088/1742-5468/2016/05/054023)

### Articles in conference journals

- [1] **V. Handziuk**, S. Pud, M. Coppola, A. Kisner, and S. Vitusevich. “Effect of molecular layers on charge transport in nanowires”, *Journal of Physics: Conference Series*, 864, 012063 (2017) [DOI :10.1088/1742-6596/864/1/012063](https://doi.org/10.1088/1742-6596/864/1/012063)
- [2] **V. Handziuk**, M. Coppola, V. Sydoruk, F. Gasparyan, D. Mayer, and S. Vitusevich. “Noise characterization of molecular junctions” *IEEE Conferences: 2017 International Conference on Noise and Fluctuations (ICNF)*, (2017) [DOI: 10.1109/ICNF.2017.7985930](https://doi.org/10.1109/ICNF.2017.7985930)
- [3] I. Zadorozhnyi, H. Hlukhova, Y. Kutovyi, M. Petrychuk, V. Sydoruk, **V. Handziuk**, and S. Vitusevich. “Analysis of charge states in GaN-based nanoribbons using transport and noise studies” *IEEE Conferences: 2017 International Conference on Noise and Fluctuations (ICNF)*, (2017) [DOI: 10.1109/ICNF.2017.7985995](https://doi.org/10.1109/ICNF.2017.7985995)

### Conference proceedings

- [1] **V. Handziuk**, Y. Kutovyi, H. Hlukhova, I. Zadorozhnyi, N. Boichuk, M. Petrychuk, and S. Vitusevich. “Nanoimprint Technology for Liquid-Gated Si Nanowire FET Biosensors: Noise Spectroscopy Analysis” **Accepted for 25<sup>th</sup> International Conference on Noise and Fluctuations (ICNF 2019)**, *Neuchâtel, Switzerland 2019*
- [2] Y. Kutovyi, I. Zadorozhnyi, **V. Handziuk**, N. Boichuk, H. Hlukhova, M. Petrychuk, and S. Vitusevich. “Single Electron Dynamics in Liquid-Gated Two-Layer Silicon Nanowire Structures: Towards Biosensing with Enhanced Sensitivity” **International Conference on Solid State Devices and Materials (SSDM-2018)**, *Tokyo, Japan 2018*
- [3] Y. Kutovyi, I. Zadorozhnyi, **V. Handziuk**, H. Hlukhova, M. Petrychuk, and S. Vitusevich. “Temperature-dependent noise and transport in two-layer silicon nanowire FETs” **34<sup>th</sup> International Conference on the Physics of Semiconductors**, *Montpellier, France 2018*
- [4] **V. Handziuk**, F. Gasparyan, L. K. J. Vandamme, M. Coppola, V. Sydoruk, M. Petrychuk, D. Mayer, and S. Vitusevich. “Transport Regimes in Tunable Gold Nanoconstrictions: Proposed Solution by Low-Frequency Noise Spectroscopy” **8<sup>th</sup> International Conference on Unsolved Problems on Noise (UPON 2018)**, *Gdańsk, Poland 2018*
- [5] Y. Kutovyi, I. Zadorozhnyi, **V. Handziuk**, H. Hlukhova, M. Petrychuk, and S. Vitusevich. “The impact of biomolecules binding on low-frequency noise in Si NW FET biosensors” **8<sup>th</sup> International Conference on Unsolved Problems on Noise (UPON 2018)**, *Gdańsk, Poland 2018*

- 
- [6] **V. Handziuk**, M. Coppola, V. Sydoruk, F. Gasparyan D. Mayer, and S. Vitusevich. “Noise Characterization of Molecular Junctions” **24<sup>th</sup> International Conference on Noise and Fluctuations (ICNF 2017)**, *Vilnius, Lithuania 2017*
- [7] **V. Handziuk**, S. Pud, M. Coppola, A. Kisner, and S. Vitusevich. “Effect of Molecular Layers on Charge Transport in Nanowires” **33<sup>rd</sup> International Conference on the Physics of Semiconductors (ICPS 2016)**, *Beijing, China 2016* (with **The Best Student Poster Award**)
- [8] **V. Handziuk**, S. Pud, A. Kisner, and S. Vitusevich. “Features of Noise in Ultrathin Gold Nanowire Structures” **7<sup>th</sup> International Conference on Unsolved Problems on Noise (UPON 2015)**, *Barcelona, Spain 2015*